

**DESIGN AND OPTIMIZATION OF FILAMENT WOUND
COMPOSITE PRESSURE VESSELS**

Proefschrift

ter verkrijging van de graad van doctor
aan de Technische Universiteit Delft,
op gezag van de Rector Magnificus prof.ir. K.C.A.M. Luyben,
voorzitter van het College voor Promoties,
in het openbaar te verdedigen op woensdag 22 februari 2012 om 12.30 uur

door

Lei ZU

Master of Science in Engineering Mechanics
Xi'an University of Technology, Xi'an, China
geboren te Anqing, China

Dit proefschrift is goedgekeurd door de promotor:

Prof. ir. A. Beukers

Copromotor:

Dr. ir. S. Koussios

Samenstelling promotiecommissie:

Rector Magnificus, voorzitter instellingen allemaal volledig uitschrijven

Prof. ir. A. Beukers, Technische Universiteit Delft, promotor

Dr. ir. S. Koussios, Technische Universiteit Delft, copromotor

Prof. dr. S.C. Mantell, University of Minnesota

Prof. dr. X. He, Harbin Institute of Technology

Prof. dr. ir. R. Akkerman, Universiteit Twente

Prof. dr. ir. M.J.L. van Tooren, Technische Universiteit Delft

Prof. dr. ir. R. Marissen, Technische Universiteit Delft

ISBN: 978-90-8891-382-2

Copyright © 2012: L. Zu

All rights reserved. No part of the material protected by this copyright notice may be reproduced or utilised in any form or by any means, electronic or mechanical, including photocopying, recording or by any information storage and retrieval system, without the prior written permission of the author.

Cover design: D. Xiao

Printed in the Netherlands by Uitgeverij BOXPress, Oosterwijk

Summary

One of the most important issues for the design of filament-wound pressure vessels reflects on the determination of the most efficient meridian profiles and related fiber architectures, leading to optimal structural performance. To better understand the design and optimization of filament-wound pressure vessels, in this dissertation we present an overview and comprehensive treatment for toroidal and domed pressure vessels. Since the geodesic winding has severe boundary conditions that confine the layup optimization, the non-geodesic trajectories are here extensively applied to enlarge the design space.

Designing optimal laminate layup is not the only issue; the fibers must be stable on the mandrel and be exactly placed along trajectories as predetermined by structural design. To obtain a stable fiber trajectory, the stability-ensuring conditions are formulated in terms of both fiber slippage and bridging tendencies; these conditions provide the basic criteria for the subsequent design of various pressure vessels. The mathematical description of the geodesics and non-geodesics on a generic shell of revolution is briefly presented.

A generalized optimality criterion that is adapted to various optimal design problems for pressure vessels is elaborated. This condition originates from the idea that the optimal pressure vessels are governed by the condition of equal shell strains, or equivalently, zero shear stress at lamina level. The specific equations and the feasible intervals of the optimality condition are also given for several types of laminations.

The basic equations of the netting analysis and their applications to the design of circular toroidal pressure vessels are here outlined. The influence of the fiber layup and the geometry of the toroid on the stability of netting-dictated fiber trajectories are evaluated.

A new possibility to improve the vessel performance can be offered by the application of adapted cross-sectional shapes instead of the conventional shapes. The isotensoid design, which leads to equal fiber tension throughout the whole structure, is conducted to determine the netting-based optimal cross-sectional shapes. The governing equations for determining

Summary

geodesic and non-geodesic isotensoids are respectively derived and their feasible intervals are also determined. In addition, a simplified method for designing isotensoid pressure vessels with unequal polar opening is also outlined, with the aid of non-geodesic trajectories.

The optimal design, based on orthotropic plate theory, is divided into two basic approaches: numerical and semi-analytical methods. A numerical optimization method is specially designed for determining the optimal meridian profiles of bellow-shaped pressure vessels. An integral design method is proposed for circular toroidal pressure vessels, with emphasis on the determination of the optimal non-geodesic trajectories and winding patterns. Based on the previously-obtained (generalized) optimality condition, semi-analytical design methods are presented for the determination of the optimal meridian profiles for continuum-based domes and toroids, respectively. The optimal cross sectional shapes lead to significantly improved vessel performance.

An extensive study of the manufacturing of filament wound toroidal pressure vessels is conducted. We here emphasize the importance of suitable winding patterns for obtaining an optimal pressure vessel, and we accordingly derived the "Diophantine"-alike pattern equations that produced such patterns. The main objective of the method presented here is to match the structure-dictated number of wound circuits to the solution of the pattern equations for determining the proper winding velocities of the mandrel and the feed eye. In addition, depending on the aimed lathe machine configuration, the underlying geometric model of the new-fashioned toroidal winder is outlined and the kinematic solutions for coupling the motion of the mandrel and the feed eye are also given. Simulations of geodesic and non-geodesic trajectories are performed for winding toroidal pressure vessels.

Last but not least, since ultra-high pressure vessels require thick-walled designs, this dissertation is also extended to three-dimensional problems where the through-thickness stress gradient is taken into account. A three-dimensional (3D) elasticity analysis on multi-layered thick-walled pressure vessels is here addressed. In order to better understand the design approaches of thick-walled composite cylinders and find ways to improve their structural performance, a review is devoted to 3D elasticity approaches for obtaining the exact solutions of the stresses and strains induced by internal pressure, and the effects of hygrothermal loading and twisting. The 3D effective elastic constants and most frequently used failure criteria for cylindrically anisotropic materials are also presented.

Samenvatting

Eén van de belangrijkste aspecten van het ontwerp van gewikkelde drukvaten is de bepaling van de meest efficiënte meridiaanprofielen en gerelateerde vezelarchitecturen die leiden tot de optimale constructieve prestatie. Voor een beter begrip van het ontwerp en de optimalisatie van gewikkelde drukvaten presenteert deze dissertatie een uitvoerige behandeling van toroïde- en koepelvormige drukvaten. Vanwege het feit dat geodetische banen strikte grenswaarden met zich meebrengen die de optimalisatie van de laminaatopbouw sterk beperken, worden niet-geodetische banen veelvuldig toegepast om de ontwerpruimte te vergroten.

Het ontwerp van de optimale laminaatopbouw is niet het enige aspect dat in ogenschouw moet worden genomen. Het vezelmateriaal moet tevens stabiel op de mal gepositioneerd zijn en bovendien exact geplaatst zijn langs de uit het constructieve ontwerp afgeleide banen. Om een stabiele vezelbaan te verkrijgen, worden condities geformuleerd waardoor de stabiliteit gegarandeerd is als functie van zowel vezelslip als overbruggingsneigingen; deze condities leveren de basiscriteria voor het daaropvolgende ontwerp van diverse drukvaten. Een korte mathematische beschrijving van geodeten en niet-geodeten op een algemeen roterende schaal wordt kort gepresenteerd.

Een veralgemeniseerd optimalisatie criterium wordt uitgewerkt en toegepast op diverse ontwerp problemen. Dit criterium komt voort uit het idee dat optimale drukvaten worden gedefinieerd door de conditie van gelijke schaalrekken of - hieraan gelijkstaand - de afwezigheid van schuifspanningen op laminaatniveau. De specifieke vergelijkingen en de uitvoerbare intervallen van het optimalisatie criterium worden ook behandeld voor verschillende typen laminaten.

De basisvergelijkingen van de ‘netting analysis’ en de toepassing hiervan op het ontwerp van circelvormige toroïde drukvaten worden besproken. De invloed van de lay-up en de geometrie van de toroïde op de stabiliteit van de netting-gedomineerde vezelbanen worden

Samenvatting

geëvalueerd.

Er wordt een nieuwe mogelijkheid gepresenteerd ter verbetering van de prestatie van het drukvat welke berust op de toepassing van aangepaste doorsnedes in plaats van conventionele doorsnedes. Het isotensoïde ontwerp welke leidt tot gelijke vezelspanning door de gehele structuur, wordt uitgevoerd ter bepaling van de netting-gebaseerde optimale doorsnedes. De vergelijkingen voor de bepaling van geodetische en niet-geodetische isotensoïdes worden afgeleid en tevens worden hun uitvoerbare intervallen bepaald. Aanvullend wordt een vereenvoudigde methode uiteengezet voor het ontwerp van isotensoïde drukvaten met ongelijke poolopeningen door gebruikmaking van niet-geodetische banen.

Het optimale ontwerp gebaseerd op de orthotrope plaat theorie wordt verdeeld in een tweetal basis methodes: numerieke en semi-analytische methodes. Een numerieke optimalisatie methode wordt speciaal opgesteld om de optimale meridiaanprofielen van balgvormige drukvaten te bepalen. Een integrale ontwerpmethode voor circelvormige toroïde drukvaten wordt voorgesteld, met de nadruk op de bepaling van de optimale niet-geodetische banen en wikkelpatronen. Gebaseerd op de eerder verkregen (gegeneraliseerde) optimalisatie conditie worden semi-analytische ontwerpmethodes gepresenteerd ter bepaling van de optimale meridiaanprofielen voor op continuüm gebaseerde koepelvormen en toroïdes. De optimale doorsnedes leiden tot significant verbeterde drukvaten.

Er wordt een omvangrijke studie uitgevoerd naar de productie van gewikkelde toroïde drukvaten. De nadruk ligt hier op de belangrijkheid van bruikbare wikkelpatronen om optimale drukvaten te verkrijgen en dienovereenkomstig leiden we de Diophantische patroonvergelijkingen af die dergelijke wikkelpatronen tot gevolg hebben. Het belangrijkste doel van die hier gepresenteerde methode is om het door de structuur gedomineerde aantal gewikkelde circuits passend te maken met de oplossing voor de patroonvergelijkingen ter bepaling van de juiste wikkelsnelheden van de mal en het wikkeloog. Dienovereenkomstig, afhankelijk van de beoogde machine configuratie, wordt een uiteenzetting gegeven van het onderliggende geometrische model van de nieuw ontworpen toroïde wikkelmachine en tevens worden de kinematische oplossingen voor de gekoppelde beweging van mal en wikkeloog gepresenteerd. Simulaties van geodetische en niet-geodetische banen worden uitgevoerd voor het wikkelen van toroïde drukvaten.

Tenslotte, omdat zeer hoge drukvaten dikwandige ontwerpen vereisen, is deze dissertatie verder uitgebreid met driedimensionale problemen waarbij de spanningsgradiënt door de dikte ook een rol speelt. Een driedimensionale elasticiteitsanalyse op meervoudig gelaagde dikwandige drukvaten wordt hier behandeld. Om de ontwerpbenaderingen van dikwandige

Samenvatting

composieten cilinders better te begrijpen en manieren te vinden om hun constructieve eigenschappen te verbeteren wordt een bespreking gewijd aan driedimensionale elasticiteitsbenaderingswijzen om de exacte oplossingen van de spanningen en rekken geïnduceerd door de interne druk te verkrijgen. Tevens worden de effecten van hygrothermale belasting en verdraaiing bestudeerd. Daarnaast worden de driedimensionale effectieve elastische constanten en de meest toegepaste faalcriteria voor cilindrische anisotrope materialen gepresenteerd.

Contents

Summary	i
Samenvatting	iii
List of Figures	xiii
List of Tables	xix
Chapter 1	
Introduction and Objectives	1
1.1 Introduction to Filament Winding	1
1.1.1 Brief history	1
1.1.2 Processing technology	4
1.1.3 Materials	5
1.1.4 Liner / Mandrel	8
1.1.5 Winding patterns	8
1.2 Composite Pressure Vessels	10
1.2.1 Brief introduction	10
1.2.2 Filament wound dome heads for pressure vessels	12
1.2.3 Toroidal pressure vessels for compressed hydrogen storage	14
1.2.4 Thick-walled pressure vessels	17
1.3 Thesis Outline	18
References	21
I FUNDAMENTALS	29
Chapter 2	
Fiber Trajectories and Their Stability	29
2.1 Introduction	29
2.2 Fiber Stability on a Surface	29
2.3 Topics Related to Differential Geometry	33
2.3.1 Fundamental forms	33
2.3.2 Curvatures	34
2.3.3 Length-minimizing curves – geodesics	36

Contents

2.4 Geodesics and Non-geodesics on Generic Shells of Revolution	38
2.5 Conclusions	41
References	41
Chapter 3	
Basic Design Theories and Optimality Conditions.....	43
3.1 Introduction	43
3.2 Netting Analysis.....	44
3.3 Classical Lamination Theory (CLT) [4]	47
3.4 Optimality Conditions	51
3.5 Optimality Conditions for Various Types of Laminations	54
3.5.1 Liner / $\pm\alpha$ layers	54
3.5.2 Liner / $\pm\alpha$ layers / 90° layers	56
3.5.3 Liner / $\pm\alpha$ layers / 0° layers	57
3.5.4 Liner / 90° layers / 0° layers	58
3.6 Feasible Range of Optimality Conditions	59
3.6.1 Boundary conditions for monolithic fiber laminates.....	59
3.6.2 Boundary conditions for fiber metal laminates (FML).....	61
3.6.3 Boundary conditions for hybrid fiber laminates	62
3.7 Conclusions	63
References	63
II NETTING-BASED APPROACHES	65
Chapter 4	
Netting-based designs for circular toroidal pressure vessels	65
4.1 Introduction	65
4.2 Minimum Weight Design.....	67
4.2.1 Basic geometry and governing equations	67
4.2.2 Optimization model.....	71
4.2.3 Solution procedure	74
4.2.4 Design example	76
4.3 Fiber Trajectory Stability of Toroidal Pressure Vessels	79
4.4 Conclusions	83
References	84
Chapter 5	
Geodesic-isotensoids.....	87

5.1 Introduction	87
5.2 Geodesic-isotenoid Domes	88
5.2.1 Geometry and governing equations.....	88
5.2.2 Feasible intervals of governing equation	91
5.3 Geodesic-isotenoid Toroids	93
5.3.1 Cross-sectional shapes.....	93
5.3.2 Evaluation and comparison	94
5.4 Conclusions	98
References	98
Chapter 6	
Non-geodesic-isotenoids	101
6.1 Introduction	101
6.2 Isotenoid Pressure Vessels with Unequal Polar Openings	103
6.2.1 Governing equations	103
6.2.2 Structural performance	106
6.2.3 Feasibility and design approach	107
6.2.4 Results and discussion.....	108
6.3 Non-geodesic-isotenoid Toroids.....	111
6.3.1 Governing equations	111
6.3.2 Cross sections and related winding angles.....	112
6.3.3 Structural performance improvement.....	115
6.4 Conclusions	116
References	117
III CONTINUUM-BASED APPROACHES	119
Chapter 7	
Bellow-shaped Pressure Vessels.....	119
7.1 Introduction	119
7.2 Mathematical Model	121
7.2.1 Description of the meridian profile	121
7.2.2 Objective function	123
7.2.3 Constraints.....	124
7.2.4 Optimization procedure.....	125
7.3 Results and Discussion.....	128
7.4 Conclusions	128

Contents

References	131
Chapter 8	
Continuum-based Domes for Pressure Vessels	133
8.1 Introduction	133
8.2 Optimal Meridian Profiles.....	135
8.3 Feasible Intervals.....	137
8.4 Results and Discussion.....	139
8.4.1 Structural performance	139
8.4.2 Determination of laminate thickness.....	140
8.4.3 Meridian shapes.....	141
8.4.4 Structural performance evaluation	142
8.5 Conclusions	146
References	147
Chapter 9	
Non-geodesics-based Circular Toroidal Pressure Vessels.....	151
9.1 Introduction	151
9.2 Non-geodesics on a Torus	153
9.3 Optimal Design for Minimum Structural Mass.....	156
9.4 Optimization Solution Procedure	157
9.5 Results and Discussion.....	159
9.6 Conclusions	165
References	166
Chapter 10	
Continuum-based Optimal Cross Sections of Toroidal Pressure Vessels.....	169
10.1 Introduction	169
10.2 General Optimal Cross-sections.....	170
10.3 Volume, Weight and Thickness	173
10.4 Evaluation and Comparison	176
10.5 Conclusions	180
References	181
Chapter 11	
Integral Design and Manufacturing of Toroidal Pressure Vessels.....	183
11.1 Introduction	183
11.2 Structural Optimization	184

11.3 Kinematic Solutions for Toroidal Winders.....	186
11.4 Uniform and Full Coverage.....	188
11.5 Numerical Examples and Simulation.....	189
11.6 Conclusions.....	193
References.....	193
IV THICK-WALLED PRESSURE VESSELS.....	195
Chapter 12	
Three-dimensional Stress, Strain & Displacement Analysis.....	195
12.1 Introduction.....	195
12.2 Three-dimensional Stress and Strain.....	196
12.2.1 Direct solution method.....	199
12.2.2 Stress function approach.....	206
12.3 Hygrothermal Effects.....	208
12.4 Twisting.....	211
12.5 Effective Elastic Properties.....	212
12.6 Three-dimensional Failure Criteria.....	217
12.6.1 Tensor polynomial interactive criteria.....	218
12.6.2 Failure modes based failure theories.....	221
12.6.3 Reviews of failure criteria.....	227
12.7 Numerical Examples and Discussion.....	227
12.8 Conclusions.....	239
References.....	242
Chapter 13	
Conclusions and Recommendations.....	249
13.1 Introduction.....	249
13.2 Conclusions.....	250
13.2.1 Fiber stability analysis for winding toroidal pressure vessels.....	250
13.2.2 Netting-based design of toroidal pressure vessels.....	250
13.2.3 Isotensoid pressure vessels with unequal polar openings.....	251
13.2.4 Continuum-based design of pressure vessels.....	251
13.2.5 Integral design and manufacturing of toroidal pressure vessels.....	252
13.2.6 Elasticity solution of thick-walled filament wound pressure vessels.....	252
13.3 Achievements.....	253
13.4 Recommendations and Future Directions.....	254

Contents

13.4.1 Strength prediction based on progressive failure analysis	254
13.4.2 Closed-form solution of composite toroidal shells	254
13.4.3 Finite element analyses	254
13.4.4 Accurate estimation for laminate thickness distribution	255
13.4.5 Shape optimization for thick-walled filament wound domes.....	255
13.4.6 Transverse shearing, liner elastoplasticity and stacking sequence.....	255
13.4.7 Advanced toroidal winders.....	256
13.4.8 Other vessel shapes, computer software and experiment.....	256
Acknowledgements.....	257
Curriculum Vitae	259
List of Publications.....	261
Journal Papers	261
Conference Proceedings.....	262
Nomenclature.....	265
Abbreviations	265
Matrices & Vectors	265
Scalars (Latin)	266
Scalars (Greek).....	268
Indices	269
Special Functions & Operations.....	270

List of Figures

Fig. 1.1: A lathe-like filament winding machine [11]	3
Fig. 1.2: Schematic of a computer-controlled winder having two degrees of freedom [15].....	3
Fig. 1.3: 6-Axis filament winding machine (Courtesy of McClean Anderson, Inc.) [18]	3
Fig. 1.4: Filament wound cylindrical (a) and spherical (b) pressure vessel.....	5
Fig. 1.5: Three basic winding patterns	10
Fig. 1.6: A pressure vessel dome and its winding path	12
Fig. 1.7: Relation between compression energy and service pressure [48]	15
Fig. 1.8: A toroidal pressure vessel [81].....	16
Fig. 2.1: An infinitesimally small element of a tensioned fiber on an arbitrary surface.....	31
Fig. 2.2: Geometrical relations for an elementary part of the fiber curve on a surface	34
Fig. 2.3: A general shell of revolution	39
Fig. 3.1: Cylindrical section overwound by helical and hoop winding.....	44
Fig. 3.2: A netting-based element of helically and hoop wound fibers	45
Fig. 3.3: Global and material axes of an angle lamina	46
Fig. 3.4: A symmetric laminate under in-plane loads (N_φ , N_θ).....	50
Fig. 4.1: Geometry of a toroidal pressure vessel with its system of coordinates	67
Fig. 4.2: An elementary orthogonal region belonging to a toroidal shell	68
Fig. 4.3: Part of a toroidal shell loaded by an internal pressure p	68
Fig. 4.4: Schematics of the helical and hoop winding layers	69
Fig. 4.5: Stress distributions relative to the stress magnitude at the equator ($R/r = 4$)	73
Fig. 4.6: Flow chart of the optimal design procedure	74
Fig. 4.7: Flow chat of the verification process for fiber stability.....	75
Fig. 4.8: Helical winding angle distributions based on the present method, geodesics and semi-geodesics ($\lambda = 0.5, 1$ and 1.5), respectively	77
Fig. 4.9: Slippage coefficient distribution of the obtained optimal fiber trajectories	77

List of Figures

Fig. 4.10: Critical winding angle envelope for ensuring non-bridging of fibers	78
Fig. 4.11: Helical and hoop layer thickness distributions along the meridional direction.....	78
Fig. 4.12: Conventionally used geodesics and the present optimal fiber trajectories	78
Fig. 4.13: Winding angle distributions for the single helical winding ($\eta = 0$) and the helical and hoop winding ($\eta = 0.5$)	80
Fig. 4.14: Minimum non-bridging-ensuring angles as compared to winding angles of the netting-based fiber trajectories	81
Fig. 4.15: Feasible field of $\{k, \eta\}$ -combinations for ensuring non-bridging (shaded area)	82
Fig. 4.16: Slippage tendency distributions along the meridional direction.....	82
Fig. 4.17: Maximum slippage coefficients of the obtained fiber trajectories for the most common K and η	83
Fig. 5.1: Loads and geometry of an isotensoidal meridian	89
Fig. 5.2: Influence of the axial force on the resulting isotensoid meridian profile	90
Fig. 5.3: Feasible $\{a, \rho_0\}$ -field (shaded area).....	92
Fig. 5.4: Cross-sectional shape for a toroidal pressure vessel [6, 7].....	93
Fig. 5.5: Resulting cross sectional shapes for iso-toroids with various ρ_0	94
Fig. 5.6: Relative bend radii for isotensoid and circular toroids at equal volumes.....	95
Fig. 5.7: Internal volumes of isotensoid and circular toroids with ρ_0	96
Fig. 5.8: Cross-sectional shapes of the isotensoid and circular toroids at equal volumes	97
Fig. 5.9: Dimensionless masses of isotensoid and circular toroids at equal volumes.....	97
Fig. 6.1: Meridian profile of a pressure vessel with unequal polar openings	103
Fig. 6.2: Loads and geometry of a shell meridian.....	103
Fig. 6.3: Elementary fiber force equilibrium [9, 10].....	104
Fig. 6.4: An infinitesimal ring element	104
Fig. 6.5: Isotensoid meridian profiles for various slippage coefficients λ	105
Fig. 6.6: Variation of dimensionless performance factors with slippage coefficients λ	107
Fig. 6.7: Meridian profiles corresponding to various $\{r_0, \lambda\}$ -combinations	107
Fig. 6.8: Design procedure for searching the slippage coefficients	109
Fig. 6.9: Isotensoid meridian profiles for $r_0=1$ and $r_0=2$	110
Fig. 6.10: Winding angle propagations for $r_0=1$ and $r_0=2$	110
Fig. 6.11: Sectional 3D profile for the isotensoids obtained using the present method.....	111
Fig. 6.12: Non-geodesic trajectories on the isotensoids obtained using the present method. 111	
Fig. 6.13: Influence of the axial force on non-geodesic isotensoidal meridian profiles	113

Fig. 6.14: Cross sections of non-geodesic-isotensoid toroids for various λ ($\rho_0 = 0.2$)	114
Fig. 6.15: A sectional view of the non-geodesic isotensoid toroid ($\rho_{\min} = 0.2, \lambda = 0.04$).....	114
Fig. 6.16: Winding angle distributions for various slippage coefficients ($\rho_0=0.2$)	114
Fig. 6.17: Rates of performance improvement for various slippage coefficients ($\rho_0 = 0.2$) ..	116
Fig. 7.1: Meridian profile of a bellow-shaped pressure vessel (3D and 2D views).....	121
Fig. 7.2: Loads and geometry of a half-cell dome structure [19, 20].....	122
Fig. 7.3: Meridian profile of a half-cell dome with $n+1$ equidistant knots	122
Fig. 7.4: Flow chart of the optimal design procedure	126
Fig. 7.5: Flow chart of the design procedure for determining the burst pressure	127
Fig. 7.6: Geodesic dome profiles dictated by the present method and by isotensoid method	129
Fig. 7.7: Half-cell dome profiles corresponding to various slippage coefficients	130
Fig. 7.8: Shell thickness distributions for the half-cell dome designed by the present method	130
Fig. 7.9: Winding angle developments corresponding to various λ	130
Fig. 8.1: Geometry and loads of a dome head.....	136
Fig. 8.2: Distribution of slippage coefficient ($c=0.3, \rho_0=0.2$)	137
Fig. 8.3: Feasible field of $\{k, \rho_0\}$ -combinations (shaded area)	138
Fig. 8.4: Geodesics and non-geodesics-based optimal meridian profiles for increasing k	141
Fig. 8.5: Increase rates (in percent) of the performance factors that non-geodesics can gain for domes made of (a) glass-epoxy; (b) carbon-epoxy; and (c) aramid-epoxy.....	143
Fig. 8.6: Winding angle developments for various slippage coefficients ($\rho_0=0.4$)	144
Fig. 8.7: Laminate stresses referred to the material principle axes ($c=0.3, \rho_0=0.4$): (a) longitudinal stress; and (b) transverse stress	145
Fig. 8.8: Distributions of the failure level for geodesics and non-geodesics-based domes ...	145
Fig. 8.9: Thickness distribution for geodesic and non-geodesic optimal domes	146
Fig. 9.1: Geometry of a toroidal vessel and its fiber path	153
Fig. 9.2: Geometrical relations for θ, φ, l and α	153
Fig. 9.3: Winding angles developments for non-geodesics with various slippage coefficients	154
Fig. 9.4: Geodesic and non-geodesic trajectories for (a) $\lambda=0.1$; (b) $\lambda=0.15$; (c) $\lambda=0.2$	155
Fig. 9.5: Design procedure for determining the thickness distribution of the toroidal shell..	158
Fig. 9.6: Effects of the number of iterations on the values of the objective functions \overline{M}	161
Fig. 9.7: Winding angle developments of the optimal geodesics and non-geodesics for (a) $K = 3$;	

List of Figures

(b) $K = 4$; (c) $K = 5$ and (d) $K = 6$	162
Fig. 9.8: Optimal geodesic and non-geodesic winding angle developments for $K = 10^5$	162
Fig. 9.9: Optimal non-geodesic trajectories determined using the present method	163
Fig. 9.10: On-axis stresses for toroidal vessels ($K = 4$) obtained using the geodesics and non-geodesics: (a) longitudinal stress; (b) transverse stress and (c) shearing stress	164
Fig. 9.11: Thickness distributions for the optimal non-geodesic and geodesic toroidal vessels	165
Fig. 10.1: Influence of the axial force on the resulting meridian profile	172
Fig. 10.2: Mandrel shape for an optimal toroids ($\rho_{\min} = 0.25$, carbon-epoxy)	172
Fig. 10.3: Optimal cross-sections for isotensoids ($k=0$) and carbon-epoxy toroids ($k=0.0977$) for various ρ_{\min}	173
Fig. 10.4: Optimal Meridians of the classical pressure vessels corresponding to various ρ_{\min}	173
Fig. 10.5: Internal volumes of circular and the present optimal toroids with various ρ_{\min}	177
Fig. 10.6: Continued cross-sectional shapes for the circular and the present optimal toroids at equal volumes (continuous line: circular; dashed line: the present)	179
Fig. 10.7: Dimensionless weight of the circular and the present optimal toroids for various composite materials.....	179
Fig. 10.8: Dimensionless performance factors of the classical vessels, the circular and the obtained optimal toroidal vessels corresponding to various ρ_{\min} (carbon-epoxy) ..	180
Fig. 11.1: Flow chart of structural optimization procedure.....	185
Fig. 11.2: Lay-out of a toroidal winder and its coordinate system.....	186
Fig. 11.3: Flow chart of winding pattern adjustment	189
Fig. 11.4: Feed-eye movement as a function of time	190
Fig. 11.5: Feed-eye movement as a function of φ	190
Fig. 11.6: Optimal geodesic trajectories after 10 rotations of the mandrel (100 wound circuits)	191
Fig. 11.7: Optimal geodesic trajectories after 30 rotations of the mandrel (300 wound circuits)	191
Fig. 11.8: Optimal non-geodesics after 10 rotations of the mandrel (40 wound circuits).....	192
Fig. 11.9: Optimal non-geodesics after 40 rotations of the mandrel (160 wound circuits)....	192
Fig. 12.1: Illustration of the cylindrical coordinate system and the stress components.....	196
Fig. 12.2: Anisotropic configuration of $\pm\alpha$ laminae.....	200

Fig. 12.3: Relation of coordinate system between principle material axes and cylindrical axes 201

Fig. 12.4: An aluminum-lined cylindrical pressure vessel with 4 composite layers..... 232

Fig. 12.5: Distributions of the axial stress through the wall of the composite overwrap..... 233

Fig. 12.6: Distributions of the hoop stress through the wall of the composite overwrap 233

Fig. 12.7: Distributions of the radial stress through the wall of the composite overwrap 234

Fig. 12.8: Distributions of the shear stress through the wall of the composite overwrap 234

Fig. 12.9: Comparison of the twisting rates for various liner thicknesses 235

Fig. 12.10: Tsai-Wu strength ratios through the wall of the composite overwrap..... 235

Fig. 12.11: The axial stress of the composite overwrap with various liner materials..... 237

Fig. 12.12: The hoop stress of the composite overwrap with various liner materials..... 237

Fig. 12.13: The radial stress of the composite overwrap with various liner materials..... 237

Fig. 12.14: Twisting rates of the composite overwrap with various liner materials 238

Fig. 12.15: Von Mises stress distributions through the wall of the metal liner 238

Fig. 12.16: Distributions of Tsai-Wu strength ratios through the composite wall 238

List of Tables

Tab. 7.1: Dimensionless performance factors and related increase rates for various λ	129
Tab. 8.1: Typical properties of unidirectional composites [28]	142
Tab. 8.2: Values of design parameters $\{c, \alpha_{eq}\}$ for various polar radii (Carbon-epoxy)	144
Tab. 9.1: Optimal values of dimensionless vessel mass \bar{M} and slippage coefficients λ	165
Tab. 10.1: Typical properties of unidirectional composites [18]	177
Tab. 12.1: Puck's criteria failure modes with corresponding mechanisms [73].....	225
Tab. 12.2: Summary of the LaRC04 criteria [75]	226
Tab. 12.3: Typical mechanical properties of unidirectional composites [94-96].....	239

Chapter 1

Introduction and Objectives

1.1 Introduction to Filament Winding

1.1.1 Brief history

Filament winding is one of the oldest composite processing methods. It was probably the first method to be automated, and remains today one of the most cost-effective methods for mass production [1]. The unique characteristics of this process caused great revolutions for many years. The concept of filament winding process had been introduced in early 40's and the first attempt was made to develop filament-winding equipment [2]. The equipment that was designed in 1950's was very basic; it performed the simplest tasks using only two axes of motion (spindle rotation and horizontal carriage). The machine design consisted of a beam, a few legs and cam rollers for support [3]. The simplistic design was sufficient to create the first filament wound parts: rocket motor cases. The pace of composite development was accelerated during World War II. The push for aerospace dominance that began in the 1950's and really picked up speed in the 1960's was a new impetus for composite development. Young R. of the W. M. Kellogg Company began using filament winding for making small rocket motors [4]. This technology was purchased by Hercules and was the basis for the large-scale rocket motor business which was at the heart of the space race. Filament wound composite pressure vessels evolved from a demonstration project at Hercules Powder Corp. in 1948. These first filament wound parts, solid rocket motor nozzles for the X248 missile, were the follow-up of the experimental and pioneering WWII work of Theodore Von Karman [5]. In 1955, North American Aviation (Rocketdyne) engaged Hercules in another demonstration project, wrapping the MATADOR motorcase with fiberglass. By 1962 the need for highly

Chapter 1

accurate filament winding machines became apparent to Ashton L., an engineer at Hercules, who founded Engineering Technology to produce these machines. By 1963, the first filament wound motor case (a strap-on booster for the TITAN missile) was in production [6].

Meanwhile, from the mid 1950's to the early 1960's, research was underway at Air Force, Navy, Military and private laboratories funded by weapons research. Material development and testing was carried out in conjunction with the design and construction of filament wound pressure vessels, rocket motor cases, nozzles and launch tubes [7]. These developments were carried out by the major industrial subcontractors. Among them were Walter Kidde & Co., Brunswick Corp., Aerojet General Corp., Rocketdyne, Thiokol, Owens-Corning and many others [8]. Techniques still considered advanced today, such as computer controlled pre-impregnated winding were being employed as early as 1961 [9].

The actual arrangement of the filament-winding apparatus can take a number of different forms, a lathe-like configuration being common (Fig. 1.1) [10, 11]. Eventually through technical innovations, engineers were able to design servo-controlled photo-optic machines with hydraulic systems. During this time the filament winding machine became increasingly sophisticated in design; the addition of a third axis of motion (radial or cross-feed carriage), profile rails and ball shafts in combination with improved gearboxes resulted in smoother, more accurate filament winding [12]. By mid-70's, the advancement of servo technology entered the realm of the machine design [13]. High-speed computers allowed for rapid data processing, resulting in smoother motion and greater fiber placement accuracy (Fig. 1.2) [14,15]. Perhaps the crowning jewel of this period (1978) was the development of the first fully filament wound aircraft fuselage, the Beech Starship, by Ashton [16]. The plane was successfully flown, but was not commercialized using the filament wound technology. Before 80's economical considerations were items of less importance; the most common application was the production of rocket engine cases. The 1980s and 90s saw increased use of computer technology. Computers and motion control cards became essential pieces of hardware that were included in almost every machine [17]. Machine speed control was greatly improved; computer control systems could track position and velocity with increased accuracy. Additional axes of motions were also incorporated into machine design, allowing for four, five and even six axes of controlled motion (Fig. 1.3) [18]. Several kinematic models have been developed in the 1990s [15, 19, 20]. At the same time, a number of companies began to experiment with the development of pattern generation software [21-23]. By creating pattern generation software, more complex configurations, such as tapered shafts [24, 25], T-shaped parts [26, 27] and non-axisymmetric parts [28-30] could be successfully wound.

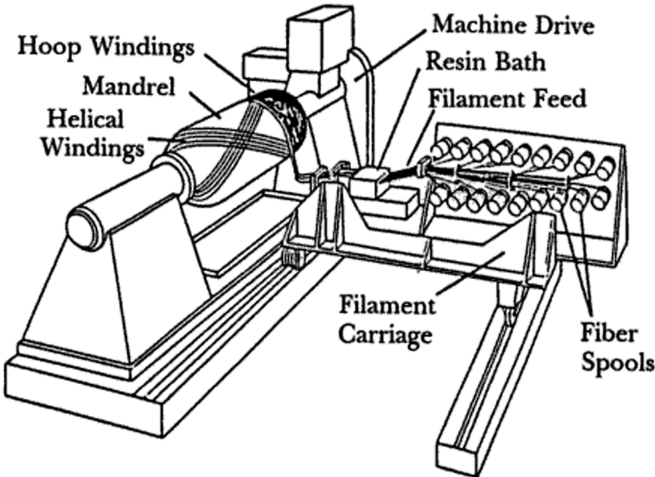


Fig. 1.1: A lathe-like filament winding machine [11]

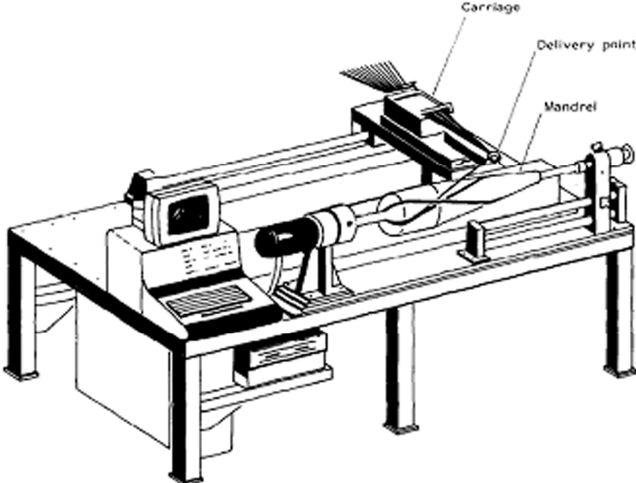


Fig. 1.2: Schematic of a computer-controlled winder having two degrees of freedom [15]

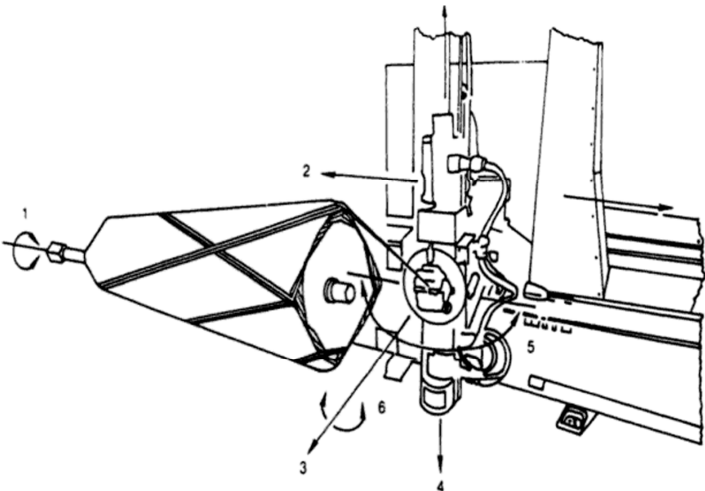


Fig. 1.3: 6-Axis filament winding machine (Courtesy of McClean Anderson, Inc.) [18]

Chapter 1

1.1.2 Processing technology

In 1964, the authors, Rosato D.V and Grove C.S. in their book titled, *Filament winding: Its Development, Manufacture, Applications and Design* defined it as a technique which "...produces high-strength and lightweight products; consists basically of two ingredients; namely, a filament or tape type reinforcement and a matrix or resin" [31]. In a filament winding process, a band of continuous resin impregnated rovings or monofilaments is wrapped around a rotating mandrel and then cured either at room temperature or in an oven to produce the final product. The technique offers high speed and is a precise method for placing many composite layers. The mandrel can be cylindrical, round or any shape that does not have re-entrant curvature. Among the applications of filament winding are cylindrical and spherical pressure vessels (Fig. 1.4), pipe lines, oxygen & other gas cylinders, rocket motor casings, helicopter blades, large underground storage tanks (for gasoline, oil, salts, acids, alkalies, water etc.). The process is not limited to axis-symmetric structures: prismatic shapes and more complex parts such as T-joints, and elbows may be wound on machines equipped with the appropriate number of degrees of freedom. Modern winding machines are numerically controlled with higher degrees of freedom for laying the exact number of layers of reinforcement. Mechanical strength of the filament wound parts not only depends on composition of component material but also on process parameters like winding angle, fiber tension, resin chemistry and curing cycle.

Filament winding has become a very popular construction technique in a wide variety of industries for creating composite structures with high stiffness-to-weight ratios. Since this fabrication technique allows production of strong, lightweight parts, it has proved particularly useful for components of aerospace, hydrospace and military applications and structures of commercial and industrial usefulness. Both the reinforcement and the matrix can be tailor-made to satisfy almost any property demand. This aids in widening the applicability of filament winding to the production of almost any commercial items wherein the strength to weight ratio is important. Apart from the strength-to-weight advantages and low cost of manufacturing, filament wound composite parts have better corrosion and electrical resistance properties.

Filament winding is an effective method to manufacture composite cylinders. In this process, composite layers are continuously wound on a rotating mandrel. This technique offers a high speed and precise method for placing many composite layers. There are two different winding methods: (1) wet winding, in which the fibers are passed through a resin

bath and wound onto a rotating mandrel; (2) prepreg winding, in which the pre-impregnated fiber tows are placed on the rotating mandrel. Among these winding methods, wet winding is more commonly used. Compared to prepreg, wet winding has several advantages: low material cost, short winding time, and the resin formulation can easily be varied to meet specific requirements.



Fig. 1.4: Filament wound cylindrical (a) and spherical (b) pressure vessel

The process of filament winding is primarily used for hollow, generally circular or oval sectioned products. Fibers can either be used dry or they can be pulled through a resin bath before being wound onto the mandrel. The winding pattern is controlled by the rotational speed of the mandrel and the movement of the fiber feed mechanism. Filament winding usually refers to the conventional filament winding process. However, some industrial companies use a so-called “Fast Filament Winder” for producing pressure vessels [32]. Basically the processes are the same (the fibers are wound around a mandrel following a certain pattern), but the way the machines work and the way the mandrel moves differs. After winding, the filament wound mandrel is subjected to curing and post curing operations during which the mandrel is continuously rotated to maintain uniformity of resin content around the circumference. After curing, the product is removed from the mandrel, either by hydraulic or mechanical extractor.

1.1.3 Materials

The mechanical properties of fibers dominantly contribute to the overall mechanical properties of the fiber/resin composite. The contribution of the fibers depends on four main factors [33]: (1) the basic mechanical properties of the fiber; (2) the surface interaction of fiber and resin (interface), (3) the amount of fibers in the composite (fiber volume fraction);

Chapter 1

(4) the orientation of the fibers in the composite; (5) the surface interaction of fiber and resin (depending on the degree of bonding between the two). This interfacial bonding is heavily influenced by the kind of surface treatment given to the fiber surface (sizing). Also, sizing minimizes the damage caused by handling. The choice in sizing depends on the desired performance of the composite, the kind of fiber and the way the fibers are going to be processed. The amount of fibers in a composite determines the strength and stiffness. As a general rule, the strength and stiffness of a laminate will increase proportional to the amount of fibers. However, above 60-70% fiber volume fraction, the tensile stiffness still increases, while the laminate strength reaches a peak and then slowly decreases. In this situation there is too little resin present to sufficiently hold the fibers together. The orientation of the fibers in a composite largely contributes to the overall strength. Reinforcing fibers are designed to be loaded along their length, which means that the properties of the composite are highly direction-specific. By placing the fibers in the loading directions, the amount of material put in directions where there is little or no load can be minimized.

The most commonly used fiber materials are carbon fiber, glass fiber and aramid fiber [34]. Compared to other fibers, carbon fibers show many advantages in providing excellent mechanical properties, e.g. low density, high tensile modulus and strength, good creep and fatigue resistance, low friction and thermal expansion, good electrical and thermal conductivity, and reduced moisture absorption. They are used as ultra-high strength structural components and reinforcements in aerospace structures and high-pressure compressed air tanks, for example aircraft fuselages and wings, satellite platforms and wind turbine blades.

Aramid fibers, which have been commercially available since the 1960s, have also found a wide field of applications. Their thermal properties facilitated their use as a substitute for asbestos. Aramid fibers, which show good vibration damping, high energy absorption, and favorable ballistic properties, are used for bullet and fragment or impact resistance applications.

Glass fibers can be divided into several groups according to their chemical composition: A-glass, C-glass, S-glass, E-glass, etc. Only E-glass is widely used in aerospace applications. Glass fibers are produced from molten glass which is either produced directly or by melting glass marbles. The molten glass is poured into a tank and held at a constant temperature to retain a constant viscosity. The flowing glass forms filaments with diameters that can range from 1-25 μm . Glass fibers provide the designer with high shear modulus, low Poisson's ratio, good electrical and thermal resistance, low thermal expansion and low production cost.

Resin matrix comprises an important part of any composite. It is basically the glue that

keeps the fibers together. A resin must have good mechanical properties, good adhesive and toughness properties, and good environmental properties. For the mechanical properties this means that an ideal resin must be initially stiff but may not suffer brittle failure. In order to achieve the full mechanical properties of the fiber, the resin must deform at least the same extent as the fiber. Good adhesion between resin and reinforcement fibers ensures that the loads will be transferred efficiently to prevent cracking and debonding. The resistance to crack propagation is a measure for the material's toughness. It is important to match the toughness with the ultimate elongation of the fiber. The environment in which the composite is used can be harsh. The resin must have good resistance to the surrounding environment, especially water and other aggressive substances. Furthermore, the resin must be able to withstand constant stress cycling.

There are two different matrix systems: Thermosets [35] and Thermoplastics [36-38]. Thermosets are produced from a chemical reaction, where the resin is mixed with a hardener or catalyst to undergo an irreversible chemical reaction which results in a hard, infusible matrix. Various types of thermosets are currently used in the composites industry, among which the most common are: polyester, vinylester and epoxy.

Thermoplastics, like metals that are soften and eventually melted when heated, then become hardened again when cooled. This process of crossing the softening or melting point on the temperature scale can be repeated as often as desired without any appreciable effect on the material properties in either state. Typical thermoplastics include Acrylic, nylon, polypropylene, polyethylene, etc; these can be reinforced, although usually only with short, chopped fibers such as glass.

By using various additives, liquid resin systems can be made suitable to provide specific mechanical/physical performance. Fillers constitute the greatest proportion of a formulation, second to the base resin. The most commonly used fillers are calcium carbonate, alumina silicate and alumina trihydrate. Calcium carbonate is primarily used as a volume extender to provide the lowest-cost resin formulation in areas in which performance is not critical. Alumina trihydrate is an additive that is used for its ability to suppress flame and smoke generation. Fillers can be incorporated into the resins in quantities up to 50% of the total resin formulation by weight. The usual volume limitation is based on the development of usable viscosity, which depends on the particle size and the characteristics of the resin. Special purpose additives include ultraviolet radiation screens for improved weatherability, antimony oxide for flame retardance, pigments for coloration and low-profile agents for surface smoothness and crack suppression characteristics. Mould release agents (metallic stearates,

Chapter 1

silicon gel or organic phosphate esters etc.) are important for adequate release from the mandrel to provide smooth surfaces and low processing friction.

1.1.4 Liner / Mandrel

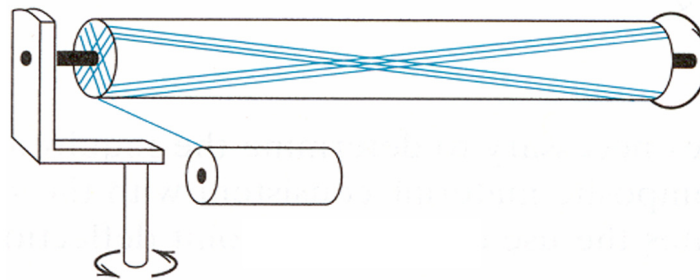
Invariably all pressure vessels or pipes made of composites have a liner. The function of the liner is to seal the liquid or gas inside the vessel or pipe. Normally the fibers provide the strength and stiffness for the structure. In cases where there are cracks in the matrix, these cracks may not cause rupture in the vessel or pipe, but the fluid inside may leak or weep out of the container. In case of flammable fluid, this can be dangerous, even though the fiber network is sufficient to contain the pressure. In order to seal the fluid, a flexible liner is usually applied. A liner can be a rubber bladder, a soft layer of thermoplastic such as PVC, or a thin layer of metal (steel, aluminum alloy, titanium alloy). When the liner is stiff enough, the liner may be used as a mandrel for overwinding the fiber and resin. In a situation where the liner is not stiff enough to withstand the compression due to the winding force, or in cases where it is essential to take the mandrel out, strategies for mandrels should be developed. There are many requirements for mandrels. The important considerations for mandrels are [39]: (1) the mandrel should be sufficiently stiff to withstand the compression imposed by the winding force; (2) the resin should not stick to the surface of the mandrel. Release agents need to be applied; (3) the mandrel should be extractable from the part after curing. Mandrels can be classified according the following categories: extractable mandrels, collapsible mandrels, breakable mandrels and dissolvable mandrels.

1.1.5 Winding patterns

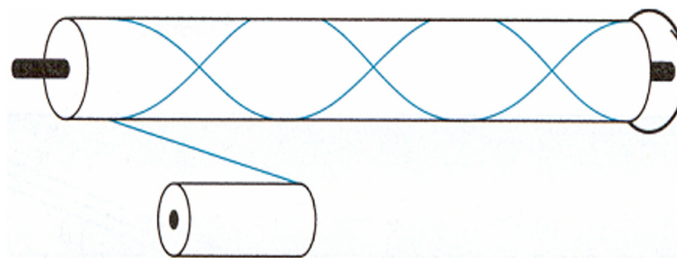
The operation of filament winding is the reverse of the conventional machining process of milling on a lathe. In milling, one starts with a cylindrical surface and one removes the material from the surface one strip at a time. In filament winding, one deposits the material on the surface of the mandrel one strip at a time. The most basic form of filament winding is a two degrees-of-freedom operation. This consists of the rotation of the mandrel and the linear movement of the feed eye along the axis of the mandrel. Pressure vessels and pipes can be wound by using at least two-axis filament winding machines. The availability of the additional degrees of freedom can be useful in winding at the end of the part, such as heads of pressure vessels, or the winding of shapes more complex than straight cylinders such as those

with variations in the cross section (i.e. cones) or spheres. For example, for the case of a four-axis winding machine, the basic movements are mandrel rotation and feed-eye traverse. The third axis is a horizontal translation perpendicular to the mandrel axis and the fourth axis of motion is the rotation of the feed eye. The latter permits more accurate fiber placement at the ends of the mandrel. Winding machines with more degrees of freedom up to the level of 7-axis robot cells are available.

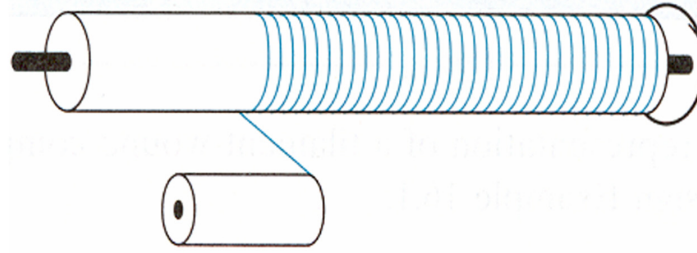
Depending on the coordination between the rotational motion and the axial motion, three basic types of winding patterns can be obtained. These are: planar, helical, and hoop (Fig.1.5) [40]. The choices made are based on the shape of the part and the reinforcement orientations required. Planar winding is used to lay down fibers less than 5° with respect to the longitudinal axis. Planar windings pass close to or around the mandrel poles. Each completed planar winding pattern covers the mandrel surface with a single layer of reinforcements. Helical winding is used to lay fibers at angles from 5° to 80° to the longitudinal axis. These fibers are wound on the mandrel surface in alternating positive and negative orientations and result in a double layer of wound material. Helical windings may pass around the end of a closed-end shape. Hoop winding is a special form of helical winding and is used to deposit fibers close to 90° to the longitudinal axis. Hoop windings are generally applied only to the cylindrical or straight portion of a mandrel and result in a single layer of reinforcement.



Planar winding



Helical winding



Hoop winding

Fig. 1.5: Three basic winding patterns

1.2 Composite Pressure Vessels

1.2.1 Brief introduction

Pressure vessels have been manufactured by filament winding for a long time. Although they appear to be simple structures, pressure vessels are difficult to design. Filament-wound composite pressure vessels have found widespread use not only for military but also for civilian applications. This technology originally developed for military use has been adapted to civilian purposes and was, in a later stage, extended to the commercial market. Applications include breathing device, such as self-contained breathing apparatuses used by fire-fighters and other emergency personnel, scuba tanks for divers, oxygen cylinders for medical and aviation cylinders for emergency slide inflation, opening doors or lowering of landing gear, mountaineering expedition equipment, paintball gas cylinders, etc.

A potential widespread application for composite pressure vessels is the automotive industry. Emphasis on reducing emissions promotes the conversion to CNG or hydrogen fuelled tanks worldwide [41-44]. Engineers are seeking to replace petroleum derivative products with natural gas or hydrogen as the energy supply in automobiles for air quality improvements and pollution elimination. Onboard compressed hydrogen storage technologies are one of the key requirements for the successful application of fuel cell vehicles [45, 46]. One of the limitations is the lack of vehicle range between refueling stops [47]. Efficiency, weight, volume and cost of the containment vessel are also important considerations [48]. Filament-wound composite pressure vessels utilizing high strength/modulus to density ratio offer significant weight savings over conventional all-metal pressure vessels for the containment of high pressure gases and fluids [50]. Composite pressure vessels are expected to withstand a maximum burst pressure at a maximum internal volume and a minimum weight.

Accordingly, a performance factor $PF = PV/W$ is used as an index for rating pressure vessels, where P , V , W are the burst pressure, the containing volume and the weight, respectively [51].

Composite vessels with very high burst pressures (≥ 70 MPa) are in service today in the aerospace and fuel cell vehicles industry [52]. Vessels with burst pressure between 200 and 400 MPa have been under investigation and such containment levels were achieved in the late 1970's through mid 1980's [53]. The vessel designs based on thin-walled theories are currently insufficient for broad application in the transportation industry; therefore further development of thick-walled composite designs is required for containing ultra-high pressurized gases. Advanced ultra-high pressure composite vessels design techniques must be employed to achieve such operations. However, current ultra-high pressure vessels are low in structural efficiency. There also exists a fundamental lack of confidence in the ability to understand and predict their structural behaviors. Higher pressures are not yet approved for use on public roads or commercial aircraft. This implies a need for advancement in composite pressure vessel technology. It is known that stress decline rapidly through the wall thickness. At first glance pretension of wound fibers appears to be able to change the distribution of stress through the wall thickness, but research has shown that the effects are limited. Most of finite element analyses on composite pressure vessels are based on shell elements which are generated using the classical lamination theory. The results appear to be good when the internal pressures are not very high and the ratio of diameter to wall thickness is greater than 15. Some FEA tools like ABAQUS and ANSYS provide a thick shell element to include the shear stress in the radial direction and capture the transverse shear deformation [54].

Cylindrical composite pressure vessels constitute an inner liner and a filament wound composite overwrap. The liner is necessary to prevent leaking, while some of the liners do also provide strength to share the internal pressure load. Composite pressure vessels should take full advantage of the extremely high tensile strength and high elastic modulus of the fibers from which they are made. Theories of laminated composite materials for evaluating these properties are relatively well established for the modulus of elasticity, and to a lesser extent for strength. Generally, there are two approaches to modeling composite material behaviors [55]: (1) micromechanics where the interaction of constituent materials is examined as the behavior of heterogeneous composite material; (2) macromechanics where the material is assumed homogeneous and the effect of the constituents are detected only as averaged properties.

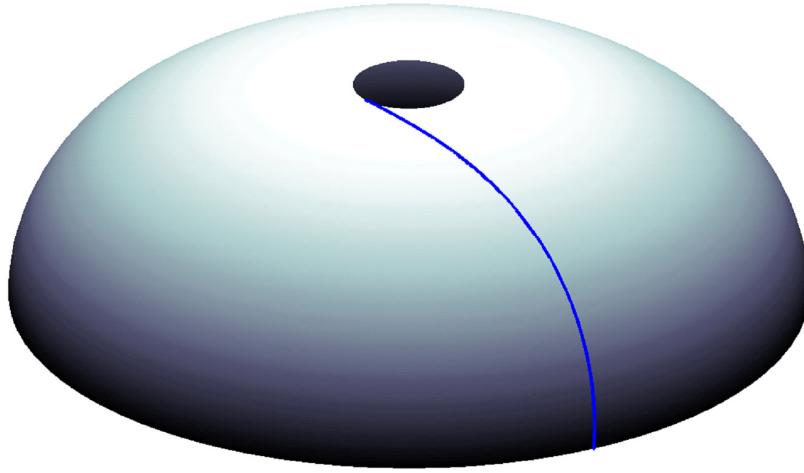


Fig. 1.6: A pressure vessel dome and its fiber trajectory

1.2.2 Filament wound dome heads for pressure vessels

Pressure vessels may theoretically be almost any shape, but shapes made of sections of spheres, cylinders, and cones are usually employed. A common design is a cylinder with end caps called domes or heads. Dome shapes are frequently either hemispherical or torispherical (Fig. 1.6). More complicated shapes have historically been much harder to be assessed by a reliable analysis tools for structural behavior and safe operation and are usually very difficult to construct.

Geodesic-isotensoid dome design [56], modified helically wound dome design [57] and planar wound dome design method [58] have been used to determine the winding patterns and the dome geometry of pressure vessels. A geodesic-isotensoid dome is assumed to support internal pressure by the fiber only and to consist of filaments that are loaded to an identical stress level. The geodesic-isotensoid equation is mainly used for domed pressure vessels with equal polar openings at the both ends. Planar winding patterns lie in a plane, which is tangent to the polar opening at one end of the part and tangent to the opposite side of the polar opening at the other end. These are mainly used in pressure vessels with length-to-diameter ratios less than 2. Planar winding equations helically wound dome equation is a revised version of the isotensoid dome equation and can be applied to pressure vessels that have different polar opening radii. This equation is mainly used in pressure vessels with a length-to-diameter greater than 2.

Because the above equations simultaneously provide the dome shape and the winding patterns for given parameters such as the radius ratio of the polar opening to a cylindrical part,

the initially determined winding patterns are maintained until the end of the winding process. The design of the mandrel shape can also be incorporated into the winding trajectory design.

Theoretically, a sphere would be the optimal shape of an isotropic dome for a pressure vessel. Unfortunately, the optimal shape of a composite dome is far more difficult to determine due to the anisotropic character of its reinforced wall. With the advent of anisotropic fiber reinforced materials with preferred stiffness and strength directions parallel to the fibers, it was discovered that the ideal dome shape was an isotenoid [59, 60]. Isotenoid implies that all locations within an internally pressurized dome undergo the same level of tensile stress, and the design is formulated so that the major stresses are carried solely by the fibers of the composite. Thus there is a direct correlation between the dome geometry, laminate stiffness parameters, and the fiber trajectories that are used within the manufacturing process. Netting analysis is used to formulate and solve the isotenoid dome equation that results from this interaction between the dome geometry and winding angles. The resulting isotenoid design solution can take into account many particular features of a filament wound pressure vessels like the size of the polar openings, the method of filament winding (e.g. (non-) geodesic or planar winding).

The relative dimensions of different sections of a pressure vessel are designed based on the space and weight requirements and the pressure levels. Since filament wound pressure vessels usually fail in their dome parts, the focus on dome design can never be lost. This is due to the fact that the dome regions undergo the highest stress levels and are the most critical locations from the viewpoint of structure failure [61]. The desired target of the dome design is to achieve a higher burst pressure and internal volume and a lower weight.

Generally, the shape optimization problem consists of finding out the best profile of a component that improves its structural performance and minimizes some properties, for example, to minimize the vessel weight or reduce high stress concentrations around the pole or the cut-outs. The choice of any parametric curve to represent the dome profile will result in a certain degree of restriction to the optimization problem. The objective of shape optimization of an engineering component is to search for a feasible solution within a prescribed tolerance. Therefore, an adequate selection of a geometric representation and the minimum number of appropriate design variables is of vital importance in order to achieve an automatic design cycle during the shape optimization, and to guarantee an effective approach that is able to provide a straightforward but reliable design for pressure vessels.

One aspect of filament wound pressure vessels that is somewhat unique, is the fact that incorrect increase of the amount of material can actually decrease the load-carrying capability

Chapter 1

of the structure. This is due to the fact that extra layers of filament wound structures do change the stiffness distribution of the shell and thus necessitate a corresponding change in the shape of the isotenoid dome profile. Since the end cap geometry is usually dictated by the mandrel on which it is formed and thus cannot be changed without re-tooling, the incorrect addition of filament wound plies leads to a design that fails below the desired load levels.

The dome/polar boss interface is one of the most highly stressed areas of a filament wound composite motor cases, because all the internal pressure acting across the polar openings must be transferred to the composite in this area. In addition, the stress concentration at the cylinder/dome junction region is sometimes overestimated due to the rapid change in thickness and curvatures.

1.2.3 Toroidal pressure vessels for compressed hydrogen storage

Hydrogen is a strong contender for future green energy. Hydrogen-powered fuel cell vehicles have emerged as an interesting alternative to lower air pollutant emission as well as to reduce our dependence on fossil fuels [62-64]. Hydrogen can be stored onboard a vehicle either as compressed gas, as cryogenic liquid, or as adsorbed elements using metal hydrides or carbon nanotubes [65-67]. Of these alternatives, high-pressure compressed hydrogen storage is considered as the most feasible and near-term solution for onboard vehicular applications, because of low cost, effective heat transfer, rapid refueling and reasonable operating temperature of gaseous hydrogen [68-70]. However, to be competitive with conventional vehicles and successfully penetrate the automobile market, hydrogen fuel cell vehicles must be able to provide an adequate driving range (≥ 500 km). Because gaseous hydrogen at atmospheric pressure has a very low energy content by volume, hydrogen storage tanks are expected to operate at a high pressure to obtain sufficient gravimetric and volumetric energy density. It should be mentioned here that 70MPa is more and more preferred to improve gaseous hydrogen storage density. It has been demonstrated that with creative packaging, the range expectations can be fulfilled by using 70MPa storage systems without seriously compromising either passenger or cargo space [48]. On-board hydrogen storage at 70MPa provides up to 1.6:1 advantage over storing at 35MPa and 2.2:1 advantage over storing at 20MPa. Fig. 1.7 displays the relationship between compression energy and various pressures of gaseous hydrogen.

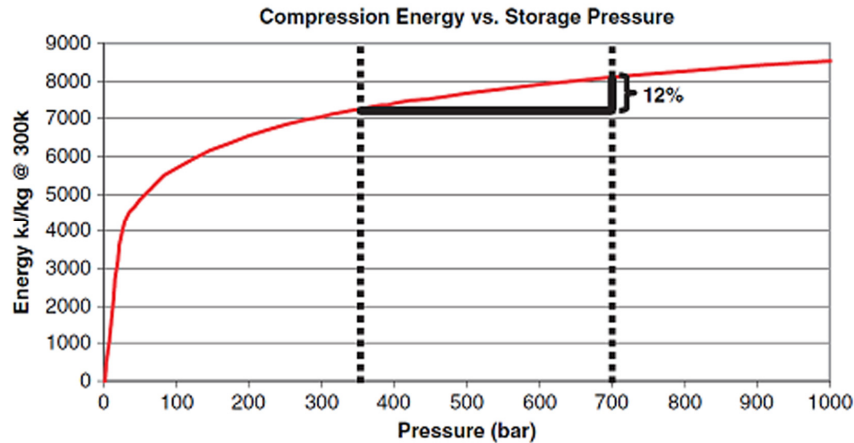


Fig. 1.7: Relation between compression energy and service pressure [48]

By increasing the pressure of hydrogen, a sufficient driving range can be achieved but at the expense of weight, payload and carrying volume within the vehicle. A key technical challenge of maximizing the gravimetric and volumetric energy efficiency of gaseous hydrogen systems is addressed through the development of a conformable composite pressure vessel, which can give a hydrogen fuel cell vehicle a comparable travel range to today's gasoline-powered vehicles [71]. To withstand the design stress, thicker walls are required for higher-pressure on-board hydrogen storage tanks that results in practical challenges like weight penalty in automotive applications. Therefore, carbon fiber-epoxy resin composites combined with filament winding technology have been widely applied to produce lightweight high-pressure hydrogen storage tanks [72]. Composite overwrapped pressure vessels designed to sustain ultra-high pressure have been increasingly used onboard hydrogen-powered fuel cell vehicles. The application of composite structures improves the vessel performance and offers a significant amount of material saving. Among various processing methods for composite structures, filament winding is a highly automated technique of laying down fiber reinforcements to create strong, lightweight products so it has gained a widespread application in the manufacturing of composite pressure vessels. Compare to other production methods for composites, the filament winding process provides significant advantages such as high fiber volume fraction, high specific strength/stiffness and exceptional fatigue life.

The United States Department of Energy (DOE) has presented a series of design targets for hydrogen storage system development, particularly for on-board hydrogen storage systems, that is, to achieve a system gravimetric density of 6% wt/kg and volumetric density of 45g H₂/L by 2010, and to achieve 9% wt/kg and 81g H₂/L by 2015 [73]. The current gravimetric and volumetric energy densities of compressed hydrogen storage systems are still far fewer

Chapter 1

than the required properties towards achieving the DOE 2010 and 2015 goals.

Current high-pressure hydrogen storage tanks are much larger and heavier than desired gas tanks for light-duty vehicles and occupy a considerable fraction of the needed passenger space. Thus, improving storage pressure without compromising weight and volume is still a key technical challenge for successful commercialization of hydrogen fuel cell vehicles. A classical hydrogen storage tank consists of a cylindrical section and two quasi-spherical domes with polar openings. To date, filament-wound classical (cylindrical) hydrogen storage tanks have been studied for years and the design and manufacturing of such tank structures is relatively simple and mature [73-78]. However, since the dome regions withstand the highest stress levels, they always need thicker walls than the cylindrical parts. In addition, a large variation in radius from the dome equator to the pole leads to severe fiber stacking and thickness accumulation near the polar area of the classical pressure vessel [79, 80].

Among possible shapes of pressure vessels, toroids are recently gaining more attention in hydrogen storage because of their high structural efficiency and unique configuration. The toroid belongs to the class of doubly curved bodies and can be regarded as a bent, endless cylinder that saves on the need for materials in the end caps (Fig. 1.8 [81]). Compared to the classical storage tank, it allows for reduced fiber stacking at the polar area of the vessel; this is mainly triggered by the relatively homogeneous thickness distribution over the vessel surface and the absence of end caps. In winding a convex axisymmetric body, a basic fiber trajectory is repeated continuously, opposed to a torus, which is a doubly-closed body having a convex-concave surface. Moreover, due to high applied loads, toroidal storage tanks require stronger structures and better load carrying capacity than composite elbows [82, 83] used in civil pipelines.



Fig. 1.8: A toroidal pressure vessel [81]

1.2.4 Thick-walled pressure vessels

With the development of design and manufacturing technologies to produce multi-layered composite vessels, there has been a growing interest in the application of the thick-walled multilayered filament-wound pressure vessels. Thick composite cylinders are important structural elements which cannot be analyzed by traditional membrane approaches due to through-thickness effects. Traditionally, composite analysis techniques rely on the assumption of plane stress, and therefore they are only applicable to thin laminates. Originally, many of the classical thin shell theories are based on the Kirchhoff-Love hypotheses [84] developed over 100 years ago: (1) straight lines normal to the undeformed middle surface remain straight and normal to the deformed middle surface; (2) the normal stresses perpendicular to the middle surface can be neglected in the stress-strain relations; and (3) the transverse displacement is independent of the thickness coordinate. These theories are expected to prove sufficiently accurate results when (1) the radius-to-thickness ratio is large; (2) the dynamic responses are within the low-frequency range; (3) the material anisotropy is not severe. It is shown in [85] that Love's strain energy expression has inherent errors of relative order $[h/R+(h/L)^2]$ (where h is the thickness of the shell, R is the smallest principal radius of curvature, and L is the characteristic wavelength at the deformation pattern of the middle surface). However, when the theories of thin shells are applied to thick shells, with h/R not small compared to unity, the error can be quite large. Application of such theories to anisotropic multilayered thick shells can lead to as much as 30% or more error magnitude in deflections, stresses and eigen frequencies [86]. To improve these results, the developed refined two-dimensional linear theories of thin shells including several important contributions [87-93], have been extensively developed in the last 40 years. However, as pointed out by Koiter [94], refinements to Love's theory for thin elastic shells are meaningless, unless the transverse shear and normal effects are taken into account.

Contrary to the theory of thin shells, the theory of thick shells has received relatively less attention by researchers up to now. The analysis of cylindrical structures by elasticity solutions can be subdivided into "thin wall" and "thick wall". The division point is often arbitrarily chosen as a radius-to-thickness ratio of 10:1. This ratio is not appropriate for composite structures, especially when designing with highly anisotropic materials [95]. Through thickness stresses are particularly important in composite laminates because they can cause delamination and other failure modes. For anisotropic composite materials the stresses through the wall thickness reduce much more rapidly than for their isotropic (metal)

Chapter 1

counterparts. This effect leads to a greatly reduced structural performance of pressure vessels. It is in general not an easy task to incorporate radial stresses in thin shell theory and to obtain nonlinear stress distributions through the shell thickness in order to describe the behavior of thick shells.

1.3 Thesis Outline

The scope of part **I** is to provide a mathematical and mechanical foundation for the design and optimization presented in this dissertation. In chapter **2**, with the aid of the so-called *Darboux frame*, the outline of fiber trajectory stability on a generic surface is provided in terms of both fiber slippage and bridging tendencies. The basic non-slippage and non-bridging criteria are presented for the formulation of design constraints in the subsequent optimization for various pressure vessels. Several basic concepts and definitions from differential geometry are also provided for formulating the fiber path equations. According to the fiber stability analysis, the mathematical description of geodesic and non-geodesic trajectories is briefly presented. In the next chapter, **3**, we present the basic concepts and formulae related to the netting theory and the continuum theory (classical lamination theory), serving here as a basis for the analysis of in-plane mechanical behavior of composite pressure vessels. Based on the minimum strain energy density criterion, the generalized optimality condition that couples the vessel geometry and the laminate layup is given, where its specific applications and feasible intervals are also presented for several types of laminations.

The main subject of part **II** is to present netting-based design approaches that will finally determine the optimal meridian shape and related fiber architectures for pressure vessels. In chapter **4**, we demonstrate here a netting-based optimization for determining the fiber trajectories and related layups of helically and hoop wound circular toroidal pressure vessels, where the helical layer angle and thickness are considered as design variables, while the minimum vessel weight acts as the objective function. In addition, the fiber trajectory stability of filament wound circular toroidal pressure vessels is evaluated for the two mostly used patterns: single helical winding, and helical and hoop winding. The influence of the relative bend radius of the torus and the hoop-to-helical thickness ratio on fiber slippage and bridging tendencies is here evaluated to offer an important design reference for filament wound circular toroids. In chapter **5**, we outline the geodesic-isotensoid design, which leads to equal fiber tension throughout the whole structure, to determine the netting-based isotensoid cross-sectional shapes for filament wound toroidal pressure vessels. The cross-sectional

shapes are obtained by forcing the geodesic-isotensoid profiles to return to zero altitude so that the resulting isotensoid shapes become closed. The influence of the theoretically required axial load on the vessel pole, needed for closing the profile, is also evaluated. Moreover, the geometry and performance of isotensoid toroids are compared to those of circular toroids, in order to demonstrate the better performance and the lower aspect ratio (height-to-width ratio) that the isotensoid design can gain for toroids. In the last chapter of this part, **6**, we present a novel design approach combining isotensoid structures with non-geodesic winding, to derive isotensoids with unequal polar openings and non-geodesic-isotensoid toroids. The performance improvement that the application of non-geodesics can gain, corresponding to various slippage coefficients, is evaluated and compared to the geodesic-isotensoid domes and toroids, respectively, in order to show the advantage of the use of non-geodesics instead of geodesics.

The main goal of part **III** is to present continuum-based design approaches that determine the optimal shape and related fiber trajectories for pressure vessels. In chapter **7**, the optimal design for determining the meridian profiles of filament-wound bellow-shaped pressure vessels is outlined, subjected to geometrical limitations, stability-ensuring conditions and the Tsai-Wu failure criterion. The stress field is modeled using classical lamination theory, and the non-geodesic trajectories are here employed to enlarge the design space and improve the structural performance. The effect the slippage coefficient has on the geometry and structural efficiency of filament wound bellow-shapes is also investigated. In chapter **8**, the optimal shapes and corresponding fiber architectures of non-geodesically overwound domes for pressure vessels are determined upon the generalized optimality condition as presented in chapter 3. Based on the classical lamination theory and the non-geodesic winding law, the system of differential equations governing the optimal meridian profiles is derived; a specific function is chosen to describe the slippage coefficient distribution for the desired non-geodesic trajectories. The meridian profiles are determined for various material anisotropy parameters; the related winding angle developments of non-geodesic trajectories are also presented. With the aid of the non-geodesic trajectories and the classical lamination theory, a design-oriented approach for determining the optimal fiber trajectories of circular toroidal pressure vessels is outlined in chapter **9**. The influence of the relative bend radius on the geometry and performance of the obtained non-geodesic trajectories is also evaluated. In addition, the calculations and comparisons of structural mass and on-axis stress of laminate shells, respectively designed by geodesics and non-geodesics are carried out, in order to show that non-geodesics form a preferable alternative for toroidal pressure vessels. In chapter **10** we

Chapter 1

determine the optimal cross-sectional shapes for filament wound toroidal pressure vessels. The continuum-based meridian profile is derived based on the optimality condition and the classical lamination theory. The comparison for the cross-sectional shapes and structural weight of equal-volume circular and continuum-based optimal toroids is then performed. In addition, for the assessment of the effect of the optimal cross-sections on the vessel performance, we respectively calculate and compare the performance factors of optimal classical vessels (quasi-ellipsoidal shell), the circular and the optimal toroidal vessels for various polar opening radii. Based on the previously presented designs of filament-wound toroidal pressure vessels, we outline an integral method for the design, optimization and manufacturing of the toroids in chapter 11. In this chapter we perform a combined evaluation of the structural optimization for vessel performance and the windability for manufacturing. With emphasis on the importance of suitable winding patterns for obtaining an optimal toroidal pressure vessel we accordingly derive the "Diophantine"-like equations that produce such patterns. The main objective of the method presented here is to match the structure-dictated number of wound circuits to the solution of the "Diophantine" equations for determining the proper relative winding velocities of the mandrel and the feed eye. Depending on the aimed lathe machine configuration, the underlying geometric model of the dedicated toroidal winder is outlined and the kinematic solution for coupling the motion of the mandrel and the feed eye are derived. An example of the implementation of these methods for winding an actual toroidal pressure vessel is given, as performed in the simulations for generating optimal fiber trajectories.

In part IV we extend two-dimensional anisotropic elasticity solutions to the three-dimensional one where the through-thickness stress gradient is taken into account, in order to better understand the design and analysis of thick-walled pressure vessels. In chapter 12 a review is devoted to 3D elasticity approaches for obtaining the exact solutions of the stresses and strains induced by internal pressure, and to the effects of hygrothermal loading and twisting in regard to the structural behavior of cylinders. The 3D effective elastic constants and most frequently used 3D failure criteria for cylindrically anisotropic materials are also presented. A multi-layered thick-walled cylindrical pressure vessel, which comprises four CFRP layers and an aluminum seamless liner is analyzed to demonstrate the effects of the liner and its thickness variation on the stress distribution of the composite overwrap. In addition, the Von Mises stress of the metal liner and the Tsai-Wu strength ratio of the composite overwrap are also calculated for various liner/fiber/resin materials to find the best combination.

Lastly, the conclusions chapter, **13**, is divided into two sections. After providing an extensive list of conclusions for the topics contained in this dissertation, some recommendations for future research are given.

References

1. Babu MS, Srikanth G, Biswas S. Composite fabrication by filament winding – an insight, 2000. Available from: <http://www.Tifac.org.in/news/acfil.html>
2. Lee SM. International encyclopedia of composites. Historical perspectives of composites, by John Delmonte (Ed.), New York: VCH Publishers, 1990.
3. Moree AC. Geodesic winding of rotational symmetric bodies. MSc thesis report. Faculty of Aerospace Engineering, Delft University of Technology, Delft, December 1986.
4. Lubin G (Ed.). Handbook of Composites, New York: Van Nostrand Reinhold Company Inc., 1982.
5. Wilson BA. Filament winding – past, present and future. 34th International SAMPE Symposium, 1989, pp. 2429-39.
6. Lauder AJ. Manufacture of rocket motor cases using advanced filament winding processes. Mater Manuf Processes 1995; 10: 75-87.
7. John EG. Overview of Filament Winding. SAMPE J 2001; 37: 7-11.
8. Brian Wilson, Filament Winding – The Jump from aerospace to Commercial Fame, SAMPE J 1997; 33: 25-32.
9. Leeds MA. Study of the use of preimpregnated roving with numerically controlled winding equipment", Rocketdyne report R-3647, Canoga Park, CA, 12 Jul 1962.
10. Peters ST, Humphrev WD, Foral RF. Filament Winding Composite Structure Fabrication. 2nd Ed. Covina CA: SAMPE International Business Office, 2000.
11. Todd RH, Allen DK, Alting L. Fundamental principles of manufacturing processes. New York: Industrial Press Inc., 1994.
12. Giacoletto HL. The art of filament winding. Reinf Plast 2002; 46: 30-1.
13. Owen MJ, Elliman DG, Middleton V, Young K, Weatherby N. Advanced manufacturing technology for filament winding. Polymer processing. Automation. The plastics & rubber institute 1986: 22.1-22.13.
14. Strong BA. History of Composite Materials – Opportunities and Necessities. Brigham Young University. 24 Jan. 2011.
15. Mazumdar SK, Hoa SV. On the Kinematics of Filament Winding on Non-Axisymmetric

Chapter 1

- Cylindrical Mandrels, Part I: A Generalized Model. *Compos Manuf* 1991; 2: 23-30.
16. Poggiali B, Busch JV. Micro-computer based cost estimation of filament winding. *Automated Composites. The plastics & rubber institute*; 1986: 7.1-7.8.
 17. Middleton V, Young KW, Elliman DG, Owen MJ. Software for filament winding. *Automated Composites. The plastics & rubber institute*; 1986: 9.1-9.6.
 18. Peters ST (Ed.). *Handbook of Composites*. 2nd ed. Chapman & Hall, London, UK. 1998.
 19. Di Vita G, Farioli M, Marchetti M. Process simulation in filament winding of composite structures. *Composite materials: design and analysis*. 1990. pp.19-37.
 20. Mazumdar SK, Hoa SV. On the kinematics of filament winding on non-axisymmetric cylindrical mandrels, part II: for convex polygonal cross-section. *Compos Manuf* 1991; 2: 31-8.
 21. Christian L. Process Simulation in Filament Winding. *Reinf Plast* 1991; No.1: 40-2.
 22. Laval C. CADWIND 2006 – 20 years of filament winding experience. *Reinf Plast* 2006; 50: 34-7.
 23. Jacob A. Automation sets filament winding on the right path. *Reinforced Plastics*, September 1998.
 24. Kim W, Argento A, Scott RA. Free Vibration of a Rotating Tapered Composite Timoshenko Shaft. *J Sound Vib* 1999; 226: 125-47.
 25. Kim W, Argento A, Scott RA. Rotating tapered composite shafts: forced torsional and extensional motions and static strength. *ASME-J Vib Acoust* 2001; 123: 24-9.
 26. Scholliers J, Van Brussel H. Computer-integrated Filament Winding: Computer-integrated Design, Robotic Filament Winding and Robotic Quality Control. *Compos Manuf* 1994; 5: 15-23.
 27. Seereeram S, Wen JT. An All-geodesic Algorithm for Filament Winding of a T-shaped Form, *IEEE Transactions on Industrial Electronics* 1991; 38: 484-90
 28. Dolan, JM, Khosla P, Talukdar SN. Surface-Closure Algorithms for Filament Winding of Non-Axisymmetric Cylindrical Parts. *Proceedings of the 25th International SAMPE Technical Conference, Vol 25, pp.680-691, October 1993.*
 29. Mazumdar SK, Hoa SV. Algorithm for filament winding of non-axisymmetric tapered composite components having polygonal cross-section on two axes filament winding machine. *Compos Eng* 1994; 4: 343-59.
 30. Liang YD, Luo G. Two-dimensional non-axisymmetric filament winding patterns. In: *Proceedings of International SAMPE Technical Conference* 1996; 29: 505-514.
 31. Rosato DV, Grove CS. *Filament winding: its development, manufacture, applications, and*

- design. Polymer engineering and technology. New York: Interscience, 1964.
32. ALE. Fast filament winder. Available at <http://www.ale.nl/index.php?cid=47>.
 33. Aastrom BT. Manufacturing of polymer composites. London: Chapman & Hall, 1997.
 34. Peters ST, Humphrey WD. Filament winding. In: Dostal CA, editor. Engineered materials handbook, Volume 1: Composites. Ohio, 1987.
 35. Olofsson SK. Filament winding of thermoset composites: process modelling and experimental verification. PhD. thesis report. Luleå tekniska universitet, Luleå, 1995.
 36. Song X. Modeling of Thermoplastic Composite Filament Winding. MSc. thesis report. Virginia Polytechnic Institute and State University, September 29, 2000
 37. Henninger F, Friedrich K. Thermoplastic filament winding with online-impregnation. Part A: process technology and operating efficiency. *Comp Part A: Appl Sci Manuf* 33: 1479-86
 38. Henninger F, Hoffmann J, Friedrich K. Thermoplastic filament winding with online-impregnation. Part B: Experimental study of processing parameters. *Comp Part A: Appl Sci Manuf* 2002; 33:1684-95
 39. Hoa SV. Principles of the Manufacturing of Composite Materials. DEStech Publications, Inc. Lancaster, PA, USA, 2009.
 40. Chen FC. A filament wound structure technology overview. *Materials Chemistry and Physics* 1995; 96-100.
 41. Mahmud ZN. Design and analysis of filament-wound compressed natural gas carbon fiber-reinforced composite tank. MSc. thesis report, Universiti Putra Malaysia, 2008.
 42. Choi JC, Kim C, Jung SY. Development of an automated design system of a CNG composite vessel using a steel liner manufactured using the DDI process. *International Journal of Advanced Manufacturing Technology* 2004; 24: 781–788.
 43. Verstraete D, Hendrick P, Pilidis P, Ramsden K. Hydrogen fuel tanks for subsonic transport aircraft. *Int J Hydrogen Energy* 2010; 35: 11085-98
 44. Young KS. Advanced composites storage containment for hydrogen. *Int J Hydrogen Energy* 1992; 17: 505-7.
 45. Takeichi N, Senoh H, Yokota T, Tsuruta H, Hamada K, et al. Hybrid hydrogen storage vessel, a novel high-pressure hydrogen storage vessel combined with hydrogen storage material, *Int J Hydrogen Energy* 2003; 28: 1121-9.
 46. Harris R, Book D, Anderson PA, Edwards PP. Hydrogen storage: the grand challenge, *The Fuel Cell Rev* 2004; 1: 17-23.
 47. Ross DK. Hydrogen storage: the major technological barrier to the development of

Chapter 1

- hydrogen fuel cell cars, *Vacuum* 2006; 80: 1084-91.
48. Sirosh N, Niedzwiecki A. Development of Storage Tanks: High-pressure Vessels. In: Léon A (Ed.), *Hydrogen Technology: Mobile and Portable Applications (Green Energy and Technology)*, Springer-Verlag Berlin Heidelberg, Berlin, 1999, pp.291-310.
 49. Weisberg AH, Myers B, Berry G. Hydrogen storage using lightweight tanks. *Proceedings of the 2002 U.S. DOE Hydrogen Program Review NREL/CP-610-32405*.
 50. Kai F, Liu Z, Fu Q, Zheng J. State-of-the-art of fiber-reinforced high-pressure hydrogen storage tanks. *Journal of Pressurized Equipment and Systems* 2004; 2: 59-63.
 51. Teng TL, Yu CM, Wu YY. Optimal Design of Filament-Wound Composite Pressure Vessels. *Mech Compos Mater* 2005; 41: 333-40.
 52. Thesken JC, Murthy PLN, Phoenix SL, Greene N, Palko JL, et al. Theoretical Investigation of Composite Overwrapped Pressure Vessel (COPV). *Mechanics Applied to NASA Full Scale Tests*. National Aeronautics and Space Administration, Houston, TX. Lyndon B. Johnson Space Center, NASA/TM—2009-215684, Sept. 2009.
 53. Joselin R, Chelladurai T. Burst pressure prediction of composite pressure chambers using acoustic emission technique: a review. *J Fail Anal Preven* 2011; 11: 344-56.
 54. Laulusa A, Bauchau O, Choi J, Tan V, Li L. Evaluation of some shear deformable shell elements. *Int J Solids Struct* 2006; 43: 5033-54.
 55. Jones RM. *Mechanics of Composite Materials*. New York: Hemisphere Publishing Corporation, 1975.
 56. Zu L, Koussios S, Beukers A. Design of filament-wound isotenoid pressure vessels with unequal polar openings. *Compos Struct* 2010; 92: 2307-13
 57. Denost JP. New Design Concepts for filament-Wound Pressure Vessel with Unequal Polar. *AIAA 18th Joint Propulsion Conference*, 1982
 58. Hartung RF. Planar-wound filamentary pressure vessels. *AIAA J* 1963; 1: 2842-4.
 59. Zickel, J. Isotenoid pressure vessels. *ARS Journal* 1962; 32: 950-951.
 60. Marketos. Optimum toroidal pressure vessel filament wound along geodesic lines. *AIAA Journal* 1963; 1: 1942-5.
 61. Vafaeesefat A. Dome shape optimization of composite pressure vessels based on rational B-spline curve and genetic algorithm. *Appl Compos Mater* 2009; 16: 321-330.
 62. Winter CJ. Hydrogen energy – Abundant, efficient, clean: a debate over the energy-system-of-change. *Int J Hydrogen Energy* 2009; 34: S1–52
 63. Moriarty P, Honnery D. Hydrogen's role in an uncertain energy future. *Int J Hydrogen Energy* 2009; 34: 31–9.

64. Balat H, Kirtay E. Hydrogen from biomass – present scenario and future prospects. *Int J Hydrogen Energy* 2010; 35: 7416–26.
65. Aceves SM, Espinosa-Loza F, Ladesma-Orozco E, Ross TO, Weisberg AH, Brunner TC, et al. High-density automotive hydrogen storage with cryogenic capable pressure vessels. *Int J Hydrogen Energy* 2010; 35: 1219–26.
66. Rajua M, Ortmannb JP, Kumarb S. System simulation model for high-pressure metal hydride hydrogen storage systems. *Intl J Hydrogen Energy* 2010; 35: 8742–54
67. Rashidi AM, Nouralishahi A, Khodadadi AA, Mortazavi Y, Karimi A, Kashefi K. Modification of single wall carbon nanotubes (SWNT) for hydrogen storage. *Int J Hydrogen Energy* 2010; 35: 9489–95.
68. Zheng JY, Bie HY, Xu P, Chen HG, Liu PF, Li X, Liu YL. Experimental and numerical studies on the bonfire test of high-pressure hydrogen storage vessels. *Int J Hydrogen Energy* 2010; 35: 8191–8.
69. Zheng JY, Ye JJ, Yang J, Tang P, Zhao L, Kern M. An optimized control method for a high utilization ratio and fast filling speed in hydrogen refueling stations. *Int J Hydrogen Energy* 2010; 35: 3011–7.
70. Zhao L, Liu YL, Yang J, Zhao YZ, Zheng JY, Bie HY, Liu XX. Numerical simulation of temperature rise within hydrogen vehicle cylinder during refueling. *Int J Hydrogen Energy* 2010; 35: 8092–100.
71. Zu L, Koussios S, Beukers A. Optimal cross sections of filament-wound toroidal hydrogen storage vessels based on continuum lamination theory. *Int J Hydrogen Energy* 2010; 35: 10419–29.
72. Zheng JY, Liu XX, Xu P, Liu PF, Zhao YZ, Yang J. Development of high pressure gaseous hydrogen storage technologies. *Int J Hydrogen Energy* 2011: Article in Press.
73. U.S. Department of Energy (DOE). Hydrogen posture plan: an integrated research, development and demonstration plan. Feb. 2004.
74. Liu PF, Xu P, Zheng JY. Artificial immune system for optimal design of composite hydrogen storage vessel. *Comput Mater Sci* 2009; 47: 261-7.
75. Xu P, Zheng JY, Chen HG, Liu PF. Optimal design of high pressure hydrogen storage vessel using an adaptive genetic algorithm, *Int J Hydrogen Energy* 2010; 35: 2840-6.
76. Xu P, Zheng JY, Liu PF. Finite element analysis of burst pressure of composite hydrogen storage vessels. *Mater Des* 2009; 30: 2295-301.
77. Zheng CX, Lei SH. Mechanical analysis and optimal design for carbon fiber resin composite wound hydrogen storage vessel with aluminum alloy liner. *J Press Vess - T*

Chapter 1

- ASME 2009; 131: 021204.1–021204.6.
78. Zheng CX, Lei SH. Stresses controllable analysis and optimal design of unique high pressure vessel applied in hydrogen charge station. *Int J Hydrogen Energy* 2007; 32: 3508–18.
 79. Zu L, Koussios S, Beukers A. Shape optimization of filament wound articulated pressure vessels based on non-geodesic trajectories. *Compos Struct* 2010; 92: 339–46.
 80. Park JS, Hong CS, Kim CG, Kim CU. Analysis of filament wound composite structures considering the change of winding angles through the thickness direction. *Compos Struct* 2002; 55(1):63–71.
 81. Zu L, He QX, Ni QQ. Pattern design for non-geodesic winding toroidal pressure vessels. *Proceedings of the 16th International Conference on Composite Materials (ICCM/16)*, Kyoto, Japan, July 2007.
 82. Li HS, Liang YD, Bao HJ. CAM system for filament winding on elbows. *J Mater Process Technol* 2005; 161(3): 491-496.
 83. Li HS, Liang YD. Computer aided filament winding for elbows. *J Software* 2002; 13(4): 518-25.
 84. Kirchhoff G. *Über das gleichgewicht und die bewegung einer elastischen scheibe*. *J. Reine Angew. Math.* 1850; 40: 51–8.
 85. Love AEH. *On the small free vibrations and deformations of the elastic shells*. *Phil. Trans. Roy. Soc. Ser. A* 1888; 17: 491-546.
 86. Niordson FI. *A note on the strain energy of elastic shells*. *Int. J. Solids Struct.* 1971; 7: 1573-9.
 87. Sanders JL. *An improved first approximation theory of thin shells*. NASA Tech. Rep. R-24, 1959. (4)
 88. Flügge W. *Stresses in Shells*. 2nd ed. New York: Springer, 1973.
 89. Niordson FI. *A consistent refined shell theory*. In: *Complete Analysis and its Applications, Vekua Anniversary Volume*. Nauka, Moscow, 1978: 421–429.
 90. Bert CW, Francis PH. *Composite material mechanics: structural mechanics*. *AIAA J* 1974; 12(9): 1173-86.
 91. Ashwell, D.G., Gallagher, R.H. (Eds.), 1976. *Finite Elements for Thin Shells and Curved Membranes*. Wiley, New York.
 92. Niordson, F.I., 1985. *Shell Theory*. North-Holland, Amsterdam.
 93. Bert CW. *Analysis of shells*. In: Broutman LJ, Krock RH, editors. *Composite Materials*, New York: Academic Press; 1975; 7: 207–58.

94. Koiter WT. A consistent first approximation in general theory of thin elastic shells. In: Koiter, W.T. (Ed.), *Theory of Thin Elastic Shells*, First IUTAM Symposium. North Holland, Amsterdam, 1960: 12–33.
95. Rohrauer G. Ultra-high pressure composite vessels with efficient stress distributions. PhD thesis, Concordia University, 1999.

I FUNDAMENTALS

Chapter 2

Fiber Trajectories and Their Stability

2.1 Introduction

This chapter deals with the derivation of geodesic and non-geodesic trajectories on generic shells of revolution. Firstly, the stability analysis of fiber trajectories on a generic surface is carried out to provide a theoretical foundation for obtaining the geodesic and non-geodesic trajectories. Secondly, we present here a summary of the most important topics of differential geometry, tailored for filament winding trajectories on a surface. After a brief presentation of the fundamental forms we proceed to the outline of several curvatures and the derivation of the geodesic trajectories. In the last section, the mathematical description of geodesics and non-geodesics on a generic shell of revolution is briefly presented.

2.2 Fiber Stability on a Surface

In this section, an important topic concerning the stability of fiber trajectories on a surface is discussed. Any deviation from geodesics will require a lateral force of friction to prevent the fiber sliding from its original trajectory. In addition, for a concave surface the condition

Chapter 2

which avoids fiber bridging should also be respected when designing winding trajectories. Therefore an analysis for the stability of fiber trajectories is imperative which allows accurate fiber placement to achieve the optimal vessel performance dictated by structural design. The overlook of fiber trajectory stability will make the optimally designed lay-up parameters difficult to be realized using filament winding process and hence invalidate the structural design and optimization.

The vector parameterization of an arbitrary mandrel surface in generalized curvilinear orthogonal coordinates can be represented as:

$$\mathbf{S} = \mathbf{S}(u, v) \quad (2.1)$$

where \mathbf{S} is a vector-valued function of the parameters (u, v) and the parameters vary within a certain domain in the parametric uv -plane. The u -curve is obtained by fixing $v = v_0$ and varying u , and the v -curve is obtained by fixing $u = u_0$ and varying v . For shells of revolution the u, v -curves denote meridians and parallels. An arbitrary fiber curve on the surface $\mathbf{S}(u, v)$ can be given by its arclength parametrization:

$$\mathbf{C}(s) = \mathbf{C}(u(s), v(s)) \quad (2.2)$$

An infinitesimal elementary piece $\mathbf{P}_0\mathbf{P}_1$ ($|\mathbf{P}_0\mathbf{P}_1| = ds$) of a fiber curve is here considered, as depicted in Fig. 2.1. $\mathbf{P}_0\mathbf{P}_1$ is subjected to longitudinal tension forces \mathbf{F}_0 and \mathbf{F}_1 , a normal reaction force \mathbf{F}_n perpendicular to the surface and a friction force \mathbf{F}_f tangential to the mandrel surface. The *Darboux frame* [1], which takes into account the fact that the curve $\mathbf{C}(s)$ lies on the surface $\mathbf{S}(u, v)$, is here considered. Using the right-handed orthonormal basis $(\mathbf{n}, \mathbf{T}, \mathbf{n} \times \mathbf{T})$ the principal normal curvature vector $\boldsymbol{\kappa}$ is in the plane spanned by $\mathbf{n} \times \mathbf{T}$ and \mathbf{n} , and can thus be decomposed into these two orthogonal vectors:

$$\boldsymbol{\kappa} = \kappa_g(\mathbf{n} \times \mathbf{T}) + \kappa_n \mathbf{n} \quad (2.3)$$

where \mathbf{n}, \mathbf{T} denote the unit normal and tangent vector, respectively; κ_n gives the component of the principal curvature vector normal to the surface at a point and is called the normal curvature; κ_g gives the component of the curvature vector tangential to the surface and is called the geodesic curvature. Please note that $\boldsymbol{\kappa}$ points towards the center of the curvature of the fiber trajectory and can be expressed by [1]:

$$\boldsymbol{\kappa} = \kappa \mathbf{N} \quad (2.4)$$

where κ is the total curvature (usually referred to as ‘‘curvature’’) of the fiber trajectory at a point (\mathbf{P}_0 or \mathbf{P}_1); \mathbf{N} is the principal normal vector in the *Frenet Frame* [1].

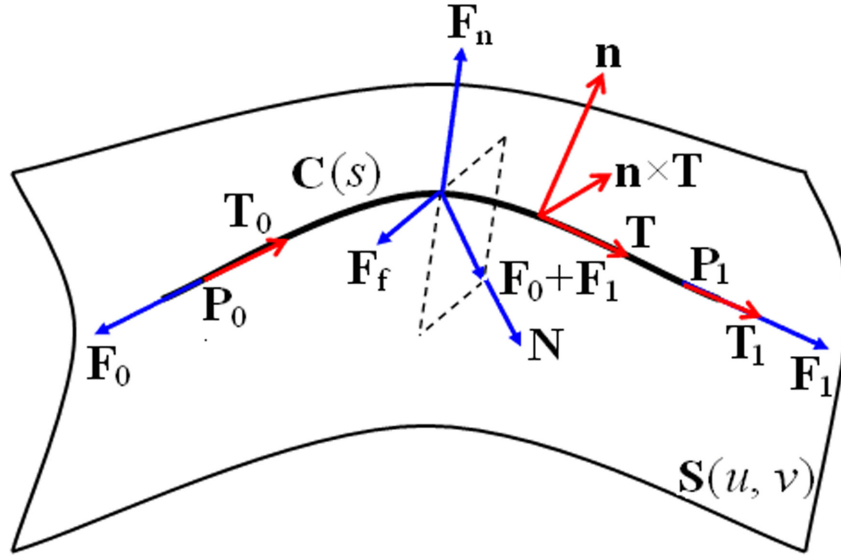


Fig. 2.1: An infinitesimally small element of a tensioned fiber on an arbitrary surface

For an infinitesimal arclength the magnitudes of the tension at both sides of $\mathbf{P}_0\mathbf{P}_1$ are considered equal:

$$|\mathbf{F}_0| = |\mathbf{F}_1| = \ell \quad (2.5)$$

Thus we have:

$$\mathbf{F}_0 = -\ell\mathbf{T}_0 \quad (2.6)$$

$$\mathbf{F}_1 = \ell\mathbf{T}_1 \quad (2.7)$$

The equilibrium equations of the forces exerting on $\mathbf{P}_0\mathbf{P}_1$ in directions normal and tangent to the surface, can respectively be formulated as:

$$[(\mathbf{F}_0 + \mathbf{F}_1) \cdot \mathbf{n}]\mathbf{n} + \mathbf{F}_n = 0 \quad (2.8)$$

$$[(\mathbf{F}_0 + \mathbf{F}_1) \cdot (\mathbf{n} \times \mathbf{T})](\mathbf{n} \times \mathbf{T}) + \mathbf{F}_f = 0 \quad (2.9)$$

Substituting equations (2.6) and (2.7) into (2.8) and (2.9), leads to:

$$\mathbf{F}_n = [-\ell (\mathbf{T}_1 - \mathbf{T}_0) \cdot \mathbf{n}]\mathbf{n} \quad (2.10)$$

$$\mathbf{F}_f = [-\ell (\mathbf{T}_1 - \mathbf{T}_0) \cdot (\mathbf{n} \times \mathbf{T})](\mathbf{n} \times \mathbf{T}) \quad (2.11)$$

Since $|\mathbf{P}_0\mathbf{P}_1| = ds$, according to differential geometry we have:

$$\mathbf{T}_1 - \mathbf{T}_0 = ds\mathbf{T}' = \kappa ds\mathbf{N} \quad (2.12)$$

Substitution of equation (2.12) into (2.10) and (2.11) yields:

$$\mathbf{F}_n = (-\ell\kappa ds\mathbf{N} \cdot \mathbf{n})\mathbf{n} \quad (2.13)$$

$$\mathbf{F}_f = [-\ell\kappa ds\mathbf{N} \cdot (\mathbf{n} \times \mathbf{T})](\mathbf{n} \times \mathbf{T}) \quad (2.14)$$

Substituting equation (2.4) into (2.3) followed by multiplying both sides of the resulting

Chapter 2

equation by the normal vector \mathbf{n} , results in:

$$\kappa \mathbf{N} \cdot \mathbf{n} = \kappa_n \quad (2.15)$$

$$\kappa \mathbf{N} \cdot (\mathbf{n} \times \mathbf{T}) = \kappa_g \quad (2.16)$$

Substitution of equations (2.15) and (2.16) into (2.13) and (2.14) yields:

$$\mathbf{F}_n = -\kappa_n \ell ds \mathbf{n} \quad (2.17)$$

$$\mathbf{F}_f = -\kappa_g \ell ds (\mathbf{n} \times \mathbf{T}) \quad (2.18)$$

To prevent fiber sliding on the supporting surface, the friction force \mathbf{F}_f should always be less than the maximum static friction between the supporting surface and the fiber bundle:

$$|\mathbf{F}_f| \leq \mu_{\max} |\mathbf{F}_n| \quad (2.19)$$

where μ_{\max} is the coefficient of maximum static friction between the fiber and the mandrel surface or between the fiber and the previously overwound layer. Note that μ_{\max} can be affected by the surface quality, fiber morphology, resin viscosity, etc [2].

Substitution of equations (2.17) and (2.18) into (2.19) gives the non-slippage criterion:

$$|\kappa_g / \kappa_n| \leq \mu_{\max} \quad (2.20)$$

The slippage coefficient λ is defined as the ratio of the geodesic curvature to the normal curvature [3, 4]:

$$\lambda = \kappa_g / \kappa_n \quad (2.21)$$

The non-slippage criterion equation (2.20) can then be rewritten as:

$$|\lambda| \leq \mu_{\max} \quad (2.22)$$

The slippage coefficient λ represents the slippage tendency between the fiber bundle and the supporting surface. The region of possible winding patterns can then be found according to λ .

In addition, the fibers may bridge on the concave surface and lose contact with the mandrel surface unless the normal force \mathbf{F}_n is acting in the same direction to the normal vector \mathbf{n} (if pointing outward), or in the opposite direction to the normal vector \mathbf{n} (if pointing inward):

$$\mathbf{F}_n \cdot \mathbf{n} \geq 0 \quad (\text{outward-pointing normal}) \quad (2.23)$$

$$\mathbf{F}_n \cdot \mathbf{n} \leq 0 \quad (\text{inward-pointing normal}) \quad (2.24)$$

Please note that the normal vector is here considered always outward-pointing. Substituting equation (2.17) into (2.23) and taking into account that the product $\ell \kappa ds$ is constantly greater than 0, leads to:

$$\kappa_n \leq 0 \quad (2.25)$$

Equation (2.25) provides the non-bridging criterion of fiber trajectories on a surface. It should be noted that the fiber bridging can generally be eliminated by modifying the winding angles.

2.3 Topics Related to Differential Geometry

2.3.1 Fundamental forms

The parametrization of a three-dimensional surface can be expressed as a vector function of two independent parameters u, v :

$$\mathbf{S}(u, v) = \{x(u, v), y(u, v), z(u, v)\} \quad (u, v \in \mathfrak{R}) \quad (2.26)$$

The length of a curve on this surface is:

$$s = \int \sqrt{dx^2 + dy^2 + dz^2} \quad (2.27)$$

If x, y and z are replaced by a general symbol $\#$, the differentials encountered in equation (2.27) can be written as:

$$d\#^2 = \left(\frac{\partial\#}{\partial u}\right)^2 (du)^2 + 2\frac{\partial\#}{\partial u}\frac{\partial\#}{\partial v} du dv + \left(\frac{\partial\#}{\partial v}\right)^2 (dv)^2 \quad (2.28)$$

Substitution of equation (2.28) into (2.26) leads to:

$$s = \int \left(\sqrt{G + 2F \frac{du}{dv} + E \left(\frac{du}{dv}\right)^2} \right) dv = \int \left(\sqrt{E + 2F \frac{dv}{du} + G \left(\frac{dv}{du}\right)^2} \right) du \quad (2.29)$$

where:

$$\begin{aligned} E &= \left(\frac{\partial x}{\partial u}\right)^2 + \left(\frac{\partial y}{\partial u}\right)^2 + \left(\frac{\partial z}{\partial u}\right)^2 = \mathbf{S}_u \cdot \mathbf{S}_u \\ F &= \frac{\partial x}{\partial u} \frac{\partial x}{\partial v} + \frac{\partial y}{\partial u} \frac{\partial y}{\partial v} + \frac{\partial z}{\partial u} \frac{\partial z}{\partial v} = \mathbf{S}_u \cdot \mathbf{S}_v \\ G &= \left(\frac{\partial x}{\partial v}\right)^2 + \left(\frac{\partial y}{\partial v}\right)^2 + \left(\frac{\partial z}{\partial v}\right)^2 = \mathbf{S}_v \cdot \mathbf{S}_v \end{aligned} \quad (2.30)$$

The coefficients E, F , and G presented in equation (2.30), are called the coefficients of the first fundamental form, where E represents the metric along the meridional direction of the shell, and G denotes the metric along the parallel direction. In addition, $\mathbf{S}_u \times \mathbf{S}_v$ is a nonzero vector orthogonal to the plane spanned by \mathbf{S}_u and \mathbf{S}_v ; we obtain the corresponding unit vector by taking:

$$\mathbf{n} = \frac{\mathbf{S}_u \times \mathbf{S}_v}{\|\mathbf{S}_u \times \mathbf{S}_v\|} \quad (2.31)$$

where \mathbf{n} is called the unit normal of the parametrized surface.

In equation (2.30) F is the inner product of the derivatives of \mathbf{S} with respect to the main directions. For a shell of revolution the meridional and parallel directions are perpendicular to

Chapter 2

each other and therefore F will be equal to zero. For an arbitrary three dimensional surface this is generally not true.

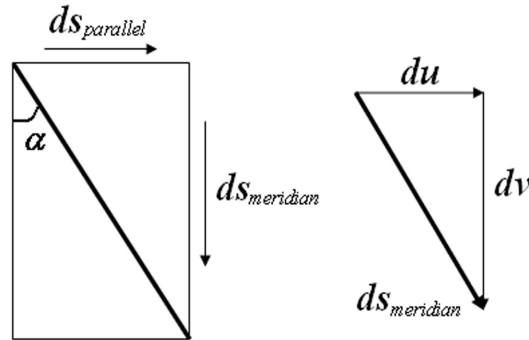


Fig. 2.2: Geometrical relations for an elementary part of the fiber curve on a surface

Next to the coefficients of the first fundamental form $\{E, F, G\}$, the coefficients of the second fundamental form exist as well. These coefficients $\{L, M, N\}$ also play a role in the derivation of curvatures. They are defined as:

$$L = \frac{\det \begin{bmatrix} \mathbf{S}_{uu} \\ \mathbf{S}_u \\ \mathbf{S}_v \end{bmatrix}}{\sqrt{EG - F^2}} = \mathbf{n}(u, v) \cdot \mathbf{S}_{uu}$$

$$M = \frac{\det \begin{bmatrix} \mathbf{S}_{uv} \\ \mathbf{S}_u \\ \mathbf{S}_v \end{bmatrix}}{\sqrt{EG - F^2}} = \mathbf{n}(u, v) \cdot \mathbf{S}_{uv} \quad (2.32)$$

$$N = \frac{\det \begin{bmatrix} \mathbf{S}_{vv} \\ \mathbf{S}_u \\ \mathbf{S}_v \end{bmatrix}}{\sqrt{EG - F^2}} = \mathbf{n}(u, v) \cdot \mathbf{S}_{vv}$$

2.3.2 Curvatures

What distinguishes a circle or a helix from a line is their *curvature*, i.e., the tendency of the curve to change direction [5]. The curvature of \mathbf{C} at a point can be seen as a measure of how sensitive its tangent line is to moving the point to other nearby points. The higher the curvature, the less the curve is straight. We consider here an infinitesimally small elementary

part of the fiber curve on a regular parametrized surface \mathbf{S} (Fig. 2.2); the lengths of its projections in the meridional and parallel directions are respectively given by:

$$ds_{meridional} = \sqrt{E} du \quad (2.33)$$

$$ds_{parallel} = \sqrt{G} dv \quad (2.34)$$

The fiber trajectory has an orientation α with respect to the meridian (Fig. 2.2); this angle relates the arclength increment in the meridional direction and that in the fiber curve orientation:

$$ds_{meridional} = \cos \alpha \cdot ds \quad (2.35)$$

$$ds_{parallel} = \sin \alpha \cdot ds \quad (2.36)$$

The derivatives of u and v with respect to s are given by inverse forms of equation (2.30):

$$\frac{du}{ds} = \frac{\cos \alpha}{\sqrt{E}} \quad (2.37)$$

$$\frac{dv}{ds} = \frac{\sin \alpha}{\sqrt{G}} \quad (2.38)$$

The second derivatives of u and v with respect to s can be expressed as follows:

$$\frac{d^2u}{ds^2} = -\frac{d\alpha}{ds} \frac{\sin \alpha}{\sqrt{E}} - \frac{E_u \cos^2 \alpha}{2E^2} - \frac{E_v \sin \alpha \cos \alpha}{2E\sqrt{EG}}, \quad (2.39)$$

$$\frac{d^2v}{ds^2} = \frac{d\alpha}{ds} \frac{\cos \alpha}{\sqrt{G}} - \frac{G_u \sin \alpha \cos \alpha}{2G\sqrt{EG}} - \frac{G_v \sin^2 \alpha}{2G^2}. \quad (2.40)$$

Then we have:

$$\mathbf{C}'(s) = \left(\frac{\cos \alpha}{\sqrt{E}}, \frac{\sin \alpha}{\sqrt{G}} \right) \quad (2.41)$$

$$\mathbf{C}''(s) = \left(-\frac{d\alpha}{ds} \frac{\sin \alpha}{\sqrt{E}} - \frac{E_u \cos^2 \alpha}{2E^2} - \frac{E_v \sin \alpha \cos \alpha}{2E\sqrt{EG}}, \right. \\ \left. \frac{d\alpha}{ds} \frac{\cos \alpha}{\sqrt{G}} - \frac{G_u \sin \alpha \cos \alpha}{2G\sqrt{EG}} - \frac{G_v \sin^2 \alpha}{2G^2} \right) \quad (2.42)$$

According to equation (2.16), κ_g can be calculated by [6]:

$$\kappa_g = \mathbf{C}'' \cdot (\mathbf{n} \times \mathbf{T}) = \det(\mathbf{C}', \mathbf{C}'', \mathbf{n}) \quad (2.43)$$

With the expression (2.31) for obtaining the unit normal vector \mathbf{n} , the geodesic curvature can be determined by substitution of equations (2.31), (2.41) and (2.42) into (2.43), leads to:

Chapter 2

$$\begin{aligned} \kappa_g = \sqrt{EG - F^2} & \left[\frac{du}{ds} \frac{d^2v}{ds^2} - \frac{dv}{ds} \frac{d^2u}{ds^2} - \frac{E_v}{2G} \left(\frac{du}{ds} \right)^3 + \frac{G_v}{G} \left(\frac{du}{ds} \right)^2 \left(\frac{dv}{ds} \right) + \frac{G_v}{2G} \left(\frac{dv}{ds} \right)^2 \left(\frac{du}{ds} \right) \right. \\ & \left. - \frac{E_u}{2E} \left(\frac{du}{ds} \right)^2 \left(\frac{dv}{ds} \right) - \frac{E_v}{E} \left(\frac{dv}{ds} \right)^2 \left(\frac{du}{ds} \right) + \frac{G_u}{2E} \left(\frac{dv}{ds} \right)^2 \right] \end{aligned} \quad (2.44)$$

Substitution of equations (2.30), (2.37) and (2.38) into (2.44) leads, after some simplifications, to:

$$\kappa_g = \frac{d\alpha}{ds} - \frac{E_v}{2\sqrt{G}} \frac{\partial \ln E}{\partial v} \cos \alpha + \frac{1}{2\sqrt{E}} \frac{\partial \ln G}{\partial u} \sin \alpha \quad (2.45)$$

equation (2.45) is the well-known *Liouville* formula [1] and provides the equation for obtaining the geodesic curvature.

Depending on this orientation, the curvature κ_n , normal to surface \mathbf{S} , will have a maximum and a minimum value at point P. These two extreme values of the curvature are called the principal curvatures. The Gaussian curvature (K) and the mean curvature (H) couple these principal curvatures to the coefficients of the first and second fundamental form, according to:

$$K = \kappa_1 \kappa_2 = \frac{LN - M^2}{EG - F^2} \quad (2.46)$$

$$H = \frac{1}{2}(\kappa_1 + \kappa_2) = \frac{LG - 2MF + NE}{2(EG - F^2)} \quad (2.47)$$

where κ_1 and κ_2 are the curvatures in the two principal directions, respectively. From equations (2.46) and (2.47), the principal curvatures are the roots of the following equation:

$$\kappa^2 - 2H\kappa + K = 0 \quad (2.48)$$

Hence the roots are:

$$k_1 = H + \sqrt{H^2 - K}, \quad k_2 = H - \sqrt{H^2 - K} \quad (2.49)$$

The normal curvature, κ_n , can be expressed in terms of the two principal curvatures at a point P [1]:

$$\kappa_n = \kappa_1 \cos^2 \alpha + \kappa_2 \sin^2 \alpha \quad (2.50)$$

2.3.3 Length-minimizing curves – geodesics

Geodesic trajectories form a class of curves which exclusively connect points via the shortest path between them. This principle is comparable to sailing or driving on the earth surface in a straight line, without any cornering. In filament winding processes, geodesic trajectories are very often used, as the wound paths are completely stable. The filaments are often exactly aligned with the loads applied to them, e.g. with fiber tension used in the

winding process. The shortest paths can be determined by minimizing the arc length, expressed in equation (2.27). In order to find this minimum, a function is needed that relates the two independent parameters u and v in such a way that the arc length integral becomes minimal. Therefore, the first expression for the arc length integral is written as:

$$s = \int f(u, v, \frac{dv}{du}) du \quad (2.51)$$

Once the begin- and endpoints are fixed, the arc length is solely dependent on the function $v(u)$. Equation has a stationary value when:

$$\begin{aligned} \delta s &= \delta \int_{u_b}^{u_e} f(u, v, v') du = \int_{u_b}^{u_e} \left(\frac{\partial f}{\partial v} \delta v + \frac{\partial f}{\partial v'} \delta v' \right) du \\ &= \int_{u_b}^{u_e} \left(\frac{\partial f}{\partial v} \delta v + \frac{\partial f}{\partial v'} \frac{d}{du} (\delta v) \right) du = 0 \end{aligned} \quad (2.52)$$

Integration of equation (2.52) by parts, gives:

$$\delta s = \int_{u_b}^{u_e} \frac{\partial f}{\partial v} \delta v du + \frac{\partial f}{\partial v'} \delta v \Big|_{u_b}^{u_e} - \int_{u_b}^{u_e} \delta v \frac{d}{du} \left(\frac{\partial f}{\partial v'} \right) du = 0 \quad (2.53)$$

where

$$v' = \frac{dv}{du} \quad (2.54)$$

With fixed start and end points, the second term in equation (2.53) equals zero and hence:

$$\delta s = \int_{u_b}^{u_e} \left(\frac{\partial f}{\partial v} - \frac{d}{du} \left(\frac{\partial f}{\partial v'} \right) \right) \delta v du = 0 \quad (2.55)$$

As the integral above must be equal to zero for any δv , equation (2.55) leads to the Euler-Lagrange equation:

$$\frac{\partial f}{\partial v} - \frac{d}{du} \left(\frac{\partial f}{\partial v'} \right) = 0 \quad (2.56)$$

Substitution of equation (2.51) for the curve length into equation (2.56), results in:

$$\frac{v'^2 E_v + 2v' F_v + G_v}{2\sqrt{Ev'^2 + 2Fv' + G}} - \frac{d}{du} \left(\frac{Ev' + F}{\sqrt{Ev'^2 + 2Fv' + G}} \right) = 0 \quad (2.57)$$

The coefficients E , F and G are functions of u and v in general, and solving equation (2.57) therefore becomes quite difficult. In [1], a numerical method is described to solve the equation by means of *Christoffel symbols*. *Christoffel symbols* are first used to express the geodesic equations by means of two second order differential equations:

Chapter 2

$$\begin{cases} v'' + \Gamma_{vv}^v v'^2 + 2\Gamma_{uv}^v u'v' + \Gamma_{uu}^v u'^2 = 0 \\ u'' + \Gamma_{vv}^u v'^2 + 2\Gamma_{uv}^u u'v' + \Gamma_{uu}^u u'^2 = 0 \end{cases} \quad (2.58)$$

where u' , u'' , v' , v'' are the first and second derivatives of u and v with respect to the arclength increment ds , respectively, and the *Christoffel* symbols are given by:

$$\begin{aligned} \Gamma_{vv}^u &= \frac{2EF_v - EE_u - FE_u}{2(EG - F^2)}, \quad \Gamma_{uv}^u = \frac{EG_v - FE_u}{2(EG - F^2)}, \quad \Gamma_{uu}^u = \frac{EG_u - 2FF_u + FG_v}{2(EG - F^2)}, \\ \Gamma_{vv}^v &= \frac{GE_v - 2FF_v + FE_u}{2(EG - F^2)}, \quad \Gamma_{uv}^v = \frac{GE_u - FG_v}{2(EG - F^2)}, \quad \Gamma_{uu}^v = \frac{2GF_u - GG_v - FG_u}{2(EG - F^2)}. \end{aligned} \quad (2.59)$$

For completeness:

$$\Gamma_{uv}^u = \Gamma_{vu}^u \quad \text{and} \quad \Gamma_{uv}^v = \Gamma_{vu}^v \quad (2.60)$$

Finally, before numerically solving equation (2.58), the system of two second-order differential equations is rewritten as a system of four first-order equations:

$$\begin{cases} v' = p \\ u' = q \\ p' = -\Gamma_{vv}^v p^2 - 2\Gamma_{uv}^v pq - \Gamma_{uu}^v q^2 = 0 \\ q' = -\Gamma_{vv}^u p^2 - 2\Gamma_{uv}^u pq - \Gamma_{uu}^u q^2 = 0 \end{cases} \quad (2.61)$$

The simultaneous solution of the above system of differential equations (2.61) will finally determine the geodesics for filament winding processes. A curve on a surface is geodesic only if the associated geodesic curvature is equal to zero. For a regular parametrized surface S ($F = 0$) this solution can be obtained by setting equation (2.45) equal to 0, given by:

$$\frac{d\alpha}{ds} = \frac{E_v}{2\sqrt{G}} \frac{\partial \ln E}{\partial v} \cos \alpha - \frac{1}{2\sqrt{E}} \frac{\partial \ln G}{\partial u} \sin \alpha \quad (2.62)$$

2.4 Geodesics and Non-geodesics on Generic Shells of Revolution

The class of shells of revolution comprises the most commonly used shapes for forming filament winding products. This is the reason for providing special attention to this class of shapes. The vector parameterization of a generic surface of revolution in polar coordinates can be given by:

$$\mathbf{S}(u, v) = \{f(u) \cos v, f(u) \sin v, g(u)\} \quad (f(u) \geq 0) \quad (2.63)$$

Here the u -curves are meridians and the v -curves are parallels. We have:

$$\mathbf{S}_u = \{f'(u) \cos v, f'(u) \sin v, g'(u)\}$$

$$\begin{aligned} \mathbf{S}_v &= \{-f(u) \sin v, f(u) \cos v, 0\} \\ \mathbf{n} &= \frac{\mathbf{S}_u \times \mathbf{S}_v}{\|\mathbf{S}_u \times \mathbf{S}_v\|} = \{-g'(u) \cos v, -g'(u) \sin v, f'(u)\} \\ \mathbf{S}_{uu} &= \{f''(u) \cos v, f''(u) \sin v, g''(u)\} \\ \mathbf{S}_{uv} &= \{-f'(u) \sin v, f'(u) \cos v, 0\} \\ \mathbf{S}_{vv} &= \{-f(u) \cos v, -f(u) \sin v, 0\} \end{aligned}$$

and so we have:

$$E = \mathbf{S}_u \cdot \mathbf{S}_u = f'^2 + g'^2, \quad F = \mathbf{S}_u \cdot \mathbf{S}_v = 0, \quad G = \mathbf{S}_v \cdot \mathbf{S}_v = f^2 \quad (2.64)$$

$$L = \mathbf{n} \cdot \mathbf{S}_{uu} = -\frac{f''g' - f'g''}{\sqrt{f'^2 + g'^2}}, \quad M = \mathbf{n} \cdot \mathbf{S}_{uv} = 0, \quad N = \mathbf{n} \cdot \mathbf{S}_{vv} = \frac{fg'}{\sqrt{f'^2 + g'^2}}. \quad (2.65)$$

Specifically, let the meridian curve be defined as $f(u) = r(z)$, e.g. $z = u = g(u)$, equation (2.63) can be rewritten as:

$$\mathbf{S}(\theta, z) = \{r(z) \cos \theta, r(z) \sin \theta, z\} \quad (2.66)$$

where r, z denote the radial and axial coordinate, respectively; θ stands for the angular coordinate in the parallel direction, as shown in Fig. 2.3.

Equations (2.64) and (2.65) become:

$$E = r'^2 + 1, \quad F = 0, \quad G = r^2, \quad (2.67)$$

$$L = -\frac{r''}{\sqrt{r'^2 + 1}}, \quad M = 0, \quad N = \frac{r}{\sqrt{r'^2 + 1}}. \quad (2.68)$$

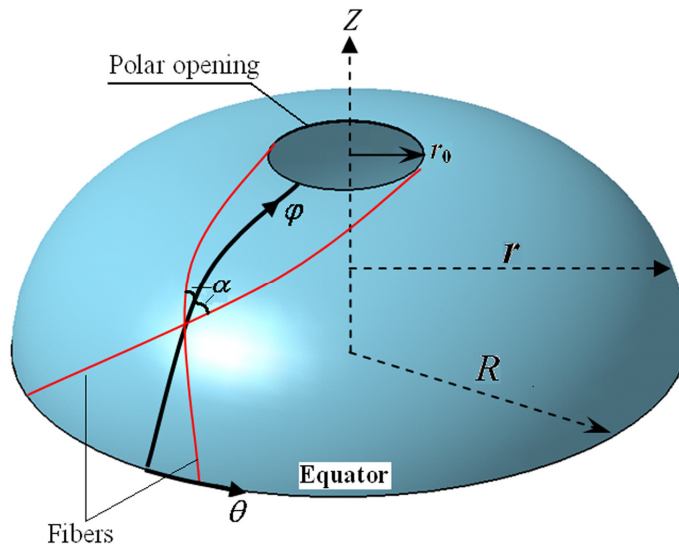


Fig. 2.3: A general shell of revolution

Chapter 2

where r' and r'' are the first and second derivative of r with respect to z , respectively. By recalling equations (2.46) and (2.47), the Gaussian curvature, K , and the mean curvature, H , can be obtained by:

$$K = -\frac{r''}{r(1+r'^2)^2}, \quad H = \frac{1+r'^2-rr''}{2r(1+r'^2)^{3/2}} \quad (2.69)$$

Then the two principal curvatures (κ_1, κ_2) can be given by substitution of equation (2.69) into (2.49):

$$\kappa_1 = -\frac{r''}{(1+r'^2)^{3/2}}, \quad \kappa_2 = \frac{1}{r\sqrt{1+r'^2}}. \quad (2.70)$$

According to equation (2.50), the normal curvature κ_n is:

$$\kappa_n = -\frac{r''}{(1+r'^2)^{3/2}} \cos^2 \alpha + \frac{1}{r\sqrt{1+r'^2}} \sin^2 \alpha \quad (2.71)$$

Substitution of equations (2.67) and (2.68) into (2.45) leads to the expression for the geodesic curvature κ_g :

$$\kappa_g = \frac{d\alpha}{ds} + \frac{r' \sin \alpha}{r\sqrt{1+r'^2}} \quad (2.72)$$

By substitution of equations (2.71) and (2.72) into (2.21), the differential equation for the non-geodesic trajectories is obtained:

$$\frac{d\alpha}{ds} = -\lambda \left(\frac{r''}{(1+r'^2)^{3/2}} \cos^2 \alpha - \frac{1}{r\sqrt{1+r'^2}} \sin^2 \alpha \right) - \frac{r' \sin \alpha}{r\sqrt{1+r'^2}} \quad (2.73)$$

The relation between dz/ds and α can be written as follows:

$$\frac{dz}{ds} = \frac{dz}{ds_{meridian}} \cdot \frac{ds_{meridian}}{ds} = \frac{dz}{\sqrt{1+r'^2}} \cdot \cos \alpha = \frac{\cos \alpha}{\sqrt{1+r'^2}} \quad (2.74)$$

Substitution of equation (2.74) into (2.73) leads, after some rearrangements, to the expression for determining non-geodesic trajectories with respect to α and z :

$$\frac{d\alpha}{dz} = \lambda \left[\frac{\sin \alpha \cdot \tan \alpha}{r} - \frac{r''}{1+r'^2} \cos \alpha \right] - \frac{r' \cdot \tan \alpha}{r} \quad (2.75)$$

For $\lambda=0$ the solution of equation (2.75) is the well-known Clairaut equation [7] for determining the geodesics on a surface of revolution, given by:

$$r \sin \alpha = r_0 \quad (2.76)$$

where r_0 is the polar opening radius of the shell of revolution (see Fig. 2.3).

In every other case ($\lambda \neq 0$), the fiber trajectories will deviate from the geodesics and are therefore renamed as non-geodesics. There is no analytical solution of equation (2.75) for $\lambda \neq 0$. With the aid of the initial winding conditions, the non-geodesic trajectories can be

calculated step by step using the *Runge-Kutta* method [8]. To avoid fiber sliding, λ should always be less than μ_{\max} ranging from 0.2 (between the fiber and the previously wound layer) to 0.35 (between the fiber and the mandrel surface) [9, 10]. It should be noted here that the slippage coefficient λ could be negative as well [11]. The ‘+’ sign refers to the fact that the presence of friction can either relatively increase or decrease the resulting winding angles.

2.5 Conclusions

In filament winding industry, perhaps the most elegant and often-used class of fiber curves on mandrel surfaces is represented by geodesic trajectories that connect two arbitrary points on a curved surface by means of the minimum arclength. The geodesics we refer here show great stability of the wound fibers on the supporting surface. However, since the geodesics are entirely determined by the initial winding conditions in terms of fiber position and orientation, restricting the winding trajectories to geodesics certainly limits the available design freedom and the possible performance improvement of pressure vessels. In fact, a fiber must not necessarily be wound geodesically to be stable; non-geodesic trajectories can also be overwrapped by a certain deviation from the geodesic paths, counting on friction to keep the fiber in its original position. It is thus desirable to exploit friction-based non-geodesics to enlarge the design space of filament wound pressure vessels. Compared to geodesic winding, the application of non-geodesic winding significantly enlarges the design space for pressure vessels. The possibility appears for modifying the λ -value to gain more design freedom for the winding trajectories. Consequently, the ability for improving the structural performance while satisfying the manufacturing requirements becomes here a fact.

References

1. Gray A. Modern differential geometry of curves and surfaces. Boca Ration: CRC press; 1993.
2. Koussios S, Bergsma OK. Friction experiments for filament winding applications. *J Thermoplast Compos* 2006; 19: 5-34.
3. De Carvalho J, Lossie M, Vandepitte D, Van Brussel H. Optimization of filament wound parts based on non-geodesic winding. *Compos Manufact* 1995; 6: 79-84.
4. Zu L, Koussios S, Beukers A. Shape optimization of filament wound articulated pressure

Chapter 2

- vessels based on non-geodesic trajectories. *Compos Struct* 2010; 92: 339-46.
5. Shifrin T. *Differential geometry: a first course in curves and surfaces*. University of Georgia, 2011.
 6. Koussios S. *Filament winding: a unified approach*. PhD Thesis Report. Design & Production of Composite Structures, Faculty of Aerospace Engineering, Delft University of Technology. Delft University Press, 2004.
 7. Zwillinger, D. "Clairaut's Equation." §II.A.38 in *Handbook of Differential Equations*, 3rd ed. Boston, MA: Academic Press, pp. 120 and 158-160, 1997.
 8. Boyce WE, DiPrima RC. *Elementary differential equations and boundary value problems*. New York: John Wiley & Sons, Inc, 1986.
 9. Wang R, Jiao W, Liu W, Yang F, He X. Slippage coefficient measurement for non-geodesic filament-winding process. *Comp Part A: Appl Sci Manuf* 2011; 42: 303-9
 10. Kim CU, Kang JH, Hong CS, Kim CG. Optimal design of filament wound structures under internal pressure based on the semi-geodesic path algorithm. *Compos Struct* 2005; 67: 443–52.
 11. Koussios S, Bergsma OK, Mitchell G. Non-geodesic filament winding on generic shells of revolution. *J Mater Part L: Des Appl* 2005; 219(1):25-35.

Chapter 3

Basic Design Theories and Optimality Conditions

3.1 Introduction

On normal isotropic materials, it is sufficient to describe their mechanical properties using just two engineering constants: usually the Young's Modulus and the Poisson's ratio. However, on anisotropic materials, much more is required to fully describe the material's behavior. An anisotropic material is a material that its properties at a specified point vary with the direction of the reference axes. For example the material's Young's Modulus in the longitudinal direction might not be the same than in the transverse direction. For this reason the engineering mechanics of composite materials are more complex to study than isotropic materials and most of the isotropic equations do not apply to composite materials and must be modified to study such behavior.

This chapter presents the basic concepts (related to the netting and continuum theory) serving here as a basis for the formulation of in-plane stress and deformation for a pressure vessel. The generalized optimality condition of equal shell strains for a pressure vessel, which couples the vessel geometry and the laminate anisotropy, is derived based on the minimum strain energy density criterion, in order to maximize the structural stiffness and load bearing capacity. The specific equations and feasible intervals of the optimality condition are also presented for several types of laminations.

3.2 Netting Analysis

Netting analysis of the stress and deformation of a balanced angle ply laminate gives a very simple result by ignoring the presence of the matrix and considering only the loading of the fibers [1-3], i.e. the stiffness of the matrix is taken to be effectively zero. These assumptions are in a certain sense consistent with pressure vessels, in which the fibers are loaded in tension and the stiffness of the matrix is considered negligible in comparison to the fiber strength. The burst failure tests demonstrated that the resin matrix starts to fail at a low level of internal pressure. However, vessels remain able to withstand loading up to fiber fracture and, therefore, the fibers at this moment act like a multilayered net-cover that supports the uniformly distributed internal pressure and the resulting in-plane membrane forces. The netting theory assumes that all loads and the membrane forces are carried by the fibers only, neglecting any contribution by the resin matrix and any interaction between the filaments. These assumptions do not cause any significant error in the analysis, as long as the fibers are primarily loaded in tension and the transverse and shear stresses in the composite laminate are low compared to the ultimate tensile strength of the fibers. It is also assumed that the load sharing contribution from the inner liner is minimal or non-existent.

Consider the cylindrical section of a closed-ended pressure vessel of radius R , subjected to an internal pressure p (see Fig. 3.1). The pressure vessel is here assumed to be overwound by a combination of helical and hoop windings, the former one at a winding angle of α with the meridian direction (φ). σ_α , σ_h , t_α , t_h are the helical and hoop fiber stress and thickness, respectively. Fig. 3.2 shows a basic element of helical and hoop wound fibers, intersecting a unit area of the torus in the meridional and parallel directions, respectively.

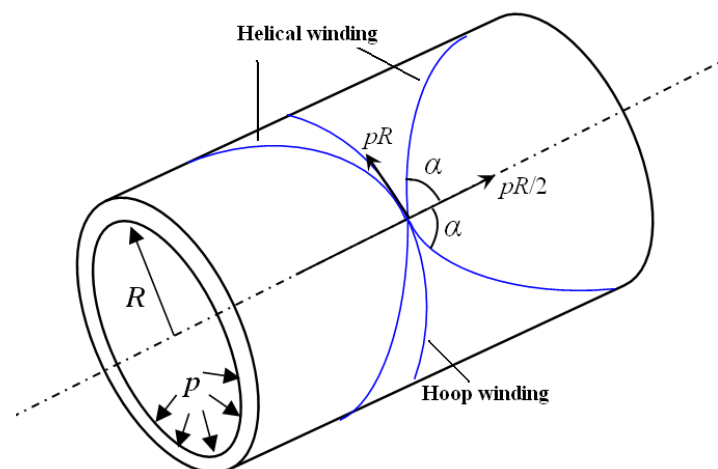


Fig. 3.1: Cylindrical section overwound by helical and hoop winding

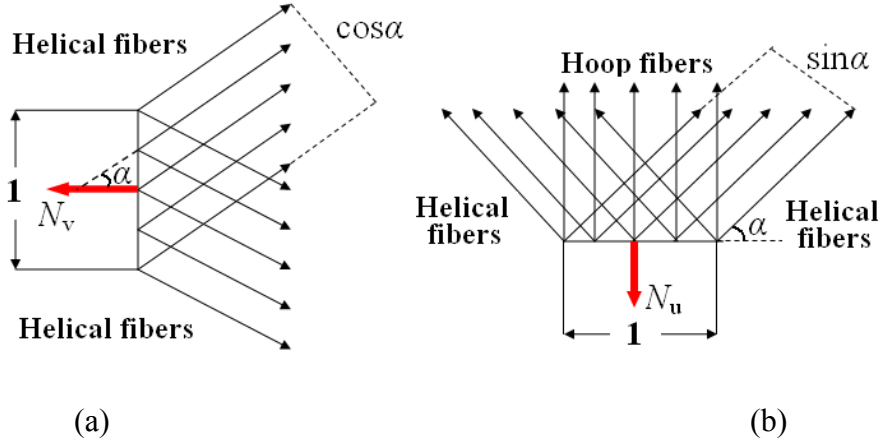


Fig. 3.2: A netting-based element of helically and hoop wound fibers

The force resultants in the axial direction should be balanced. The contribution of the stress resultants from the hoop fibers in the axial direction can be neglected. The component of the force resultants from the helical fibers in the axial direction is $\sigma_\alpha t_\alpha \cos^2 \alpha$ (Fig. 3.2(a)). This needs to be in equilibrium with the force resultant in the cylindrical shell due to the internal pressure in the axial direction, $pR/2$:

$$\sigma_\alpha t_\alpha \cos^2 \alpha = \frac{pR}{2} \quad (3.1)$$

Secondly, the force balance in the hoop direction needs to take into consideration a combination of hoop and helical fibers (Fig. 3.2(b)). The force resultant in the hoop direction of the cylindrical shell due to internal pressure is pR :

$$\sigma_\alpha t_\alpha \sin^2 \alpha + \sigma_h t_h = pR \quad (3.2)$$

The condition of the netting theory implies:

$$\sigma_\alpha = \sigma_h \quad (3.3)$$

Combining equations (3.1), (3.2) and (3.3) and solving for α , results in:

$$\alpha = \tan^{-1} \sqrt{\frac{2 - t_h/t_\alpha}{1 + t_h/t_\alpha}} \quad (3.4)$$

It is here assumed that the cylindrical shell is designed in such a way that the ultimate strength of the fibers, σ_f is attained simultaneously along the hoop and helical directions at the vessel's burst pressure, p_b . Combination of equations (3.1), (3.2) and (3.3) gives the thickness of the hoop and helical layers for the cylindrical pressure vessel:

$$t_\alpha = \frac{p_b R}{2\sigma_f \cos^2 \alpha}, \quad t_h = \frac{p_b R}{\sigma_f} \left(1 - \frac{\tan^2 \alpha}{2}\right) \quad (3.5)$$

Chapter 3

Therefore, for a pressure vessel with a design burst pressure of p_b , the netting analysis estimates the total thickness of the composite shell in its cylindrical section to be:

$$t = t_\alpha + t_\beta = \frac{3p_b R}{2\sigma_f} \quad (3.6)$$

Please note here that the calculation above does not include any consideration of a safety factor. For the single helical winding (which implies $t_h = 0$), equations (3.4) and (3.6) reduce to:

$$\alpha = \tan^{-1} \sqrt{2} = 54.7^\circ, \quad t = t_\alpha = \frac{3p_b R}{2\sigma_f} \quad (3.7)$$

For any given biaxial stress, there is just one critical winding angle at which the laminate can support stress. In a well-known example, a filament-wound cylindrical pressure vessel usually contains fibers wound at an angle: $\alpha_{net} = \arctan \sqrt{2}$ with respect to the axis of the rotational symmetry. Since internal pressure produces a hoop-to-axis stress ratio of 2:1, reinforcement at this angle would ideally support the stress in the wall material. According to the predictions of netting analysis, the strains in the two principal directions will be equal, given by

$$\varepsilon_\varphi = \varepsilon_\theta = \frac{3}{2} \cdot \frac{pR}{E_f t} \quad (3.8)$$

where ε_φ , ε_θ are the shell strains in the meridional and parallel direction, respectively. If the initial winding angle was different to α_{net} , no stress could be supported. In this situation, the fibers would rotate until they would reach the angle where they could support stress. For example, if the initial winding angle was less than α_{net} , the shell strain would initially increase under an infinitesimally small stress. In other words, the material would have zero effective stiffness.

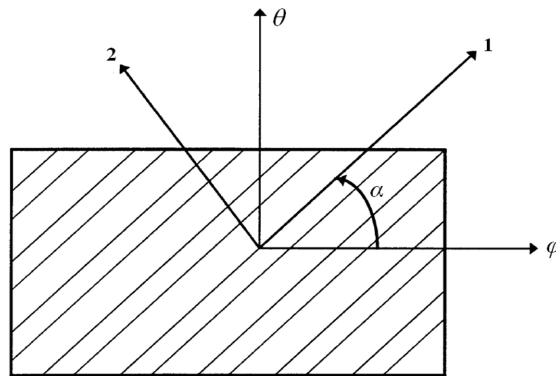


Fig. 3.3: Global and material axes of an angle lamina

3.3 Classical Lamination Theory (CLT) [4]

Generally, a laminate does not consist only of unidirectional laminae because of their low stiffness and strength properties in the transverse direction. Therefore, in most laminates, some laminae are placed at an angle. It is thus necessary to develop the stress-strain relationship for an angle lamina. The coordinate system used for showing an angle lamina is as given in Fig. 3.3. A unidirectional lamina falls under the orthotropic material category. If the lamina is thin and does not carry any out-of-plane loads, one can assume plane stress conditions for the lamina. The through-thickness normal strain is not an independent strain (because it is a function of the two in-plane normal strains) and can thus be omitted from the stress-strain relationship. Also, the through-thickness shearing strains can also be omitted as they are based on the plane stress assumption.

The axes in the 1-2 coordinate system are called the material axes or the on-axes, where 1, 2 denote the fiber and transverse direction, respectively. The axes in the φ - θ coordinate system are called the global axes or the off-axes. The angle between the two axes is denoted by the winding angle α . For an orthotropic plane stress problem the strain-stress relationship in the 1-2 coordinate system is established as:

$$\begin{bmatrix} \varepsilon_1 \\ \varepsilon_2 \\ \gamma_{12} \end{bmatrix} = \begin{bmatrix} S_{11} & S_{12} & 0 \\ S_{12} & S_{22} & 0 \\ 0 & 0 & S_{66} \end{bmatrix} \begin{bmatrix} \sigma_1 \\ \sigma_2 \\ \tau_{12} \end{bmatrix} \quad (3.9)$$

where S_{ij} ($i, j = 1, 2, 6$) are the elements of the compliance matrix, given by:

$$S_{11} = \frac{1}{E_1}, \quad S_{12} = -\frac{\nu_{12}}{E_1}, \quad S_{22} = \frac{1}{E_2}, \quad S_{66} = \frac{1}{G_{12}}. \quad (3.10)$$

in which E_1 and E_2 are the Young's elastic moduli in the fiber and transverse directions (1-2), respectively; ν_{12} and ν_{21} are the Poisson's ratios satisfying the following symmetry condition:

$$E_1 \nu_{21} = E_2 \nu_{12} \quad (3.11)$$

Inverting equation (3.9) gives the stress-strain relationship as

$$\begin{bmatrix} \sigma_1 \\ \sigma_2 \\ \tau_{12} \end{bmatrix} = \begin{bmatrix} Q_{11} & Q_{12} & 0 \\ Q_{12} & Q_{22} & 0 \\ 0 & 0 & Q_{66} \end{bmatrix} \begin{bmatrix} \varepsilon_1 \\ \varepsilon_2 \\ \gamma_{12} \end{bmatrix} \quad (3.12)$$

where $[Q]$ is the reduced stiffness matrix, which is related to the compliance coefficients:

$$Q_{11} = \frac{S_{22}}{S_{11}S_{22} - S_{12}^2} = \frac{E_1}{1 - \nu_{12}\nu_{21}}, \quad Q_{12} = -\frac{S_{12}}{S_{11}S_{22} - S_{12}^2} = \frac{\nu_{21}E_1}{1 - \nu_{12}\nu_{21}},$$

Chapter 3

$$Q_{22} = \frac{S_{11}}{S_{11}S_{22} - S_{12}^2} = \frac{E_2}{1 - \nu_{12}\nu_{21}}, \quad Q_{66} = \frac{1}{S_{66}} = G_{12} \quad (3.13)$$

The stresses refer to the material and global axes; in an angle lamina they are related to each other through the angle of the lamina, α :

$$\begin{bmatrix} \sigma_1 \\ \sigma_2 \\ \tau_{12} \end{bmatrix} = \mathbf{T} \begin{bmatrix} \sigma_\varphi \\ \sigma_\theta \\ \tau_{\varphi\theta} \end{bmatrix} \quad (3.14)$$

where \mathbf{T} stands for the transformation matrix, defined as:

$$\mathbf{T} = \begin{bmatrix} c^2 & s^2 & 2cs \\ s^2 & c^2 & -2cs \\ -cs & cs & c^2 - s^2 \end{bmatrix} \quad (3.15)$$

Its inverse matrix is

$$\mathbf{T}^{-1} = \begin{bmatrix} c^2 & s^2 & -2cs \\ s^2 & c^2 & 2cs \\ cs & -cs & c^2 - s^2 \end{bmatrix} \quad (3.16)$$

in which $c = \cos\alpha$, $s = \sin\alpha$. Using the stress-strain equation (3.12) in the material axes, Equation (3.14) can be rewritten as

$$\begin{bmatrix} \sigma_\varphi \\ \sigma_\theta \\ \tau_{\varphi\theta} \end{bmatrix} = \mathbf{T}^{-1} \mathbf{Q} \begin{bmatrix} \sigma_1 \\ \sigma_2 \\ \tau_{12} \end{bmatrix} \quad (3.17)$$

The strains with respect to the global and material axes are also related through the transformation matrix:

$$\begin{bmatrix} \varepsilon_1 \\ \varepsilon_2 \\ \gamma_{12}/2 \end{bmatrix} = \mathbf{T} \begin{bmatrix} \varepsilon_\varphi \\ \varepsilon_\theta \\ \gamma_{\varphi\theta} \end{bmatrix} \quad (3.18)$$

which can be rewritten as

$$\begin{bmatrix} \varepsilon_1 \\ \varepsilon_2 \\ \gamma_{12} \end{bmatrix} = \mathbf{RTR}^{-1} \begin{bmatrix} \varepsilon_\varphi \\ \varepsilon_\theta \\ \gamma_{\varphi\theta} \end{bmatrix} \quad (3.19)$$

where \mathbf{R} is the *Reuter matrix* and is defined as

$$\mathbf{R} = \begin{bmatrix} 1 & 0 & 0 \\ 0 & 1 & 0 \\ 0 & 0 & 2 \end{bmatrix} \quad (3.20)$$

Then, substituting equation (3.19) in (3.12) and plugging the results into equation (3.17), gives

$$\begin{bmatrix} \sigma_\varphi \\ \sigma_\theta \\ \tau_{\varphi\theta} \end{bmatrix} = \mathbf{T}^{-1} \mathbf{Q} \mathbf{R} \mathbf{T} \mathbf{R}^{-1} \begin{bmatrix} \varepsilon_\varphi \\ \varepsilon_\theta \\ \gamma_{\varphi\theta} \end{bmatrix} \quad (3.21)$$

Multiplication of the first five matrices on the right-hand side of equation (3.21) leads to:

$$\begin{bmatrix} \sigma_\varphi \\ \sigma_\theta \\ \tau_{\varphi\theta} \end{bmatrix} = \begin{bmatrix} \bar{Q}_{11} & \bar{Q}_{12} & \bar{Q}_{16} \\ \bar{Q}_{21} & \bar{Q}_{22} & \bar{Q}_{26} \\ \bar{Q}_{16} & \bar{Q}_{26} & \bar{Q}_{66} \end{bmatrix} \begin{bmatrix} \varepsilon_\varphi \\ \varepsilon_\theta \\ \gamma_{\varphi\theta} \end{bmatrix} \quad (3.22)$$

where \bar{Q}_{ij} ($i, j = 1, 2, 6$) are called the elements of the transformed reduced stiffness matrix and are given by:

$$\begin{cases} \bar{Q}_{11} = Q_{11}c^4 + 2(Q_{12} + 2Q_{66})c^2s^2 + Q_{22}s^4 \\ \bar{Q}_{12} = (Q_{11} + Q_{12} - 4Q_{66})c^2s^2 + Q_{12}(c^4 + s^4) \\ \bar{Q}_{22} = Q_{11}s^4 + 2(Q_{12} + 2Q_{66})c^2s^2 + Q_{22}c^4 \\ \bar{Q}_{16} = -Q_{22}cs^3 + Q_{11}c^3s - (Q_{12} + 2Q_{66})(c^2 - s^2)cs \\ \bar{Q}_{26} = -Q_{22}c^3s + Q_{11}cs^3 + (Q_{12} + 2Q_{66})(c^2 - s^2)cs \\ \bar{Q}_{66} = (Q_{11} + Q_{12} - 2Q_{12})c^2s^2 + Q_{66}(c^2 - s^2)^2 \end{cases} \quad (3.23)$$

Note that six elements are in the $\bar{\mathbf{Q}}$ matrix. However, by looking at equation (3.23), it can be seen that they are just functions of the four stiffness elements, Q_{11} , Q_{12} , Q_{22} , and Q_{66} , and the angle of the lamina, α . Inverting equation (3.22) gives:

$$\begin{bmatrix} \varepsilon_\varphi \\ \varepsilon_\theta \\ \gamma_{\varphi\theta} \end{bmatrix} = \begin{bmatrix} \bar{S}_{11} & \bar{S}_{12} & \bar{S}_{16} \\ \bar{S}_{21} & \bar{S}_{22} & \bar{S}_{26} \\ \bar{S}_{16} & \bar{S}_{26} & \bar{S}_{66} \end{bmatrix} \begin{bmatrix} \sigma_\varphi \\ \sigma_\theta \\ \tau_{\varphi\theta} \end{bmatrix} \quad (3.24)$$

where \bar{S}_{ij} ($i, j = 1, 2, 6$) are the elements of the transformed reduced compliance matrix and are given by:

$$\begin{cases} \bar{S}_{11} = S_{11}c^4 + 2(S_{12} + 2S_{66})c^2s^2 + S_{22}s^4 \\ \bar{S}_{12} = (S_{11} + S_{22} - S_{66})c^2s^2 + S_{12}(c^4 + s^4) \\ \bar{S}_{22} = S_{11}s^4 + (2S_{12} + S_{66})c^2s^2 + S_{22}c^4 \\ \bar{S}_{16} = (2S_{11} - 2S_{12} - S_{66})c^3s - (2S_{22} - 2S_{12} - S_{66})cs^3 \\ \bar{S}_{26} = (2S_{11} - 2S_{12} - S_{66})cs^3 - (2S_{22} - 2S_{12} - S_{66})c^3s \\ \bar{S}_{66} = 2(2S_{11} + 2S_{22} - 4S_{12} - S_{66})c^2s^2 + S_{66}(c^4 + s^4) \end{cases} \quad (3.25)$$

Chapter 3

With these equations it is now possible to study the mechanical behavior of a composite lamina. For a unidirectional lamina loaded in the material axes directions, no coupling occurs between the normal and shearing terms of strains and stresses. However, for an angle lamina, from equations (3.22) and (3.24), coupling takes place between the normal and shearing terms of strains and stresses. If only normal stresses are applied to an angle lamina, the shear strains are nonzero; if only shearing stresses are applied to an angle lamina, the normal strains are nonzero. Equations (3.22) and (3.24) provide the stress-strain equations for a generally orthotropic lamina. In pressure vessel design, it is important to find the optimal angle of fiber orientation that will maximally utilize the tensile limits along the material axes (1-2).

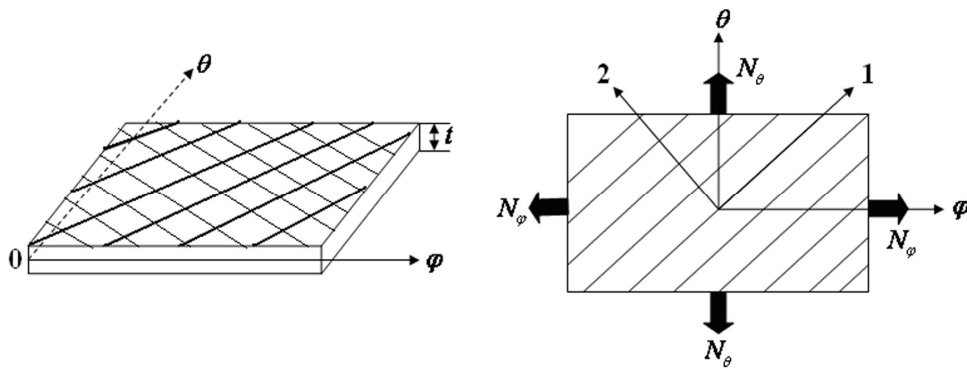


Fig. 3.4: A symmetric laminate under in-plane loads (N_φ , N_θ)

The shell of a pressure vessel is assumed to consist of helically wound layers, each of which forms an angle-ply configuration consisting of $\pm\alpha$ layers. We consider here a symmetric laminate element under in-plane forces per unit length (N_φ , N_θ), as shown in Fig.3.4. Since there is rotational symmetry for the shape and the applied load (internal pressure, axial force, etc), the shear stress and strain components must vanish. The constitutive equation of a symmetric laminate in the global coordinate system is given as follows:

$$\begin{pmatrix} N_\varphi \\ N_\theta \end{pmatrix} = \begin{bmatrix} A_{11} & A_{12} \\ A_{21} & A_{22} \end{bmatrix} \cdot \begin{pmatrix} \varepsilon_\varphi \\ \varepsilon_\theta \end{pmatrix} \quad (3.26)$$

where A_{ij} are the components of the extensional stiffness matrix \mathbf{A} , which can be calculated by:

$$A_{ij} = \sum_{k=1}^n \bar{Q}_{ij}^k \cdot t^k = t \cdot \bar{Q}_{ij}^k \quad (i,j=1,2) \quad (3.27)$$

where the superscript k denotes the k^{th} layer; t is the total thickness of the laminate. The

relation between the plane stress vector $\{\sigma_{12}\}^k$ relative to the material axis (1-2) and the resultant force vector $\{N_{\varphi\theta}\}$ is given by substitution of equations (3.26) and (3.19) into (3.12):

$$\{\sigma_{12}\}^k = \mathbf{T}^k \mathbf{Q}^k \mathbf{A}^{-1} \{N_{\varphi\theta}\} \quad (3.28)$$

By multiplication of the first three matrices on the right-hand side of equation (3.28), the stress components relative to the material axes in the k^{th} layer are rewritten as follows:

$$\begin{cases} \sigma_1^k = \frac{1}{t} (m_{11} N_\varphi + m_{12} N_\theta) \\ \sigma_2^k = \frac{1}{t} (m_{21} N_\varphi + m_{22} N_\theta) \\ \tau_{12}^k = \frac{1}{t} (m_{31} N_\varphi + m_{32} N_\theta) \end{cases} \quad (3.29)$$

where constants m_{ij} are functions of the fiber angle and material properties, given by:

$$\begin{aligned} m_{11} &= c^2 + 2cs \frac{\bar{Q}_{22}\bar{Q}_{16} - \bar{Q}_{12}\bar{Q}_{26}}{\bar{Q}_{11}\bar{Q}_{22} - \bar{Q}_{12}^2}, & m_{12} &= s^2 + 2cs \frac{\bar{Q}_{11}\bar{Q}_{26} - \bar{Q}_{12}\bar{Q}_{16}}{\bar{Q}_{11}\bar{Q}_{22} - \bar{Q}_{12}^2}, \\ m_{21} &= s^2 - 2cs \frac{\bar{Q}_{22}\bar{Q}_{16} - \bar{Q}_{12}\bar{Q}_{26}}{\bar{Q}_{11}\bar{Q}_{22} - \bar{Q}_{12}^2}, & m_{22} &= c^2 - 2cs \frac{\bar{Q}_{11}\bar{Q}_{26} - \bar{Q}_{12}\bar{Q}_{16}}{\bar{Q}_{11}\bar{Q}_{22} - \bar{Q}_{12}^2}, \\ m_{31} &= -sc + (c^2 - s^2) \frac{\bar{Q}_{22}\bar{Q}_{16} - \bar{Q}_{12}\bar{Q}_{26}}{\bar{Q}_{11}\bar{Q}_{22} - \bar{Q}_{12}^2}, & m_{32} &= sc + (c^2 - s^2) \frac{\bar{Q}_{11}\bar{Q}_{26} - \bar{Q}_{12}\bar{Q}_{16}}{\bar{Q}_{11}\bar{Q}_{22} - \bar{Q}_{12}^2}. \end{aligned} \quad (3.30)$$

3.4 Optimality Conditions

The inverse form of equation (3.26) is:

$$\begin{pmatrix} \varepsilon_\varphi \\ \varepsilon_\theta \end{pmatrix} = \begin{bmatrix} a_{11} & a_{12} \\ a_{21} & a_{22} \end{bmatrix} \cdot \begin{pmatrix} N_\varphi \\ N_\theta \end{pmatrix} \quad (3.31)$$

where a_{ij} ($i,j=1,2$) denote the components of the extensional compliance matrix \mathbf{a} , which can be expressed in terms of the extensional stiffnesses A_{ij} ($i,j=1,2$):

$$a_{11} = \frac{A_{22}}{A_{11}A_{22} - A_{12}^2}, \quad a_{22} = \frac{A_{11}}{A_{11}A_{22} - A_{12}^2}, \quad a_{12} = a_{21} = -\frac{A_{12}}{A_{11}A_{22} - A_{12}^2} \quad (3.32)$$

The elastic strain energy density of a laminate (as shown in Fig. 3.4) is given by [5]:

$$U = \frac{1}{2} (\sigma_\varphi \varepsilon_\varphi + \sigma_\theta \varepsilon_\theta + \tau_{\varphi\theta} \gamma_{\varphi\theta}) \quad (3.33)$$

where σ_{ij} and ε_{ij} ($i,j=\varphi,\theta$) are the in-plane stress and strain components for the laminate relative to the global axes ($\varphi-\theta$).

Chapter 3

Substituting equations (3.31) and (3.32) into (3.33) gives:

$$U = \frac{N_\varphi^2}{2} \frac{A_{22} - 2\chi A_{12} + \chi^2 A_{11}}{A_{22}A_{11} - A_{12}^2} \quad (3.34)$$

where χ is the ratio of the in-plane shell forces (membrane forces) in the parallel and meridional directions, given by:

$$\chi = \frac{N_\theta}{N_\varphi} \quad (3.35)$$

χ is also referred to as the biaxial stress ratio. The following invariant equation is now provided for the given ply configuration:

$$A_{11} + 2A_{12} + A_{22} = C \quad (3.36)$$

where C is a constant value, determined by the commonly known material constants and layer thicknesses.

Next we will obtain the optimal laminate configuration for minimizing the strain energy density in equation (3.34), subjected to the equality constraint (3.36). Introducing this constraint with the aid of the Lagrange multiplier β [6], we should minimize the following augmented function:

$$f(A_{11}, A_{22}, A_{12}) = \frac{N_\varphi^2}{2} \frac{A_{22} - 2\chi A_{12} + \chi^2 A_{11}}{A_{22}A_{11} - A_{12}^2} - \beta(A_{11} + 2A_{12} + A_{22} - C) \quad (3.37)$$

Here the components of the extensional stiffness A_{ij} ($i, j = 1, 2$) are considered as the design variables. The minimum conditions are active when:

$$\frac{\partial f}{\partial A_{11}} = 0, \quad \frac{\partial f}{\partial A_{22}} = 0, \quad \frac{\partial f}{\partial A_{12}} = 0 \quad (3.38)$$

The simultaneous solution of the system (3.38) in conjunction with the constraint (3.36) results in the optimality condition for a pressure vessel under biaxial stress condition:

$$\chi = \frac{A_{22} + A_{12}}{A_{11} + A_{12}} \quad (3.39)$$

where:

$$A_{ij} = \sum_{k=1}^n \bar{Q}_{ij}^k \cdot t_k \quad (i, j = 1, 2) \quad (3.40)$$

The strain ratio $\varepsilon_\theta / \varepsilon_\varphi$ can be expressed in terms of χ by substitution of equation (3.39) into (3.26):

$$\frac{\varepsilon_\theta}{\varepsilon_\varphi} = \frac{A_{11}\chi - A_{12}}{A_{22} - A_{12}\chi} \quad (3.41)$$

Subtraction of 1 from the both sides of equation (3.41), leads to:

$$\frac{\varepsilon_\theta - \varepsilon_\varphi}{\varepsilon_\varphi} = \frac{A_{11} + A_{12}}{A_{22} - A_{12}\chi} \left(\chi - \frac{A_{22} + A_{12}}{A_{11} + A_{12}} \right) \quad (3.42)$$

Substitution of equation (3.39) into (3.42), leads to:

$$\varepsilon_\varphi = \varepsilon_\theta \quad (3.43)$$

Then, the strains in the global axes can be obtained by substitution of equation (3.43) into (3.26):

$$\varepsilon_\varphi = \varepsilon_\theta = \frac{N_\varphi}{A_{11} + A_{12}} = \frac{N_\theta}{A_{22} + A_{12}} \quad (3.44)$$

Substituting equation (3.44) into (3.19), leads to:

$$\varepsilon_1 = \varepsilon_2 = \varepsilon_\varphi = \varepsilon_\theta = \frac{N_\varphi}{A_{11} + A_{12}} = \frac{N_\theta}{A_{22} + A_{12}} \quad (3.45)$$

with:

$$\tau_{12} = 0 \quad (3.46)$$

Since the angle α in the transformation matrix \mathbf{T} can be chosen arbitrarily in a plane, equation (3.45) holds true irrespective of the direction of the material axes (1-2). Therefore, under the optimality condition, the strain at each point is the same in all directions in a lamina.

The third row of equation (3.29) can be expanded and rewritten as:

$$\tau_{12} = \frac{G_{12} \tan 2\alpha}{ct \cos 2\alpha} \left[N_\theta \left(\frac{\sin^2 \alpha (1 + \nu_{12})}{E_1} + \frac{\cos^2 \alpha (1 + \nu_{21})}{E_2} \right) - N_\varphi \left(\frac{\cos^2 \alpha (1 + \nu_{12})}{E_1} + \frac{\sin^2 \alpha (1 + \nu_{21})}{E_2} \right) \right] \quad (3.47)$$

Substitution of equation (3.46) into (3.47) takes another form of the optimality condition:

$$\chi = \frac{1 - (1 - k_e) \cos^2 \alpha}{k_e + (1 - k_e) \cos^2 \alpha} \quad (3.48)$$

where:

$$k_e = \frac{E_2 (1 + \nu_{12})}{E_1 (1 + \nu_{21})} \quad (3.49)$$

Substitution of equation (3.48) into the first two rows of equation (3.29), after some arrangements, leads to:

$$\sigma_1 = \frac{N_\varphi E_1 (1 + \nu_{21})}{E_1 (1 + \nu_{21}) \cos^2 \alpha + E_2 (1 + \nu_{12}) \sin^2 \alpha} \quad (3.50)$$

$$\sigma_2 = \frac{N_\varphi E_2 (1 + \nu_{12})}{E_1 (1 + \nu_{21}) \cos^2 \alpha + E_2 (1 + \nu_{12}) \sin^2 \alpha} \quad (3.51)$$

Chapter 3

Dividing each side of equation (3.51) by equation (3.50), gives:

$$\frac{\sigma_2}{\sigma_1} = \frac{E_2(1+\nu_{12})}{E_1(1+\nu_{21})} = k_e \quad (3.52)$$

The specific laminate properties can be characterized by the parameter k_e , equation (3.49), which in fact expresses the degree of material anisotropy [7]. For $k_e = 1$ the engineering constants are identical, hence the considered material will be isotropic. The assumption $k_e = 0$ represents the netting case where the contribution of the matrix to the mechanical properties of the lamina is insignificant. Equation (3.48) gives another form of the optimality condition and relates the optimal winding angle with the material anisotropy.

Although condition (3.48) is able to provide zero shear stress in the layers of the pressure vessel, it is sometimes convenient to select k in such a way that the laminate strength is fully utilized. To achieve this, the optimal biaxial force ratio N_θ / N_ϕ would be [7, 8]:

$$k_\sigma = \frac{\sigma_2}{\sigma_1} = \left(\frac{S_2}{S_1}\right)^2 \quad (3.53)$$

where S_1, S_2 are the tensile-compressive strength values of a lamina in the fiber and transverse direction (1-2), respectively. As a design rule, for shear sensitive laminae condition (3.52) should be satisfied and for maximizing strength, condition (3.53) needs to be respected [9]. As the stiffness-dominated and strength-dominated k -parameters that are respectively given in equations (3.52) and (3.53) do generally not match, the sensitivity of the laminate for shear stress will play here an important role. In every case other than given in equation (3.48), the pressure vessel will contain a shearing mechanism that loads the matrix. The k -value will usually lie between k_e and k_σ ; ideally, for the best laminate k_e and k_σ should be equal. However, it seems that the best possible performance is always achieved with the netting solution ($k_e = k_\sigma = 0$). Nevertheless, an important condition to justify this k -value is that the employed laminae do indeed sufficiently approach this condition and will not prematurely suffer from matrix defects.

3.5 Optimality Conditions for Various Types of Laminations

3.5.1 Liner / $\pm\alpha$ layers

The in-plane membrane forces N_ϕ, N_θ can be respectively divided into two parts:

$$N_\phi = N_\phi^L + N_\phi^\alpha \quad (3.54)$$

$$N_\theta = N_\theta^L + N_\theta^\alpha \quad (3.55)$$

where the superscripts L , α denote the metal liner and the $\pm\alpha$ layers, respectively. With the aid of the optimality condition of equal shell strains, substitution of equation (3.27) into (3.26) together with equation (3.23) for \bar{Q}_{ij} , leads to:

$$\begin{cases} N_{\phi}^{\alpha} = \varepsilon t_{\alpha} (Q_{11}^{\alpha} \cos^2 \alpha + Q_{22}^{\alpha} \sin^2 \alpha + Q_{12}^{\alpha}) \\ N_{\theta}^{\alpha} = \varepsilon t_{\alpha} (Q_{22}^{\alpha} \cos^2 \alpha + Q_{11}^{\alpha} \sin^2 \alpha + Q_{12}^{\alpha}) \end{cases} \quad (3.56)$$

where t_{α} is the thickness of the $\pm\alpha$ layers. According to the isotropic elasticity theory, N_{ϕ}^L, N_{θ}^L can be given by:

$$N_{\phi}^L = N_{\theta}^L = \varepsilon t_L \cdot \frac{E_L}{1-\nu_L} \quad (3.57)$$

where E_L and ν_L are the elastic modulus and the Poisson's ratio of the liner, respectively; t_{α} is the thickness of the metal liner. Substitution of equations (3.56)~(3.57) into (3.55) leads to:

$$\begin{cases} N_{\phi} = \varepsilon t_{\alpha} (Q_{11}^{\alpha} \cos^2 \alpha + Q_{22}^{\alpha} \sin^2 \alpha + Q_{12}^{\alpha} + \frac{\eta_0 E_L}{1-\nu_L}) \\ N_{\theta} = \varepsilon t_{\alpha} (Q_{22}^{\alpha} \cos^2 \alpha + Q_{11}^{\alpha} \sin^2 \alpha + Q_{12}^{\alpha} + \frac{\eta_0 E_L}{1-\nu_L}) \end{cases} \quad (3.58)$$

where η_0 is the thickness ratio of the metal liner and the $\pm\alpha$ layers, defined as:

$$\eta_0 = \frac{t_L}{t_{\alpha}} \quad (3.59)$$

The optimality condition for a laminate consisting of the metal liner and the $\pm\alpha$ layers can thus be given by:

$$\chi = \frac{Q_{22}^{\alpha} \cos^2 \alpha + Q_{11}^{\alpha} \sin^2 \alpha + Q_{12}^{\alpha} + \eta_0 \frac{E_L}{1-\nu_L}}{Q_{11}^{\alpha} \cos^2 \alpha + Q_{22}^{\alpha} \sin^2 \alpha + Q_{12}^{\alpha} + \eta_0 \frac{E_L}{1-\nu_L}} \quad (3.60)$$

In addition, the optimal winding angle α and corresponding thickness ratio η_0 are respectively obtained as follows by rewriting equation (3.60):

$$\alpha = \tan^{-1} \sqrt{\frac{\chi(Q_{11}^{\alpha} + Q_{12}^{\alpha} + \eta_0 \frac{E_L}{1-\nu_L}) - (Q_{22}^{\alpha} + Q_{12}^{\alpha} + \eta_0 \frac{E_L}{1-\nu_L})}{Q_{11}^{\alpha} + Q_{12}^{\alpha} + \eta_0 \frac{E_L}{1-\nu_L} - \chi(Q_{22}^{\alpha} + Q_{12}^{\alpha} + \eta_0 \frac{E_L}{1-\nu_L})}} \quad (3.61)$$

$$\eta_0 = \frac{1-\nu_L}{E_L} \cdot \frac{\chi(Q_{11}^{\alpha} \cos^2 \alpha + Q_{22}^{\alpha} \sin^2 \alpha + Q_{12}^{\alpha}) - (Q_{22}^{\alpha} \cos^2 \alpha + Q_{11}^{\alpha} \sin^2 \alpha + Q_{12}^{\alpha})}{(1-\chi)} \quad (3.62)$$

The equal strains ε can also be given by:

$$\varepsilon = \frac{N_\varphi}{(Q_{11}^\alpha \cos^2 \alpha + Q_{22}^\alpha \sin^2 \alpha + Q_{12}^\alpha + \eta_0 \frac{E_L}{1-\nu_L})t_\alpha} \quad (3.63)$$

3.5.2 Liner / $\pm\alpha$ layers / 90° layers

The in-plane membrane forces N_φ , N_θ can be correspondingly divided into three parts:

$$N_\varphi = N_\varphi^L + N_\varphi^\alpha + N_\varphi^h \quad (3.64)$$

$$N_\theta = N_\theta^L + N_\theta^\alpha + N_\theta^h \quad (3.65)$$

where the superscript h denote the 90° layers. Substitution of $\alpha = 90^\circ$ into equation (3.56), gives:

$$N_\varphi^h = \varepsilon t_\alpha (Q_{22}^h + Q_{12}^h) \quad (3.66)$$

$$N_\theta^h = \varepsilon t_\alpha (Q_{11}^h + Q_{12}^h) \quad (3.67)$$

Substitution of equations (3.56), (3.57), (3.66) and (3.67) into (3.64) and (3.65) leads to:

$$N_\varphi = \varepsilon t_\alpha [(Q_{11}^\alpha \cos^2 \alpha + Q_{22}^\alpha \sin^2 \alpha + Q_{12}^\alpha) + \eta_h (Q_{22}^h + Q_{12}^h) + \eta_0 \frac{E_L}{1-\nu_L}] \quad (3.68)$$

$$N_\theta = \varepsilon t_\alpha [(Q_{22}^\alpha \cos^2 \alpha + Q_{11}^\alpha \sin^2 \alpha + Q_{12}^\alpha) + \eta_h (Q_{11}^h + Q_{12}^h) + \eta_0 \frac{E_L}{1-\nu_L}] \quad (3.69)$$

where η_h is the thickness ratio of the 90° layers and the $\pm\alpha$ layers, given by:

$$\eta_h = \frac{t_h}{t_\alpha} \quad (3.70)$$

The optimality condition for a laminate consisting of the metal liner, the $\pm\alpha$ layers and the 90° layers is obtained as:

$$\chi = \frac{(Q_{22}^\alpha \cos^2 \alpha + Q_{11}^\alpha \sin^2 \alpha + Q_{12}^\alpha) + \eta_h (Q_{11}^h + Q_{12}^h) + \eta_0 \frac{E_L}{1-\nu_L}}{(Q_{11}^\alpha \cos^2 \alpha + Q_{22}^\alpha \sin^2 \alpha + Q_{12}^\alpha) + \eta_h (Q_{22}^h + Q_{12}^h) + \eta_0 \frac{E_L}{1-\nu_L}} \quad (3.71)$$

Under the given χ the optimal winding angle α and related thickness ratio λ_h can respectively be determined by:

$$\alpha = \tan^{-1} \sqrt{\frac{\chi(Q_{11}^\alpha + Q_{12}^\alpha + \eta_h(Q_{22}^h + Q_{12}^h) + \frac{\eta_0 E_L}{1-\nu_L}) - (Q_{22}^\alpha + Q_{12}^\alpha + \eta_h(Q_{11}^h + Q_{12}^h) + \frac{\eta_0 E_L}{1-\nu_L})}{[Q_{11}^\alpha + Q_{12}^\alpha + \eta_h(Q_{11}^h + Q_{12}^h) + \frac{\eta_0 E_L}{1-\nu_L}] - \chi[Q_{22}^\alpha + Q_{12}^\alpha + \eta_h(Q_{22}^h + Q_{12}^h) + \frac{\eta_0 E_L}{1-\nu_L}]}} \quad (3.72)$$

$$\lambda_h = \frac{\chi(Q_{11}^\alpha \cos^2 \alpha + Q_{22}^\alpha \sin^2 \alpha + Q_{12}^\alpha + \eta_0 \frac{E_L}{1-\nu_L}) - (Q_{22}^\alpha \cos^2 \alpha + Q_{11}^\alpha \sin^2 \alpha + Q_{12}^\alpha + \eta_0 \frac{E_L}{1-\nu_L})}{(Q_{22}^h + Q_{12}^h) - \chi(Q_{11}^h + Q_{12}^h)} \quad (3.73)$$

According to equation (3.68), the equal strains ε can also be expressed by:

$$\varepsilon = \frac{N_\varphi}{t_\alpha [(Q_{11}^\alpha \cos^2 \alpha + Q_{22}^\alpha \sin^2 \alpha + Q_{12}^\alpha) + \eta_h (Q_{22}^h + Q_{12}^h) + \eta_0 \frac{E_L}{1-\nu_L}]} \quad (3.74)$$

3.5.3 Liner / $\pm\alpha$ layers / 0° layers

On a way similar to section 3.5.2, the membrane forces N_φ , N_θ for this case are expressed as:

$$N_\varphi = \varepsilon t_\alpha [(Q_{11}^\alpha \cos^2 \alpha + Q_{22}^\alpha \sin^2 \alpha + Q_{12}^\alpha) + \eta_m (Q_{11}^m + Q_{12}^m) + \eta_0 \frac{E_L}{1-\nu_L}] \quad (3.75)$$

$$N_\theta = \varepsilon t_\alpha [(Q_{22}^\alpha \cos^2 \alpha + Q_{11}^\alpha \sin^2 \alpha + Q_{12}^\alpha) + \eta_m (Q_{22}^m + Q_{12}^m) + \eta_0 \frac{E_L}{1-\nu_L}] \quad (3.76)$$

where η_m is the thickness ratio of the 0° layers and the $\pm\alpha$ layers, given by:

$$\eta_m = \frac{t_m}{t_\alpha} \quad (3.77)$$

The optimality condition for a laminate consisting of the metal liner, the $\pm\alpha$ layers and the 0° layers:

$$\chi = \frac{(Q_{22}^\alpha \cos^2 \alpha + Q_{11}^\alpha \sin^2 \alpha + Q_{12}^\alpha) + \eta_m (Q_{11}^m + Q_{12}^m) + \eta_0 \frac{E_L}{1-\nu_L}}{(Q_{11}^\alpha \cos^2 \alpha + Q_{22}^\alpha \sin^2 \alpha + Q_{12}^\alpha) + \eta_m (Q_{22}^m + Q_{12}^m) + \eta_0 \frac{E_L}{1-\nu_L}} \quad (3.78)$$

Under the given χ , α and η_m should also be chosen according to the following equations, in order to satisfy the optimality condition:

$$\alpha = \tan^{-1} \sqrt{\frac{\chi(Q_{11}^\alpha + Q_{12}^\alpha + \eta_m (Q_{11}^m + Q_{12}^m) + \frac{\eta_0 E_L}{1-\nu_L}) - (Q_{22}^\alpha + Q_{12}^\alpha + \eta_m (Q_{22}^m + Q_{12}^m) + \frac{\eta_0 E_L}{1-\nu_L})}{[Q_{11}^\alpha + Q_{12}^\alpha + \eta_m (Q_{22}^m + Q_{12}^m) + \frac{\eta_0 E_L}{1-\nu_L}] - \chi[Q_{22}^\alpha + Q_{12}^\alpha + \eta_m (Q_{11}^m + Q_{12}^m) + \frac{\eta_0 E_L}{1-\nu_L}]}} \quad (3.79)$$

Chapter 3

$$\eta_m = \frac{\chi(Q_{11}^\alpha \cos^2 \alpha + Q_{22}^\alpha \sin^2 \alpha + Q_{12}^\alpha + \eta_0 \frac{E_L}{1-\nu_L}) - (Q_{22}^\alpha \cos^2 \alpha + Q_{11}^\alpha \sin^2 \alpha + Q_{12}^\alpha + \eta_0 \frac{E_L}{1-\nu_L})}{(Q_{22}^m + Q_{12}^m) - \chi(Q_{11}^m + Q_{12}^m)} \quad (3.80)$$

The equal strains ε throughout the whole structure can then be obtained as:

$$\varepsilon = \frac{N_\phi}{t_\alpha [(Q_{11}^\alpha \cos^2 \alpha + Q_{22}^\alpha \sin^2 \alpha + Q_{12}^\alpha) + \eta_m (Q_{11}^m + Q_{12}^m) + \eta_0 \frac{E_L}{1-\nu_L}]} \quad (3.81)$$

3.5.4 Liner / 90° layers / 0° layers

Likewise, N_ϕ , N_θ are respectively given by:

$$N_\phi = \varepsilon t_m [(Q_{11}^m + Q_{12}^m) + \eta_{mh} (Q_{22}^h + Q_{12}^h) + \eta_0 \frac{E_L}{1-\nu_L}] \quad (3.82)$$

$$N_\theta = \varepsilon t_m [(Q_{22}^m + Q_{12}^m) + \eta_{mh} (Q_{11}^h + Q_{12}^h) + \eta_0 \frac{E_L}{1-\nu_L}] \quad (3.83)$$

where η_{mh} is the thickness ratio of the 90° and the 0° layers, expressed as:

$$\eta_{mh} = \frac{t_h}{t_m} \quad (3.84)$$

Substitution of equations (3.82) and (3.83) into (3.35) leads to the optimality condition for the laminate consisting of the metal liner, the 90° and the 0° layers:

$$\chi = \frac{(Q_{22}^m + Q_{12}^m) + \eta_{mh} (Q_{11}^h + Q_{12}^h) + \eta_0 \frac{E_L}{1-\nu_L}}{(Q_{11}^m + Q_{12}^m) + \eta_{mh} (Q_{22}^h + Q_{12}^h) + \eta_0 \frac{E_L}{1-\nu_L}} \quad (3.85)$$

Under the given χ the optimal thickness ratio η_{mh} is determined by:

$$\eta_{mh} = \frac{\chi(Q_{11}^m + Q_{12}^m + \eta_0 \frac{E_L}{1-\nu_L}) - (Q_{22}^m + Q_{12}^m + \eta_0 \frac{E_L}{1-\nu_L})}{Q_{11}^h + Q_{12}^h - \chi(Q_{22}^h + Q_{12}^h)} \quad (3.86)$$

The equal strains ε can also be obtained by:

$$\varepsilon = \frac{N_\phi}{t_m [(Q_{11}^m + Q_{12}^m) + \eta_{mh} (Q_{22}^h + Q_{12}^h) + \eta_0 \frac{E_L}{1-\nu_L}]} \quad (3.87)$$

It is worth noting that under the optimality condition the influence of the metal liner on the fiber lay-up design can be eliminated only if $\chi = 1$.

3.6 Feasible Range of Optimality Conditions

In this section we will provide the boundary conditions for the optimality condition. Equation (10) in fact represents a geometrical criterion that leads to equal shell strains in all directions, and thus achieves the best distribution of the laminate stiffness throughout the whole structure. Under the given biaxial stress ratio χ , the best combination of the laminate stiffness components A_{ij} can be deliberately designed to achieve the optimal condition ($\chi = \frac{A_{22} + A_{12}}{A_{11} + A_{12}}$). However, the A_{ij} elements strongly depend on the laminate lay-up and thus cannot be chosen freely; the optimality condition is confined by certain limitations under the given lay-up configuration.

The right-hand side of equation (3.39) has a maximum and minimum value, given by:

$$\chi_{\min} = \left(\frac{A_{22} + A_{12}}{A_{11} + A_{12}} \right)_{\min} \quad (3.88)$$

$$\chi_{\max} = \left(\frac{A_{22} + A_{12}}{A_{11} + A_{12}} \right)_{\max} \quad (3.89)$$

If the following relation holds:

$$\chi < \left(\frac{A_{22} + A_{12}}{A_{11} + A_{12}} \right)_{\min} \quad \text{or} \quad \chi > \left(\frac{A_{22} + A_{12}}{A_{11} + A_{12}} \right)_{\max} \quad (3.90)$$

Recalling equation (3.42) we will have:

$$\varepsilon_{\varphi} < \varepsilon_{\theta} \quad \text{or} \quad \varepsilon_{\varphi} > \varepsilon_{\theta} \quad (3.91)$$

Equation (3.91) shows unequal shell strains and thus leads to a non-zero shear stress. In other words, the optimality condition can only be satisfied if the biaxial stress ratio χ satisfies:

$$\chi_{\min} \leq \chi \leq \chi_{\max} \quad (3.92)$$

3.6.1 Boundary conditions for monolithic fiber laminates

(1) *Angle-ply laminates ($\pm\alpha$):*

With the aid of the classical lamination theory, for angle-ply laminates equation (3.39) becomes:

$$\chi = \frac{A_{22} + A_{12}}{A_{11} + A_{12}} = \frac{Q_{22} \cos^2 \alpha + Q_{11} \sin^2 \alpha + Q_{12}}{Q_{11} \cos^2 \alpha + Q_{22} \sin^2 \alpha + Q_{12}} \quad (3.93)$$

For anisotropic materials the following condition holds:

$$Q_{11} > Q_{22} \quad (3.94)$$

Chapter 3

Therefore the boundary conditions can be obtained by respective substitution of $\alpha = 0^\circ$ and $\alpha = 90^\circ$ into equation (3.93):

$$\frac{Q_{22} + Q_{12}}{Q_{11} + Q_{12}} \leq \chi \leq \frac{Q_{11} + Q_{12}}{Q_{22} + Q_{12}} \quad (3.95)$$

According to equation (3.95), the feasible range of the optimality condition becomes larger when the difference between Q_{11} and Q_{22} becomes larger. It is indicated that for the laminate with a higher anisotropy the biaxial stress ratio χ can be chosen in a larger range to satisfy the optimality condition. For the most extreme case: the netting theory, the difference of Q_{11} and Q_{22} is maximal hence the feasible range of the optimality condition also reaches largest. The netting theory assumes:

$$Q_{22} = Q_{12} = 0 \quad (3.96)$$

Substituting equation (3.96) into (3.95), yields:

$$0 \leq \chi < \infty \quad (3.97)$$

From equation (3.97) it is demonstrated that the optimality condition always holds for netting-dictated angle-ply laminates.

(2) *Double angle-ply laminates ($\pm\alpha$ and $\pm\beta$):*

For a double angle-ply laminate equation (3.39) becomes:

$$\chi = \frac{A_{22} + A_{12}}{A_{11} + A_{12}} = \frac{(Q_{22} \cos^2 \alpha + Q_{11} \sin^2 \alpha + Q_{12}) + \eta_{\alpha\beta} (Q_{22} \cos^2 \beta + Q_{11} \sin^2 \beta + Q_{12})}{(Q_{11} \cos^2 \alpha + Q_{22} \sin^2 \alpha + Q_{12}) + \eta_{\alpha\beta} (Q_{11} \cos^2 \beta + Q_{22} \sin^2 \beta + Q_{12})} \quad (3.98)$$

where $\eta_{\alpha\beta}$ is the thickness ratio of the $\pm\beta$ and $\pm\alpha$ layers, defined as:

$$\eta_{\alpha\beta} = \frac{t_\beta}{t_\alpha} \quad (3.99)$$

Notably the boundary conditions can be determined by substitution of $\eta_{\alpha\beta} = 0$ ($t_\beta = 0$) and $\eta_{\alpha\beta} \rightarrow \infty$ ($t_\alpha = 0$) into equation (3.98):

$$\chi_{\min} = \left(\frac{A_{22} + A_{12}}{A_{11} + A_{12}} \right)_{\eta_{\alpha\beta}=0} = \frac{Q_{22} \cos^2 \alpha + Q_{11} \sin^2 \alpha + Q_{12}}{Q_{11} \cos^2 \alpha + Q_{22} \sin^2 \alpha + Q_{12}} \quad (3.100)$$

$$\chi_{\max} = \left(\frac{A_{22} + A_{12}}{A_{11} + A_{12}} \right)_{\eta_{\alpha\beta} \rightarrow \infty} = \frac{Q_{22} \cos^2 \beta + Q_{11} \sin^2 \beta + Q_{12}}{Q_{11} \cos^2 \beta + Q_{22} \sin^2 \beta + Q_{12}} \quad (3.101)$$

Then χ should satisfy:

$$\frac{Q_{22} \cos^2 \alpha + Q_{11} \sin^2 \alpha + Q_{12}}{Q_{11} \cos^2 \alpha + Q_{22} \sin^2 \alpha + Q_{12}} \leq \chi \leq \frac{Q_{22} \cos^2 \beta + Q_{11} \sin^2 \beta + Q_{12}}{Q_{11} \cos^2 \beta + Q_{22} \sin^2 \beta + Q_{12}} \quad (3.102)$$

For the netting case, substitution of equation (3.96) into (3.102) leads to:

$$\tan^2 \alpha \leq \chi \leq \tan^2 \beta \quad (3.103)$$

In contrast to the angle-ply laminates, the optimality condition for netting-dictated double angle-ply laminates does have a certain limitation; the feasible range can become larger with increasing the difference between α and β and extends to infinity when $\alpha = 0^\circ$ & $\beta = 90^\circ$.

3.6.2 Boundary conditions for fiber metal laminates (FML)

(1) *Combination of $\pm\alpha$ layers and metal layers:*

The optimality condition can be given in the same form as equation (3.60):

$$\chi = \frac{A_{22} + A_{12}}{A_{11} + A_{12}} = \frac{Q_{22} \cos^2 \alpha + Q_{11} \sin^2 \alpha + Q_{12} + \frac{E_0}{1-\nu_0} \eta_0}{Q_{11} \cos^2 \alpha + Q_{22} \sin^2 \alpha + Q_{12} + \frac{E_0}{1-\nu_0} \eta_0} \quad (3.104)$$

where E_0 and ν_0 represent the young's modulus and the Poisson's ratio of the metal material, respectively; η_0 is the thickness ratio of the metal layers to the $\pm\alpha$ layers, defined as:

$$\eta_0 = \frac{t_0}{t_\alpha} \quad (3.105)$$

Similar to equation (3.93), the boundary conditions can be determined by respective substitution of $\alpha = 0^\circ$ and $\alpha = 90^\circ$ into equation (3.105):

$$\frac{Q_{22} + Q_{12} + \frac{E_0}{1-\nu_0} \eta_0}{Q_{11} + Q_{12} + \frac{E_0}{1-\nu_0} \eta_0} \leq \chi \leq \frac{Q_{11} + Q_{12} + \frac{E_0}{1-\nu_0} \eta_0}{Q_{22} + Q_{12} + \frac{E_0}{1-\nu_0} \eta_0} \quad (3.106)$$

(2) *Combination of $\pm\alpha$ layers, $\pm\beta$ and metal layers:*

On a way similar to the calculation in subsection 3.5.1, the optimality condition for this case can be given by:

$$\chi = \frac{A_{22} + A_{12}}{A_{11} + A_{12}} = \frac{(Q_{22} \cos^2 \alpha + Q_{11} \sin^2 \alpha + Q_{12})t_\alpha + (Q_{22} \cos^2 \beta + Q_{11} \sin^2 \beta + Q_{12})t_\beta + \frac{E_0}{1-\nu_0} t_0}{(Q_{11} \cos^2 \alpha + Q_{22} \sin^2 \alpha + Q_{12})t_\alpha + (Q_{11} \cos^2 \beta + Q_{22} \sin^2 \beta + Q_{12})t_\beta + \frac{E_0}{1-\nu_0} t_0} \quad (3.107)$$

The following dimensionless parameters (thickness ratios) are now introduced:

$$\eta_0 = t_0 / (t_\alpha + t_\beta), \quad \eta_\alpha = t_\alpha / (t_\alpha + t_\beta) \quad (3.108)$$

Using equation (3.108), equation (3.107) can be rewritten as a function of η_α :

Chapter 3

$$\chi(\eta_\alpha) = \frac{(Q_{22} \cos^2 \alpha + Q_{11} \sin^2 \alpha - Q_{22} \cos^2 \beta - Q_{11} \sin^2 \beta) \eta_\alpha + (Q_{22} \cos^2 \beta + Q_{11} \sin^2 \beta + Q_{12}) + \frac{E_0}{1-\nu_0} \eta_0}{(Q_{11} \cos^2 \alpha + Q_{22} \sin^2 \alpha - Q_{11} \cos^2 \beta - Q_{22} \sin^2 \beta) \eta_\alpha + (Q_{11} \cos^2 \beta + Q_{22} \sin^2 \beta + Q_{12}) + \frac{E_0}{1-\nu_0} \eta_0} \quad (3.109)$$

Considering $\alpha \leq \beta$ and $Q_{11} > Q_{22}$, the following condition holds:

$$\frac{d\chi}{d\eta_\alpha} < 0 \quad (3.110)$$

equation (3.110) shows that χ is a monotone decreasing function of η_α . Since $0 \leq \eta_\alpha \leq 1$, χ reaches its maximum and minimum values at $\eta_\alpha = 0$ and $\eta_\alpha = 1$, respectively. The boundary conditions can then be given by:

$$\frac{Q_{22} \cos^2 \alpha + Q_{11} \sin^2 \alpha + Q_{12} + \frac{E_0}{1-\nu_0} \eta_0}{Q_{11} \cos^2 \alpha + Q_{22} \sin^2 \alpha + Q_{12} + \frac{E_0}{1-\nu_0} \eta_0} \leq \chi \leq \frac{Q_{22} \cos^2 \beta + Q_{11} \sin^2 \beta + Q_{12} + \frac{E_0}{1-\nu_0} \eta_0}{Q_{11} \cos^2 \beta + Q_{22} \sin^2 \beta + Q_{12} + \frac{E_0}{1-\nu_0} \eta_0} \quad (3.111)$$

3.6.3 Boundary conditions for hybrid fiber laminates

We consider here only the netting analysis using two different fiber materials that are overwound with the angles $\pm\alpha$ and $\pm\beta$, respectively. According to the netting theory, we have:

$$\chi = \frac{A_{22} + A_{12}}{A_{11} + A_{12}} = \frac{E_{f1} t_{f1} \sin^2 \alpha + E_{f2} t_{f2} \sin^2 \beta}{E_{f1} t_{f1} \cos^2 \alpha + E_{f2} t_{f2} \cos^2 \beta} \quad (3.112)$$

We introduce the thickness ratio of two fiber materials:

$$\eta_f = \frac{t_{f1}}{t_{f2}} \quad (3.113)$$

Substitution of equation (3.113) into (3.112), leads to:

$$\chi = \frac{E_{f1} \sin^2 \alpha + E_{f2} \eta_f \sin^2 \beta}{E_{f1} \cos^2 \alpha + E_{f2} \eta_f \cos^2 \beta} \quad (3.114)$$

Obviously equation (3.114) has its maximum and minimum values at $\eta_f = 0$ ($t_{f2} = 0$) and $\eta_f \rightarrow \infty$ ($t_{f1} = 0$). We have:

$$\chi_{\min} = \tan^2 \alpha \quad \text{and} \quad \chi_{\max} = \tan^2 \beta \quad (3.115)$$

The boundary condition for this case can then be given by:

$$\tan^2 \alpha \leq \chi \leq \tan^2 \beta \quad (3.116)$$

Equation (3.116) has the same form as equation (3.103) for netting-dictated double angle-ply

laminates using monolithic fiber material. It is revealed that for the netting analysis the boundary limitations of the optimality condition are independent of the elastic properties of the used fibers; the fiber lay-up can here be regarded as a mechanism.

3.7 Conclusions

Netting analysis is perhaps the simplest of the analytical techniques used in design and evaluation of composite pressure vessels, but it is well suited for filament-wound pressure vessels. The analysis establishes the relationship between the stresses resulting in the composite layers of the pressure vessel and the internal pressure, material properties and fiber trajectories.

The optimality condition shows that optimal pressure vessels are governed by the condition of equal shell strains or, in other words, zero shear stress at lamina level. The tensile strength of filaments is completely utilized when the participating individual layers are aligned with the direction of the maximum principal stress. Please note that this condition is valid only if the shear effects in the global coordinates are considered negligible in the laminate with rotational symmetry for the geometry and the applied load. The same condition, based on the assumption of the equal strains or minimum mass, has also been derived by other authors [7, 8, 10, 11]. The present derivation of the optimality condition is based on the criterion of minimum strain energy density and the results demonstrate how the material anisotropy and the optimal fiber angle of a thin lamina depend on the biaxial stress ratio of the involved laminated shell.

The optimality condition of equal shell strains always holds true for netting-dictated angle-ply laminates. It should additionally be mentioned here that due to the nature of filament winding, the resulting laminate may be regarded as a symmetric, balanced angle-ply. Therefore, the optimality condition is always achieved for filament wound pressure vessels with the netting solutions.

References

1. Krikanov AA, Composite pressure vessels with higher stiffness. *Compos Struct* 2000; 48: 119-27.
2. Zu L, Koussios S, Beukers A. Design of filament-wound isotensoid pressure vessels with

Chapter 3

- unequal polar openings. *Compos Struct* 2010; 92: 2307-13.
3. Evans J T, Gibson AG. Composite angle ply laminates and netting analysis. *Proc R Soc Lond A* 2002; 458: 3079-88.
 4. Kaw AK. *Mechanics of composite materials*, 2nd Edition, Boca Raton: CRC Press, 2006.
 5. Bower, Allan (2009). *Applied Mechanics of Solids*. CRC Press
 6. Vapnyarskii, I.B. (2001), "Lagrange multipliers", in Hazewinkel, Michiel, *Encyclopaedia of Mathematics*, Springer.
 7. Vasiliev VV, Krikanov AA. New generation of filament-wound composite pressure vessels for commercial applications. *Compos Struct* 2003; 62(3): 449-59.
 8. Vasiliev VV, Morozov EV. *Advanced mechanics of composite materials*. UK: Elsevier Ltd; 2007.
 9. Koussios S, Beukers A. Influence of Laminate Thickness Approximation Methods on the Performance of Optimal Filamentary Pressure Vessels. 23rd Annual Conference of the American Society for Composites. Memphis, TN, September 9-11, 2008.
 10. Jong de Th. A theory of filament wound pressure vessels. Report LR-379. Structures and materials laboratory, Faculty of Aerospace Engineering, Delft University of Technology. Delft, April, 1983.
 11. Wasiutynski Z., Brandt A. The present state of knowledge in the field of optimum design of structures. *Appl. Mech. Rev.* 1963; 16(5): 341-50.

II NETTING-BASED APPROACHES

Chapter 4

Netting-based designs for circular toroidal pressure vessels

4.1 Introduction

During the past decades, the design and analysis for filament-wound toroidal pressure vessels have been developed in a variety of directions. Li and Cook [1] considered a toroid consisting of an inner metal liner and an outer fiber overwrap, and developed a full mathematical approach to the design of meridionally overwound toroids using a membrane shell theory, taking into account the load-bearing capability of the overwrap and its interaction with the liner. Cook et al. [2] employed a metal-aramid fiber hybrid construction into the design of light-weight toroidal breathing apparatus, taking into account stress rupture and stress relaxation effects in aramid fibers and the fatigue arising from repeated filling-discharge cycles. Marketos [3] only considered geodesic winding patterns and assumed the toroidal shell undergoes in-plane membrane forces. The circular cross section proved to be not structurally optimal because the change in the meridional stress around the cross-section is not compatible with the change of the geodesic winding angle. Maksimyuk and

Chapter 4

Chernyshenko [4] examined the distribution of the displacements, strains, and stresses in orthotropic toroidal shells made of nonlinearly elastic composites. Blachut [5] presented a numerical study into strength and static stability of externally pressurized filament wound CFRP toroids with closed circular and non-circular cross-sections.

Previous studies have concentrated on the use of geodesic or semi-geodesic trajectories; however, the design freedom of geodesics is severely limited because once the initial winding conditions of fiber position and orientation have been chosen, the entire fiber trajectory and corresponding thickness distribution are determined. Semi-geodesic winding offers more design freedom but still remains limited to a constant slippage coefficient during the winding process. In general neither geodesic nor semi-geodesic winding can place fibers in the principal stress direction of the toroid-shaped shell under internal pressure. It is thus desirable to determine the strength-dominated fiber trajectories that are based on the maximum principal stress [6-8] and that consequently lead to the optimal lay-up structure.

Designing optimal laminate lay-up is not the only issue; the fibers must be stable on the mandrel and be exactly placed along trajectories as predetermined by strength calculation. The fiber trajectories and corresponding winding angles cannot be chosen arbitrarily because of the requirements of windability. Any deviation from geodesics will require a lateral force of friction to prevent the fiber sliding from its original trajectory. In addition, since a half torus is concave the condition which avoids fiber bridging should also be respected when designing winding trajectories. Therefore an analysis for the stability of fiber trajectories is imperative. The overlook of fiber trajectory stability will make the optimally designed lay-up parameters difficult to be realized using filament winding technology and hence invalidate the structural design and optimization.

The main objective of this chapter is to simultaneously attain the minimum weight and the minimum strain energy density of helically and hoop overwound toroidal pressure vessels, and to evaluate the fiber trajectory stability for the two most commonly used patterns: single helical winding, helical and hoop winding. In section 4.1 a netting-based optimization model is developed to minimize the weight of the toroidal pressure vessel, subjected to several design constraints: the vessel's burst pressure, non-slippage and non-bridging of wound fibers. The strength constraints are derived based on the analysis of stress distribution in the toroidal shell; the fiber stability-ensuring constraints are formulated using differential geometry and the non-geodesic law. The fiber composite overwrap consists of helical and hoop winding layers, with the helical angle α (between the fiber trajectory and the parallel direction of the torus). The optimal design problem can be described in the following manner: for prescribed

Netting-based designs for circular toroidal pressure vessels

internal pressure and shell geometry determine the laminate parameters (winding angles and layer thicknesses) that result in a minimum structural weight and consequently a maximum structural performance. A two-level optimization method is developed: firstly, the aforementioned optimality condition is used to determine the optimal relation for linking the helical winding angle and hoop-to-helical thickness ratio, in order to maximize the average stiffness of the laminate. Secondly, the minimization of structural weight is carried out to determine the optimal fiber trajectories and related thickness distributions while satisfying the design constraints. In section 4.2 we emphasize the importance of the stability analysis for fiber trajectories and accordingly derive the general criteria and equations that determine the distributions of the fiber slippage and bridging tendencies. The distributions of slippage coefficients along the meridional direction and the minimum winding angles that avoid fiber bridging are outlined to evaluate the fiber trajectory stability of toroidal pressure vessels. The primary goal of the stability analysis is to offer an important reference for the design of toroidal pressure vessels.

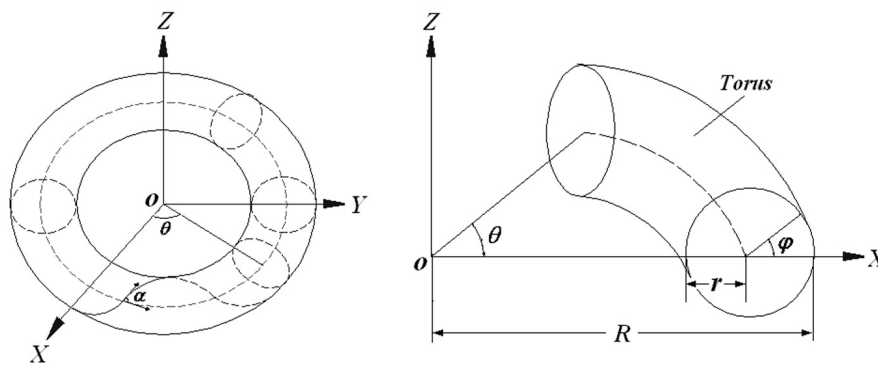


Fig. 4.1: Geometry of a toroidal pressure vessel with its system of coordinates

4.2 Minimum Weight Design

4.2.1 Basic geometry and governing equations

A toroidal pressure vessel is an axisymmetric shell of revolution with a circular cross-section that does not intersect the axis of revolution. The torus (surface of a closed doughnut) is formed by revolving a circle of radius r about a circle of radius $R > r$ lying in an orthogonal plane, as pictured in Fig. 4.1. R is the distance between the center of the cross-section and the axis of rotation, being referred to as the major radius; r is the radius of the tube, being called the minor radius. The meridional direction φ for a circular toroid is

Chapter 4

tangent to the cross-section and the parallel direction θ follows the circle of revolution for the toroid. The regular parameterization of the torus is given by:

$$\mathbf{S}(\theta, \varphi) = \begin{cases} (R + r \cos \varphi) \cos \theta \\ (R + r \cos \varphi) \sin \theta \\ r \sin \varphi \end{cases} \quad (0 \leq \varphi \leq 2\pi, 0 \leq \theta \leq 2\pi) \quad (4.1)$$

We consider here an infinitesimal elementary piece of a surface being part of the thin toroidal vessel (Fig. 4.2). The normal reaction force is acting as a counterbalance to the internal pressure [9]:

$$F_n = p \cdot R_\varphi \Delta\varphi \cdot R_\theta \Delta\theta \quad (4.2)$$

where p is the internal pressure; R_φ and R_θ are the meridional and parallel radii of curvatures, respectively, given by:

$$R_\varphi = r, \quad R_\theta = \frac{R + r \cos \varphi}{\cos \varphi}.$$

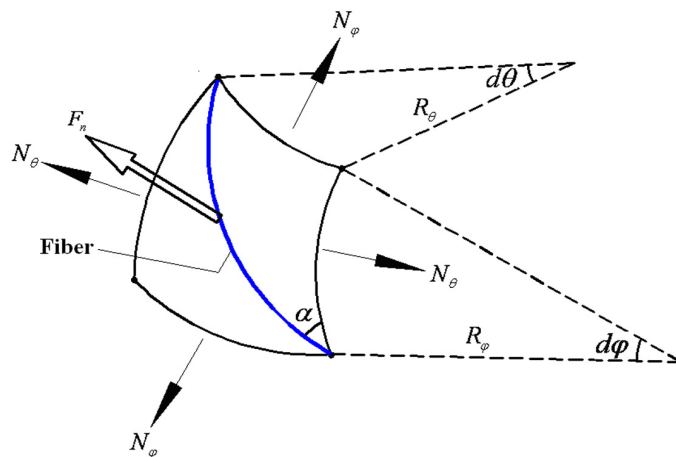


Fig. 4.2: An elementary orthogonal region belonging to a toroidal shell

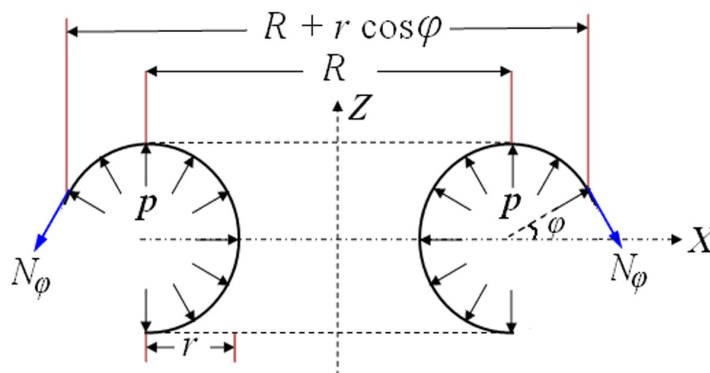


Fig. 4.3: Part of a toroidal shell loaded by an internal pressure p

Netting-based designs for circular toroidal pressure vessels

For a thin-walled pressure vessel, the membrane approximation theory for the stress analysis is here considered. According to the force equilibrium in the direction normal to the surface element, F_n can be expressed in terms of the membrane forces in two principal directions:

$$F_n = N_\varphi R_\theta \Delta\theta \sin \Delta\varphi + N_\theta R_\varphi \Delta\varphi \sin \Delta\theta \quad (4.3)$$

where N_φ , N_θ are the in-plane forces per unit length in the meridional and parallel directions.

The equality relation for the membrane forces can be obtained by equalizing the right-hand expression of equation (4.2) with that of equation (4.3):

$$\frac{N_\varphi}{R_\varphi} + \frac{N_\theta}{R_\theta} = p \quad (4.4)$$

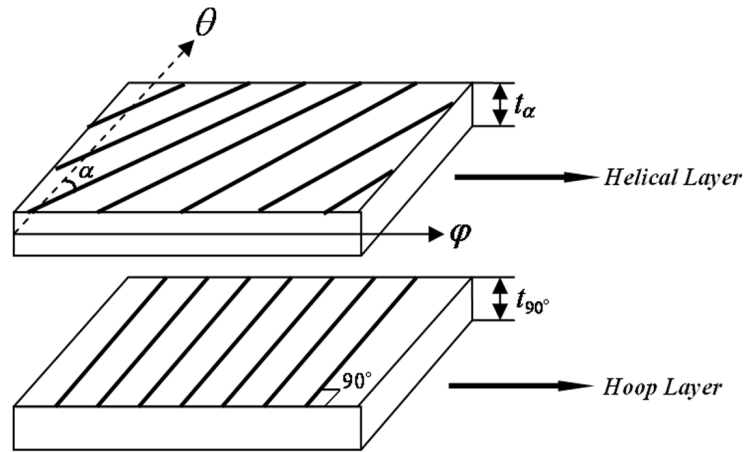


Fig. 4.4: Schematics of the helical and hoop winding layers

The axial equilibrium of a toroidal shell can be formulated as shown in Fig. 4.3:

$$\pi p[(R + r \cos \varphi)^2 - R^2] - 2\pi(R + r \cos \varphi)N_\varphi \cos \varphi = 0 \quad (4.5)$$

Hence:

$$N_\varphi = \frac{pr}{2} \cdot \frac{2R + r \cos \varphi}{R + r \cos \varphi} \quad (4.6)$$

N_θ can be solved by substitution of equation (4.6) into (4.4):

$$N_\theta = \frac{pr}{2} \quad (4.7)$$

For thin shells, the membrane forces are considered to be constant through the thickness. The meridional force, N_φ , increases as the parameter φ decreases while the parallel force, N_θ , remains constant throughout the toroid.

Helical winding is usually combined with hoop winding in order to reinforce the laminate

Chapter 4

structure both in longitudinal and hoop directions (Fig. 4.4). According to the classical lamination theory [10], the optimality condition (equation (3.39)) for the combination of helical and hoop winding layers can be expressed as:

$$\chi = \frac{\bar{Q}_{11}^{\alpha} + \bar{Q}_{12}^{\alpha} + (\bar{Q}_{11}^{90^{\circ}} + \bar{Q}_{12}^{90^{\circ}})\eta}{\bar{Q}_{22}^{\alpha} + \bar{Q}_{12}^{\alpha} + (\bar{Q}_{22}^{90^{\circ}} + \bar{Q}_{12}^{90^{\circ}})\eta} \quad (4.8)$$

where η is the hoop-to-helical thickness ratio, defined as:

$$\eta = \frac{t_h}{t_{\alpha}} \quad (4.9)$$

where t_{α} and t_h are the helical and hoop layer thicknesses, respectively.

This section is based upon the assumption that the shell can be treated as a membrane and, therefore, the ratio of in-plane shell forces (membrane forces) due to uniformly distributed internal pressure can be given by [11]:

$$\chi = \frac{R + r \cos \varphi}{2R + r \cos \varphi} \quad (4.10)$$

According to the netting theory, the effect of the matrix is considered negligible. Substituting equation (4.10) into (4.8) and representing \bar{Q}_{ij}^{α} and \bar{Q}_{ij}^h in terms of the winding angle α , yields the optimality relation between α and η :

$$\tan^2 \alpha = \frac{2R + r \cos \varphi}{R + r \cos \varphi} - \eta \quad (4.11)$$

Considering the winding process that starts from the doffing point $P(R, 0, 0)$ at the equator, we have:

$$\eta_0 = \frac{2R + r}{R + r} - \tan^2 \alpha_0 \quad (4.12)$$

where η_0 is the hoop-to-helical thickness ratio at the equator:

$$\eta_0 = \frac{t_h^0}{t_{\alpha}^0} \quad (4.13)$$

where t_{α}^0 and t_h^0 are the thickness of the $\pm\alpha$ and the hoop layers at the equator, respectively.

In calculating the thickness, the following two assumptions are made [12]: firstly the fiber volume fraction is maintained consistently; secondly, the number of filaments in a cross section is always constant. With these assumptions, the thickness distributions along the shell meridian can be formulated by:

Netting-based designs for circular toroidal pressure vessels

$$t_\alpha = \frac{(R+r)\sin\alpha_0}{(R+r\cos\varphi)\sin\alpha} \cdot t_\alpha^0, \quad t_{90^\circ} = \frac{(R+r)}{(R+r\cos\varphi)} \cdot t_h^0 \quad (4.14)$$

which leads to:

$$\eta = \frac{\sin\alpha}{\sin\alpha_0} \eta_0 \quad (4.15)$$

Simultaneous solution of the system of equations consisting of (4.11), (4.12) and (4.15) will finally provide the winding angle distribution along the meridional coordinate φ , for the toroidal pressure shell with the minimum strain energy density. After dropping the negative solution, we obtain:

$$\alpha = \arcsin \frac{\sqrt{1+4A^2B(B-1)}-1}{2AB} \quad (4.16)$$

in which

$$A = \frac{(R+r)\sin\alpha_0}{(3R+2r)\cos^2\alpha_0 - (R+r)}, \quad B = \frac{3R+2r\cos\varphi}{R+r\cos\varphi}$$

4.2.2 Optimization model

We address here the problem of finding the minimum structural weight of toroidal hydrogen tanks. The helical layer angle and layer thickness at the equator are considered as the design variables, as stated by:

$$\mathbf{X} = (\alpha_0, t_\alpha^0) \quad (4.18)$$

The weight of the fiber composite overwrap is chosen as the objective of the optimal design, given by:

$$W = 2\pi r \gamma (R+r) \left(\int_0^{2\pi} \frac{\sin\alpha_0}{\sin\alpha} \cdot t_\alpha^0 d\varphi + 2\pi \cdot t_h^0 \right) \quad (4.19)$$

where γ is the specific weight of the laminate; α is a function of φ , which can be determined by equation (4.16). Substituting equation (4.12) into (4.19) leads, after some rearrangements, to:

$$W(\mathbf{X}) = 2\pi r \gamma t_\alpha^0 (R+r) \left[\frac{2\pi}{1+\tan^2\alpha_0} \left(\frac{2R+r}{R+r} - \tan^2\alpha_0 \right) + \int_0^{2\pi} \frac{\sin\alpha_0}{\sin\alpha} d\varphi \right] \quad (4.20)$$

The winding tension induced by the feed eye may drive the fibers to slip on the mandrel surface and to bridge on concave sections. To keep the fibers stable, the following condition should be fulfilled (equation (2.20)):

Chapter 4

$$\left| k_g / k_n \right| \leq \mu_{\max} \quad (4.21)$$

The coefficients of the first fundamental form of $\mathbf{S}(\theta, \varphi)$ are obtained by substitution of equation (4.1) into equations (2.30) and (2.32):

$$\begin{aligned} E &= (R + r \cos \varphi)^2, \quad F = 0, \quad G = r^2, \\ L &= -(R + r \cos \varphi) \cos \varphi, \quad M = 0, \quad N = -r. \end{aligned} \quad (4.22)$$

Substitution of equation (4.22) into (2.45), k_g is given by:

$$k_g = \frac{d\alpha}{dl} + \frac{\sin \varphi}{R + r \cos \varphi} \cos \alpha \quad (4.23)$$

Substitution of equation (4.22) into (2.46) and (2.47), followed by plugging the resulting K and H into equation (2.49), leads to:

$$\kappa_1 = -\frac{1}{r}, \quad \kappa_2 = -\frac{\cos \varphi}{R + r \cos \varphi}, \quad (4.24)$$

The normal curvature k_n is related to the principle curvatures (recall equation (2.50)):

$$k_n = -\frac{\cos \varphi}{R + r \cos \varphi} \cos^2 \alpha - \frac{1}{r} \sin^2 \alpha \quad (4.25)$$

In addition, the following relation holds:

$$\frac{d\varphi}{dl} = \frac{\sin \alpha}{r} \quad (4.26)$$

Substituting equations (4.23), (4.25) and (4.26) into (4.21), the non-slippage constraint can be formulated by:

$$\left| \frac{\frac{d\alpha}{d\varphi} \sin \alpha + \frac{r \sin \varphi}{R + r \cos \varphi} \cos \alpha}{\frac{r \cos \varphi}{R + r \cos \varphi} \cos^2 \alpha + \sin^2 \alpha} \right| - \mu_{\max} \leq 0 \quad (4.27)$$

in which $d\alpha/d\varphi$ is calculated by the first derivative of both sides of equation (4.16) with respect to the variable φ :

$$\frac{d\alpha}{d\varphi} = \frac{Rr \sin \varphi \cos^2 \alpha \sin \alpha_0}{(R + r \cos \varphi)(3R + 2r \cos \varphi) \sin 2\alpha \sin \alpha_0 + \eta_0 \cos \alpha (R + r \cos \varphi)^2} \quad (4.28)$$

The allowable coefficient of friction that is used as a threshold for checking if fiber slippage occurs during the winding process, is closely related to the smoothness of the mandrel surface, the wound fibers and resin, the manufacturing process, etc. In addition, since the torus has a concave surface ($90^\circ < \varphi < 270^\circ$), the fiber bridging tendency should also be examined. The fiber may bridge and is not closely attached to the supporting surface unless $k_n \leq 0$ (see equation (2.25)). From equation (4.25) we have:

Netting-based designs for circular toroidal pressure vessels

$$\frac{-r \cos \varphi}{R + r \cos \varphi} - \tan^2 \alpha < 0 \quad (4.29)$$

The stress ratio K is here defined as:

$$K = \frac{\sigma}{\sigma_0} \quad (4.30)$$

where σ and σ_0 are the fiber stress at an arbitrary parallel periphery ($\varphi \equiv \text{Constant}$) and the equatorial periphery ($\varphi = 0$), respectively. K reflects the stress distribution relative to the stress level at the outermost periphery (equator). According to the netting theory, we have:

$$\sigma = E_f \cdot \varepsilon \quad (4.31)$$

where E_f is the Young's elastic module of the used fibers. Substituting equation (3.45) into (4.31) and plugging the result into equation (4.30) leads, after some arrangements, to:

$$K = \frac{(R + r \cos \varphi) \sin \alpha \cos^2 \alpha_0}{(R + r) \sin \alpha_0 \cos^2 \alpha} \quad (4.32)$$

K can be determined by substitution of equation (4.16) into (4.32) for the given α_0 , as shown in Fig. 4.5 ($R/r = 4$). It is observed that the smaller initial winding angle leads to a more homogeneous stress distribution throughout the shell. Without proceeding into details, it can be proved that the following condition always holds true for the entire structure:

$$K \leq 1 \quad (4.33)$$

It is revealed that the fiber stress at the equator ($\varphi = 0$) arrives at the maximum and thus, the burst of the toroidal tank will take place at the equatorial periphery. The strength constraint can then be expressed in terms of the fiber stress at the equator:

$$\sigma_0 = \frac{pr}{2t_\alpha^0(1+\eta_0)} \cdot \frac{3R+2r}{R+r} \leq X_f \quad (4.34)$$

where X_f is the ultimate tensile strength of the used fibers.

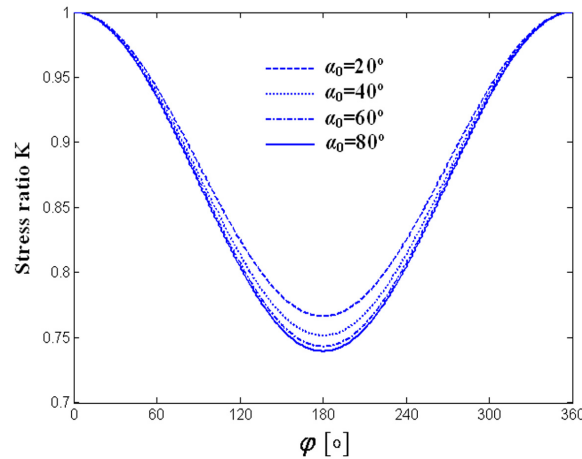


Fig. 4.5: Stress distributions relative to the stress magnitude at the equator ($R/r = 4$)

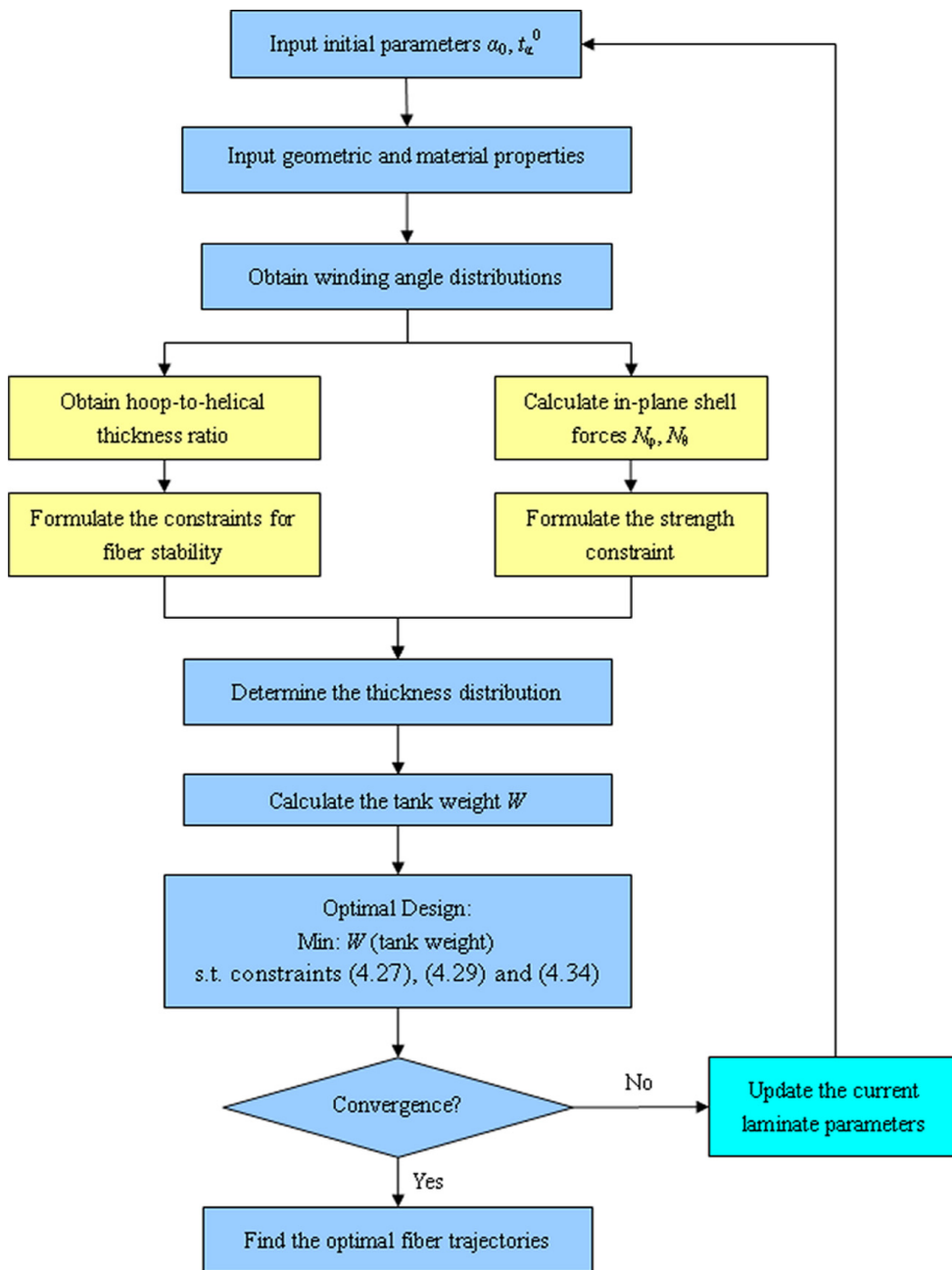


Fig. 4.6: Flow chart of the optimal design procedure

4.2.3 Solution procedure

The optimal design issue here refers to the nonlinear constrained optimization and involves minimizing the structural weight W , subjected to the non-linear design constraints of equations (4.27), (4.29) and (4.34). The *SQP* (sequential quadratic programming) algorithm is here used to solve the optimization problem [13]. The flow chart below (Fig. 4.6) illustrates

Netting-based designs for circular toroidal pressure vessels

the optimal design procedure. In every iteration step, when a netting-dictated fiber trajectory and adapted thickness distribution are determined by equations (4.14) and (4.16), the expressions on the left-hand side of equations (4.27) and (4.29) are evaluated at all points assigned along the meridional coordinate φ within a complete wound circuit ($\varphi = 0^\circ \sim 360^\circ$). Their maximum value is then selected to verify if the constraints are enabled. The objective function W is then calculated by equation (4.20) using Gaussian quadrature rule. The current design values are then updated as a new set of values by this procedure. The above steps are repeated until a user-defined termination criterion is satisfied. The flow chart of the verification for fiber stability constraints (non-slippage and non-bridging conditions) is represented in Fig. 4.7.

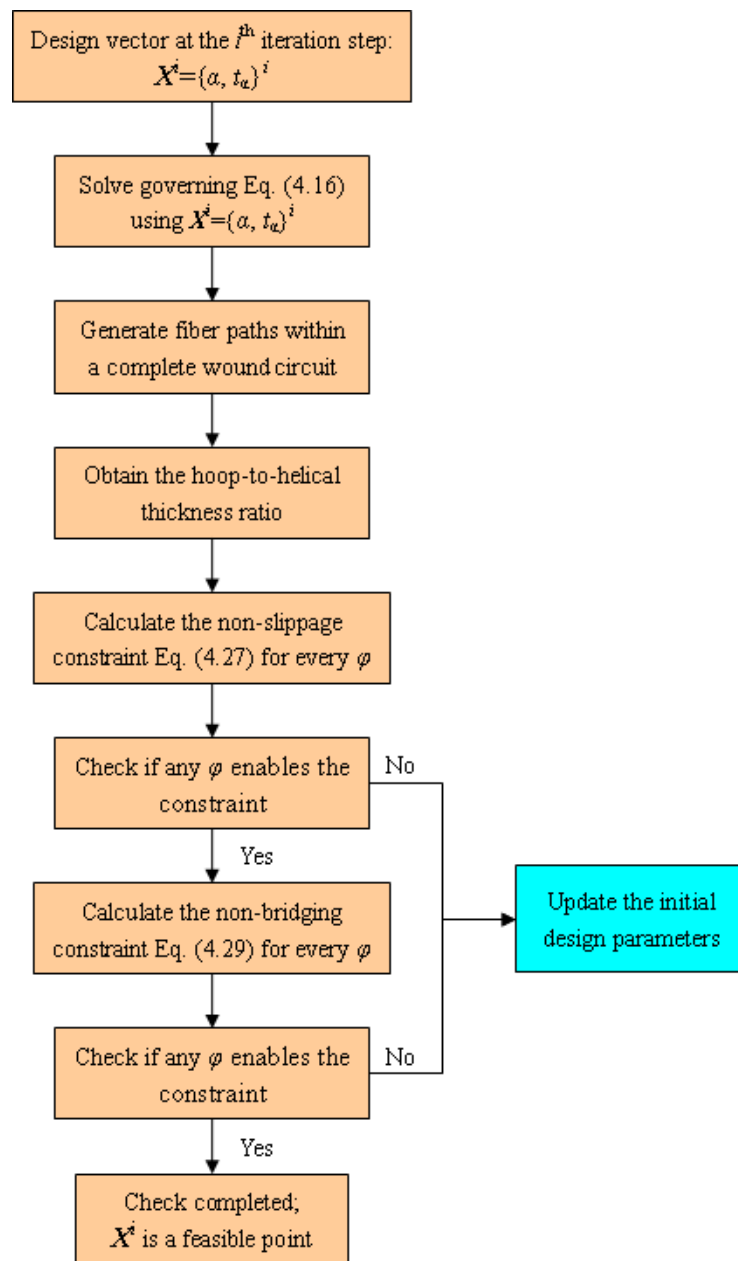


Fig. 4.7: Flow chat of the verification process for fiber stability

4.2.4 Design example

In the following example, a composite toroidal hydrogen storage tank, where $R = 400\text{mm}$, $r = 100\text{mm}$, $\mu = 0.3$, is considered. The tank is filament wound using a combination of hoop and helical windings. The tensile strength of the used fibers is $X_f = 4.9\text{ GPa}$, while the uniform internal pressure is $p = 70\text{ MPa}$. The specific weight of the overwrapped composite laminate is $\gamma = 1.57 \times 10^3\text{ kg/m}^3$. Using the present optimization approach (as elaborated in subsection 4.23), the optimal design variables are converged to $(\alpha_0, t_a^0) = (50.83^\circ, 1.8\text{ mm})$, where the structural weight W reaches a minimum of 6.07 kg. The optimization procedure provides both good convergence performance and global searching ability.

We recall here that λ in equation (2.21) is the slippage coefficient that represents the tendency of fiber slippage on the mandrel surface, defined by $\lambda = k_g / k_n$. Fig. 4.8 illustrates the optimal winding angle distribution as compared to those dictated by geodesics ($\lambda = 0$) and semi-geodesics ($\lambda = 0.5, 1$ and 1.5). This winding angle of optimal fiber trajectories increases from 50.8° at the equator to 54.5° at the inner parallel periphery. It is revealed that the winding angle distribution determined by using the present method is centralizing in the small range and is almost identical with the optimal winding angle (e.g., 55° [14]) for internally pressurized cylindrical tanks subjected to the well-known hoop-to-axial stress ratio of 2. On the other hand, the geodesic and semi-geodesic angles are located in relatively wide ranges and their initial angles are bigger. It can be concluded that the present method leads to a more reasonable distribution of the fiber stress in the toroidal shell; the toroidal hydrogen storage tanks designed using the present method can thus have higher structural performance as compared to those based on either geodesics or semi-geodesics.

Fig. 4.9 shows the distribution of slippage coefficient λ of the obtained optimal fiber trajectories along the meridional direction. It can be seen that the maximum absolute value of λ is 0.3 in a complete wound circuit ($\varphi = 0^\circ \sim 360^\circ$). Fig. 4.10 outlines the non-feasible region of winding angles that may result in fiber bridging on the mandrel surface. The results indicated that the optimal winding angles determined using the present method are remarkably bigger than the minimal allowable angles for satisfying the non-bridging condition. Accordingly, the obtained optimal fiber trajectories entirely comply with the stability-ensuring conditions for the winding process as given in equations (4.27) and (4.29). Furthermore, the maximum slippage tendency occurs at the positions of $\varphi = 109^\circ$ and $\varphi = 251^\circ$. Fig. 4.11 provides the thickness distributions of helical and hoop layers, respectively. Since the parallel radius gradually decreases from the outer equator to the inner periphery of the

Netting-based designs for circular toroidal pressure vessels

torus, the layer thickness increases from outside to inside and reaches the maximum at the inner periphery. Furthermore, an explicit simulation of the optimal fiber trajectories using the present method is performed in Fig. 4.12, compared to the conventionally used geodesic trajectories that satisfy the design constraints. The results also demonstrate that the optimal winding angles determined using the present method are much smaller than the geodesic angles. Therefore, a better distribution of the fiber strength in meridional and parallel directions can be achieved and consequently improve the structural efficiency of toroidal pressure vessels.

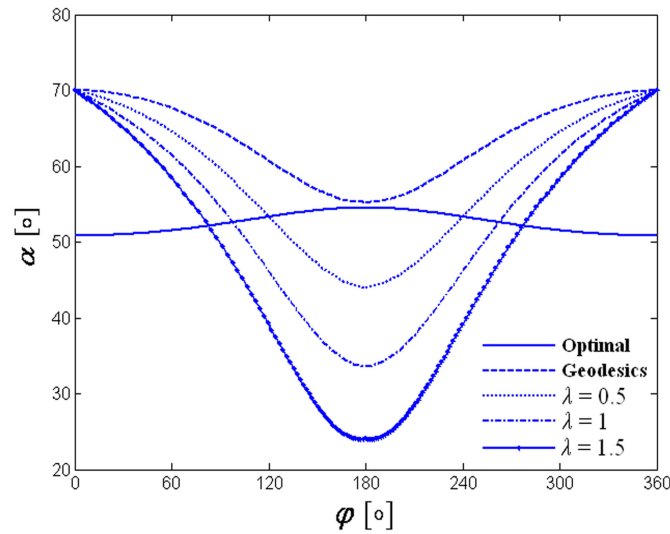


Fig. 4.8: Helical winding angle distributions based on the present method, geodesics and semi-geodesics ($\lambda = 0.5, 1$ and 1.5), respectively

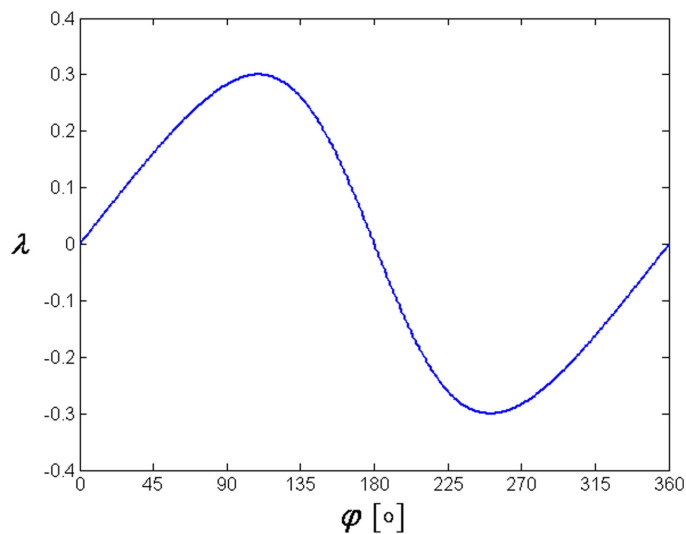


Fig. 4.9: Slippage coefficient distribution of the obtained optimal fiber trajectories

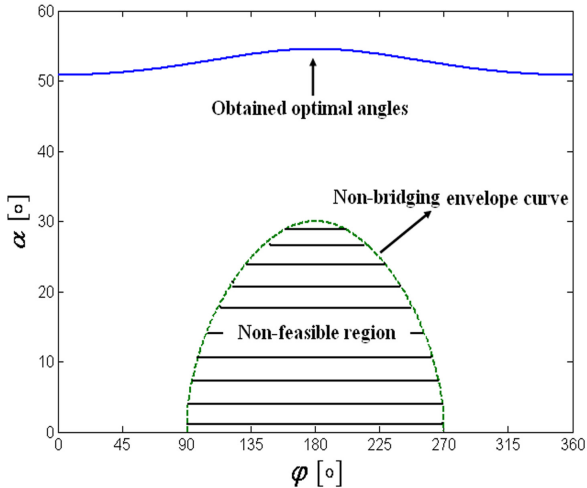


Fig. 4.10: Critical winding angle envelope for ensuring non-bridging of fibers

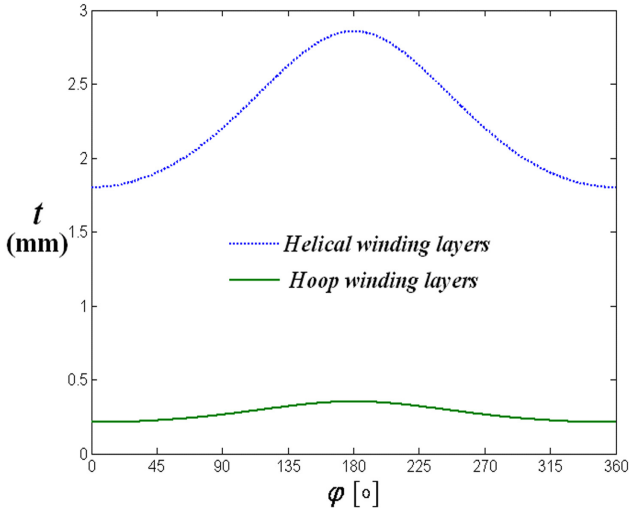


Fig. 4.11: Helical and hoop layer thickness distributions along the meridional direction

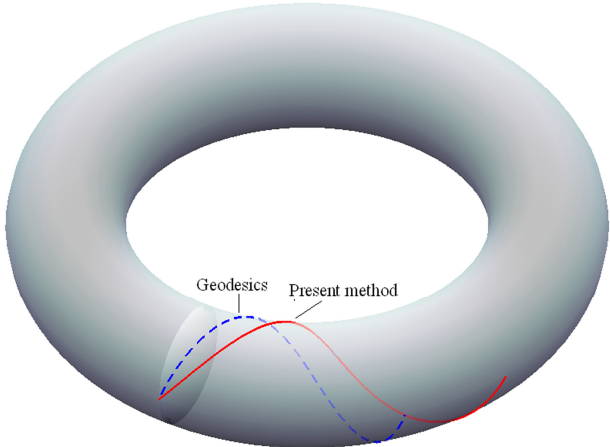


Fig. 4.12: Conventionally used geodesics and the present optimal fiber trajectories

4.3 Fiber Trajectory Stability of Toroidal Pressure Vessels

The influence of the geometry and lay-up of the toroid on the netting-dictated fiber trajectory stabilities is here evaluated. For convenience in subsequent evaluation, the hoop-to-helical thickness ratio η is here considered constant along the meridional direction. This assumption does not lead to any significant error in the analysis, because a toroid is a doubly-closed body of revolution and has a relatively homogeneous thickness distribution over the surface. In addition, the relative bend radius K , which is defined as the ratio of the bend radius R to the tube radius r , is here used to characterize the geometry of the torus:

$$K = R / r \quad (4.35)$$

It should be noted here that K in fact describes the slenderness of the toroid. According to the above definitions, equation (4.16) becomes:

$$\alpha = \tan^{-1} \sqrt{\frac{1 - \eta + \frac{K}{K + \cos \varphi}}{1 + \eta}} \quad (0 \leq \varphi \leq 2\pi) \quad (4.36)$$

The winding angle of the netting-based fiber trajectories depends on K and η . The initial winding condition of fiber position is able to completely determine the fiber trajectories for the given K and η . Note that for the single helical winding we have $\eta = 0$ and equation (4.36) can accordingly be rewritten as:

$$\alpha = \tan^{-1} \sqrt{1 + \frac{K}{K + \cos \varphi}} \quad (0 \leq \varphi \leq 2\pi) \quad (4.37)$$

Fig. 4.13 presents the netting-based winding angle developments for the single helical winding and the helical and hoop winding ($K = 3\text{--}6$, $\eta = 0.5$), respectively. The results show that at each position along the meridional direction the single helical winding provides a bigger fiber angle than the helical and hoop winding.

By substituting equations (4.23) and (4.25) into (2.21), the slippage coefficient λ can be expressed as a function of φ :

$$\lambda(\varphi) = \left| \frac{\frac{d\alpha}{d\varphi} \sin \alpha + \frac{\sin \varphi}{K + \cos \varphi} \cos \alpha}{\frac{\cos \varphi}{K + \cos \varphi} \cos^2 \alpha + \sin^2 \alpha} \right| \quad (4.38)$$

where $d\alpha/d\varphi$ can be obtained by the first derivative of equation (4.36) with respect to φ :

$$\frac{d\alpha}{d\varphi} = \frac{K \sin \varphi \sqrt{1 + \eta}}{2(3K + 2 \cos \varphi) \sqrt{(K + \cos \varphi)[(2 - \eta)K + (1 - \eta) \cos \varphi]}} \quad (4.39)$$

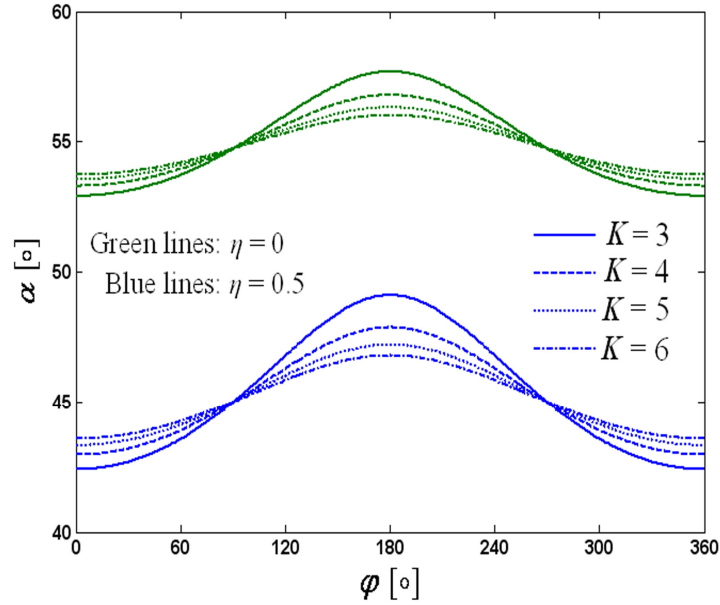


Fig. 4.13: Winding angle distributions for the single helical winding ($\eta = 0$) and the helical and hoop winding ($\eta = 0.5$)

Substituting equation (4.39) into (4.38), the expression for determining the slippage coefficient λ is rewritten as:

$$\lambda = \frac{2 \sin \varphi (3K + 2 \cos \varphi) \sqrt{K + (K + \cos \varphi)(1 - \eta)} + K \sqrt{(1 + \eta)(2K + \cos \varphi)}}{4(K + \cos \varphi)^{3/2} \sqrt{(3K + 2 \cos \varphi)[(K + \cos \varphi)(1 - \eta) + K]}} \quad (4.40)$$

The condition for preventing fiber bridging over the torus is transformed into:

$$\tan^2 \alpha = \frac{\frac{K}{K + \cos \varphi} + 1 - \eta}{1 + \eta} \geq \frac{-\cos \varphi}{K + \cos \varphi} \quad (4.41)$$

Equation (4.41) can further reduce to:

$$\eta = t_h / t_\alpha < 2(1 - 1/K) \quad (4.42)$$

Equation (4.42) provides the non-bridging criterion for fiber trajectories on the torus. Please note that for single helical winding this criterion is always satisfied since $\eta = 0$. Accordingly the single helical winding trajectories determined using the netting theory will never bridge over the torus.

Equations (4.40) and (4.41) give the criteria for assessing the stability of a fiber trajectory designed using the netting-based approach. It is shown that for the helical and hoop winding the fiber stability is influenced by the relative bend radius K and the hoop-to-helical layer thickness ratio η while for the single helical winding K is the only influential parameter.

Fig. 4.14 outlines the distribution of the minimum required winding angles as dictated by

Netting-based designs for circular toroidal pressure vessels

the non-bridging criterion, as compared to the winding angles of fiber trajectories obtained using the netting analysis. It can be seen that for the most common K -range [3, 6], the netting-based winding angles are much bigger than the critical angles for avoiding fiber bridging; the obtained fiber trajectories will therefore not bridge over the entire surface. In addition, for a given k there is a maximum value for η able to guarantee the validity of the non-bridging criterion. The result is depicted in Fig. 4.15, where the non-bridging-ensuring feasible $\{K, \eta\}$ -field is dashed. It should be noted here that the non-bridging criterion is consistently valid for the convex surface because equation (4.41) always holds true for the range $\varphi = [-90^\circ, 90^\circ]$. Fig. 4.16 shows the distributions of the slippage tendency $|\lambda|$ along the meridional coordinate φ , corresponding to various K ($K = 3\sim 6$, $\eta = 0.5$). The results reveal that the fiber trajectories exhibit an increasing slippage tendency from the inner/outer equator towards the crest of the toroid; however, the maximum slippage tendency is not present exactly at the crest but somewhere between the crest and the inner equator, depending on the K -value. It is thus suggested that more attention should be paid to the winding of the concave surface of the toroid. Fig. 4.17 illustrates the maximum slippage coefficients of the obtained fiber trajectories corresponding to the most common combinations of K and η ($K = 3\sim 6$, $\eta = 0\sim 1.5$). It is shown that the fiber slippage tendency significantly decreases with the increase of K , and slightly increases with the increase of η . The relative bend radius proves to be the most influential factor on fiber slippage tendency, while the thickness ratio has less influence.

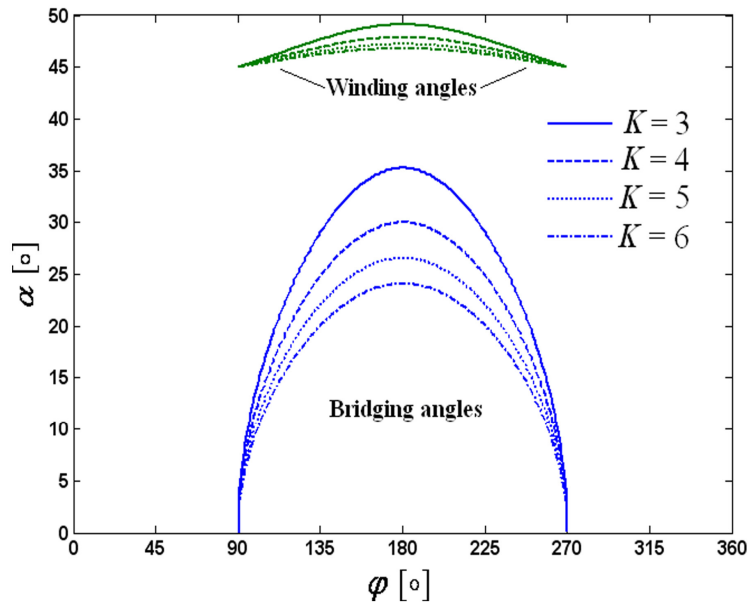


Fig. 4.14: Minimum non-bridging-ensuring angles as compared to winding angles of the netting-based fiber trajectories

Chapter 4

As seen in the results of the stability analysis, it is shown that for toroidal pressure vessels with $K \geq 4$ the fiber trajectories determined using the netting theory can well satisfy the stability-ensuring criteria; for toroidal vessels with $3 \leq K \leq 4$, the maximum coefficient of friction between the supporting surface and the placed fiber should be guaranteed to reach 0.4~0.5, in order to prevent fiber trajectories deviating from the netting-dictated trajectories. However, for toroids with $K < 3$ & $\eta > 1.5$, it is strongly suggested to employ geodesic or semi-geodesic trajectories instead of the present netting-based trajectories, with a compromise between structural performance and windability.

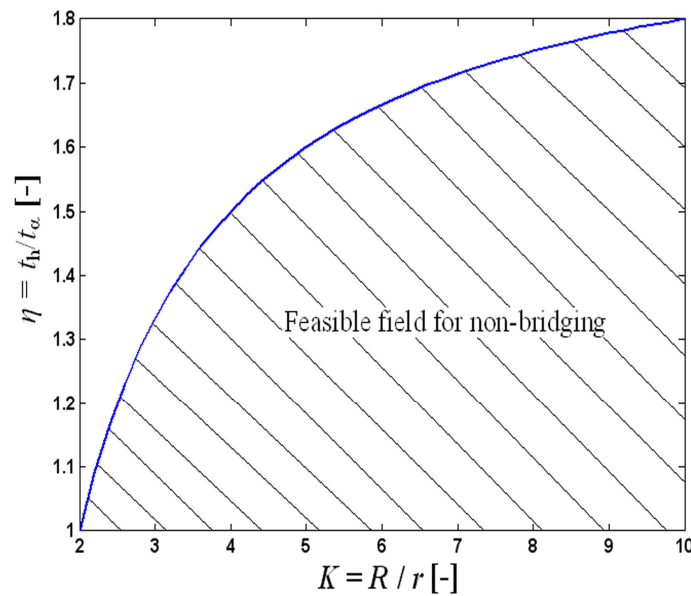


Fig. 4.15: Feasible field of $\{k, \eta\}$ -combinations for ensuring non-bridging (shaded area)

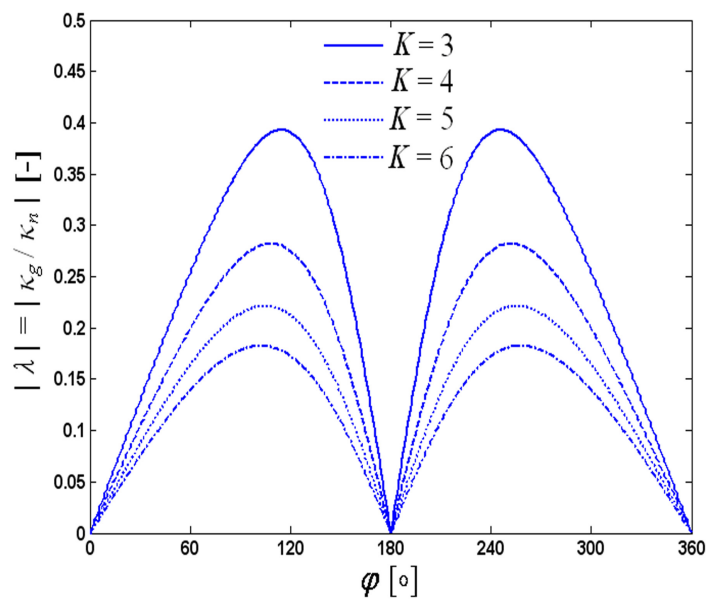


Fig. 4.16: Slippage tendency distributions along the meridional direction

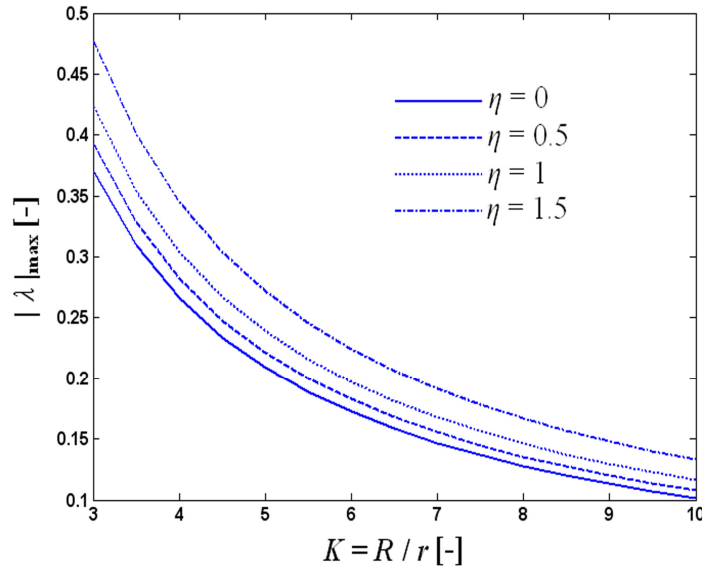


Fig. 4.17: Maximum slippage coefficients of the obtained fiber trajectories for the most common K and η

4.4 Conclusions

A netting-based design method is outlined regarding the optimal design of helically and hoop wound toroidal pressure vessels. The structural efficiency can be improved by changing the helical fiber orientation and the hoop-to-helical thickness ratio. The optimal values of the layup parameters at the equator are determined to create optimal fiber trajectories. The netting theory is employed for predicting the structural behavior and the *SQP* method was utilized as a non-linear optimization algorithm. To obtain the strength constraints, the relative stress distribution along the meridional direction is outlined and the stress level at the outermost periphery has proven to be the maximum in the toroidal vessel. The present method is based on non-constant slippage coefficient and determines the optimal fiber trajectories that are aligned in the principal stress direction throughout the whole structure. Therefore, the obtained optimal laminate configuration has a minimum structural weight (and therefore a maximum vessel performance) and can be regarded as the most efficient in terms of the netting-based design.

As a result of the optimal design, the helical winding angle increases along the meridional direction from the outer equator towards the inner periphery. The optimization procedure is well convergent to stable solutions while the resulting fiber trajectories satisfy all the design constraints. The minimum point of the weight function is just on the boundary of the

Chapter 4

non-slippage and the ultimate strength constraints. The practicality and effectiveness of the present method are verified by computer simulations where the obtained optimal fiber trajectories satisfy the winding principles of the toroid. Compared to the geodesic winding, the results also demonstrate that the fiber trajectories determined using the present method lead to a better stress distribution and hence maximize the utilization of the fiber strength under internal pressure. Accordingly, the structural performance of toroidal pressure vessels can be significantly improved using the present method.

To evaluate the effect of the geometry and the lay-up on the stability of the netting-based trajectories, the fiber slippage and bridging tendencies of the obtained fiber trajectories are illustrated for various relative bend radii and hoop-to-helical thickness ratios. It is revealed that toroidal pressure vessels with larger relative bend radius and lower hoop-to-helical thickness ratio lead to better fiber stability in terms of either slippage or bridging tendency. The results also conclude that for the most commonly used toroids, the winding trajectories designed by the netting theory satisfy both the non-slippage and non-bridging criteria, and show sufficient fiber stability for the winding process. In addition, it is worth mentioning that the netting-based fiber trajectories will in general fulfill the non-bridging condition if they satisfy the non-slippage criterion.

Despite the fact that the small relative bend radii ($K < 3$) result in the instability of fiber trajectories on the torus, the present netting-based winding trajectories do satisfy the stability-ensuring requirements for the most commonly used toroids ($K \geq 3$) in today's industries.

References

1. Cook J, Chambers JK, Richards BJ. Toroidal pressure vessels for breathing apparatus. Proc. of International SAMPE Europe conference, Paris, France, April 1998.
2. Li SG, Cook J. An analysis of filament overwound toroidal pressure vessels and optimum design of such structures. *J Press Vessel Technol* 2002; 124: 215-22.
3. Marketos JD. Optimum toroidal pressure vessel filament wound along geodesic lines. *AIAA Journal* 1963; 1: 1942-5.
4. Maksimyuk V A, Chernyshenko IS. Nonlinear elastic state of thin-walled toroidal shells made of orthotropic composites. *Int Appl Mech* 1999; 35:1238-45.
5. Blachut J. Buckling and first ply failure of a composite toroidal pressure hull. *Comput Struct* 2004; 82:1981–92.

Netting-based designs for circular toroidal pressure vessels

6. Zinoviev PA. Pressure vessels of minimum mass made by winding of orthotropic tapes. In: Proceedings of MVTU – Application of Plastics in Machinery 1975; 14: 48–58.
7. Vasiliev VV, Krikanov AA. New generation of filament-wound composite pressure vessels for commercial applications. *Compos Struct* 2003; 62(3): 449-59.
8. Hojjati M, Safavi AV, Hoa SV. Design of domes for polymeric composite pressure vessels. *Compos Eng* 1995; 5(1): 51-9.
9. Koussios S, Bergsma OK. Analysis of Filament Wound Pressure Vessels Considering the Laminate Thickness Variation through the Meridional Direction. In: Proceedings of the 14th International Conference on Composite Materials. San Diego, CA, July 2002.
10. Kaw AK. *Mechanics of composite materials*, 2nd Edition, Boca Raton: CRC Press, 2006.
11. Zu L, Koussios S, Beukers A. Design of filament-wound circular toroidal hydrogen storage vessels based on non-geodesic fiber trajectories. *Int J Hydrogen Energy* 2010; 35(2): 660-70.
12. Park JS, Hong CS, Kim CG, Kim CU. Analysis of filament wound composite structures considering the change of winding angles through the thickness direction. *Compos Struct* 2002; 55(1):63-71.
13. Jorge Nocedal and Stephen J. Wright (2006). *Numerical Optimization*. Springer.
14. Rosenow MWK. Wind angle effects in the glass fiber-reinforced polyester filament wound pipes. *Comp Part A: Appl Sci Manuf* 1984; 15(2): 144-52.

Chapter 5

Geodesic-isotensoids

5.1 Introduction

The generalized optimality condition (see chapter 3) originates from the idea that the optimal pressure vessels are governed by the condition of equal shell strains and that the laminate strength can be completely utilized when the participating individual layers are aligned according to the principal stress direction. It has been proved that the optimal shape profile for a filament-wound dome is an isotensoid [1], on the basis of the netting theory [2]. The isotensoid, which provides the pressure vessel with the minimum weight and maximum carrying capacity, implies that all the fibers undergo uniform tension along their length. It can be designed in such a way that the principal stresses are carried only by the fibers of the laminate [3-5]. The solution may be regarded as optimal since it guarantees uniform stress distribution, minimum vessel weight and maximum occupation of the fiber strength.

The design of filament wound pressure vessels must take full account of the stress field as well as the material properties. Constraints imposed by the manufacturing process need to be respected, and the geometry that may restrict the structural efficiency must be properly determined. The netting-based optimal design and fiber stability analysis for circular toroidal pressure vessels have been carried out in chapter 4. However, one of the shortcomings of the application of circular cross sections to toroids is that the tensile strength of the filaments cannot be completely utilized, because the structural efficiency of a toroidal pressure vessel is entirely governed by the cross-sectional shape. Previous investigations merely considered the architecture of reinforcement layers, but overlooked the design of adapted cross-sectional shapes (i.e. meridian profiles) for toroids. It is thus desirable to obtain the most efficient cross-sectional shapes for these structures. A new possibility to improve the performance of

Chapter 5

toroidal vessels has been offered by Koussios et al. [6, 7] in which a novel configuration combining isotenoids with toroids is developed.

With the aid of the netting theory and geodesic winding law, in this chapter we outline the governing equation for determining geodesic-isotenoids and its feasible intervals. Depending on the magnitude of the axial forces as related to the internal pressure, various geodesic-isotenoid meridian shapes can be obtained. The cross-sectional shapes of isotenoid toroids are derived, leading to constant fiber stress throughout the whole torus. The influence of the theoretically required axial load on the isotenoid meridian shape to close it is also evaluated. The calculations and comparisons of cross-sectional shapes and structural masses of circular and isotenoid toroids are carried out to indicate that isotenoid toroids form a preferable alternative for the design of toroidal structures.

5.2 Geodesic-isotenoid Domes

5.2.1 Geometry and governing equations

The domes can represent the general class of shells of revolution. The geometry and applied loads of a dome meridian is schematized in Fig. 5.1. R and r_0 are the radius of the equator and the radius of the polar opening, respectively; p is a uniformly distributed internal pressure and A is an externally applied axial line load. $\mathbf{S}(\theta, z)$ represents the vector of a generic shell of revolution in polar coordinates, given by:

$$\mathbf{S}(\theta, z) = \{r(z) \cos \theta, r(z) \sin \theta, z\} \quad (5.1)$$

where θ denotes the angular coordinate in parallel direction, while r and z stand for the radial and axial distance.

Under an internal pressure p and an A , the axial equilibrium of the shell is given by:

$$A + \pi r^2 p = 2\pi r N_\varphi / \sqrt{1+r'^2} \quad (5.2)$$

The shell force N_φ can be obtained from equation (5.2):

$$N_\varphi = \left(\frac{A}{2\pi r} + \frac{pr}{2} \right) \sqrt{1+r'^2} \quad (5.3)$$

According to the netting theory, equation (3.51) for obtaining the fiber stress can reduce to:

$$\sigma = \frac{N_\varphi}{t \cos^2 \alpha} \quad (5.4)$$

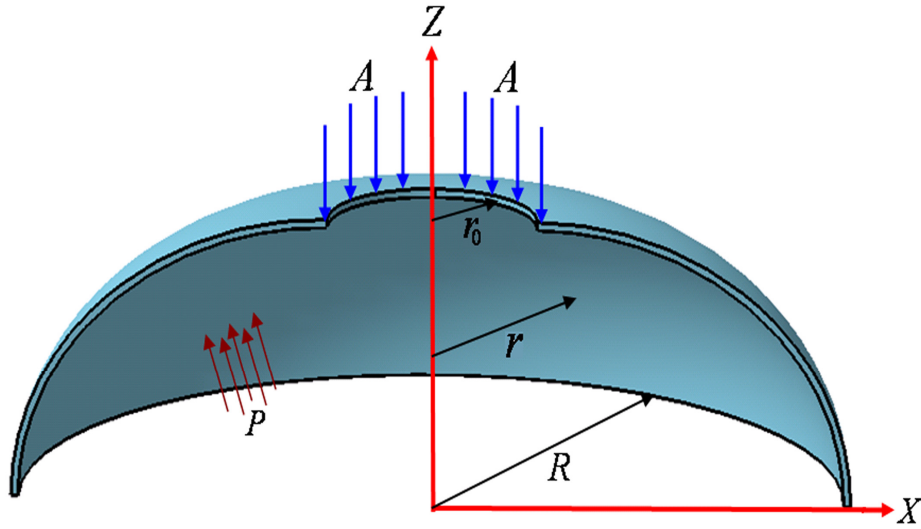


Fig. 5.1: Loads and geometry of an isotensoidal meridian

After substituting equation (5.3) into (5.4), the fiber stress at any point can be expressed as:

$$\sigma = \frac{\left(\frac{A}{2\pi r} + \frac{pr}{2}\right)\sqrt{1+r'^2}}{t \cos^2 \alpha} \quad (5.5)$$

Considering the geometrical condition at the equator ($r = R$, $r' = 0$), the fiber stress at the equator is given by:

$$\sigma_0 = \frac{\left(\frac{A}{2\pi R} + \frac{pR}{2}\right)}{t_0 \cos^2 \alpha_0} \quad (5.6)$$

The aim of the isotensoid design is to determine the meridian profile providing equal fiber tension everywhere. To achieve this goal, the fiber stress at any point should be equal to that at the equator. Thus we have:

$$\frac{\left(\frac{A}{2\pi r} + \frac{pr}{2}\right)\sqrt{1+r'^2}}{t \cos^2 \alpha} = \frac{\left(\frac{A}{2\pi R} + \frac{pR}{2}\right)}{t_0 \cos^2 \alpha_0} \quad (5.7)$$

Recalling equation (4.14) and using the same assumption [8], the thickness distribution along the meridional direction is given by:

$$\frac{t}{t_0} = \frac{R}{r} \cdot \frac{\cos \alpha_0}{\cos \alpha} \quad (5.8)$$

We consider here the geodesic condition (2.76) in which the Clairaut's equation is satisfied:

$$r \sin \alpha = r_0 \quad (5.9)$$

Chapter 5

To obtain a system of generalized governing equations that adapt to arbitrary geometry and internal pressure load, the major geometric and load parameters are normalized using appropriate non-dimensional scales:

$$\rho = \frac{r}{R}, \quad \zeta = \frac{z}{R}, \quad a = \frac{A}{\pi \rho R^2} \quad (5.10)$$

Substitution of equations (5.8), (5.9) and (5.10) into (5.7) leads, after expressing the winding angle in terms of ρ and ρ_0 , to:

$$\rho'^2 \rho^2 (a + \rho^2)^2 (1 - \rho_0^2) = (a + 1)^2 (\rho^2 - \rho_0^2) - \rho^2 (a + \rho^2)^2 (1 - \rho_0^2) \quad (5.11)$$

The differential equation for describing the meridian profile thus becomes:

$$\rho' = \sqrt{\frac{(a + 1)^2 (\rho^2 - \rho_0^2)}{\rho^2 (a + \rho^2)^2 (1 - \rho_0^2)} - 1} \quad (5.12)$$

The above governing equation provides the shapes of isotensoid meridian profiles for various $\{a, \rho_0\}$ values. For a given dimensionless opening radius ρ_0 , the resulting meridian profile will strongly depend on the a -value. The $\{a, \rho_0\}$ -parameter set is able to completely determine the cross-sectional shapes of the isotensoids. Depending on the magnitude of the axial forces as related to the internal pressure, several isotensoid meridian profiles ($\rho_0 = 0.4$) are obtained (see Fig. 5.2).

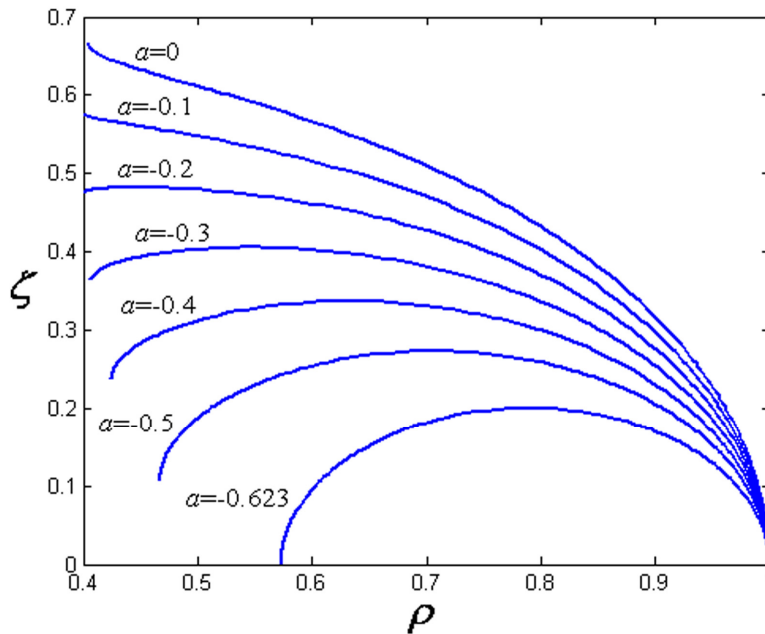


Fig. 5.2: Influence of the axial force on the resulting isotensoid meridian profile ($\rho_0 = 0.4$)

5.2.2 Feasible intervals of governing equation

The governing equation (5.12) can be rewritten as:

$$\rho' = \sqrt{\frac{(1-\rho^2)[(1-\rho_0^2)\rho^4 + (1-\rho_0^2)(2a+1)\rho^2 - (a+1)^2\rho_0^2]}{\rho^2(a+\rho^2)^2(1-\rho_0^2)}} \quad (5.13)$$

Setting the both sides of equation (5.13) equal to zero, e.g. $\rho'=0$, gives two pairs of real and one pair of imaginary roots:

$$\rho_{1,2} = \pm 1, \quad \rho_{3,4} = \pm \sqrt{-a - \frac{1}{2} + \frac{1}{2} \sqrt{\frac{(2a+1)^2 + (4a+3)\rho_0^2}{1-\rho_0^2}}}, \quad (\text{Real roots}) \quad (5.14)$$

$$\rho_{5,6} = \pm \sqrt{-a - \frac{1}{2} - \frac{1}{2} \sqrt{\frac{(2a+1)^2 + (4a+3)\rho_0^2}{1-\rho_0^2}}} \cdot i \quad (\text{Imaginary roots}) \quad (5.15)$$

By selecting the minimum and maximum real roots by ρ_{\min} and ρ_{\max} , the biggest and smallest radii of the geodesic-isotensoids are:

$$\rho_{\min} = \sqrt{-a - \frac{1}{2} + \frac{1}{2} \sqrt{\frac{(2a+1)^2 + (4a+3)\rho_0^2}{1-\rho_0^2}}}, \quad \rho_{\max} = 1 \quad (5.16)$$

equation (5.12) is therefore only valid for the interval $[\rho_{\min}, 1]$. The minimum and maximum real roots define the interval where integration of equation (5.12) is possible. Although the maximum real root $\rho_{\max} = 1$ does provide exact value for the radius at the equator, the minimum root (ρ_{\min}) does in general not coincide with the opening radius at the pole. It should be noted here that ρ_0 only mathematically represents the radius of the polar opening and the real polar radius ρ_{\min} is generally bigger than ρ_0 because the argument contained in the square root of equation (5.13) nullifies before ρ can reduce to ρ_0 . In this case the winding angle at the poles becomes less than 90° and decreases as the magnitude of the axial force a increases. In practice however, in order to ensure a smooth transition of one wound circuit to the other, the winding angle should exactly reach 90° when passing the poles. This implies that ρ_{\min} should be equal to ρ_0 in accordance with the Clairaut's equation. Substitution of this requirement together with $\rho_{\min}'=0$ into equation (5.11), leads to:

$$a = -\rho_0^2 \quad (5.17)$$

This result can alternatively be obtained by setting N_ϕ (equation (5.2)) equal to 0. Hence, one should keep the a -parameter as close as possible to $-\rho_0^2$.

Furthermore, we indicate here that the $\{a, \rho_0\}$ -combination is limited according to the following statement, dictated by the numerator contained in the root argument of equation

Chapter 5

(5.13):

$$(1 - \rho_0^2)\rho^4 + (1 - \rho_0^2)(2a + 1)\rho^2 - (a + 1)^2 \rho_0^2 \geq 0 \quad (5.18)$$

Since the left-hand side expression of equation (5.18) is less than 0 at $\rho=0$, its value has to be more than 0 at $\rho = 1$, in order to make the above inequality valid before ρ rises to 1. Thus we have:

$$(a^2 + 4a + 3)\rho_0^2 < 2(a + 1) \quad (5.19)$$

Another important limitation on a is that the right-hand side of equation (5.2) should be more than 0, otherwise the fiber stress at the equator will become compressive (physically impossible for isotensoids). This limitation leads to:

$$a > -1 \quad (5.20)$$

Then the following relation holds true:

$$(a^2 + 4a + 3) > 0 \quad (5.21)$$

equation (5.19) can thus be rewritten as:

$$\rho_0 < \sqrt{\frac{2(a + 1)}{a^2 + 4a + 3}} \quad (5.22)$$

The result is depicted in Fig. 5.3, where the feasible $\{a, \rho_0\}$ field is dashed.

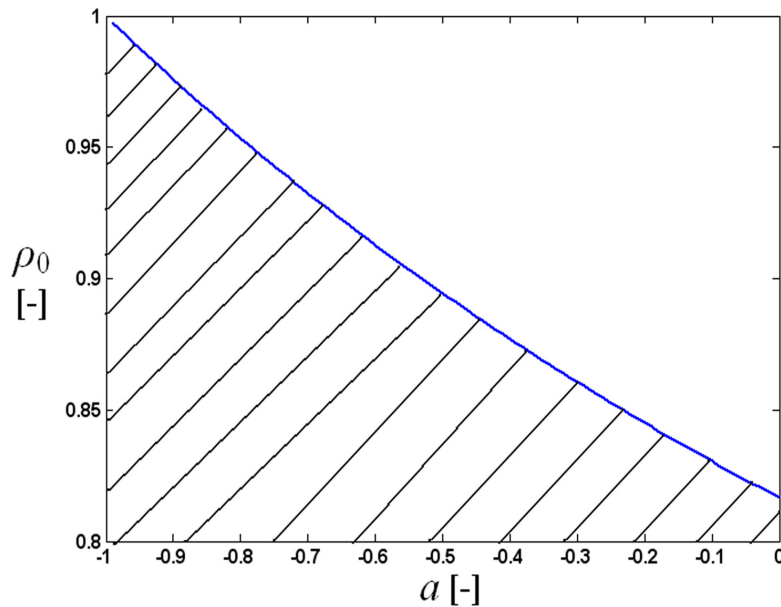


Fig. 5.3: Feasible $\{a, \rho_0\}$ -field (shaded area)

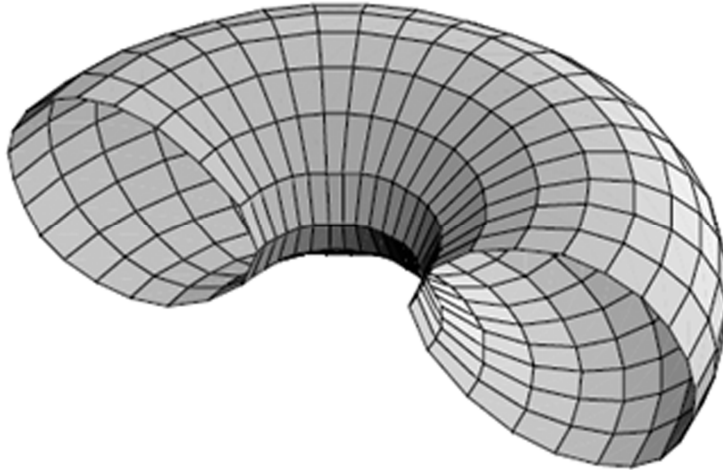


Fig. 5.4: Cross-sectional shape for a toroidal pressure vessel [6, 7]

5.3 Geodesic-isotensoid Toroids

A toroidal pressure vessel can be regarded as a particular form of the shell of revolution, in which the revolved meridian profile is a closed curve (Fig. 5.4 [6, 7], not necessarily circular). In this section the differences of geometry and performance between circular and geodesic-isotensoid toroids are outlined to demonstrate the favorable properties of toroids with isotensoid-based cross sections.

5.3.1 Cross-sectional shapes

In Section 5.1, several isotensoid dome profiles are obtained using various magnitude of dimensionless axial force (recall Fig. 5.2). When the axial force is sufficiently large for forcing the resulting meridian profile to become closed, the shape of the isotensoid becomes a toroid. Note that the tensional forces of the rovings that proceed from the polar area towards the equator replace here the theoretically required external axial force A , which is applied on the polar cap. The resulting meridian profiles, i.e. cross-sections of isotensoid toroids for different polar openings, are shown in Fig. 5.5. The resulting cross-sectional shape is quasi-elliptic. The isotensoid toroid belongs to the class of doubly curved surfaces, and is an interesting alternative for spaces having limited height.

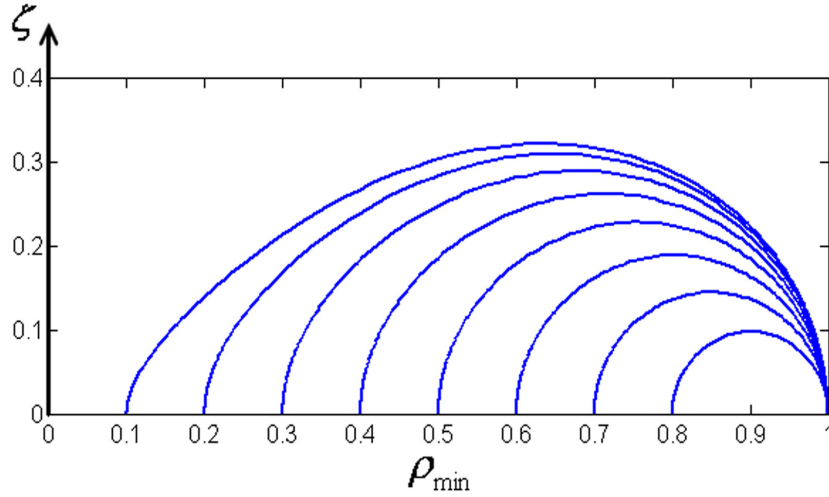


Fig. 5.5: Resulting cross sectional shapes for iso-toroids with various ρ_0

5.3.2 Evaluation and comparison

The dimensionless internal volume and structural mass are defined as follows:

$$\bar{V} = V / 2R^3, \quad \bar{M} = M \cdot \frac{X_T}{2\gamma p \pi R^3} \quad (5.23)$$

The dimensionless volume of an isotensoid toroid is then given by:

$$\bar{V}_{iso} = \int_0^{\delta_m} \pi \rho^2 d\zeta \quad (5.24)$$

where ζ_m is the maximum height of the meridian profile, at which the first derivative of ρ tends to infinity. When setting the denominator of equation (5.13) equal to zero, the radial coordinate ρ_m of the maximum point can be calculated as follows:

$$a + \rho_m^2 = 0 \Rightarrow \rho_m = \sqrt{-a} \quad \text{where } a < 0 \quad (5.25)$$

With the aid of *Runge-Kutta* formulae, ζ_m can be further calculated by equation (5.13):

$$\zeta_m = \zeta(\rho) \Big|_{\rho=\sqrt{-a}} \quad (5.26)$$

The structural mass can be calculated by:

$$M_{iso} = \int_0^{\zeta_m} 4\pi r t \sqrt{1+r'^2} dz \quad (5.27)$$

Solving equation (5.9) for the winding angle α and substituting the results into equation (5.5), the thickness distribution of isotensoid toroids is obtained by:

$$t = \frac{\left(\frac{A}{2\pi r} + \frac{pr}{2}\right) \sqrt{1+r'^2}}{X_T (1-r_0^2/r^2)} \quad (5.28)$$

By substitution of equation (5.28) into (5.27) together with equations (5.10) and (5.23), the mass (in dimensionless form) is given by:

$$\overline{M}_{iso} = \int_0^{\zeta_m} \frac{\rho^2(\rho^2 + a)(\rho'^2 + 1)}{\rho^2 - \rho_0^2} d\zeta \quad (5.29)$$

The dimensionless internal volume and mass of a circular toroid are given by the expressions [9]:

$$\overline{V}_c = \frac{\pi^2(1 + \rho_0)(1 - \rho_0)^2}{8} \quad (5.30)$$

$$\overline{M}_c = \frac{(1 - \rho_0)^2 \sqrt{(3 + \rho_0)(5 + \rho_0)}}{8} \int_0^\pi \frac{1}{\sin \alpha} d\varphi \quad (5.31)$$

where ρ_0 is the relative bend radius of torus.

To equalize the internal volume of an isotensoid toroid with that of a circular one, the cross-sectional shape of an isotensoid toroid is obtained using *Newton-Raphson* method [10]. When a relative bend radius ρ_0 is assigned, the minimum radial distance ρ_{min} of an isotensoid toroid is calculated by setting equation (5.24) equal to equation (5.30). The relations for the relative bend radii of equal-volume isotensoid and circular toroids are shown in Fig.5.6.

Fig. 5.7 displays the distribution of internal volumes of isotensoid and circular toroids respectively, corresponding to various relative bend radii. The results indicate that the internal volumes of circular and isotensoid toroids can be equal only if the relative bend radius of the circular toroid is above 0.29.

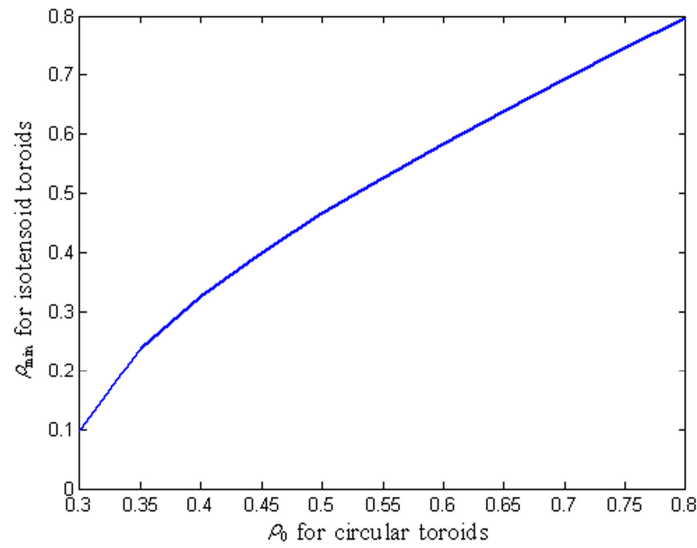


Fig. 5.6: Relative bend radii for isotensoid and circular toroids at equal volumes

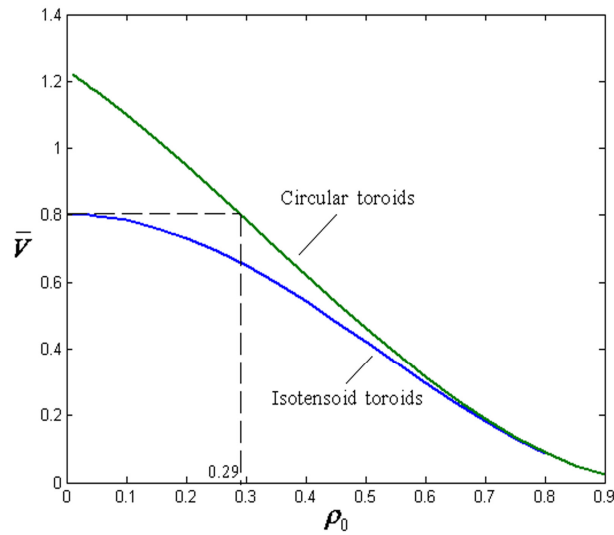
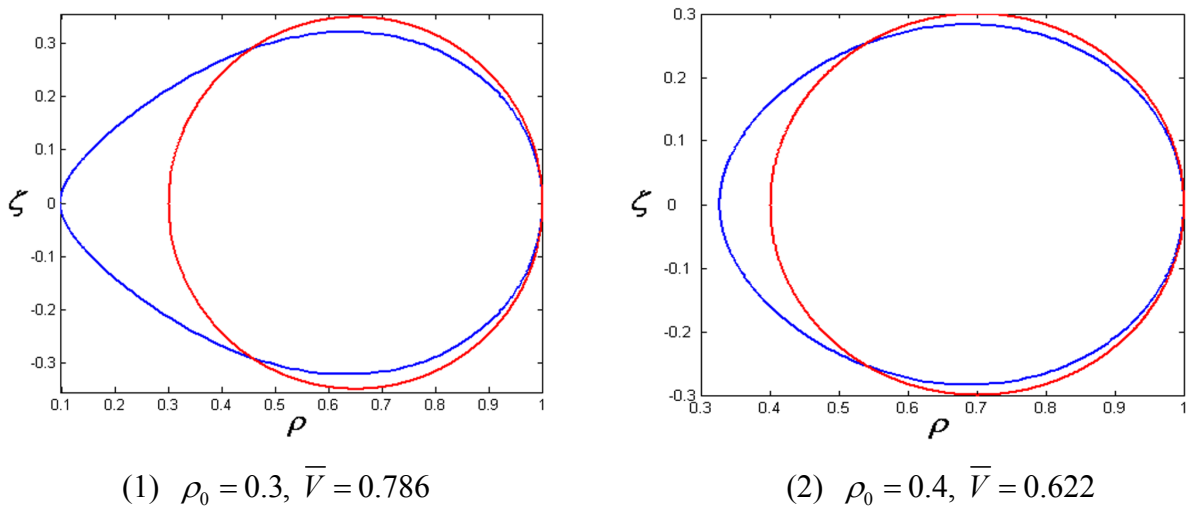
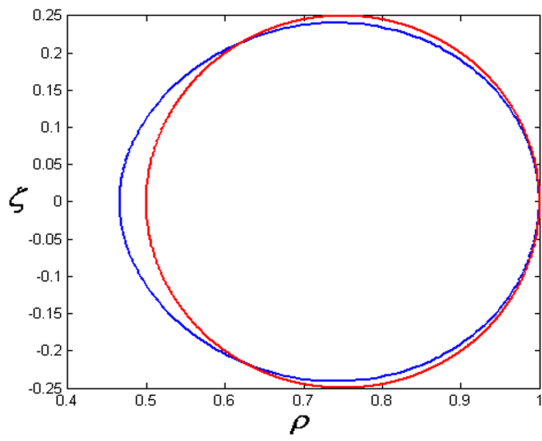


Fig. 5.7: Internal volumes of isotensoid and circular toroids with ρ_0

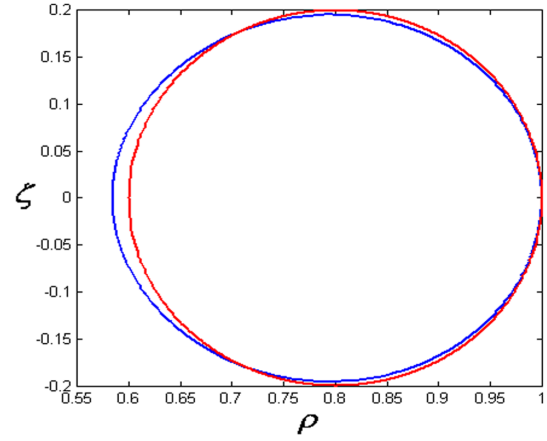
Fig. 5.8 depicts the cross-sectional shapes of isotensoid and circular toroids at equal volumes. It is shown that the aspect ratio of the isotensoid meridian profile is always lower than that of the circular one and increases with the raise of relative bend radius. Additionally, the isotensoid-based cross-sectional shape becomes identical with the circular one at small internal volumes and large bend radii.

The total mass of circular and isotensoid toroids is respectively calculated at equal volumes. Fig. 5.9 illustrates the comparison of dimensionless mass of isotensoid and circular toroids, as a function of internal volume. The results show that the isotensoid toroid is consistently lighter than the circular one at any equal volume and internal pressure. The mass values of isotensoid toroids show about 30% maximal reduction compared with circular toroids. It is therefore desirable to employ isotensoid-based cross sections instead of circular toroids for toroidal pressure vessels.

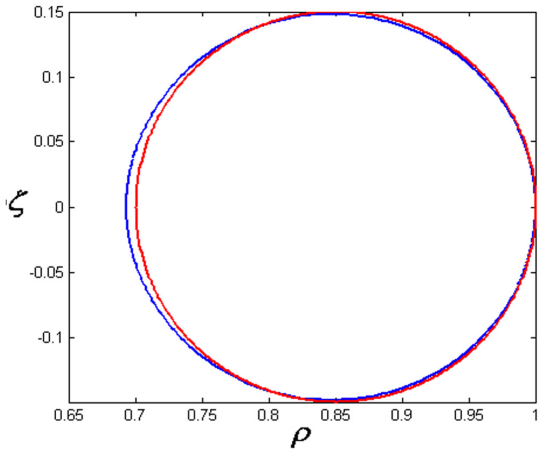




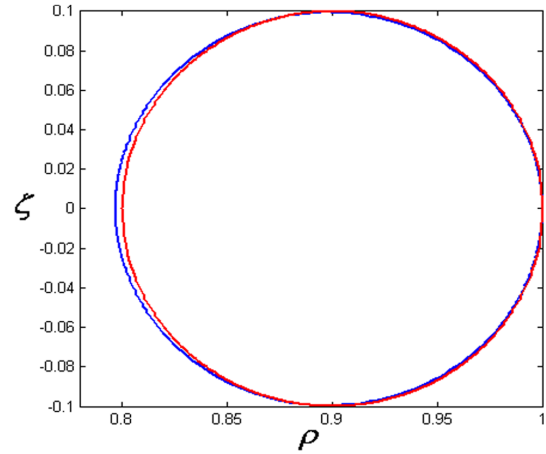
(3) $\rho_0 = 0.5, \bar{V} = 0.463$



(4) $\rho_0 = 0.6, \bar{V} = 0.316$



(5) $\rho_0 = 0.7, \bar{V} = 0.189$



(6) $\rho_0 = 0.8, \bar{V} = 0.089$

Fig. 5.8: Cross-sectional shapes of the isotensoid and circular toroids at equal volumes

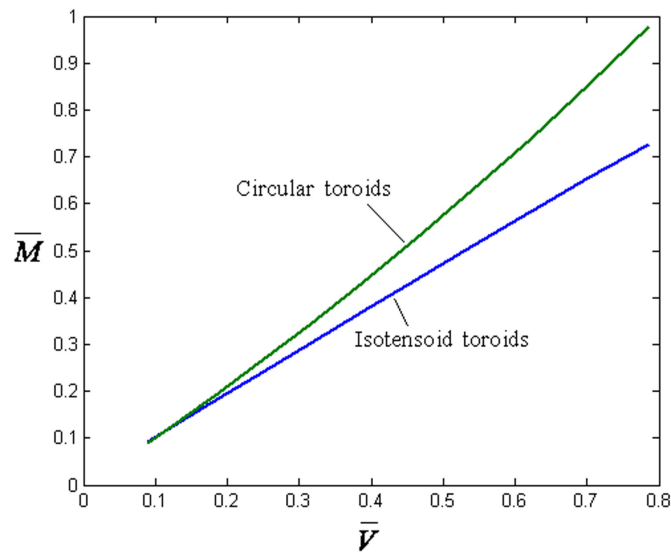


Fig. 5.9: Dimensionless masses of isotensoid and circular toroids at equal volumes

5.4 Conclusions

The main goal of this chapter is to provide a design method for determining the cross-sectional shapes of isotenoid toroids, and to evaluate the effect of the isotenoid design on the geometry and performance of toroids. The results indicate that the isotenoid meridian curve can only become closed if the axial load reaches a sufficient value. The cross-sectional shapes of isotenoid toroids have been determined for various internal volumes, and the structural masses of circular and isotenoid toroids have been calculated in order to demonstrate the preferable performance and robustness of isotenoid toroids. It is concluded that the isotenoid toroid has a significantly lower weight and a lower aspect ratio than the circular one at any equal volume and internal pressure. Therefore the structural performance and the conformability to limited-height storage space of filament-wound toroidal pressure vessels can be remarkably improved using the isotenoid-based cross sections.

References

1. Zickel, J. Isotenoid pressure vessels. *ARS Journal* 1962; 32: 950-951.
2. Rosato DV, Grove CS. *Filament winding: its development, manufacture, applications, and design*. New York: Interscience, 1964.
3. Vasiliev VV, Krikanov AA. New generation of filament-wound composite pressure vessels for commercial applications. *Compos Struct* 2003; 62: 449–59.
4. De Jong Th. *A theory of filament wound pressure vessels*. Report LR-379. Structures and materials laboratory, Faculty of Aerospace Engineering, Delft: Delft University of Technology; 1983.
5. Hojjati M, Safavi AV, Hoa SV. Design of domes for polymeric composite pressure vessels. *Compos Eng* 1995; 5: 51–9.
6. Koussios S. *Filament Winding: A Unified Approach*. PhD Thesis report, Design and Production of Composite Structures Group, Faculty of Aerospace Engineering, Delft University of Technology, Delft, 2004.
7. Koussios S, Beukers A. “Composing composites: a paradigm of reversed design”. *J. Design Research*, 2007; 5(3): 302-316.
8. Park JS, Hong CS, Kim CG, Kim CU. Analysis of filament wound composite structures considering the change of winding angles through the thickness direction. *Compos Struct* 2002; 55(1):63-71.

9. Zu L, Koussios S, Beukers A. "Pattern design and optimization for filament wound toroidal pressure vessels". Proc. 23rd Annual Conference of the American Society for Composites, Memphis, TN, September 2008.
10. P. Deuffhard, Newton Methods for Nonlinear Problems. Affine Invariance and Adaptive Algorithms. Springer Series in Computational Mathematics, Vol. 35. Springer, Berlin, 2004.

Chapter 6

Non-geodesic-isotensoids

6.1 Introduction

A number of studies have been conducted on the design of isotensoid pressure vessels. de Jong [1] presented the geometry and structural properties for isotensoid pressure vessels with the aid of the continuum theory, in which the behavior of matrix in composites has been taken into account. Koussios et al. [2] evaluated the influence of the fiber bundle geometry and thickness build-up on the final performance of the isotensoid pressure vessel. Zu et al [3] determined the geodesic-isotensoid cross sectional shapes for toroidal pressure vessels. Marketos [4] presented the optimal geodesic trajectories in combination with the isotensoid meridian shape of the toroidal mandrel. Vasiliev et al. [5] investigated optimal fibrous structures and composite laminates of uniform strength by means of a parameter k that in fact expresses the degree of laminate orthotropy, and then derived the optimal profile shapes and fiber paths for isotensoid domes. Hojjati et al. [6] developed a technique to design the optimal dome profile, which depends on the ratio of the Young's modulus in longitudinal and transverse directions, based on the isotensoid condition. A key factor in their design and development process is the creation of equally stressed structures that are mainly based on the principle of geodesic winding. The geodesics we refer here represent the shortest paths connecting any two points on a continuous surface; these paths show great stability on a curved surface and are relatively easy to calculate with the Clariaut equation. However, as the geodesic path is entirely determined by the underlying meridian profile and the initial winding angle, their geometry combined with the tangential requirements on the polar area for fiber paths is certainly limiting the available design space [7, 8]. Typical examples of this restriction are the limit for creating isotensoid structures with unequal polar openings at both

Chapter 6

ends (Fig. 6.1), and the restriction for further improving the structural performance of isotenoid toroidal pressure vessels. The possibility appears now for applying non-geodesic trajectories instead of geodesics. In fact, a fiber must not necessarily be wound geodesically to be stable; non-geodesic trajectories can also be overwrapped by a certain deviation from the geodesic paths, counting on friction to keep the fiber in its predetermined position. While having enlarged design possibilities by using non-geodesics, the principle of constant fiber tension can still remain valid. It is therefore desirable to employ non-geodesic trajectories to enlarge the design space of isotenoid structures. Recent progress on such structures has been offered by Koussios et al. [9, 10] in which a method for determining the non-geodesic-isotenoid shapes is developed based on maximum-friction-utilizing non-geodesic trajectories.

The main goal of this chapter is to present the design approach for isotenoid domes having unequal polar openings, and to determine the cross-sectional shapes of non-geodesic-isotenoid toroids. In section 6.2, the system of differential equations that governs the non-geodesic-isotenoid meridians and related non-geodesic trajectories are derived based on the isotenoid condition. The dimensionless performance factor is employed to compare the structural performance of the geodesic and non-geodesic isotenoid domes. The meridian curve and roving trajectories must have C^1 and C^0 continuity when passing the equator, respectively. A root searching procedure with the aid of the *Newton* method [11] is applied to find a pair of slippage coefficients as related to both upper and lower domes. In addition, the simulations for the resulting domes with unequal opening and related non-geodesic trajectories are performed. Based upon the obtained non-geodesic-isotenoid domes, in section 6.3 the cross-sectional shapes of non-geodesic-isotenoid toroids are derived by forcing the non-geodesic isotenoid dome meridians to return to zero altitude and the resulting isotenoid shapes to become closed toroids. The influence of the magnitude of the axial load on the non-geodesic isotenoids, which forces the meridian curve to be closed, is also evaluated. The related winding angle distributions for various slippage coefficients are presented and compared to each other. Furthermore, the rates of performance improvement that the application of non-geodesics can gain, corresponding to various slippage coefficients, are also given.

6.2 Isotensoid Pressure Vessels with Unequal Polar Openings

6.2.1 Governing equations

The geometry of an isotensoid meridian with unequal polar openings is given in Fig. 6.1. The shapes for this class of structures are similar to oblate spheroids. The vessel here is regarded as the combination of two general isotensoid domes, i.e., part I and part II. r_1, r_2 are the polar radii of both domes. A schematic representation of a general dome profile is shown in Fig. 6.2. When rotated around the Z-axis, a shell of revolution is obtained. The basic input parameters are the internal pressure p , the axial load A (as applied on the dome opening) and the polar opening radius r_0 .

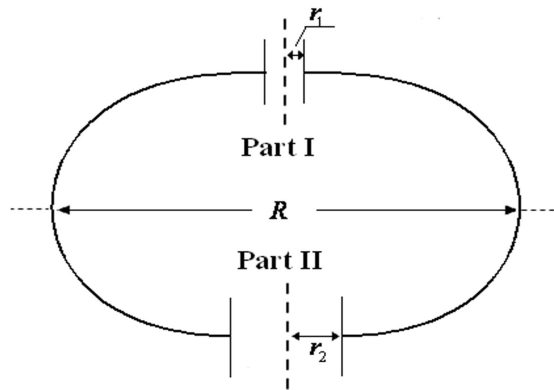


Fig. 6.1: Meridian profile of a pressure vessel with unequal polar openings

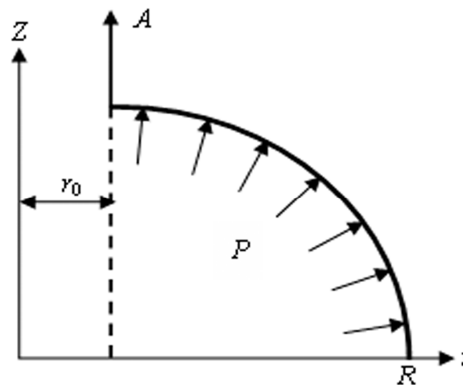


Fig. 6.2: Loads and geometry of a shell meridian

An elementary piece of a shell of revolution is here considered, as depicted in Fig. 6.3. The fiber trajectory placed on the surface is subjected to a longitudinal force F , a normal force per unit length f_n and a lateral force per unit length f_g . The static equilibrium of the forces in the

Chapter 6

direction perpendicular to the surface can be expressed as follows [9, 10]:

$$f_n R_n \Delta v = 2F \sin\left(\frac{\Delta v}{2}\right) \Rightarrow f_n \approx F \cdot \kappa_n \quad (6.1)$$

The lateral fiber force is generated by the friction between the fiber bundle and the supporting surface. Similarly to equation (6.1), for the calculation of the lateral force we have:

$$f_\mu R_g \Delta \omega = 2F \sin\left(\frac{\Delta \omega}{2}\right) \Rightarrow f_\mu \approx F \cdot \kappa_g \quad (6.2)$$

where R_g and R_n are the radii of geodesic and normal curvatures, respectively. When placing a roving band on the mandrel by the path of non-geodesics, a lateral force will be required to keep that roving in place.

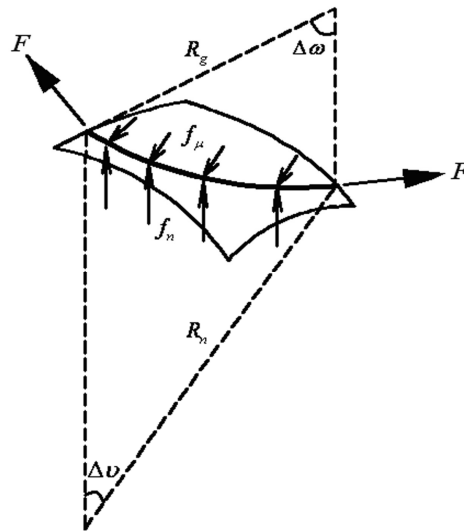


Fig. 6.3: Elementary fiber force equilibrium [9, 10]

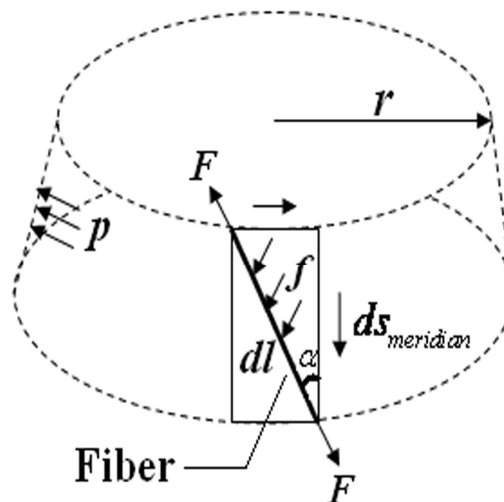


Fig. 6.4: An infinitesimal ring element

An infinitesimal ring element is shown in Fig. 6.4. The elementary piece must be in equilibrium with the forces generated by internal pressure. The shell under consideration is covered with N fiber bundles, where each of them generates a force F . Assuming that the resultant force per length unit from the supporting surface is f , the equilibrium of the forces can be given as:

$$Nf \cdot dl = p \cdot 2\pi r ds_{meridian} \quad (6.3)$$

f can be decomposed into f_n and f_g with the aid of equations (6.1), (6.2) and (2.21):

$$f = \sqrt{f_n^2 + f_g^2} = Fk_n \sqrt{1 + \lambda^2} \quad (6.4)$$

Substitution of equation (6.4) into (6.3) yields:

$$\frac{NF}{\pi P} = \frac{2r \cos \alpha}{k_n \sqrt{1 + \lambda^2}} \quad (6.5)$$

The isotensoid design principle is here used to determine the meridian profile. Therefore the fiber force F is constant along its entire length. Substitution of equation (2.71) into (6.5) leads, after some arrangements, to the second derivative of the meridian profile:

$$z'' = - \frac{(1 + z'^2)(S \cdot z' \cdot \tan^2 \alpha \cdot \sqrt{1 + \lambda^2} + 2r^2 \cdot \sec \alpha \cdot \sqrt{1 + z'^2})}{S \cdot r \cdot \sqrt{1 + \lambda^2}} \quad (6.6)$$

in which $S = NF / \pi p$. Plugging equation (6.6) into non-geodesic equation (2.75) leads to:

$$\frac{d\alpha}{dr} = - \frac{\tan \alpha}{r} - \frac{2\lambda r \sqrt{1 + z'^2}}{S \sqrt{1 + \lambda^2}} \quad (6.7)$$

The simultaneous solution of the system of differential equations (6.6) and (6.7) will finally provide the isotensoid meridians and related non-geodesic trajectories. Fig. 6.5 presents a collection of meridian profiles determined using the present method, corresponding to various slippage coefficients ranging from 0 to 0.4.

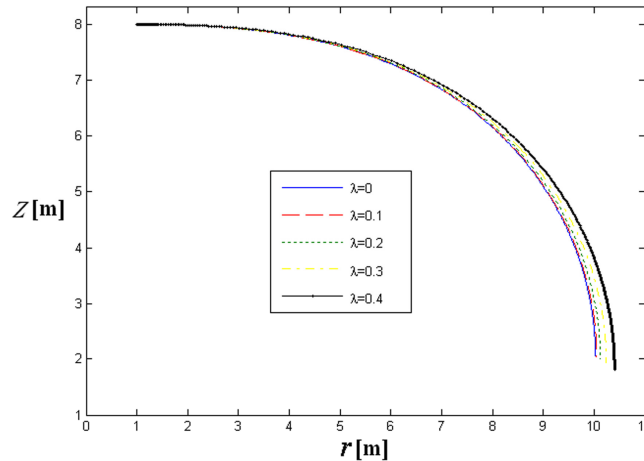


Fig. 6.5: Isotensoid meridian profiles for various slippage coefficients λ

6.2.2 Structural performance

The performance factor $PF = pV/W$ is used as an index for rating pressure vessels, where P , V and W are the burst pressure, the internal volume and the shell weight, respectively. Accordingly, the performance factor of a dome is given by:

$$PF = \frac{p \cdot \int_R^{r_0} \pi r^2 z' dr}{\gamma \cdot \int_R^{r_0} 2\pi r t \sqrt{1+r'^2} z' dr} \quad (6.8)$$

where γ is the specific weight of the used material. The dimensionless factor is defined as:

$$\overline{PF} = PF \cdot \frac{\gamma}{X_t} \quad (6.9)$$

where X_t is the tensile strength of the laminate in the fiber direction. Based on the netting theory, the filaments are assumed to carry all the loads. Thus the laminate thickness of the dome shell can be calculated by:

$$t = \frac{pS}{2X_t r \cos \alpha} \quad (6.10)$$

where α can be determined by the simultaneous solution of the differential equations (6.6) and (6.7). We introduce:

$$\rho = \frac{r}{r_0}, \quad \zeta = \frac{z}{r_0}, \quad q = \frac{NF}{\pi p r_0^2} \quad (6.11)$$

Substituting equation (6.10) and (6.11) into (6.8) and plugging the dimensionless parameters shown in equation (6.9), we obtain:

$$\overline{PF} = - \frac{\int_1^{\rho_{eq}} \rho^2 \zeta' d\rho}{\int_1^{\rho_{eq}} \frac{q \sqrt{1+\zeta'^2}}{\cos \alpha} d\rho} \quad (6.12)$$

To evaluate the influence of the slippage coefficients on the structural performance of non-geodesics-based isotensoids, the dimensionless performance factors obtained using the present method with the slippage coefficients ranging from 0 to 0.5, are shown in Fig. 6.6. The results prove that the non-geodesics-based isotensoid dome has better performance than the geodesic-isotensoid one. It is also indicate that the structural efficiency of the dome can be considerably improved with increasing slippage coefficients. The performance factor of the isotensoid dome at $\lambda = 0.5$ shows about 10.88% improvement compared with that of the geodesic-isotensoid. It is accordingly desirable to employ non-geodesic trajectories with allowable slippage coefficients for the design and production of isotensoid domes.

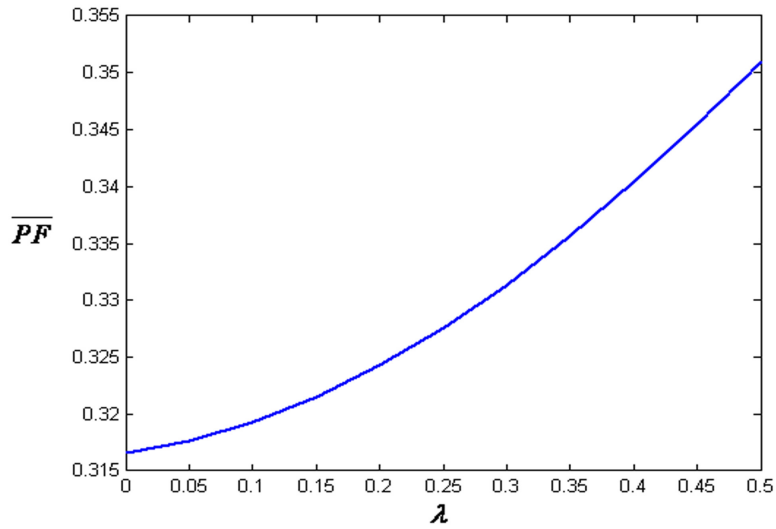


Fig. 6.6: Variation of dimensionless performance factors with slippage coefficients λ

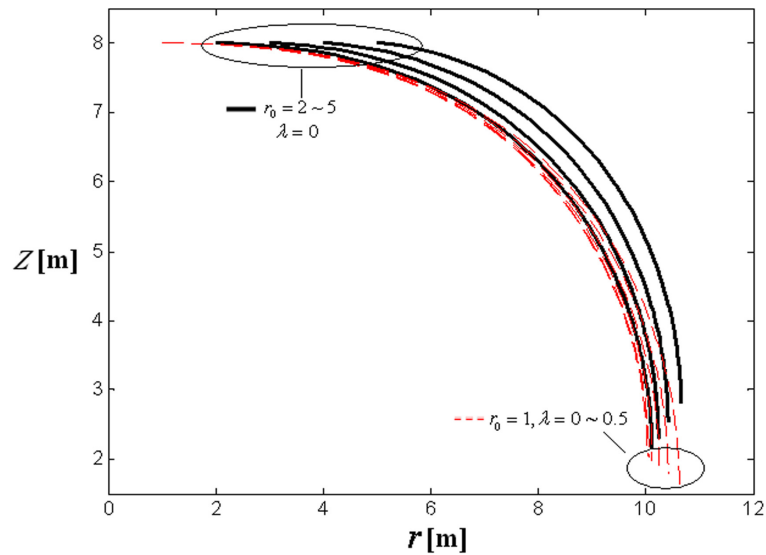


Fig. 6.7: Meridian profiles corresponding to various $\{r_0, \lambda\}$ -combinations

6.2.3 Feasibility and design approach

To verify the feasibility of the present method to create isotensoid pressure vessels with unequal polar openings, we present the isotensoid meridian profiles with various slippage coefficients for r_0 range [1, 5] (Fig. 6.7). It is shown that the equator radius R has a slight change with a large increase in the polar radius r_0 . Therefore the equators of the domes with different polar openings can be perfectly matched based on the selection of slippage coefficients for both domes.

A key factor in this design is the determination of adapted slippage coefficients and their

Chapter 6

corresponding isotenoid meridians between unequal polar openings at both ends. The filament winding process requires perfectly tangent placement of the fibers when passing the polar areas of the dome structure, to make continuous to a next wound circuit. Therefore, by application of a non-geodesic trajectory, this requirement must be satisfied. The winding angle at the polar area should reach 90° . Moreover, the first derivative of the $z(r)$ function at the polar area, which reflects on the manufactured meridian shape, must be equal to zero (Fig.6.2). To ensure C^1 continuity of the meridian curve when passing the equator, the radii and the derivatives of the meridian curves at the equators of part I and part II (see Fig. 6.1) must have the same value. Thus the following geometrical constraints can be defined:

$$R_{part1} = R_{part2} = R, \quad \left. \frac{dr_{part1}}{dz} \right|_{r=R} = \left. \frac{dr_{part2}}{dz} \right|_{r=R} = 0 \quad (6.13)$$

In addition, the winding angle at both equators must be equal, that is:

$$\alpha_{eq1} = \alpha_{eq2} \quad (6.14)$$

We assume here that the slippage coefficient is given by a piecewise function for both upper and lower dome parts:

$$\begin{cases} \lambda \equiv \lambda_1 & \text{Part I} \\ \lambda \equiv \lambda_2 & \text{Part II} \end{cases} \quad (6.15)$$

For given S and both polar radii r_0 , the solution procedure is outlined in the flow chart (see Fig. 6.8). The goal is now to provide a pair of slippage coefficients (λ_1, λ_2) that ensure winding angle of 90° at exactly both polar openings. The design variable vector (λ_1, λ_2) is determined up to a desired level of accuracy ε and must belong to a predetermined feasible friction interval $\{-\mu, \mu\}$. It should be noted here that the slippage coefficient λ could be negative as well [12]. Recalling the non-slippage condition λ should meet:

$$|\lambda| \leq \mu_{\max} \quad (6.16)$$

6.2.4 Results and discussion

The present design method is applied to determine an isotenoid pressure vessel with $r_0 = 1$ and $r_0 = 2$. A pair of slippage coefficients (λ_1, λ_2) for both dome parts is taken as the design variables. The initial set of values here consists of $Z_0 = 8$ (arbitrary value), $Z_0' = 0$ and $\alpha_0 = 90^\circ$. In the numerical solution procedure, however, a slightly reduced initial value for α is rather desirable (herein $\alpha = 0.4999\pi$), in order to avoid infinity during the solution procedure of the differential equations. After application of the calculation routine (Fig. 6.8), we find two slippage coefficients for both dome parts, $\lambda_1 = -0.228$ and $\lambda_2 = -0.146$. Additionally, substitute

the resulting λ_1 and λ_2 into the system of equations (6.6) and (6.7) and obtain the equator radii for both parts as $R = 10.154$. Fig. 6.9 illustrates the meridian profiles of non-geodesics-based isotensoid domes with $r_1 = 1$ and $r_2 = 2$. In Fig. 6.10, a comparison of non-geodesic trajectories on both dome parts is provided, in terms of winding angle developments along the radial direction. The results show that the radii and winding angles obtained using the present method, are matched exactly at the equators of both dome parts.

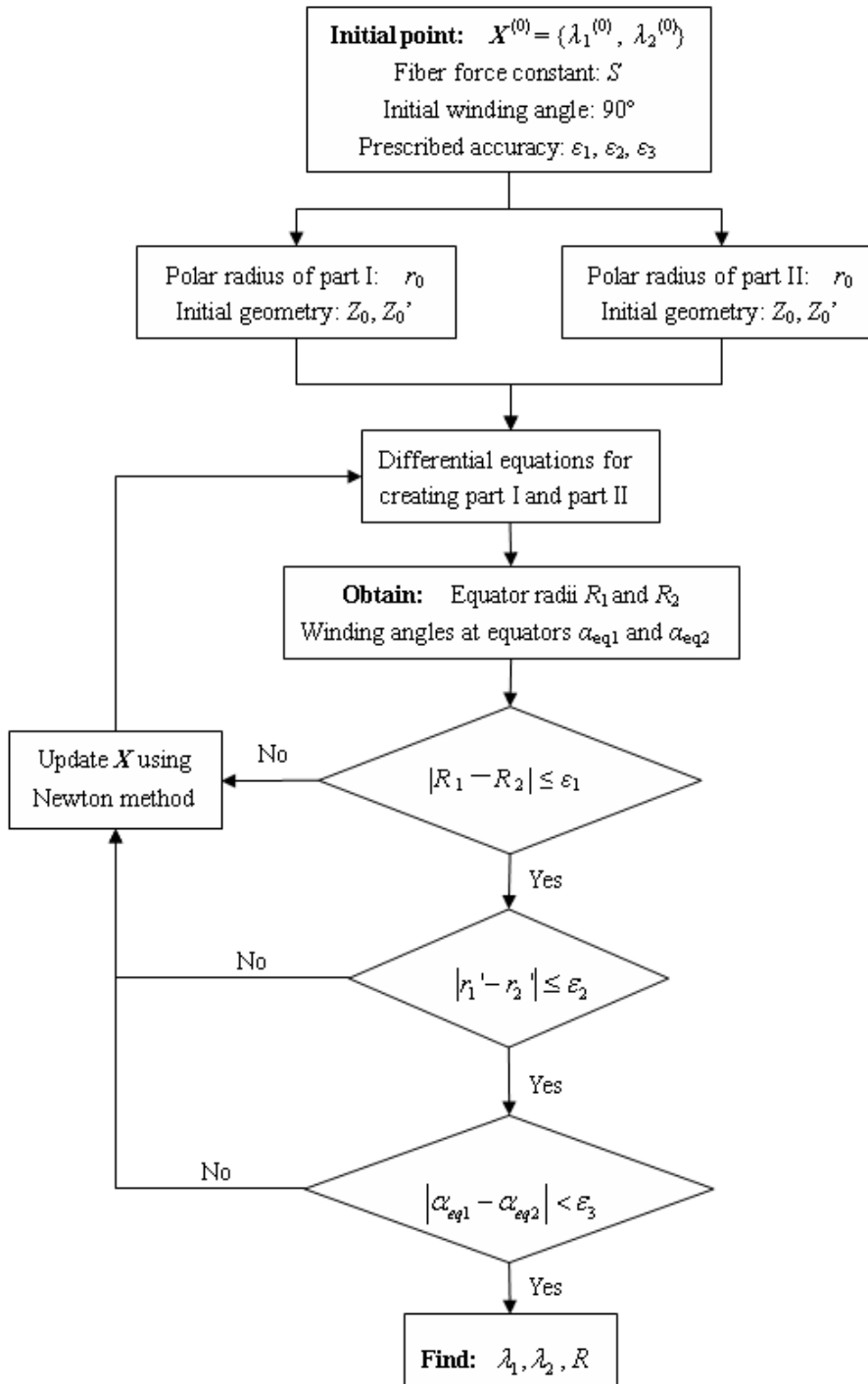


Fig. 6.8: Design procedure for searching the slippage coefficients

Chapter 6

The sectional 3D views for the isotensoid pressure vessel designed using the present method, are given in Fig. 6.11. Furthermore, Fig. 6.12 shows the corresponding non-geodesic trajectories that proceed from one polar area towards the other. It is shown that the non-geodesic trajectory obtained using the present method satisfies the winding conditions perfectly. Simulation results also conclude that the present method is able to successfully create an isotensoid structure with unequal polar openings.

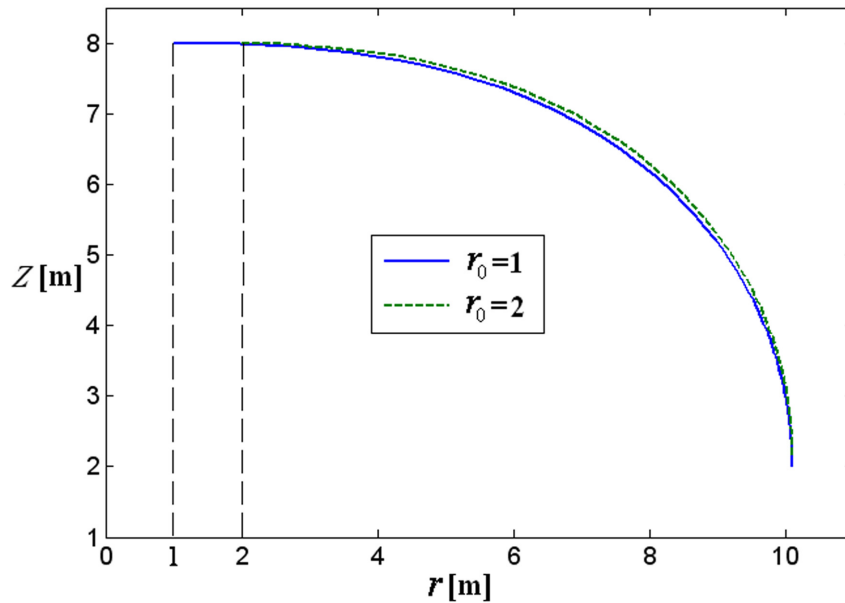


Fig. 6.9: Isotensoid meridian profiles for $r_0=1$ and $r_0=2$

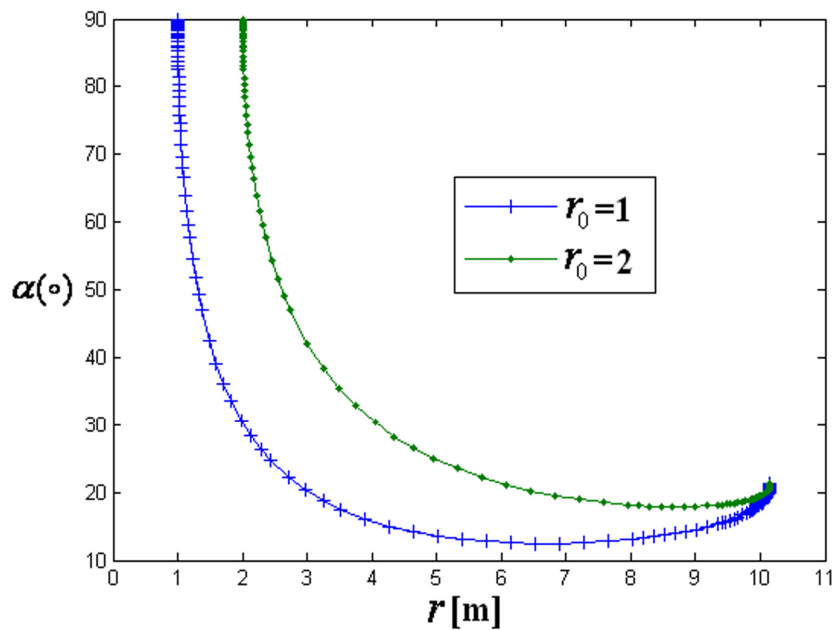


Fig. 6.10: Winding angle propagations for $r_0=1$ and $r_0=2$



Fig. 6.11: Sectional 3D profile for the isotensoids obtained using the present method

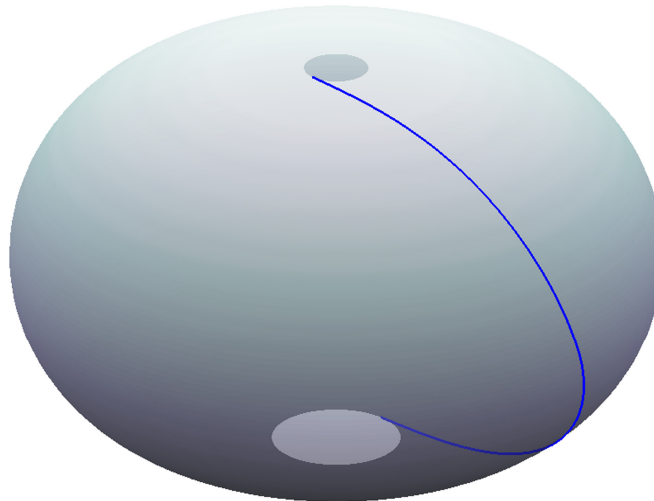


Fig. 6.12: Non-geodesic trajectories on the isotensoids obtained using the present method

6.3 Non-geodesic-isotensoid Toroids

6.3.1 Governing equations

In this section we provide the design solution to determine the cross-sectional shapes of isotensoidal toroids based on non-geodesic trajectories. Pressure vessels are governed by the condition of equal shell strains (principal stress design), which results in the complete occupation of the fiber strength and the participating layers aligned in the direction of the maximum principal stress.

Chapter 6

If we remove the geodesic condition (5.9) in subsection 5.2 for geodesic-isotensoids, substitution of only equations (5.8) and (5.10) into (5.7) will lead to the basic equation for non-geodesic-isotensoids:

$$\rho' = -\frac{\sqrt{C^2 \cdot \cos^2 \alpha - (a + \rho^2)^2}}{a + \rho^2} \quad (6.17)$$

where:

$$C = (a + 1) / \cos \alpha_0 \quad (6.18)$$

This design considers the non-geodesic equation for which equation (2.7) is satisfied. One should note that equation (2.75) contains the second-order derivative of ρ , which can be reduced to the first-order derivative. By differentiating both sides of equation (6.17) with respect to z , ρ'' can be obtained by:

$$\rho'' = \left[\tan^2 \alpha - \frac{2\rho' \rho^2}{(a + \rho^2)(\rho' - \lambda \sin \alpha)} \right] \cdot \frac{1 + \rho'^2}{\rho} \quad (6.19)$$

Substituting equation (6.19) into (2.75) and plugging the dimensionless parameters listed in equation (6.11), the non-geodesic equation can be simplified as:

$$\frac{d\alpha}{d\zeta} = -\frac{\rho'}{\rho} \tan \alpha + \frac{2\lambda\rho\rho' \cos \alpha}{(a + \rho^2)(\rho' - \lambda \sin \alpha)} \quad (6.20)$$

Simultaneous solution of the system of differential equations (6.17) and (6.20) will finally provide the isotensoidal meridian profiles and related non-geodesic fiber trajectories. equation(6.17) has two pairs of real, and one pair of imaginary roots. This expression is only valid for the interval $[\rho_{\min}, 1]$ (selected positive real solutions by setting the argument of the numerator equal to zero). For a given slippage coefficient λ , the resulting meridian profile will strongly depend on the value of the axial load a and the initial winding angle α_0 . The $\{a, \alpha_0\}$ -parameter set is able to completely determine the cross-sectional shapes of the non-geodesic isotensoids.

6.3.2 Cross sections and related winding angles

For numerically solve the coupling equations (6.17) and (6.20), we choose the geometrical parameters at the equator as the initial set of values, consisting of $\rho'_0 = 0$, $z_0 = 0$ and α_0 . In addition, a slightly reduced initial value for ρ is required ($\rho_0 = 0.9999$) in order to avoid singularities during the solution procedure of equations (6.17) and (6.20).

Depending on the magnitude of the axial forces as related to the internal pressure, several

non-geodesic isotensoidal meridian profiles are obtained (Fig. 6.13) with $\alpha_0 = 5^\circ$ and $\lambda = 0.04$. When the axial force is sufficiently large for forcing the resulting meridian profile to be closed, the shape of the isotensoid becomes here a toroid. One should note that the tensional forces of the fibers that proceed from the pole towards the equator replace the theoretically required external axial force applied on the polar cap. A collection of meridian profiles, i.e. cross-sectional shapes of non-geodesic isotensoidal toroids with the given polar radius $\rho_0=0.2$ corresponding to different slippage coefficients, is depicted in Fig. 6.14. It is revealed that the resulting cross-sectional profiles are almost identical to each other. Fig. 6.15 illustrates a 3D sectional view of an obtained isotensoidal toroid ($\rho_0 = 0.2, \lambda = 0.04$). In Fig. 6.16 the fiber trajectories for various slippage coefficients are outlined in terms of winding angle development. The results show that the winding angle varies from a relatively small value around 5° at the outer periphery of the toroid to about 50° at the inner periphery, and its value decreases with increasing slippage coefficient.

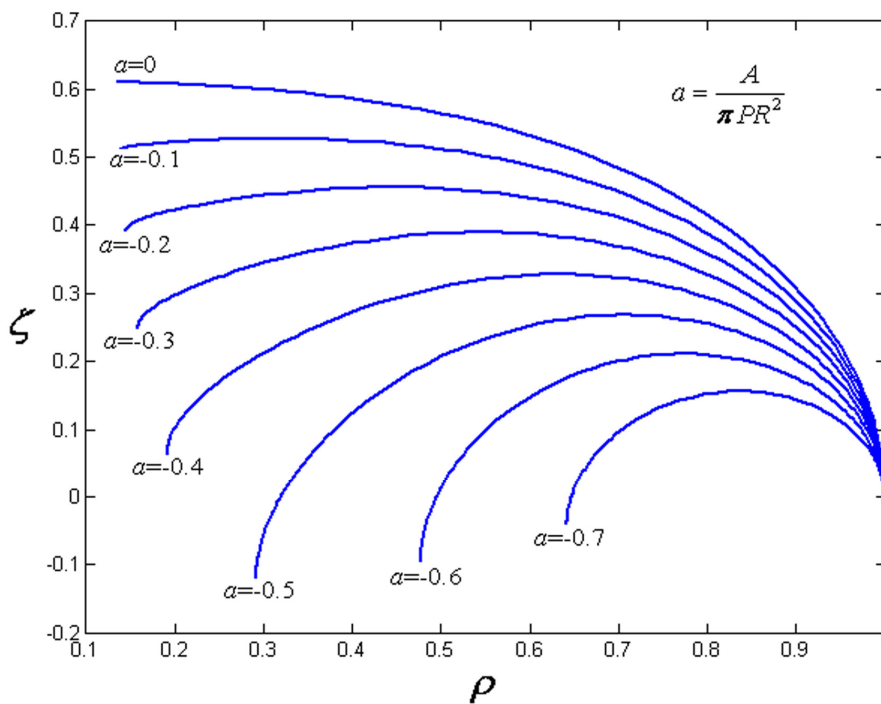


Fig. 6.13: Influence of the axial force on non-geodesic isotensoidal meridian profiles

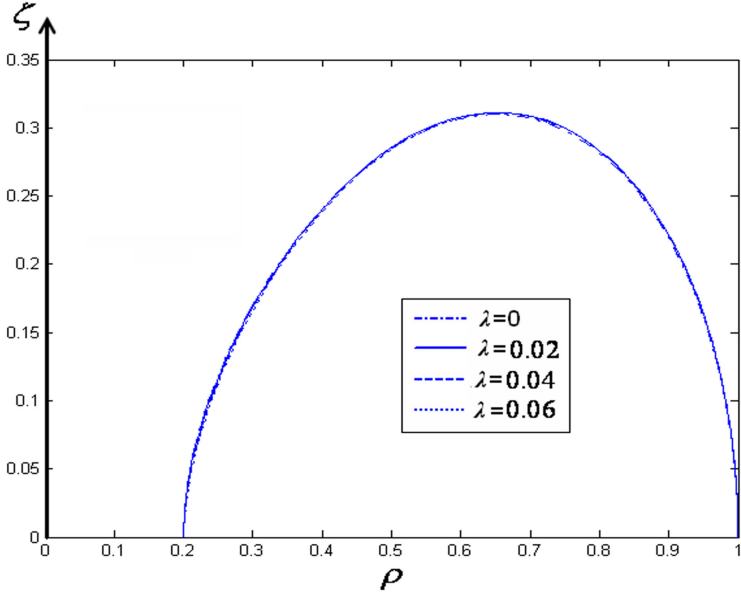


Fig. 6.14: Cross sections of non-geodesic-isotensoid toroids for various λ ($\rho_0 = 0.2$)

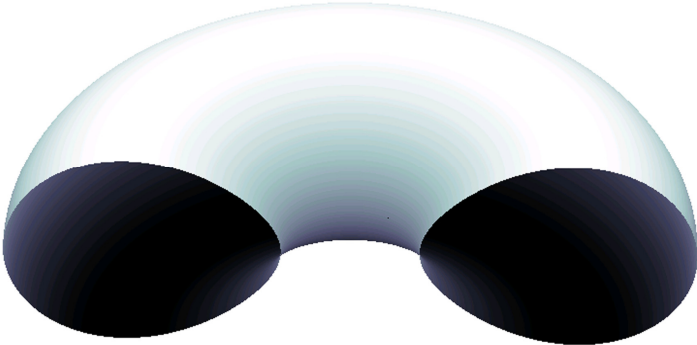


Fig. 6.15: A sectional view of the non-geodesic isotensoid toroid ($\rho_{\min} = 0.2, \lambda = 0.04$)

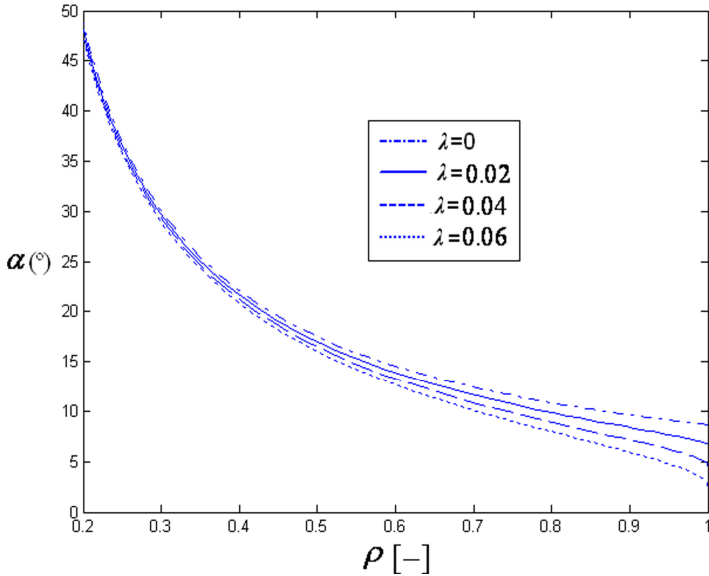


Fig. 6.16: Winding angle distributions for various slippage coefficients ($\rho_0 = 0.2$)

6.3.3 Structural performance improvement

In this section the performance factors $PF = PV/W$ of the non-geodesic isotensoid torods are determined to demonstrate the favorable alternative of non-geodesics to the winding on the isotensoid toroids.

According to equation (5.5), the minimally allowable laminate thickness t can be written as:

$$t = \frac{\left(\frac{A}{2\pi r} + \frac{pr}{2}\right)\sqrt{1+r'^2}}{X_f \cos^2 \alpha} \quad (6.21)$$

We recall here expression (6.8) for calculating PF for an isotensoid; substitution of equations (6.21) into (6.8) with the aid of equations (6.11) and (6.9), leads to:

$$\overline{PF} = \frac{\int_{\rho_{\min}}^1 \rho^2 \zeta' d\rho}{\int_{\rho_{\min}}^1 \frac{(a + \rho^2)^2 (1 + \rho'^2) \zeta'}{\cos^2 \alpha} d\rho} \quad (6.22)$$

where ρ_{\min} is the minimum radial distance of the meridian profile with respect to z -axis, at which the first derivative of ρ is exactly zero. By setting the numerator of equation (6.17) equal to zero, the radial coordinate ρ_{\min} can be obtained as follows:

$$\begin{aligned} C \cdot \cos \alpha_{\min} &= a + \rho_{\min}^2 \\ \Rightarrow \rho_{\min} &= \sqrt{C \cdot \cos \alpha_{\min} - a} \quad \text{where } a < 0 \end{aligned} \quad (6.23)$$

where α_{\min} represents the fiber angle at the inner circle of the toroid, corresponding to ρ_{\min} . With the aid of the *Runge-Kutta* formulae [13], α_{\min} can be determined by equation (6.20) for a given set of initial conditions.

Once a non-geodesic isotensoidal meridian profile is determined, the integrands in the right-hand side of equation (6.22) are evaluated at several grid points within the interval $[\rho_{\min}, 1]$ and then the dimensionless performance factor \overline{PF} is given using n -point Gaussian quadrature rule [14]. The values of variables ρ , ζ' and α required for evaluations are calculated by solving the system of differential equations (6.17) and (6.20). Fig. 6.17 presents the rates of performance improvement that the non-geodesic winding can obtain for isotensoidal toroids with various slippage coefficients (range: $[0 - 0.07]$, $\rho_0=0.2$). The results show that the performance factor improves as the slippage coefficient λ increases. Particularly, the performance factor of the isotensoidal toroid for $\lambda=0.07$ show over 2% increase as compared to that for $\lambda=0$ (the geodesic one). It is demonstrated that the non-geodesics-based isotensoidal toroids have slightly better structural efficiency than the geodesics-based ones.

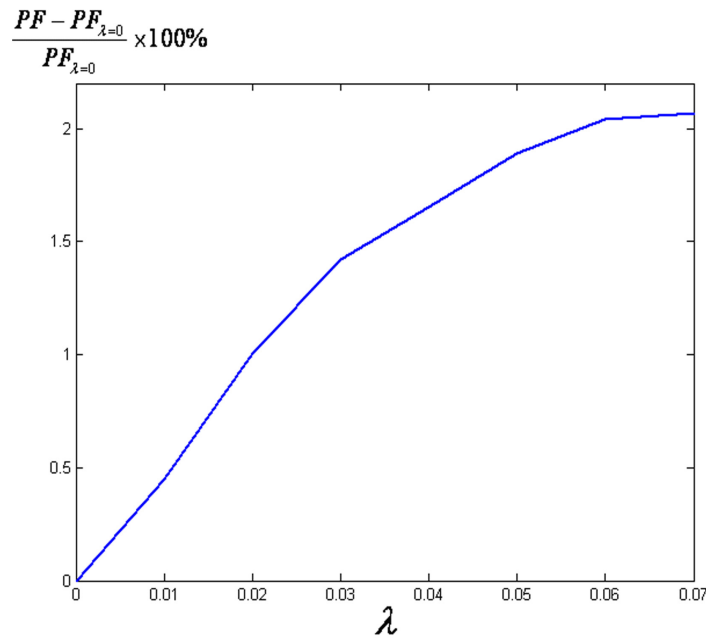


Fig. 6.17: Rates of performance improvement for various slippage coefficients ($\rho_0 = 0.2$)

6.4 Conclusions

In this chapter we have presented a novel design approach combining isotenoidal conditions with non-geodesic trajectories, which is able to improve the geometric flexibility and structural performance of filament wound pressure vessels. It is shown that the performance factor of non-geodesics-isotenoids increases compared to the one relying on geodesics.

With the proper initialization and root searching algorithm for determining two slippage coefficients that fulfill the winding conditions of both upper and lower dome parts, the isotenoids with unequal polar openings are obtained. The proposed method for non-geodesic trajectories, specifically applied on isotenoid domes with unequal polar openings, performs well in terms of accuracy, flexibility and winding demands. By creating a perfect tangential roving passage at the end openings, continuation to the following wound circuits does become in this case feasible. It provides a straightforward tool for immediate creation of possible dome shapes with unequal polar openings.

In this chapter the key factor of the creation of isotenoid toroidal pressure vessels is that the isotenoid design is based on the principle of non-geodesic winding. The non-geodesic equations for deriving fiber trajectories on an axisymmetric body of revolution are already known but the emphasis of this research is mainly oriented towards the relation between the

isotensoid conditions and the non-geodesic law. With these equations we can develop non-geodesically overwound toroidal pressure vessels that provide equal fiber tension everywhere.

References

1. Jong de Th. A theory of filament wound pressure vessels. Report LR-379. Structures and materials laboratory, Faculty of Aerospace Engineering, Delft University of Technology. Delft, April, 1983.
2. Koussios S, Bergsma OK. Analysis of filament wound pressure vessels considering the laminate thickness variation through the meridional direction. Proceedings of the 14th International Conference on Composite Materials (ICCM/14), San Diego, CA, July 2002.
3. Zu L, Koussios S, Beukers A. Application of isotensoid-based cross sections to filament-wound toroidal pressure vessels Proceedings of the 17th International Conference on Composite Materials (ICCM/17), Edinburgh, UK, July 2009.
4. Marketos JD. Optimum toroidal pressure vessel filament wound along geodesic lines. AIAA Journal 1963; 1: 1942-5.
5. Vasiliev VV, Morozov EV. Mechanics and analysis of composite materials. UK: Elsevier, 2001.
6. Hojjati M, Safavi AV, Hoa SV. Design of domes for polymeric composite pressure vessels. Composites Engineering 1995; 5(1): 51-59.
7. Koussios S, Beukers A, Stathis PT. Manufacturability of composite pressure vessels: Application of non-geodesic winding. Proceedings of the 16th International Conference on Composite Materials (ICCM/16), Kyoto, Japan, July 2007.
8. Park JS, Hong CS, Kim CG, Kim CU. Analysis of filament wound composite structures considering the change of winding angles through the thickness direction. Composite Structures 2002; 55: 63-71.
9. Koussios S, Bergsma OK, Beukers A. Isotensoid pressure vessels based on non-geodesic roving trajectories. Proc. of 15th International Conference on Composite Materials (ICCM/15), Durban, South Africa, June-July, 2005.
10. Koussios S. Filament Winding: A Unified Approach. PhD Thesis report, Design and Production of Composite Structures Group, Faculty of Aerospace Engineering, Delft University of Technology, Delft, 2004.
11. P. Deuffhard, Newton Methods for Nonlinear Problems. Affine Invariance and Adaptive

Chapter 6

Algorithms. Springer Series in Computational Mathematics, Vol. 35. Springer, Berlin, 2004.

12. Koussios S, Bergsma OK, Mitchell G. Non-geodesic filament winding on generic shells of revolution. Proc. IMechE Part L: J. Materials: Design and Applications 2005; 219(1):25-35.
13. Boyce WE, DiPrima RC. Elementary differential equations and boundary value problems. New York: John Wiley & Sons, Inc, 1986.
14. Gil, Amparo; Segura, Javier; Temme, Nico M. (2007), "§5.3: Gauss quadrature", Numerical Methods for Special Functions, SIAM.

III CONTINUUM-BASED APPROACHES

Chapter 7

Bellow-shaped Pressure Vessels

7.1 Introduction

The axial load carrying capability of pressure vessels is mainly the result of the internal pressure that transforms compressive roving stresses into tensional ones. The combination of this property with an extended degree of flexibility introduces a new range of applications where rather large forces can be translated over certain distances. These distances however, are not unlimited, since the dimensions of such a vessel are finite. The solution for this problem is a novel configuration of vessels being stacked on top of each other and overlapped in an integral fashion, i.e., bellow-shaped pressure structures. Recently, filament wound bellow-shaped structures have emerged as an attractive alternative in aerospace and underwater fields where high loading capacity, translational and rotational flexibility, and theoretically infinite length are required. The bellow-shaped pressure vessels are light-weight structures possessing higher flexibility than the current composite vessels [1, 2].

A major advantage of composite materials is the large number of design variables available

Chapter 7

to the designer. To realize this potential and to maximize the structural efficiency which composites can offer, the design has to properly capture the specific requirements of the problem. Optimal design is an effective way of achieving this goal. Various methods have been presented for designing optimal shapes of rotationally symmetrical shells. Several authors have performed detailed analysis of optimal shape profiles by using the netting theory and anisotropic elasticity theory (continuum theory). For the design objectives, the minimization of weight [3] and strain energy [4], the maximization of structural performance [5] and burst pressure [6], were discussed. The deformation and strength conditions [7] in combination with the Tsai-Wu failure criterion [8] were used as constraints. The meridian shape, fiber orientations, stacking sequences, and layer thickness were considered as design variables. A sensitivity analysis of a finite element model was also conducted during the shape optimization stage for a pressure vessel, although only thickness discontinuity was considered [9]. Koussios et al. [10, 11] systematically studied geometrical and structural properties of bellow-shaped vessels based on the isotensoid-netting theory. They pointed out that the available design space and flexibility of isotensoid bellow-shaped structures can be sufficiently enlarged when using non-geodesic trajectories.

Little research has focused on the design method using the continuum theory in combination with non-geodesic winding law. Most of the previous models have employed the geodesic winding principle [12] and the netting theory assumption [13] to design rotationally convex structures. However, restricting the winding trajectory to a geodesic path certainly limits the opportunity to match the fiber orientation to the applied stress system. The method based on the netting theory has a major defect in that design calculations are based on fiber strength alone, and the matrix effect is considered negligible. Moreover, both convex and concave parts of bellow-shaped structures should be considered, whereas no investigation so far has addressed how to optimally design a convex-concave combined structure overwound by non-geodesic trajectories.

This study aims to determine the optimal geometry for the meridian profiles of filament wound bellow-shaped pressure vessels, subjected to the Tsai-Wu failure criterion, by means of maximizing the performance factor. The performance factor $PF = PV / W$ is used to estimate the efficiency of bellow-shaped pressure vessels. The coordinates of the internal knots which interpolate the meridian curve are used as design variables to search under a given slippage coefficient. The stress field is modeled using classical lamination theory, and the slippage coefficient, which is related to the friction between the placed fiber bundle and the supporting surface, is here introduced to find the region of possible winding trajectories. The geometrical

continuity at the dome-dome conjunction should be ensured to avoid stress jumps. The formulation of the optimal design problem is regarded as a nonlinear constrained optimization problem and the SQP algorithm is here used to find the optimal profile shape. A practical design example is presented and investigated by this design procedure. The effect of the slippage coefficients on the structural efficiency and optimal shape is also studied.

7.2 Mathematical Model

7.2.1 Description of the meridian profile

The verticality of the dome profile at the end points creates the ability for interconnecting several pressure vessels without roving interruption. This is the basic idea for the geometry of articulated pressure vessels, as shown in Fig. 7.1. For the convenience of outlining the present method, we choose half of one cell of an articulated vessel as the design objective, which is here referred to as a “half-cell dome”. The loads and geometry of a half-cell dome structure is depicted as Fig. 7.2, where φ and θ are the angular coordinates in meridional and parallel directions, while r and z stand for the radial and axial coordinates. The vector representation of a half-cell dome structure in polar coordinates is:

$$\mathbf{S}(\theta, z) = \{r(z) \cos \theta, r(z) \sin \theta, z\} \quad (7.1)$$

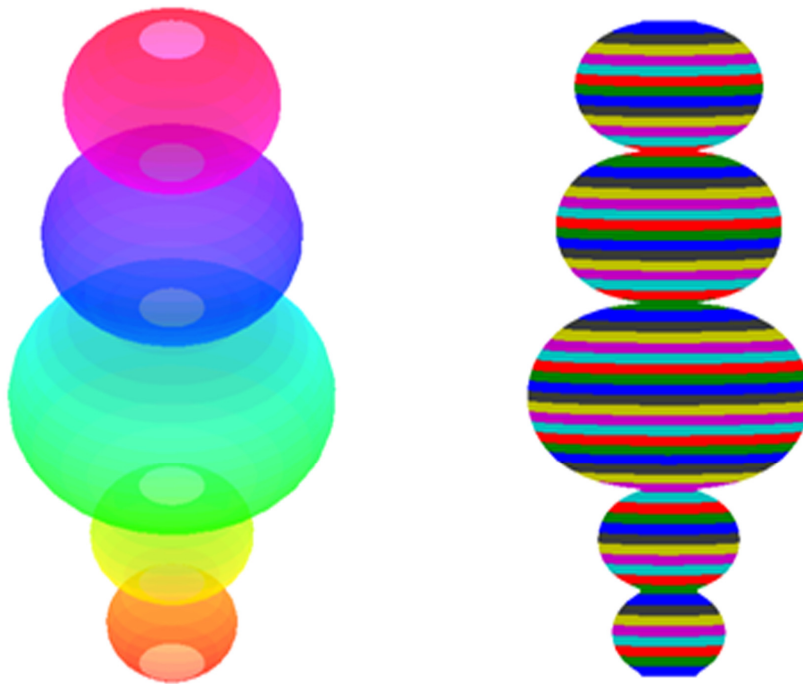


Fig. 7.1: Meridian profile of a bellow-shaped pressure vessel (3D and 2D views)

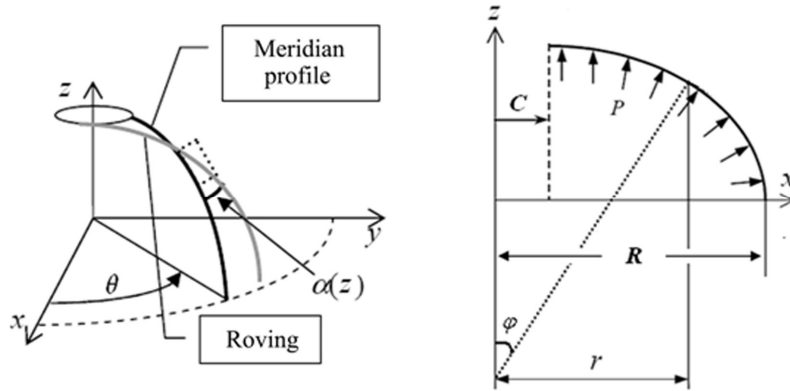


Fig. 7.2: Loads and geometry of a half-cell dome structure [19, 20]

There exists no general rule for the mathematical description of the shape to be optimized. The approximations are typically used to approach the desired optimal shape in the best possible way. For this reason, the approximation should be as adjustable as possible. For a specific selection of the type of approximate functions, some information and values about the expected optimal shape can be very helpful. The meridian profile of such half-cell dome can be described by a convex-concave joint curve with several equidistant interpolation knots between P_0 and P_n , as shown in Fig. 7.3. Its meridian shape is formed from several individual segments which are joined at internal knots P_i ($i=1, 2, 3, \dots, n-1$) with continuous first and second derivatives. No assumptions are made about continuity of the third or higher derivatives, but it is postulated that the profile is composed of both convex and concave parts. Considering the satisfaction of C^0 , C^1 and C^2 continuity conditions, cubic splines which intersect at a knot with the same slope and curvature are very suitable for the approximation of the dome profiles.

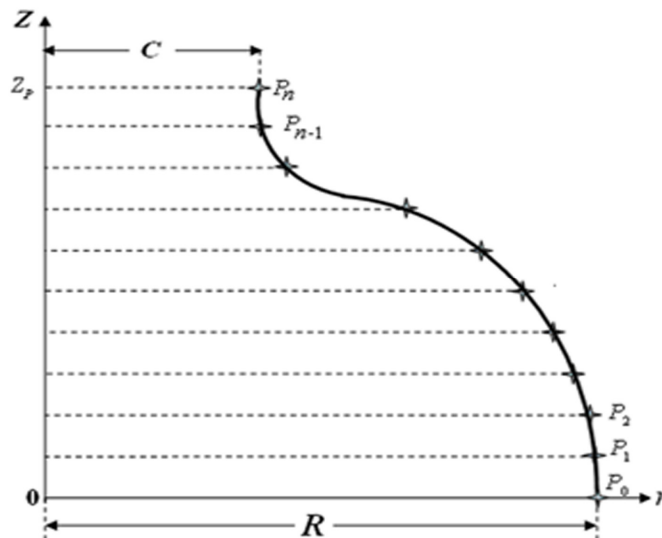


Fig. 7.3: Meridian profile of a half-cell dome with $n+1$ equidistant knots

7.2.2 Objective function

The mathematical model of the optimal design for domes includes the design variables, objective function and design constraints. For convenience in subsequent computations, the dimensionless internal pressure is here introduced:

$$\rho = r/R, \quad \zeta = z/R, \quad \bar{p} = \frac{R}{2t_0 Y_t} \cdot p \quad (7.2)$$

where R and t_0 are the radius and the thickness of the dome equator, respectively.

The material properties and polar opening radius r_0 are taken as pre-assigned parameters, with both being given at the outset. The $n-1$ unknown interpolation knots, P_i ($i=1, 2, 3, \dots, n-1$) and the depth of the dome ζ_p are taken as the design variables, so the design variable vector is $\mathbf{X} = \{\rho_1, \rho_2, \dots, \rho_{n-1}, \zeta_p\}$. These values are employed to describe a half-cell dome profile and calculate the performance factor by a numerical integration technique.

Composite pressure vessels are expected to withstand a maximum burst pressure at a maximum internal volume and a minimum weight. Therefore, the evaluation criterion is pV/W , where p , V and W are the burst pressure, the internal volume and the weight of the half-cell dome, respectively. For an axisymmetrical dome shell, the performance factor PF is given by:

$$PF = \frac{p \cdot \int_0^{\zeta_p} \pi r^2 dz}{\gamma \cdot \int_0^{\zeta_p} 2\pi r t \sqrt{1+r'^2} dz} \quad (7.3)$$

where γ is the specific weight of the used composite material.

The dimensionless performance factor is defined as:

$$\overline{PF} = PF \cdot \frac{\gamma}{Y_t} \quad (7.4)$$

Substituting equation (7.3) into (7.4) and plugging the dimensionless parameters as shown in equation (7.2), we obtain:

$$\overline{PF} = \frac{\bar{p} \cdot \int_0^{\zeta_p} \rho^2 d\zeta}{\int_0^{\zeta_p} \rho \sqrt{1+\rho'^2} \cdot \frac{t}{t_0} d\zeta} \quad (7.5)$$

With the assumptions presented in section 4.2, the laminate thickness along the meridional direction can be written as:

$$\frac{t}{t_0} = \frac{1}{\rho} \cdot \frac{\cos \alpha_0}{\cos \alpha} \quad (7.6)$$

where α_0 is the winding angle at the dome equator, which can be determined by non-geodesic equation (2.75).

Chapter 7

Substitution of equation (7.6) into (7.5) leads to the final form of the objective function:

$$\overline{PF}(\mathbf{X}) = \frac{\bar{p} \cdot \int_0^{\zeta_p} \rho^2 d\zeta}{\int_0^{\zeta_p} \sqrt{1 + \rho'^2} \cdot \frac{\cos \alpha_0}{\cos \alpha} d\zeta} \quad (7.7)$$

7.2.3 Constraints

Both the design constraints of geometry and ultimate strength are here considered. The geometrical conditions at $\zeta = 0$ and $\zeta = \zeta_m$, where the coordinate and slope at the dome-dome conjunction should be continuous, give the following equations:

$$\begin{aligned} \zeta = 0: \quad & \rho = 1 \quad \text{and} \quad \rho' = 0 \\ \zeta = \zeta_m: \quad & \rho = \rho_0 \quad \text{and} \quad \rho' = 0 \end{aligned} \quad (7.8)$$

where ρ_0 is the dimensionless polar opening radius of a half-cell dome.

The convex and concave parts of a half-cell dome must be maintained. Assuming that the point of inflexion on the meridian curve is $P(\rho_{ip}, \zeta_{ip})$, which is determined by interpolating the result of cubic splines, the following conditions should be met:

$$\begin{aligned} 0 < \zeta < \zeta_{ip}: \quad & \rho'' < 0 \\ \zeta_{ip} < \zeta < \zeta_m: \quad & \rho'' > 0 \end{aligned} \quad (7.9)$$

The shell is assumed to consist of helically wound layers, each of which forms an angle-ply configuration of $\pm\alpha$ layers. The stress components referred to the material axes in an individual layer are given by (recall equation (3.29)):

$$\begin{cases} \sigma_1 = \frac{1}{t}(m_{11}N_\varphi + m_{12}N_\theta) \\ \sigma_2 = \frac{1}{t}(m_{21}N_\varphi + m_{22}N_\theta) \\ \tau_{12} = \frac{1}{t}(m_{31}N_\varphi + m_{32}N_\theta) \end{cases} \quad (7.10)$$

where m_{ij} ($i, j=1,2,3$) are functions of ply angles and material properties; these are given in equation (3.30).

The failure of a composite pressure vessel includes generally two main steps: firstly, cracks appear in the matrix, and then the pressure is taken up by the fibers until they fail [14]. However, in a commercial storage vessel, e.g., a hydrogen storage pressure vessel, leakage always happens prior to fiber failure and can be disastrous as the leaked gas or liquid might pose a number of hazards to human safety. Hence a leak-before-break safety assessment plays a vital role for avoiding pressure loss and fluid leakage of pressure vessels. The matrix failure

thus becomes a major issue for the safety of a pressure vessel. In this study, the Tsai-Wu failure criterion [15] is used:

$$F = F_i \sigma_i + F_{ij} \sigma_i \sigma_j \leq 1 \quad (i, j = 1, 2, 6) \quad (7.11)$$

in which the strength parameters $F_{11}, F_{22}, F_{12}, F_{66}, F_1, F_2$ and F_6 are given by:

$$F_{11} = \frac{1}{X_T X_C}, \quad F_{22} = \frac{1}{Y_T Y_C}, \quad F_{66} = \frac{1}{S^2}, \quad F_{12} = -\frac{1}{2\sqrt{X_T X_C Y_T Y_C}},$$

$$F_1 = \frac{1}{X_T} - \frac{1}{X_C}, \quad F_2 = \frac{1}{Y_T} - \frac{1}{Y_C}, \quad F_6 = 0 \quad (7.12)$$

where X_T, X_C, Y_T, Y_C are the tensile and compressive strengths of the unidirectional layer in the fiber and transverse directions, and S is the in-plane shear strength. Substituting the stresses from equation (7.10) and the dimensionless variables from equation (7.2) into (7.11), we obtain a quadratic failure criterion in terms of the dimensionless burst pressure \bar{p} :

$$\begin{aligned} & \frac{1}{\bar{p}^2} \cdot Y_t^2 \cdot \frac{\cos^2 \alpha}{\cos^2 \alpha_0} \cdot \rho^4 (1 + \rho^2) [F_{11} (m_{11} + m_{12} J)^2 + F_{22} (m_{21} + m_{22} J)^2 \\ & + F_{66} (m_{31} + m_{32} J)^2 + 2F_{12} (m_{11} + m_{12} J)(m_{21} + m_{22} J)] \\ & + \bar{p} \cdot Y_t \cdot \frac{\cos \alpha}{\cos \alpha_0} \cdot \rho^2 \sqrt{1 + \rho^2} [F_1 (m_{11} + m_{12} J) + F_2 (m_{21} + m_{22} J)] - 1 = 0 \end{aligned} \quad (7.13)$$

where $J = 2 + \frac{\rho \rho''}{1 + \rho'^2}$. In addition, since the surface near the conjunction area of two dome cells is concave, the fiber non-bridging condition should also be considered. Substituting equation (2.71) for κ_n into the non-bridging criterion (2.25), leads to:

$$\text{tg}^2 \alpha \geq \frac{\rho \rho''}{1 + \rho'^2} \quad (7.14)$$

7.2.4 Optimization procedure

The optimization problem is attributed to the maximization of the dimensionless performance factor under the constraints given by equations (7.8), (7.9), (7.13) and (7.14). This design case can be classified as a nonlinear constrained optimization problem. The *SQP* (sequential quadratic programming) method [16] is here employed to find the optimal solution. In this method, the function solves a quadratic programming (*QP*) sub-problem at each step. The current point is updated as a new point by this procedure, until a termination criterion is met. The flow chart of the optimization procedure is shown as Fig. 7.4.

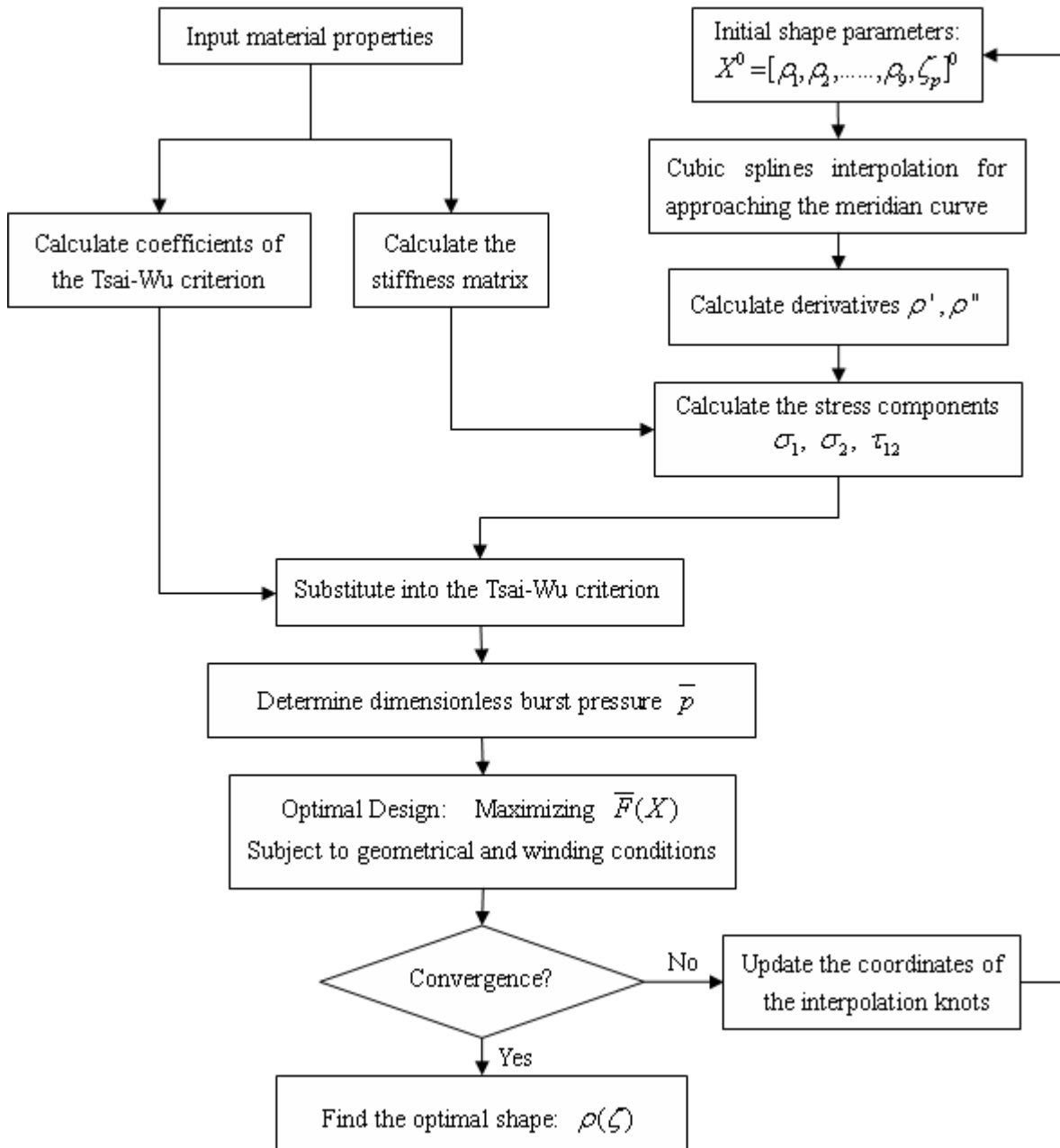


Fig. 7.4: Flow chart of the optimal design procedure

Solving the quadratic equation (7.13) yields the burst pressure $\bar{p}(\rho)$ (selected positive real solution) corresponding to the failure of that point with the given radial coordinate ρ . The burst pressure of the vessel is further given by:

$$\bar{p} = \min_{\rho_0 \leq \rho \leq 1} \bar{p}(\rho) \quad (7.15)$$

When a meridian profile that satisfies the constraint conditions, is determined by a set of design variables (interpolation knots) in the i^{th} iteration step of optimization procedure, the

values of \bar{p} in equation (7.13) are evaluated at many points along the non-geodesics and their minimum value is employed as the burst pressure of the bellow-shaped vessel. At each iteration step, the points used for the evaluation are determined by solving the dimensionless differential equation of non-geodesic trajectories on the half-cell dome shell:

$$\frac{d\alpha}{d\zeta} = \lambda \left[\frac{\sin \alpha \cdot \tan \alpha}{\rho} - \frac{\rho''}{1 + \rho'^2} \cos \alpha \right] - \frac{\rho' \cdot \tan \alpha}{\rho} \quad (7.16)$$

In regard to the windability of the vessel, the winding angle at the polar areas should rapidly approach the value $\pi/2$. Thus the initial value is $\alpha(c) = \pi/2$ for the solution of the equation (7.16). For the numerical solution, however, a slightly reduced initial value for α is preferable. The solution procedure for determining the burst pressure of the structure is shown in Fig. 7.5. The dimensionless performance factor \bar{PF} is then calculated using n -point Gaussian quadrature rule.

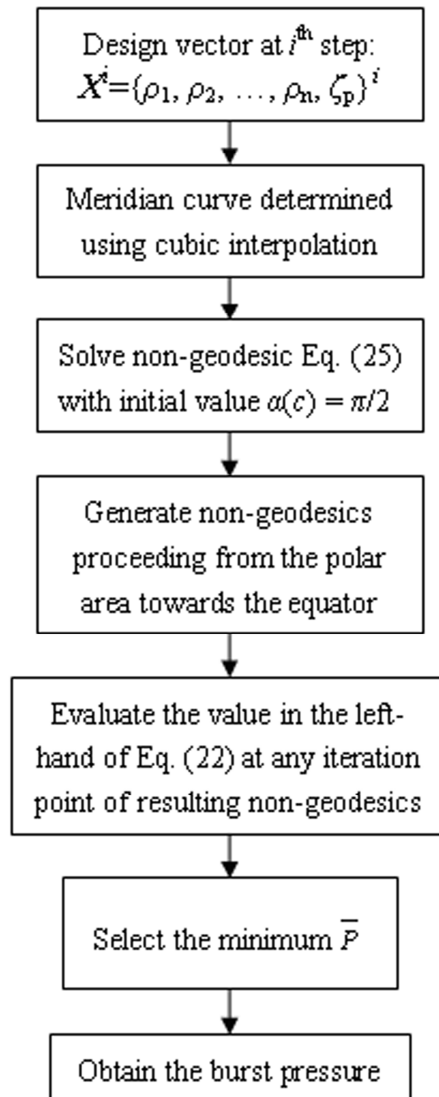


Fig. 7.5: Flow chart of the design procedure for determining the burst pressure

7.3 Results and Discussion

The optimization process of the bellow-shaped pressure vessel is carried out by considering a half-cell dome with the given polar opening radius $\rho_0 = 0.4$. The laminate is made of T300/5208 graphite/epoxy the elastic constants of which are $E_1 = 142$ GPa, $E_2 = 10.8$ GPa, $G_{12} = 5.49$ GPa and $\nu_{12} = 0.3$. The strength values are $X_t = 1568$ MPa, $Y_t = 57$ MPa, $X_c = 1341$ MPa, $Y_c = 212$ MPa, and $S = 80$ MPa. The values for the material properties are taken from Ref. [17].

Fig. 7.6 illustrates the geodesics-based half-cell dome profiles determined using the isotenoid design method and the present method, respectively. The maximum value of the objective function \overline{PF} is 2.2547 herein. On the other hand, substitution of the dome profile using isotenoid design method into the objective function, gives a result of 2.1694. It is visible that the optimal profile obtained by the present method has better performance and greater internal volume than the isotenoid one. Fig. 7.7 shows the optimal half-cell dome profiles determined by the present method corresponding to various slippage coefficients ranging from 0 to 0.3. The optimal values of performance factor, \overline{PF} , obtained using the present method with the slippage coefficients ranging from 0 to 0.4, are listed in Tab. 7.1. The results reveal that the performance of the half-cell dome can be improved with increasing λ .

Fig. 7.8 displays the laminate thickness distributions of the half-cell dome shell designed using the present method, with slippage coefficients range [0-0.3]. Since the winding angle near the region of polar opening approaches 90° , the shell thickness tends to infinity due to fiber accumulation. Owing to the same winding conditions being considered, the thickness distributions all share similar tendencies. However, due to the different slippage coefficients being applied, different thickness distributions are obtained. Fig. 7.9 illustrates the winding angle developments on the half-cell dome determined by the present method. The winding angle has risen from a relatively small angle at the equator to 90° at the polar opening region. The tangential requirement at the polar region for the roving paths is perfectly satisfied.

7.4 Conclusions

In this chapter, the optimal design problem of a half-cell dome profile for filament wound bellow-shaped pressure vessels is presented. A design-oriented optimization method, which aims to maximize the structural performance of pressure vessels, is outlined based on the continuum theory and the Tsai-Wu failure criterion. The classical lamination theory is

employed for the stress analysis and the SQP method is used as a non-linear optimization algorithm. Moreover, the method proposed here is dedicated to non-geodesic trajectories and therefore is very flexible for the optimal design of pressure vessels.

An actual example with a given polar opening is here outlined to demonstrate the favorable performance of the proposed method. The optimal meridian profiles are obtained using various slippage coefficients. The results indicate that the optimal pressure vessel designed using the present method has a lighter structure and greater internal volume than the one using the geodesic-isotensoid design method. The distributions of the laminate thickness and the winding angle obtained using both methods show similar development tendencies. The performance factor improves with increasing slippage coefficients, and the dome height becomes greater with the increase in slippage coefficient. It is thus concluded that the structural performance of bellow-shaped pressure vessels can further be improved using non-geodesic winding.

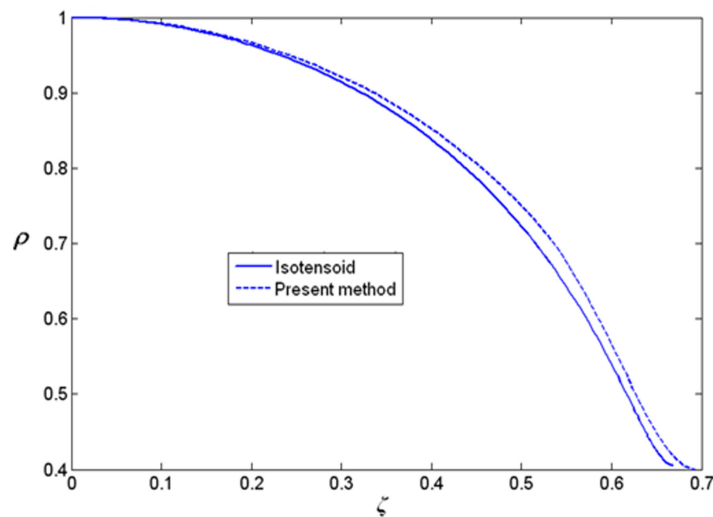


Fig. 7.6: Geodesic dome profiles dictated by the present method and by isotensoid method

Tab. 7.1: Dimensionless performance factors and related increase rates for various λ

Slippage coefficient	Performance factor (PF)	Increase rate (%)
$\lambda = 0$	2.2547	0
Present Method ($\rho_0 = 0.4$)	$\lambda = 0.1$	7.97
	$\lambda = 0.2$	10.20
	$\lambda = 0.3$	12.61
	$\lambda = 0.4$	15.85

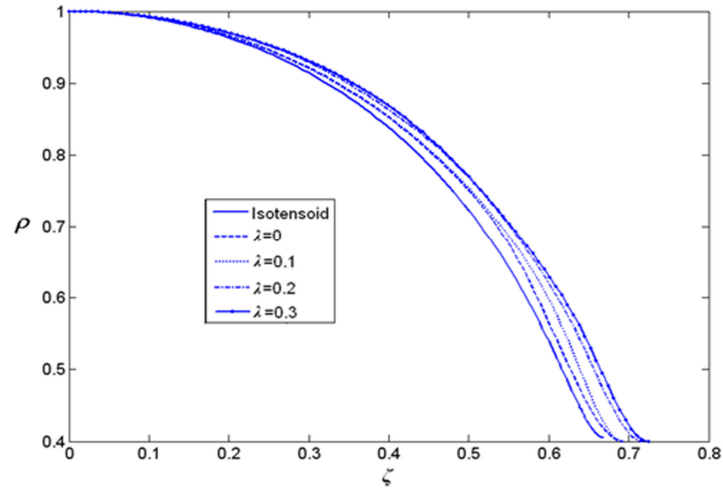


Fig. 7.7: Half-cell dome profiles corresponding to various slippage coefficients

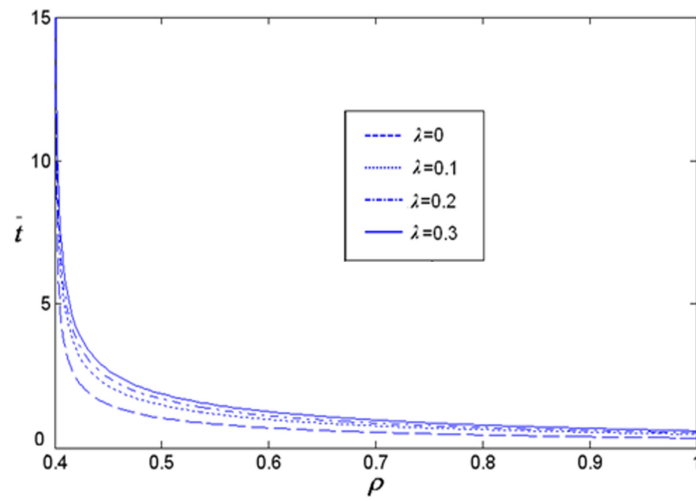


Fig. 7.8: Shell thickness distributions for the half-cell dome designed by the present method

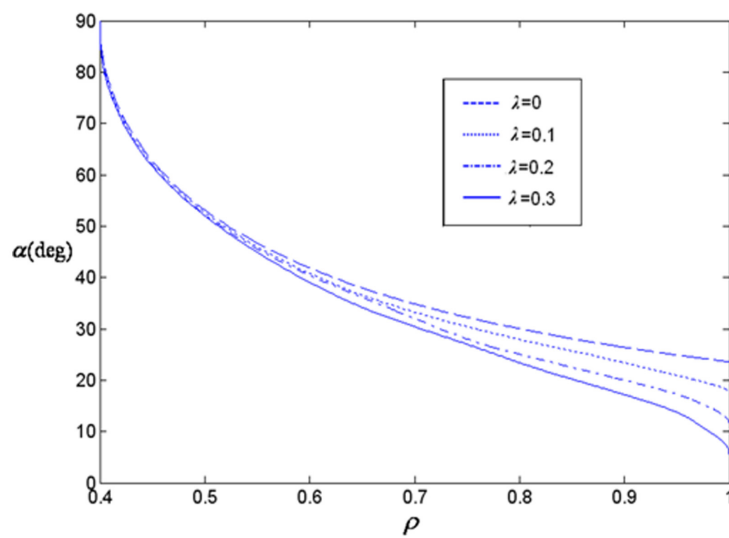


Fig. 7.9: Winding angle developments corresponding to various λ

References

1. Koussios S, Beukers A, Bergsma OK. A novel class of flexible pressurisable composite structures. Proc. of 21th Annual Conference of the ASC, Dearborn, MI, Sept. 2006.
2. Koussios S, Beukers A, Bergsma OK. "Isotensoid related composite structures. Proc. of 21th Annual Conference of the ASC, Dearborn, MI, Sept. 2006.
3. Kim CU, Kang JH, Hong CS, Kim C G. Optimal design of filament wound structures under internal pressure based on the semi-geodesic path algorithm. *Composite Structures* 2005; 67(4): 443-452.
4. Fukunaga H, Sekine H. Optimum design of composite structures for shapes, layer angles, layer thickness distributions. *Journal of Composite Materials* 1993; 27(15): 1479-1492.
5. Fukunaga H, Uemura M. Optimum design of helically wound composite pressure vessels. *Composite Structures* 1983; 1(1): 31-49.
6. Adali S, Summers EB and Verijenko VE. Optimization of laminated cylindrical pressure vessels under strength criterion. *Composite Structures* 1993; 25: 305-312.
7. Fukunaga H, Chou TW. Simplified design techniques for laminated cylindrical pressure vessels under stiffness and strength constraints. *Journal of Composite Materials* 1988; 22: 1156-1169.
8. Liang CC, Chen HW, Wang CH. Optimum design of dome contour for filament-wound composite pressure vessels based on a shape factor," *Composite Structures*, 2002; 58(4): 469-482.
9. Younsheng L, Ji L. Sensitivity analysis in shape optimization design for pressure vessel. *Journal of Pressure Vessel and Piping* 1992; 114(4): 428-432.
10. Koussios S, Bergsma OK, Beukers A. "Isotensoid pressure vessels based on non-geodesic roving trajectories," Proc. of 15th International Conference on Composite Materials. Durban, South Africa, June-July, 2005.
11. Koussios S. Filament Winding: a Unified Approach. PhD Thesis Report. Design & Production of Composite Structures, Faculty of Aerospace Engineering, Delft University of Technology. Delft University Press, 2004.
12. Vasiliev VV, Krikanov AA. New generation of filament-wound composite pressure vessels for commercial applications. *Composite Structures* 2003; 62(3): 449-459.
13. Krikanov AA. Composite pressure vessels with higher stiffness. *Composite Structures* 2000; 48: 119-127.
14. Vasiliev VV. Composite Pressure Vessels - Analysis, Design, and Manufacturing. Bull

Chapter 7

Ridge Publishing, Blacksburg, Virginia, USA, 2009.

15. Tsai SW, Wu EM. A general theory of strength for anisotropic materials. *Journal of Composite Materials* 1971;5(1):58-80.
16. Nocedal J, Wright SJ. *Numerical optimization*. Springer. 2006.
17. Tsai, SW, Hahn HT. *Introduction to composite Materials*. Westport, Conn.: Technomic Publishing Company, Inc., 1980.

Chapter 8

Continuum-based Domes for Pressure Vessels

8.1 Introduction

The quality of composite pressure vessels is usually expressed in terms of the performance factor, which is defined as pressure times volume divided by weight (PV/W). From this formulation it becomes evident that accurate estimations of the burst pressure and the resulting vessel weight are of vital importance. For the calculations of the required properties one can distinguish two approaches: the netting theory and the continuum theory. In both approaches, the basic idea is to maximally utilize the available strength. During pressurization, the structure is under uniform through-thickness strain and consequently no bending or discontinuity stresses are here assumed. The netting theory provides results according to analytical or graphical approaches [1-3]; however, it has a major defect in that design calculations are solely based on fiber strength and the matrix effect is not considered. The mechanical and structural performance is predicted by neglecting the contribution of the resin system. In addition, the continuum theory is more accurate and shows the ability to cover the complete range from fully orthotropic to entirely isotropic materials. Considering the current availability of computational resources and the accessibility of the numerical operations that have to be undertaken, the continuum theory is actually preferred, unless the designer seeks for a preliminary dimensioning procedure. One should note that the netting approach is a special case of the continuum theory.

The geometrical determination of the dome is the major part of designing pressure vessels. Various methods have been presented for determining optimal domes, based on the continuum

Chapter 8

theory. de Jong [4] compared the shapes of optimal profiles determined by the netting and the continuum theory and indicated that the geometry and performance of optimal domes are dependent on the elastic properties of the materials used. Hojjati et al. [5] evaluated the effect of mechanical properties of composites on the dome profiles and proved that the matrix properties have a major role in the dome design. Vasiliev et al. [6, 7] derived the optimality conditions for a pressure vessel based on the classical lamination theory and outlined the shapes of optimal dome profiles corresponding to various anisotropic characteristics. Liang et al. [8] presented the optimal design of dome profiles by maximizing the shape factor and evaluated the effect of the dome depth on the structural performance. Zu et al. [9] developed an optimal design method for the class of bellow-shaped pressure vessels comprising various dome cells that are axially stacked on each other. Fukunaga et al. [10] determined optimal meridian shapes using several failure criteria and presented an analytic approach for the optimal design of dome structures. Tackett et al. [11] conducted a combined analytical and experimental effort to characterize dome reinforcement requirements for intermediate modulus carbon/epoxy pressure vessels and evaluated the influence of shallow dome profiles on their performance. Vita et al. [12] outlined the process simulation in filament winding of composite structures. Blachut [13, 14] investigated the optimal meridian shape and thickness distributions in a filament wound dome closure, and discussed the relevant details of manufacture, testing and numerical analysis of the torispherical heads. In recent years, researchers have carried out many investigations into shape optimization problems which are proving useful for different optimization problems. They usually use the nodal coordinates of the discrete model as design variables [9, 15-17]. These approaches require a large number of design variables and constraints, which significantly complicate the design procedure.

Although the continuum-based design is sufficiently covered in the literature, there are some deficiencies. The majority of previous research has merely considered the dome design based on geodesics, and overlooked the application of non-geodesics to the optimal design of meridian profiles and their related fiber trajectories. Geodesics represent the shortest paths connecting two arbitrary points on a surface, and they show great stability on a surface and calculability with the Clairaut equation [18]. However, as geodesics are entirely determined by the underlying meridian profile and initial winding angle, their geometry, combined with the requirement for tangential placement of the fibers at the polar areas, certainly limits the design opportunities of domes [19, 20]. A typical example of this restriction is the limit for improving the structural performance of domes. The possibility appears now for applying friction-based non-geodesics to the design of roving trajectories for pressure vessels.

The optimal dome design relies on the most efficient distribution of laminate thickness and stress, in order to maximize the structural performance. As the strength-dominated and manufacturing-dominated thickness distributions do generally not match, the laminate strength cannot be maximally utilized. A well-known solution for this problem comprises geodesic-isotensoid designs, based on the netting analysis. However, geodesics do generally not result in optimal solutions for vessel design problems whereby the matrix strength has to be taken into account [9, 21, 22]. It is thus desirable to exploit non-geodesics to enlarge the design space for obtaining the optimal meridian shapes and related roving trajectories, so that the minimum required thickness distributions as determined by strength analysis can maximally coincide to the manufactured thickness distributions as determined by the winding process. In section 8.2 the non-geodesics-based optimal meridian profiles are determined with the aid of the generalized optimality condition, and the influence of the material orthotropy on geometrical issues, such as the resulting meridian shape and the tangentiality of the fibers at the polar opening. The feasible intervals for the system of governing equations are also elaborated in section 8.3. The method is then demonstrated by three typical composite materials, reflecting on the most general design scenarios of domes (section 8.4). To assess the effect of non-geodesic paths on the structural performance of the dome, we calculate and compare the performance factors of non-geodesics-based optimal domes for various slippage coefficients and polar opening radii. The shell thicknesses are determined by the combination of a strength criterion and the geometric (winding) condition. Lastly, the distributions of laminate stresses are obtained in order to illustrate that non-geodesics-based optimal domes are relatively thinner than the geodesics-based ones, mainly triggered by the efficient utilization of the laminate strength.

8.2 Optimal Meridian Profiles

In this section we provide the governing equations for determining the dome profiles based on the optimality condition and non-geodesic roving trajectories. The geometry and loads of a generic shell of revolution is given in Fig. 8.1. The classical lamination theory [23] is employed in this study, that is, the role of the matrix is indeed considered. To satisfy the optimality condition, equation (18), the domes should have equal shell strains.

Under an internal pressure P , the in-plane shell forces N_φ , N_θ are given by [24]:

$$N_\varphi = \frac{Pr\sqrt{1+r'^2}}{2}, \quad N_\theta = \frac{Pr\sqrt{1+r'^2}}{2} \left(2 + \frac{rr''}{1+r'^2}\right) \quad (8.1)$$

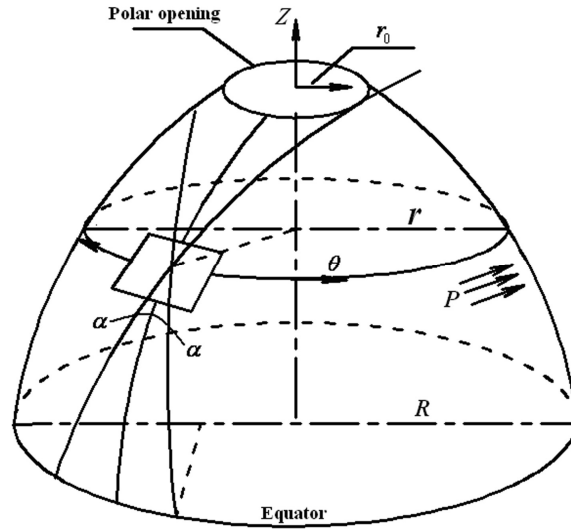


Fig. 8.1: Geometry and loads of a dome head

We consider here dome shells made by winding of angle-ply rovings. Recalling the optimality condition, equation (3.48), the ratio of the biaxial shell forces N_θ / N_ϕ can be determined:

$$\frac{N_\theta}{N_\phi} = \frac{1 - (1-k) \cos^2 \alpha}{k + (1-k) \cos^2 \alpha} \quad (8.2)$$

where:

$$k = \frac{E_2(1+\nu_{12})}{E_1(1+\nu_{21})} \quad (8.3)$$

We introduce now:

$$\rho = r/R, \quad \zeta = z/R \quad (8.4)$$

Substituting equations (8.1) and (8.4) into (8.2), the differential equation which links the geometry, the fiber angle and the material properties of the dome shell can be formulated by:

$$\frac{d^2 \rho}{d\zeta^2} = \left[\frac{1 - (1-k) \cos^2 \alpha}{k + (1-k) \cos^2 \alpha} - 2 \right] \cdot \frac{1 + \rho'^2}{\rho} \quad (8.5)$$

where ρ' is the first derivative of ρ with respect to ζ . Substitution of equation (8.5) into the non-geodesic equation (2.75) results in:

$$\frac{d\alpha}{d\zeta} = \frac{\lambda[k + 2(1-k) \cos^4 \alpha]}{\rho \cos \alpha [k + (1-k) \cos^2 \alpha]} - \frac{\rho' \cdot \tan \alpha}{\rho} \quad (8.6)$$

For the creation of C^1 continuity for the roving path when passing the equator, the derivative of the winding angle must have the same value as the derivative of a geodesic path at exactly that place. Therefore, the slippage coefficient at that point should be equal to zero.

For this reason we introduce the following distribution for the slippage coefficient (Fig. 8.2):

$$\lambda = c \cos\left(\frac{\pi}{2} \cdot \frac{\rho - \rho_0}{1 - \rho_0}\right) \quad (8.7)$$

where c is a constant which in fact represents the top value of the slippage coefficients (Friction between the fiber and the supporting surface). Substituting equation (8.7) into (8.6) gives:

$$\frac{d\alpha}{d\zeta} = c \cos\left(\frac{\pi}{2} \cdot \frac{\rho - \rho_0}{1 - \rho_0}\right) \left\{ \frac{k + 2(1-k) \cos^4 \alpha}{\rho \cos \alpha [k + (1-k) \cos^2 \alpha]} \right\} - \frac{\rho' \cdot \tan \alpha}{\rho} \quad (8.8)$$

Simultaneous solution of the system of differential equations (8.5) and (8.8) will finally provide the optimal meridian profiles and related winding angle distributions along the coordinate ζ . The initial set of values consists of $\zeta_0 = 0, \rho_{\text{eq}} = 1, \rho_{\text{eq}}' = 0$.

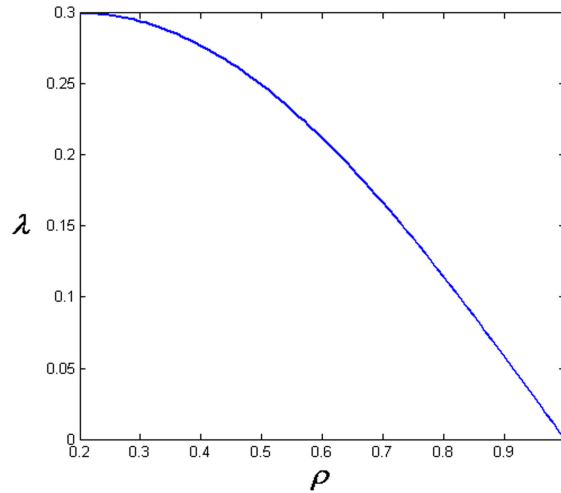


Fig. 8.2: Distribution of slippage coefficient ($c=0.3, \rho_0=0.2$)

For a given polar radius ρ_0 , the resulting meridian profile will strongly depend on the value of c and the initial winding angle α_{eq} . The $\{c, \alpha_{\text{eq}}\}$ -parameter set is able to completely determine the optimal meridian shapes of non-geodesics-based domes for the given distribution for the slippage coefficient. One should note that the slippage coefficient and the winding angle are assumed to be constant through the thickness direction.

8.3 Feasible Intervals

As previously stated, the optimal dome geometry is in essence governed by equation (8.5) for which the winding angle development is determined by equation (8.8). Therefore, the

Chapter 8

parameter set $\{k, \rho_0, c\}$ is able to entirely capture a particular design case.

As the fiber trajectory approaches the polar opening, the winding angle α should attain 90° . Therefore, for $\rho = \rho_0$, we require that $\alpha = 90^\circ$. Depending on the $\{k, \rho_0, c\}$ -combinations, the system of equations (8.5) and (8.8) might run into imaginary solutions for $\rho > \rho_0$. Hence, for a given ρ_0 and c , there is a (minimum) value for k , able to guarantee the existence of a real-valued solution for the system of equations (8.5) and (8.8), over the entire $[\rho_0, 1]$ interval (recall that $\rho=1$ represents the dimensionless equator radius). For the determination of this k -value as a function of $\{\rho_0, c\}$ it can be shown that the worst case scenario is given by $c = 0$. The limiting k -value obtained on basis of this assumption is the most conservative one and will thus guarantee feasible solutions for every positive c . With $c = 0$, equation (8.8) becomes:

$$\sin \alpha = \frac{\rho_0}{\rho} \quad (8.9)$$

Substitution of this expression into the shape equation (8.5), followed by integration gives:

$$\frac{d\rho}{d\zeta} = \frac{1}{\rho^3} \cdot \sqrt{\left[\frac{\rho^2 - (1-k)\rho_0^2}{1 - (1-k)\rho_0^2} \right]^{1+k} - \rho^6} \quad (8.10)$$

The square root argument must be non-negative for $\rho \in [\rho_0, 1]$. This implies that:

$$k \geq [1 - (1-k)\rho_0^2] \cdot \rho_0^{\left(\frac{6}{1+k} - 2\right)} \quad (8.11)$$

With a standard numerical root searching procedure the k -value that nullifies equation (8.10) for a given ρ_0 , can now be determined. The result is depicted in Fig. 8.3, where the feasible $\{k, \rho_0\}$ field is dashed.

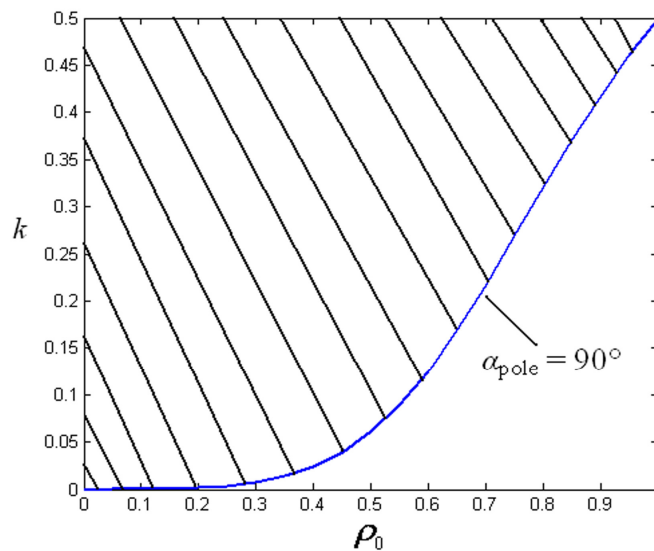


Fig. 8.3: Feasible field of $\{k, \rho_0\}$ -combinations (shaded area)

8.4 Results and Discussion

8.4.1 Structural performance

The performance factor $PF = pV/W$ is used as an index for rating pressure vessels, where p , V and W are the burst pressure, the internal volume and the shell weight, respectively. Accordingly, the performance factor of a dome is given by:

$$PF = \frac{p \int_0^{z_p} \pi r^2 dz}{\gamma \cdot \int_0^{z_p} 2\pi r t \sqrt{1+r'^2} dz} \quad (8.12)$$

where γ is the specific weight of the used composite material; z_p is the height of the dome, which can be determined by solving the system of equations (8.5) and (8.8) for the given $\{c, \alpha_{eq}\}$ combination. The dimensionless performance factor and thickness are defined as:

$$\overline{PF} = PF \cdot \frac{\gamma}{Y_T}, \quad \bar{t} = \frac{2Y_T}{pR} \cdot t \quad (8.13)$$

where Y_T is the tensile strength, transverse to fibers.

Substitution of equation (8.13) into (8.12) yields:

$$\overline{PF} = \frac{\int_0^{\zeta_p} \rho^2 d\zeta}{\int_0^{\zeta_p} \rho \sqrt{1+\rho'^2} \cdot \bar{t} d\zeta} \quad (8.14)$$

Recalling equation (7.6), the laminate thickness along the meridional direction is formulated as:

$$\frac{t}{t_{eq}} = \frac{1}{\rho} \cdot \frac{\cos \alpha_{eq}}{\cos \alpha} \quad (8.15)$$

Substitution of equation (8.15) into (8.14) leads to the final form of the objective function:

$$\overline{PF} = \frac{\int_0^{\zeta_p} \rho^2 d\zeta}{\int_0^{\zeta_p} \bar{t}_{eq} \cdot \sqrt{1+\rho'^2} \cdot \frac{\cos \alpha_{eq}}{\cos \alpha} d\zeta} \quad (8.16)$$

8.4.2 Determination of laminate thickness

The on-axis stress components in an individual layer are given by (recall equation (3.29)):

$$\begin{cases} \sigma_1 = \frac{1}{t}(m_{11}N_\varphi + m_{12}N_\theta) \\ \sigma_2 = \frac{1}{t}(m_{21}N_\varphi + m_{22}N_\theta) \\ \tau_{12} = \frac{1}{t}(m_{31}N_\varphi + m_{32}N_\theta) \end{cases} \quad (8.17)$$

where m_{ij} ($i,j=1,2,3$) are given in equation (3.30).

The Tsai-Wu failure criterion [25] is here employed:

$$F = F_i\sigma_i + F_{ij}\sigma_i\sigma_j \leq 1 \quad (i, j = 1, 2, 6) \quad (8.18)$$

We introduce:

$$\bar{t} = \frac{2Y_T}{PR} \cdot t, \quad \bar{N}_\varphi = \left(\frac{2}{PR}\right) \cdot N_\varphi, \quad \bar{N}_\theta = \left(\frac{2}{PR}\right) \cdot N_\theta \quad (8.19)$$

Substituting equation (8.16) into (8.18) and plugging the dimensionless variables in equation (8.19) into the results, leads to a quadratic failure criterion in terms of the dimensionless thickness:

$$\begin{aligned} & \bar{t}^{-2} - \bar{t}Y_T[F_1(m_{11}\bar{N}_\varphi + m_{12}\bar{N}_\theta) + F_2(m_{21}\bar{N}_\varphi + m_{22}\bar{N}_\theta)] \\ & - Y_T^2[F_{11}(m_{11}\bar{N}_\varphi + m_{12}\bar{N}_\theta)^2 + F_{22}(m_{21}\bar{N}_\varphi + m_{22}\bar{N}_\theta)^2 \\ & + F_{66}(m_{31}\bar{N}_\varphi + m_{32}\bar{N}_\theta)^2 + 2F_{12}(m_{11}\bar{N}_\varphi + m_{12}\bar{N}_\theta)(m_{21}\bar{N}_\varphi + m_{22}\bar{N}_\theta)] \geq 0 \end{aligned} \quad (8.20)$$

where the dimensionless in-plane shell forces are given by:

$$\bar{N}_\varphi = \rho\sqrt{1 + \rho'^2}, \quad \bar{N}_\theta = \rho\sqrt{1 + \rho'^2} \left(2 + \frac{\rho\rho''}{1 + \rho'^2}\right) \quad (8.21)$$

When a meridian shape and related non-geodesic trajectory are determined, the minimally required strength-dominated thickness $t(\rho)$ at each point assigned on the dome is evaluated by solving equation (8.20). Then, the equatorial thicknesses $t_{eq}(\rho)$ corresponding to each $t(\rho)$ are calculated using the “geometric” equation (8.15), and their maximum value t_{eqmax} is selected as the final shell thickness at the equator:

$$\bar{t}_{eqmax} = \max_{\rho_0 \leq \rho \leq 1} \left[\frac{\rho \cos \alpha(\rho)}{\cos \alpha_{eq}} \bar{t}(\rho) \right] \quad (8.22)$$

Once t_{eqmax} is obtained, the dimensionless performance factor \overline{PF} can be computed by equation (8.16) according to the Gaussian quadrature rule [26].

8.4.3 Meridian shapes

In the numerical solution procedure, the goal is now to provide a pair of design variables $\{c, \alpha_{eq}\}$ that ensures a winding angle of 90° at exactly the polar opening which should be achievable. Here c must belong to a predetermined feasible friction interval $\{-\mu, \mu\}$. It should be noted here that the slippage coefficient λ could be negative as well [27]. The influence of k on the resulting meridian profile is demonstrated in Fig. 8.4 for $\rho_0 = 0.4$. The continuous lines denote the non-geodesics-based optimal meridians and the dashed lines stand for the geodesics-based optimal meridians (i.e. $c \equiv 0$). The optimal meridian profile is additionally governed by the material anisotropy parameter k . Such an optimal dome would have a spherical shape in the case of isotropic materials ($k = 1$). In general, due to the anisotropic character of the reinforced wall the resulting meridian shape is oblate-spherical. For a vessel loaded only by internal pressure, the “flatness” of the dome is entirely dependent on k . The parameter k can be regarded as an interpolator between two extreme cases: the sphere and the netting solution. The results also show that for the same material anisotropy, the non-geodesics-based optimal dome has a slightly smaller volume and lower aspect ratio than the geodesics-based one.

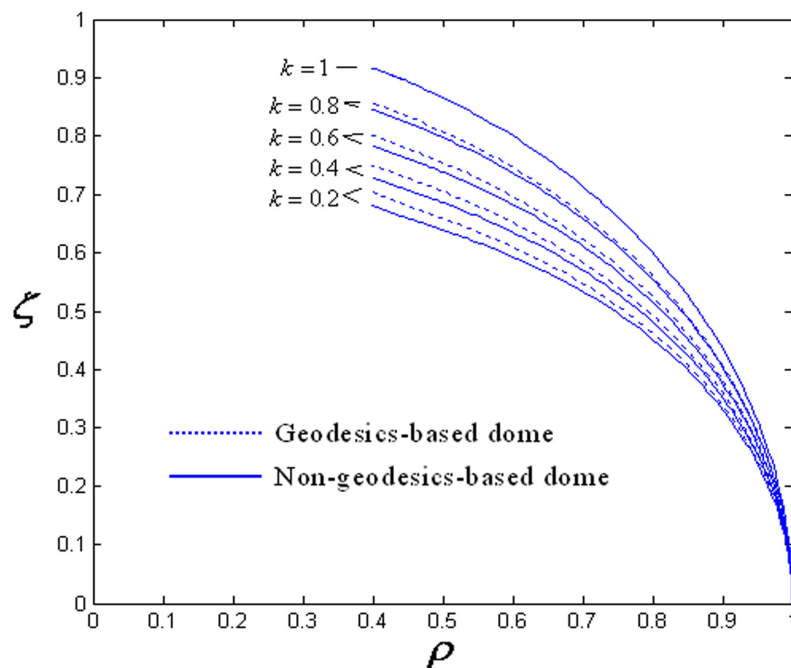


Fig. 8.4: Geodesics and non-geodesics-based optimal meridian profiles for increasing k

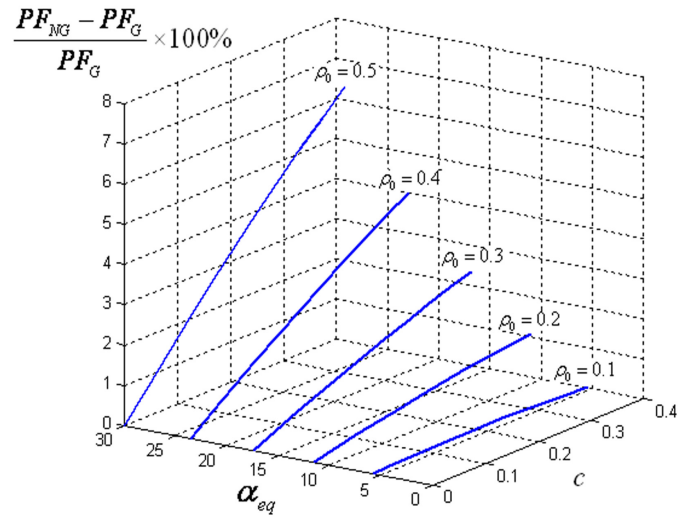
8.4.4 Structural performance evaluation

The evaluation of the structural performance is illustrated by considering composite materials with various fibers and matrices: glass-epoxy ($k = 0.2645$), carbon-epoxy ($k=0.0977$) and aramid-epoxy ($k = 0.0706$). Typical values for the mechanical properties for these composites are given in Tab. 8.1 [28]. Fig. 8.5 presents the gain of the performance factors, triggered by application of non-geodesic trajectories. PF_G and PF_{NG} are the performance factors of the geodesics and non-geodesics-based domes, respectively. It is observed that the structural performance of the dome improves with the coefficient c (top value of the assumed distribution of slippage coefficient). The performance factor of a non-geodesics-based aramid-epoxy dome for $\rho_0=0.5$ shows about 13.7% increase as compared to the geodesics-based one. It is therefore suggested that the maximum allowable coefficient of friction μ should be selected as the optimal value of c . For the winding process however, a slightly reduced value for μ is rather desirable (e.g. multiply μ with a safety factor), in order to ensure the stability of fibers. The results also indicate that the increase rate of the performance factor can be further improved by using composites of which the orthotropy tends to the netting configuration ($k = 0$).

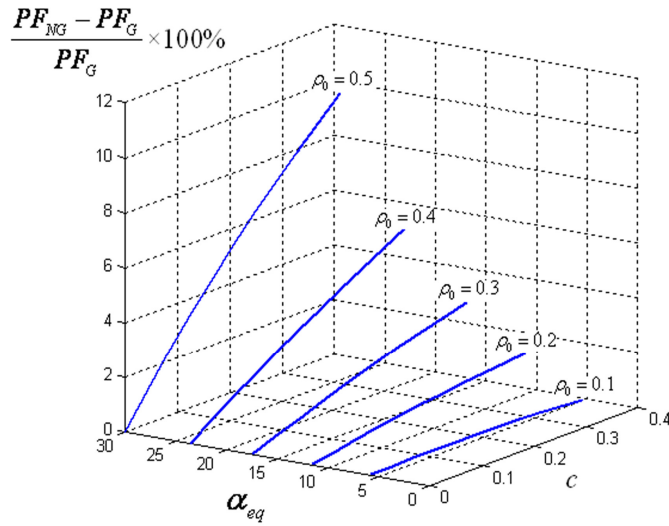
Tab. 8.1: Typical properties of unidirectional composites [28]

Properties	Glass-epoxy	Carbon-epoxy	Aramid-epoxy
Longitudinal modulus (GPa)	60	140	95
Transverse modulus (GPa)	13	11	5.1
Shear modulus (GPa)	3.4	5.5	1.8
Poisson's ratio ν_{12}	0.3	0.27	0.34
Longitudinal tensile strength (MPa)	1800	2000	2500
Transverse tensile strength (MPa)	40	50	30
Longitudinal compressive strength (MPa)	650	1200	300
Transverse compressive strength (MPa)	90	170	130
In-plane shear strength (MPa)	50	70	30

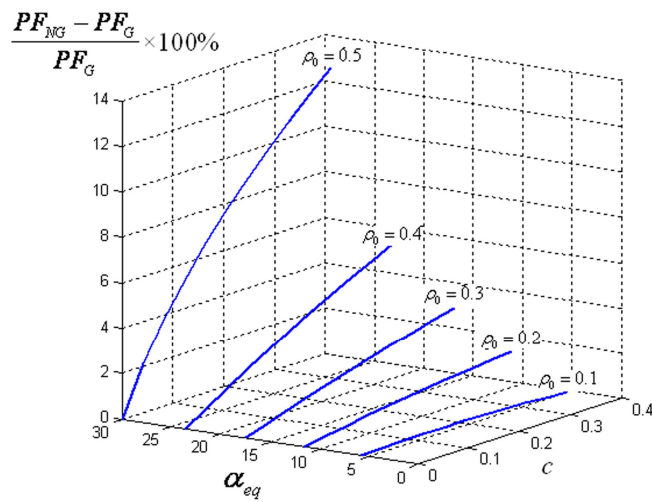
Continuum-based Domes for Pressure Vessels



(a)



(b)



(c)

Fig. 8.5: Increase rates (in percent) of the performance factors that non-geodesics can gain for domes made of (a) glass-epoxy; (b) carbon-epoxy; and (c) aramid-epoxy

Chapter 8

Assuming that the allowable coefficient of friction is 0.3, Tab. 8.2 lists the values of the design parameters $\{c, \alpha_{eq}\}$ for geodesics and non-geodesics-based optimal domes with various polar opening radii. Fig. 8.6 illustrates the winding angle developments on the domes for various c values [0-0.3]. The results show that the winding angle rises from a relatively small value at the equator to 90° at the polar opening region, and it reduces with increasing c . The tangential requirement at the polar region for the roving paths is perfectly satisfied. Fig. 8.7 depicts the distributions of laminate stresses referred to the material coordinates for geodesics and non-geodesics-based optimal domes ($c = 0.3, \rho_0 = 0.4$). It appears that the σ_T/Y_T is much higher than σ_L/X_T and that structural failure is always triggered by the transverse stress at the region near the dome equator. The results indicate that the laminated shell determined by non-geodesics produces higher stresses than the one relying on geodesics. Fig. 8.8 gives the distributions of ply failure level for geodesics and non-geodesics-based optimal domes. Apparently, the laminate strength of the dome is more efficiently utilized by using non-geodesics. Therefore, the non-geodesics-based optimal dome is relatively thinner than the geodesics-based one, as shown in Fig. 8.9.

Tab. 8.2: Values of design parameters $\{c, \alpha_{eq}\}$ for various polar radii (Carbon-epoxy)

Design parameters	$\rho_0 = 0.1$	$\rho_0 = 0.2$	$\rho_0 = 0.3$	$\rho_0 = 0.4$	$\rho_0 = 0.5$
c	0.3	0.3	0.3	0.3	0.3
α_{eq} for geodesics ($^\circ$)	5.7392	11.5370	17.4576	23.5782	30.0000
α_{eq} for non-geodesics ($^\circ$)	0.3505	5.9366	11.7675	17.8789	24.2987

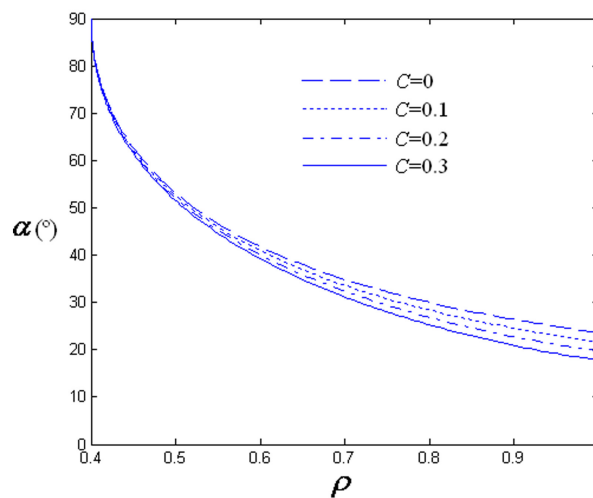
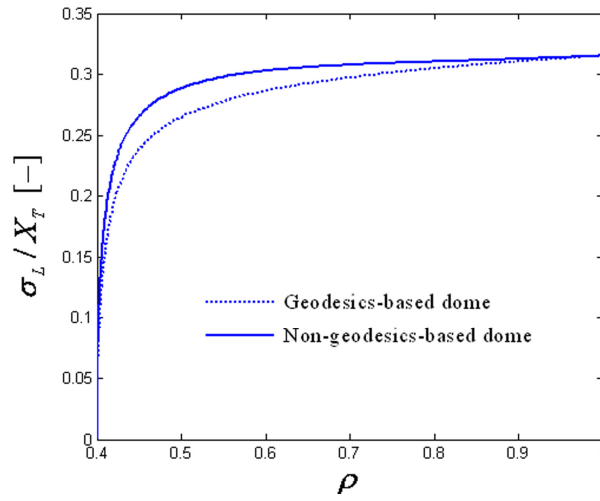
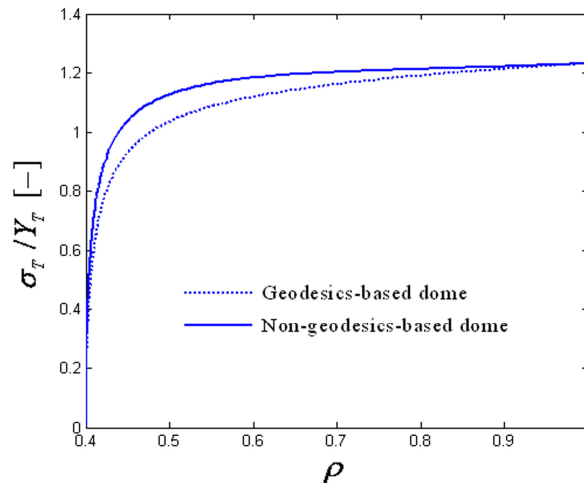


Fig. 8.6: Winding angle developments for various slippage coefficients ($\rho_0=0.4$)

Continuum-based Domes for Pressure Vessels



(a)



(b)

Fig. 8.7: Laminate stresses referred to the material principle axes ($c=0.3, \rho_0=0.4$): (a) longitudinal stress; and (b) transverse stress

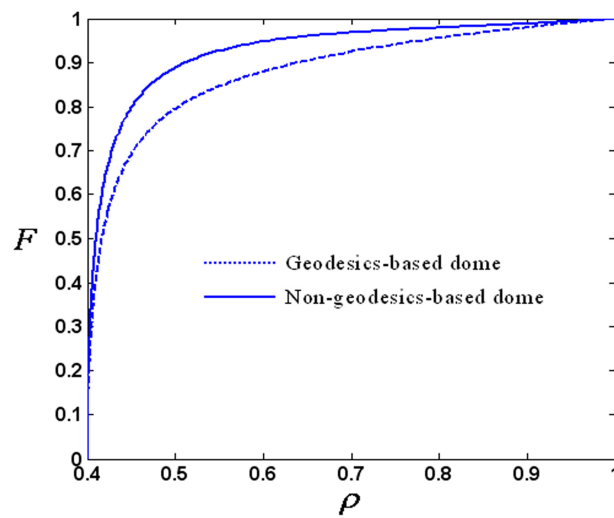


Fig. 8.8: Distributions of the failure level for geodesics and non-geodesics-based domes

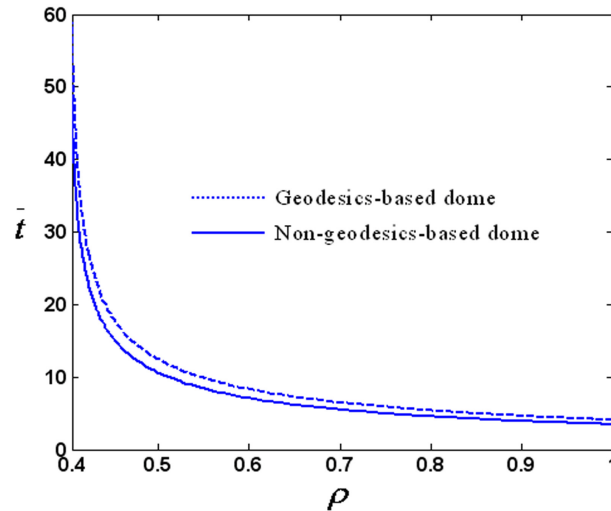


Fig. 8.9: Thickness distribution for geodesic and non-geodesic optimal domes

8.5 Conclusions

The main goal of this paper is to outline a design method for determining the optimal meridian shape and related structural efficiency for non-geodesically overwound domes, and to evaluate the effect of the application of non-geodesic trajectories on the geometry and structural performance of domes. With the aid of the minimum strain energy criterion, an explicit optimality relation, which relates the roving angle and the shell stress ratio, is derived with the material anisotropy parameter k . A specific function is chosen to describe the distribution of the slippage coefficient along the coordinate ρ for the desired non-geodesic paths, in order to ensure C^1 continuity of the roving paths when passing the dome-cylinder conjunction. The optimal meridian shapes of non-geodesics-based domes have been outlined for various material anisotropy parameters k , based on the continuum lamination theory and the equal shell strains condition. The laminate thickness distributions are determined using the Tsai-Wu failure criterion, and the dimensionless performance factors for geodesics and non-geodesics-based optimal domes have been respectively calculated, in order to demonstrate the gain in structural performance that the non-geodesics can result in. The on-axis stress of the laminated shells designed by the geodesic and non-geodesic are respectively presented to show that the non-geodesic paths determined here maximize the utilization of laminate strength and consequently minimize the shell thickness. It is concluded that the structural efficiency of filament-wound domes can be improved by using non-geodesic paths, and that the performance factor increases with the maximum slippage coefficient c . The results also reveal that the non-geodesics-based domes form a preferable

alternative for storage spaces having limited height.

Although the shape differences in geodesics and non-geodesics-based meridian profiles are relatively small, the available design space is sufficiently enlarged. This increase of possibilities particularly reflects on improved structural performance, while still being able to satisfy the conditions of the winding process.

References

1. Krikanov AA. Composite pressure vessels with higher stiffness. *Compos Struct* 2000; 48: 119-27.
2. Zu L, Koussios S, Beukers A. Design of filament-wound isotenoid pressure vessels with unequal polar openings. *Compos Struct* 2010; 92: 2307-13
3. Koussios S, Bergsma OK, Beukers A. Filament Winding Part 1: Determination of the Wound Body Related Parameters. *Comp Part A: Appl Sci Manuf* 2004; 35(2): 181-95.
4. Jong de Th. A theory of filament wound pressure vessels. Report LR-379. Structures and materials laboratory, Faculty of Aerospace Engineering, Delft University of Technology. Delft, April, 1983.
5. Hojjati M, Safavi AV, Hoa SV. Design of domes for polymeric composite pressure vessels. *Compos Eng* 1995; 5(1): 51-59.
6. Vasiliev VV, Krikanov AA. New generation of filament-wound composite pressure vessels for commercial applications. *Compos Struct* 2003; 62(3): 449-59.
7. Vasiliev VV, Morozov EV. *Advanced mechanics of composite materials*. UK: Elsevier Ltd, 2007.
8. Liang CC, Chen HW, Wang CH. Optimum design of dome contour for filament-wound composite pressure vessels based on a shape factor. *Compos Struct* 2002; 58(4): 469-82.
9. Zu L, Koussios S, Beukers A. Shape optimization of filament wound articulated pressure vessels based on non-geodesic trajectories. *Compos Struct* 2010; 92(2): 339-46.
10. Fukunaga H, Uemura M. Optimum design of helically wound composite pressure vessels. *Compos Struct* 1983; 1(1): 31-49.
11. Tackett EW, Merrell GA, Kulkarni SB. Carbon pressure vessel performance with changing dome profiles. In: *Proc. of 20th AIAA/SAE/ASME Joint Propulsion Conference*, Cincinnati, OH, June 11-13, 1984.
12. Di Vita G, Farioli M, Marchetti M. Process simulation in filament winding of composite structures. In: W.P. de Wilde, W.R. Blain, (eds). *Composite Materials Design and*

Chapter 8

- Analysis. Berlin: Springer-Verlag, 1990. p.19-37.
13. Blachut J. Externally pressurized filament wound domes – scope for optimization. *Computers & Structures* 1993, 48(1): 153-60.
 14. Blachut J. Filament wound torispheres under external pressure. *Compos Struct* 1993; 26: 47-54.
 15. Waldman, W., Heller, M., Chen, G.: Optimal free-form shapes for shoulder fillets in flat plates under tension and bending. *Int J Fatigue* 23, 185–90 (2001).
 16. Heller, M., Kaye, R., Rose, L.R.: A gradientless finite element procedure for shape optimization. *J Strain Anal Eng Des* 34(5), 323–36 (1999)
 17. Tran, D., Nguyen, V.: Optimal hole profile in finite plate under uniaxial stress by finite element simulation of Durelli's photoelastic stress minimisation method. *Finite Elem Anal Des* 32, 1–20 (1999)
 18. Zwillinger, D. "Clairaut's Equation." §II.A.38 in *Handbook of Differential Equations*, 3rd ed. Boston, MA: Academic Press, pp. 120 and 158-160, 1997.
 19. Koussios S, Beukers A, Stathis PT. Manufacturability of composite pressure vessels: Application of non-geodesic winding. In: *Proceedings of the 16th International Conference on Composite Materials (ICCM/16)*, Kyoto, Japan, July 2007.
 20. Koussios S. *Filament Winding: a Unified Approach*. PhD Thesis Report. Design & Production of Composite Structures, Faculty of Aerospace Engineering, Delft University of Technology. Delft University Press, 2004.
 21. Bunakov VA, Radovinskii AL. Rationalization of the shape of wound membrane shells of revolution composed of high-modulus material. *Mechanics of Composite materials* 1975; 11(5): 704-9.
 22. Kim CU, Kang JH, Hong CS, Kim CG. Optimal design of filament wound structures under internal pressure based on the semi-geodesic path algorithm. *Compos Struct* 2005; 67: 443-52.
 23. Kaw AK. *Mechanics of composite materials*, 2nd Edition, Boca Raton: CRC Press, 2006.
 24. C. R. Calladine. *Theory of Shell Structures*. Cambridge University Press, Cambridge, UK. 1989
 25. Tsai SW, Wu EM. A general theory of strength for anisotropic materials. *Journal of Composite Materials* 1971; 5(1):58-80.
 26. Gil, Amparo; Segura, Javier; Temme, Nico M. (2007), "§5.3: Gauss quadrature", *Numerical Methods for Special Functions*, SIAM
 27. Koussios S, Bergsma OK, Mitchell G. Non-geodesic filament winding on generic shells

Continuum-based Domes for Pressure Vessels

- of revolution. Proc. IMechE Part L: J. Materials: Design and Applications 2005; 219(1):25-35.
28. Tsai, SW, Hahn HT. Introduction to composite Materials. Westport, Conn.: Technomic Publishing Company, Inc., 1980.

Chapter 9

Non-geodesics-based Circular Toroidal Pressure Vessels

9.1 Introduction

Previous investigations on filament-wound toroidal pressure vessels have merely considered the winding patterns based on geodesic trajectories, and overlooked the application of non-geodesic paths to the design of toroids. In 1963, Marketos presented geodesic-isotensoid cross-sections for the optimum toroidal pressure vessels [1]. Zu et al. [2, 3] proposed a design method for determining the fiber paths and laminated configuration of filament-wound toroidal vessels using a two-level optimization approach, and developed a CAD system for their design and production. Li et al. [4] outlined a full mathematical approach to the design of overwound toroids using the membrane shell theory, considering the load-bearing capability of the wound layer and its interaction with the metallic liner. Mitkevich et al. [5] developed a model for calculating the winding trajectory and the profile shape of a mandrel and its transformation into given surface elements, based on the example of a toroidal membrane. Chen [6] determined the equations to quantify the burst pressure of toroidal vessels with various types of winding, based on the equal-strains condition. Yu et al. [7] provided a winding pattern for geodesically overwound toroidal vessels and carried out the computer simulation for such pattern. Koussios [8] and Zu [9] presented the cross-sectional shapes of isotensoid toroids and compared the structural efficiency of such toroids with the circular ones. A key factor in their design process is the creation of filament-wound toroidal pressure vessels that are mainly based on the principle of geodesic winding, the netting theory and the equal-strains condition.

Chapter 9

Geodesics fiber paths show great stability on a curved surface and calculability with the Clariaut equation [10]. However, as geodesics are entirely determined by the underlying meridian profile and initial winding angle, their utilization is certainly limiting the available design possibilities [11, 12]. One of the disadvantages of the application of geodesics is that the structural efficiency of a toroidal vessel is entirely predetermined under a given initial condition. A typical example of this restriction is the limited space for improving the structural performance. However, the possibility appears now for modifying the fiber trajectories by the utilization of the friction available between the fiber bundles and the supporting surface. Furthermore, previous studies have failed to consider the optimal design of the winding trajectories based on the continuum theory of orthotropic laminates. The method based on the netting theory has a major defect in that design calculations are based on fiber strength alone, and the matrix contribution is considered negligible. In addition, despite the fact that toroidal vessels, which are governed by the condition of equal shell strains or, in other words, zero shear stress at lamina level, do show great performance, the rigorous friction coefficients required during the winding process certainly confine the smaller relative bending radius a toroids can achieve. It is thus desirable to exploit friction-based non-geodesics to enlarge the design space of circular toroidal vessels and determine the most efficient winding paths for such structures using the continuum theory.

In this chapter we outline a design-oriented method for determining the optimal non-geodesic fiber trajectories for filament-wound circular toroidal vessels under uniform internal pressure. Firstly we present the system of differential equations for determining non-geodesics on the surface of circular toroids. Then, the optimal design for non-geodesically overwound toroids is outlined for obtaining the preferred fiber path, while taking the laminate thickness build-up along the meridional direction into account. The influence of the relative bending radii on the geometry and performance of the optimal non-geodesic paths is also evaluated. Lastly, the calculations and comparisons of structural mass and on-axis stress of laminate shells designed by the optimal geodesics and non-geodesics are carried out to show that non-geodesic paths form a preferable alternative for the design and production of toroidal pressure vessels.

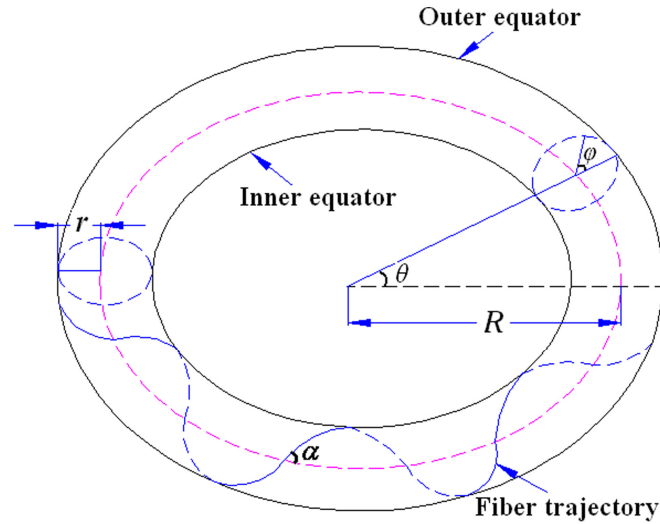


Fig. 9.1: Geometry of a toroidal vessel and its fiber path

9.2 Non-geodesics on a Torus

The vector parameterization of a torus can be given by:

$$\mathbf{S}(\theta, \varphi) = \begin{cases} (R + r \cos \varphi) \cos \theta \\ (R + r \cos \varphi) \sin \theta \\ r \sin \varphi \end{cases} \quad (9.1)$$

where θ and φ stand for the angular coordinates along the parallel and meridional direction of the torus respectively, as shown in Fig. 9.1.

Substitution of equations (4.23) and (4.25) into (2.21), the basic non-geodesic equation for the torus is given by:

$$\frac{d\alpha}{dl} = -\left(\frac{\cos \varphi}{R + r \cos \varphi} \cos^2 \alpha + \frac{1}{r} \sin^2 \alpha\right) \lambda - \frac{\sin \varphi}{R + r \cos \varphi} \cos \alpha \quad (9.2)$$

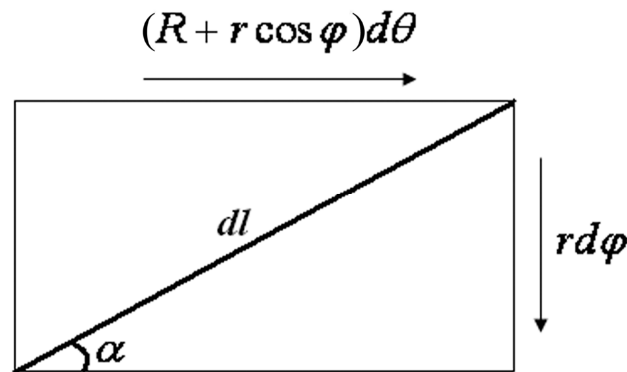


Fig. 9.2: Geometrical relations for θ , φ , l and α

Chapter 9

Since the fiber curve has an orientation α with respect to the parallel circle of the torus, the relation among geometric parameters $d\theta/dl$, $d\varphi/dl$ and α , can be given by (Fig. 9.2):

$$\frac{d\theta}{dl} = \frac{\cos \alpha}{R+r \cos \varphi}, \quad \frac{d\varphi}{dl} = \frac{\sin \alpha}{r} \quad (9.3)$$

Substituting equation (9.3) into (9.2) leads, after some algebraic manipulations, to a system of differential equations for determining non-geodesic trajectories on a circular toroid:

$$\begin{cases} \frac{d\alpha}{d\varphi} = \pm \left[\frac{r \cos \varphi \cos \alpha}{(R+r \cos \varphi) \operatorname{tg} \alpha} + \sin \alpha \right] \lambda - \frac{r \sin \varphi}{(R+r \cos \varphi) \operatorname{tg} \alpha} \\ \frac{d\alpha}{d\theta} = \pm \left[\cos \varphi \cos \alpha + \frac{(R+r \cos \varphi) \operatorname{tg} \alpha \sin \alpha}{r} \right] \lambda - \sin \varphi \end{cases} \quad (9.4)$$

The simultaneous solution of the above system of differential equations will provide the non-geodesic winding trajectories on a torus. Fig. 9.3 shows several winding angle developments for non-geodesics with slippage coefficients ranging from 0 to 0.2. Fig. 9.4 depicts various geodesics ($\lambda = 0$) and non-geodesics ($\lambda \neq 0$) starting from the equally initial winding angle, corresponding to various slippage coefficients.

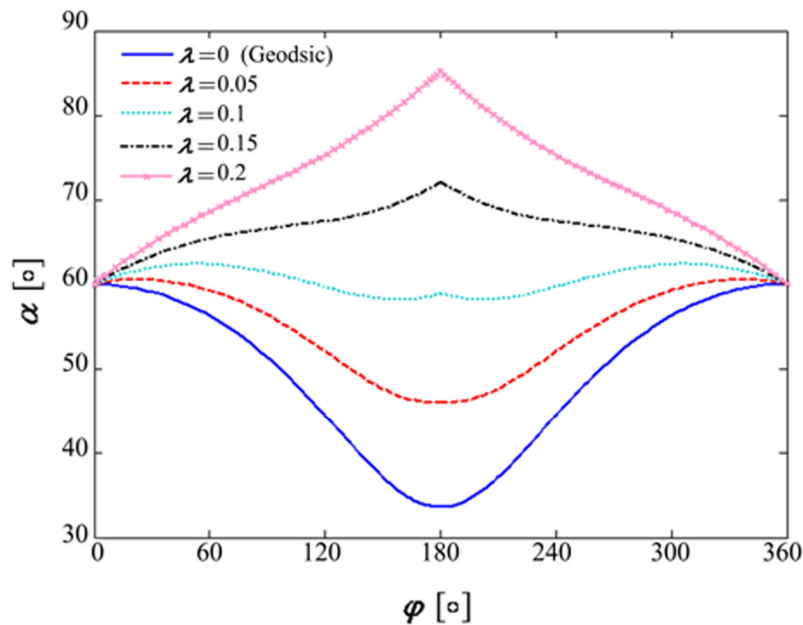
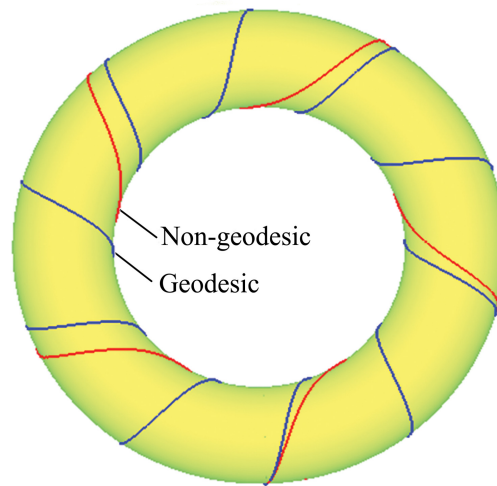
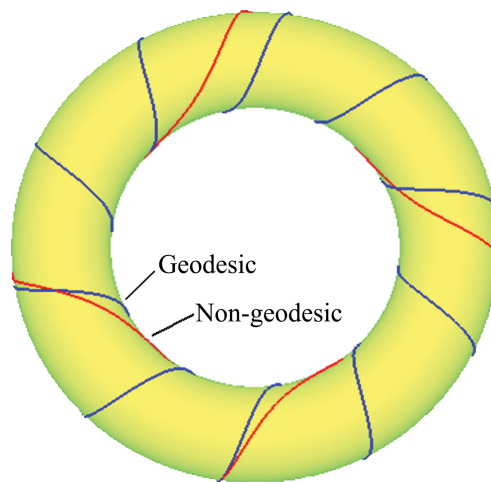


Fig. 9.3: Winding angles developments for non-geodesics with various slippage coefficients

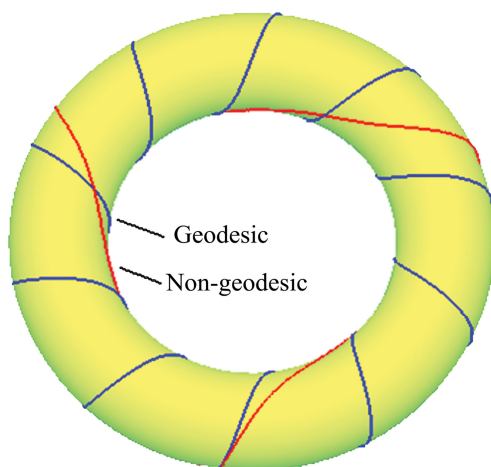
Non-geodesics-based Circular Toroidal Pressure Vessels



(a) $\lambda = 0.1$



(b) $\lambda = 0.15$



(c) $\lambda = 0.2$

Fig. 9.4: Geodesic and non-geodesic trajectories for (a) $\lambda=0.1$; (b) $\lambda=0.15$; (c) $\lambda=0.2$

9.3 Optimal Design for Minimum Structural Mass

In this section, we address the problem of searching the minimum mass of a laminate structure for internally pressurized toroidal vessels. The initial winding angle at the equator and the slippage coefficient of the non-geodesic trajectories are considered as the design variables, as stated by:

$$\mathbf{X} = (\alpha_0, \lambda) \quad (9.5)$$

The laminate mass of a toroidal shell is supposed to be the objective function of the optimal design problem, given by:

$$M = 2\pi r \gamma (R+r) \sin \alpha_0 t_0 \int_0^{2\pi} \csc \alpha d\varphi \quad (9.6)$$

where γ is the density of the used composite laminate, α is a function of meridional coordinate φ , which is given by equation (9.4).

To simplify the mathematical modeling and computation, the following dimensionless variables are introduced:

$$K = \frac{R}{r}, \quad \bar{M} = M \cdot \frac{Y_T}{2\gamma p \pi r^3}, \quad \bar{t} = t \cdot \frac{2Y_T}{pr} \quad (9.7)$$

where K is the so-called relative bending radius, \bar{M} and \bar{t} denote the dimensionless mass and thickness of the toroidal shell, p is the uniform internal pressure, and Y_T is the tensile strength transverse to fibers.

Substituting equation (9.7) into (9.6), the dimensionless mass of a toroidal vessel becomes:

$$\bar{M} = (K+1) \sin \alpha_0 \bar{t}_0 \int_0^{2\pi} \csc \alpha d\varphi \quad (9.8)$$

To keep the fibers stable on a mandrel surface, the winding path must meet the following criterion (recall equation (4.27)):

$$\left| \frac{\frac{d\alpha}{d\varphi} \sin \alpha + \frac{\sin \varphi}{K + \cos \varphi} \cos \alpha}{\frac{\cos \varphi}{K + \cos \varphi} \cos^2 \alpha + \sin^2 \alpha} \right| - \mu \leq 0 \quad (9.9)$$

where μ is the allowable friction coefficient between the fiber bundles and the supporting surface of application.

For the satisfaction of fiber non-bridging condition (2.25), the winding angle α on the concave part ($-1 \leq \cos \varphi < 0$) should comply with the following condition:

$$\frac{-\cos \varphi}{K + \cos \varphi} - \operatorname{tg}^2 \alpha < 0 \quad (9.10)$$

Non-geodesics-based Circular Toroidal Pressure Vessels

The internal resultant forces of the toroidal shell are evaluated using the membrane theory. From the static equilibrium equations of the shell element under internal pressure p , the internal resultant forces in geometric coordinates are given by [13]:

$$N_\varphi = \frac{pr}{2} \cdot \frac{2K + \cos \varphi}{K + \cos \varphi}, \quad N_\theta = \frac{pr}{2} \quad (9.11)$$

where the subscripts φ and θ indicate the meridional and parallel directions, respectively. The membrane shear force vanishes identically in the problem as a result of the axisymmetry of the structure and the load.

The stress components in the material axes for a layer are given by (equation (3.29)):

$$\begin{cases} \sigma_1 = \frac{1}{t}(m_{11}N_\varphi + m_{12}N_\theta) \\ \sigma_2 = \frac{1}{t}(m_{21}N_\varphi + m_{22}N_\theta) \\ \tau_{12} = \frac{1}{t}(m_{31}N_\varphi + m_{32}N_\theta) \end{cases} \quad (9.12)$$

where m_{ij} ($i,j=1,2,3$) are given in equation (3.30).

The FPF mode of the Tsai-Wu failure criterion (recall equation (7.11)) is here used to check the failure of a lamina:

$$F_i \sigma_i + F_{ij} \sigma_i \sigma_j \leq 1 \quad (i, j = 1, 2, 6) \quad (9.13)$$

9.4 Optimization Solution Procedure

The design problem involves minimizing the structural mass M , subjected to the constraint equations (9.9), (9.10) and (9.13). This design procedure is in essence a nonlinear constrained optimization problem. The *SQP* method [14] is here employed to solve the optimization problem. As the fibers proceed from the outer periphery to the inner periphery of the pressure vessel, it is expected that the laminate thickness will grow rapidly. Since the number of fibers passing through the cross section of a slice of the torus at any meridional location is constant, the thickness distribution can be expressed as a function of the meridional coordinate φ as follows (recall equation (4.14)):

$$\bar{t} = \frac{(K+1) \sin \alpha_0}{(K + \cos \varphi) \sin \alpha} \cdot \bar{t}_0 \quad (9.14)$$

When a winding trajectory, which satisfies the constraint conditions, is assigned as a set of design variables in the i^{th} iteration step of optimization procedure, the values of minimum

Chapter 9

thicknesses $t(\varphi)$ required at many points along the non-geodesic path are calculated by solving equation (9.13). The related equatorial thicknesses $t_0(\varphi)$ are evaluated using the “geometric” equation (9.14) and their maximum value $t_{0\max}$ is selected as the real laminate thickness at the equator. Once $t_{0\max}$ is obtained, the thickness distribution on the torus is determined by equation (9.14), and the objective weight M is computed using the Gaussian quadrature rule at each iteration step. The current design point is updated as a new point by this procedure. The above steps are repeated until a termination criterion is satisfied. At each iteration step, the points used for the evaluation are determined by solving the differential equations of non-geodesic trajectories. The flow chart of the solution procedure for determining the thickness distribution of the laminate shell is shown in Fig. 9.5.

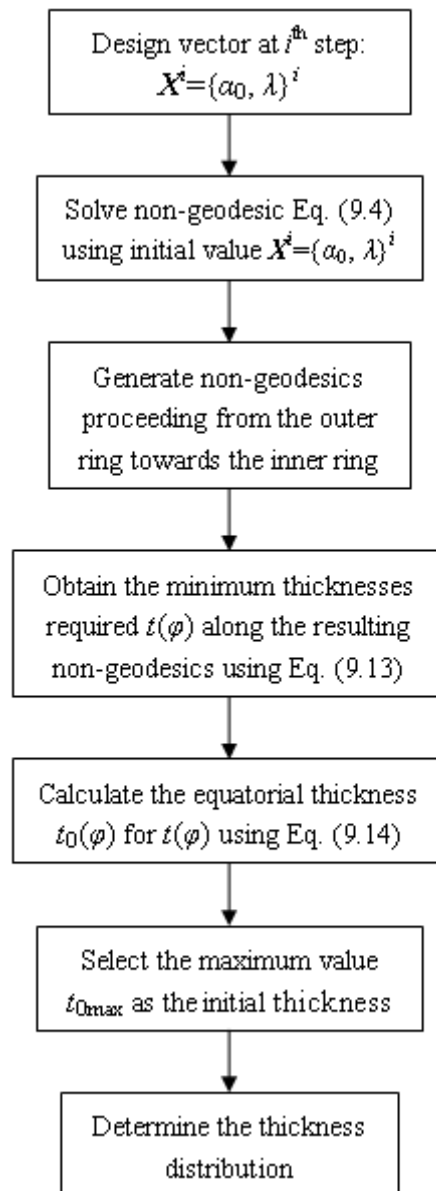
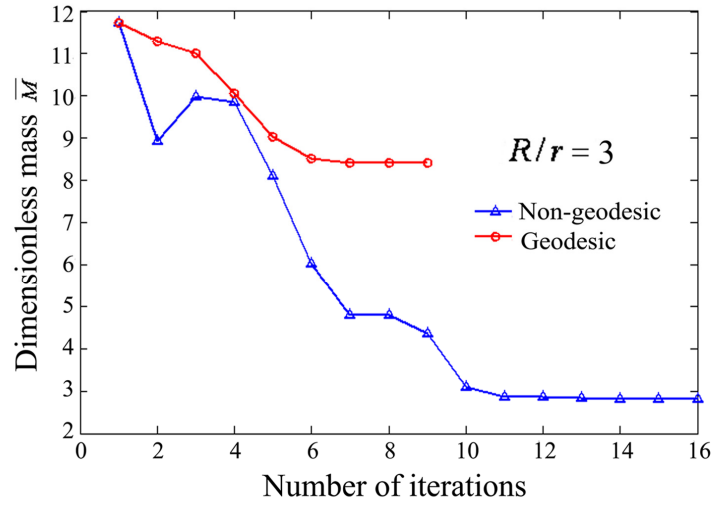


Fig. 9.5: Design procedure for determining the thickness distribution of the toroidal shell

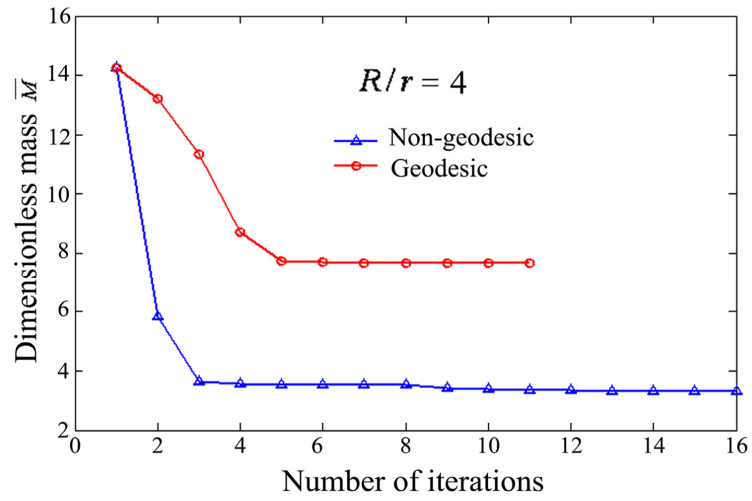
9.5 Results and Discussion

The optimization of the toroidal hydrogen storage vessel is here carried out by considering a collection of tori with various relative bending radii K . The laminate is made of T300/5208 graphite/epoxy the elastic constants of which are $E_1 = 142$ GPa, $E_2 = 10.8$ GPa, $G_{12} = 5.49$ GPa and $\nu_{12} = 0.3$. The strength values are $X_T = 1568$ MPa, $Y_T = 57$ MPa, $X_C = 1341$ MPa, $Y_C = 212$ MPa, and $S = 80$ MPa. The values for the material properties are obtained from Ref. [15].

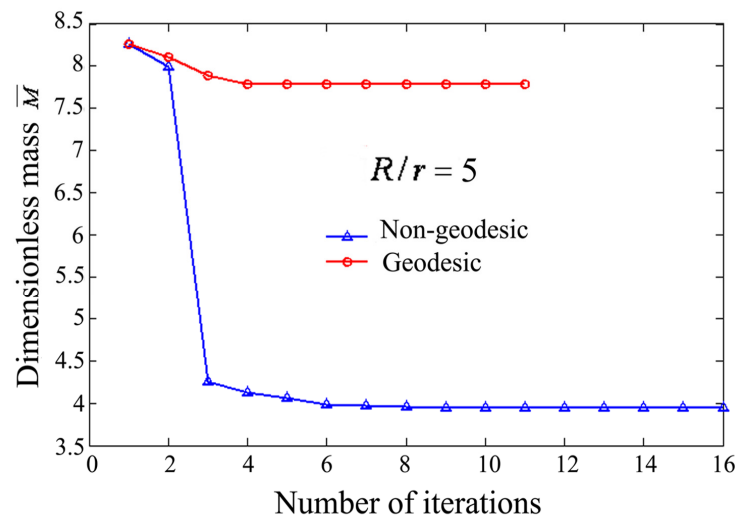
Fig. 9.6 shows the effects of the number of iterations on the values of the objective functions, i.e. dimensionless masses of toroids ($K = 3\sim 6$). It is revealed that the optimization procedure provides both good convergence performance and global searching ability. Since the geometry of geodesics certainly limits the available design possibilities while the non-geodesics give more design freedom by searching the optimal value of the slippage coefficient λ , the difference of masses between geodesics- and non-geodesics-based toroids becomes relatively larger as the number of iterations increases. Fig. 9.7 illustrates the winding angle developments of the optimal non-geodesic and geodesic trajectories along the meridional coordinate φ . The results show that the winding angle determined using the optimal non-geodesics is centralizing in the small range of $50^\circ\text{-}56^\circ$, which is almost identical with the optimal winding angle for internally pressurized cylindrical vessels. Fig. 9.8 shows the winding angle development for $K = 10^5$ and demonstrates that the winding angles of optimal geodesic and non-geodesic paths become identical to each other and tend to the value of the optimal angle of a cylinder subjected to the well-known hoop-to-axial stress ratio of 2. A toroid can actually be regarded as a bent, endless cylinder that saves on the need for material in the end caps. As a shape, it is thus at least as structurally efficient as a cylinder. On the other hand, the optimal geodesic angles lie in a relatively large range, of which the initial angles are always about 60° or even bigger. Therefore, the toroidal vessel obtained using the present method shows better performance as compared to the geodesics-based toroid. At the same time, the fiber path entirely meets the stability-ensuring conditions for the winding process as given in equations (9.9) and (9.10). The simulation results for the optimal fiber trajectories determined by the present method are depicted in Fig. 9.9, where it is demonstrated that the winding pattern satisfies the mathematical principles of winding a torus.



(a)

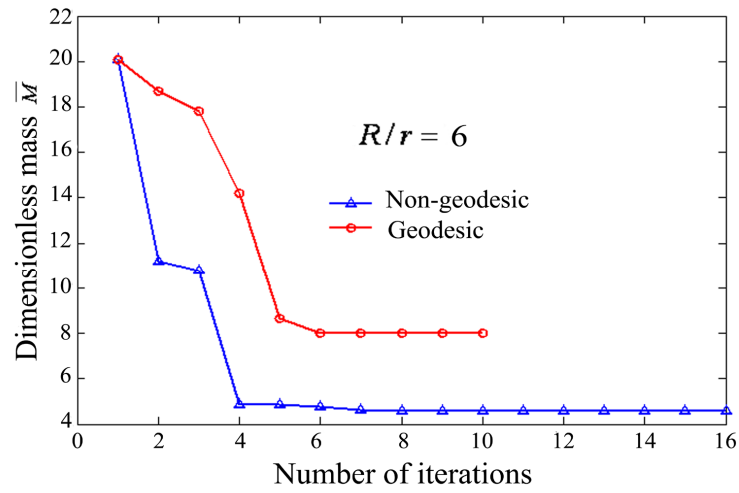


(b)



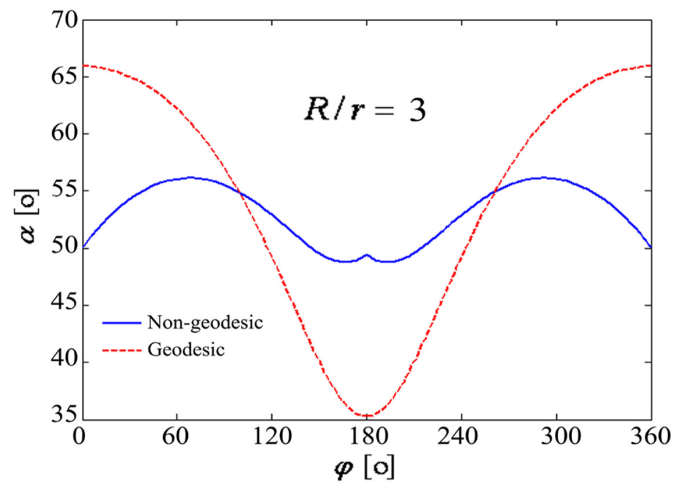
(c)

Non-geodesics-based Circular Toroidal Pressure Vessels

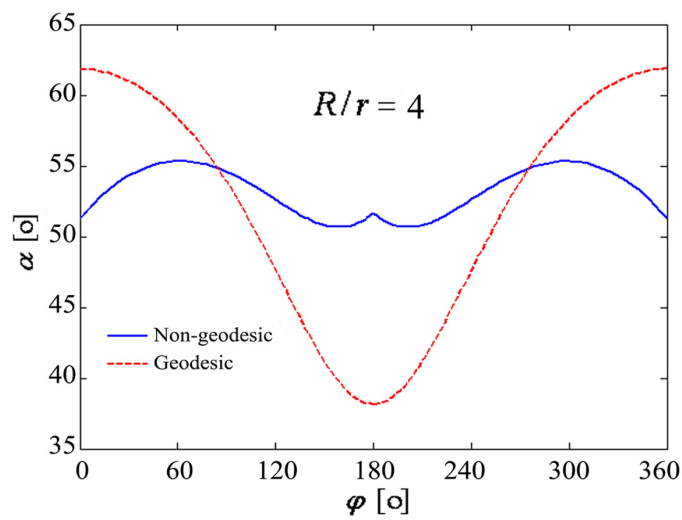


(d)

Fig. 9.6: Effects of the number of iterations on the values of the objective functions \bar{M}



(a) $K=3$



(b) $K=4$

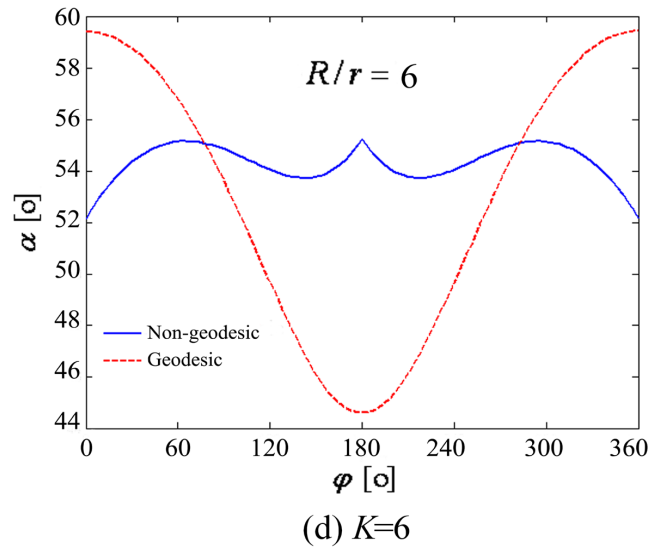
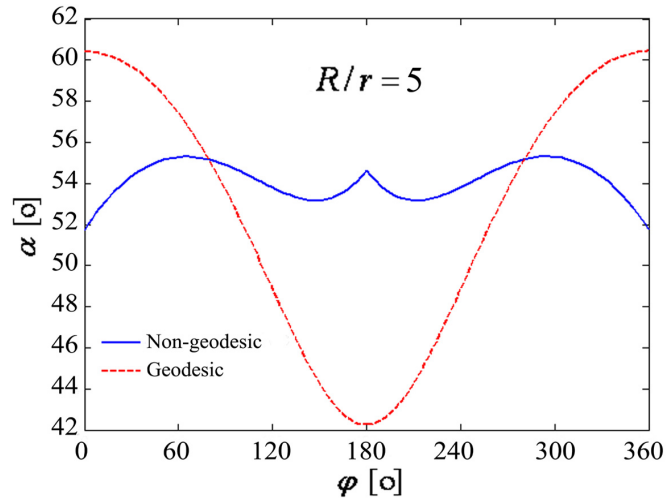


Fig. 9.7: Winding angle developments of the optimal geodesics and non-geodesics for (a) $K = 3$; (b) $K = 4$; (c) $K = 5$ and (d) $K = 6$

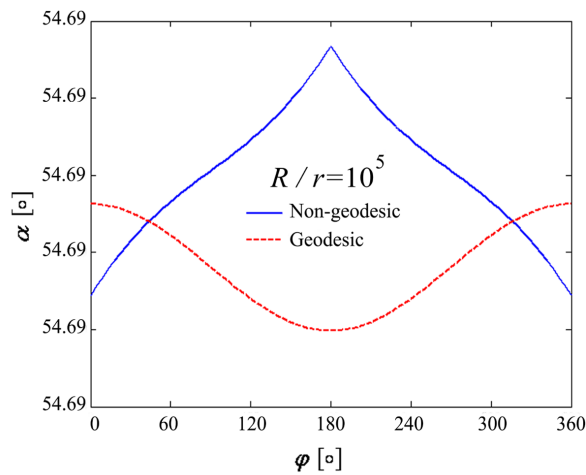


Fig. 9.8: Optimal geodesic and non-geodesic winding angle developments for $K = 10^5$

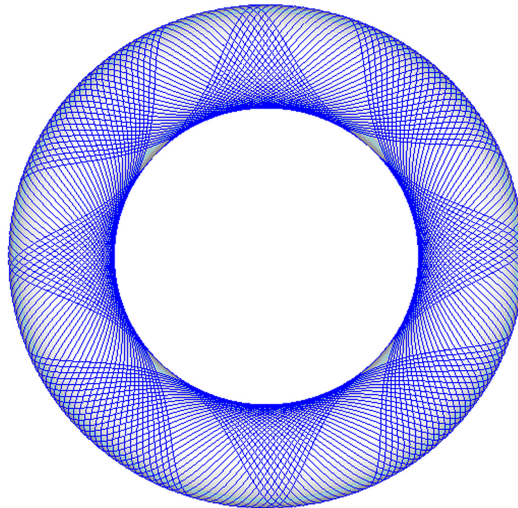


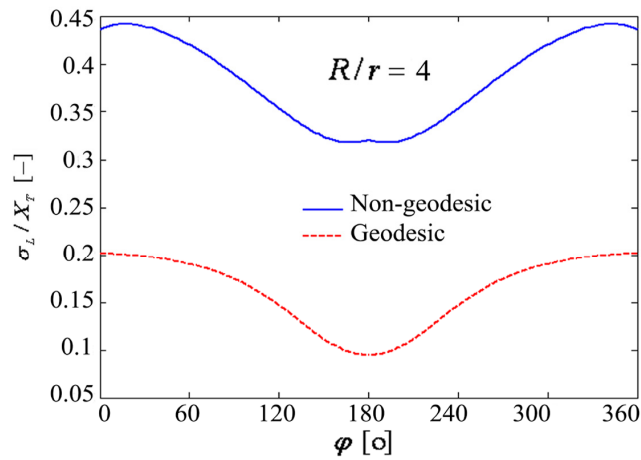
Fig. 9.9: Optimal non-geodesic trajectories determined using the present method

Fig. 9.10 shows the distributions of laminate stresses with respect to material coordinates for toroidal vessels ($K = 4$) determined by the present method and the geodesic winding method. It appears that the σ_T is relatively high and that structural failure is always governed by the transverse stress at the region near the outer periphery. The results indicate that the laminate shell obtained here produces higher stresses than the one relying on the geodesic winding, while the Tsai-Wu criterion is satisfied throughout the whole structure. Therefore, the strength of the toroidal vessel can be maximally utilized. As a result of this, the non-geodesics-based optimal laminate shell of the toroid is considerably thinner than the geodesics-based one, as shown in Fig. 9.11.

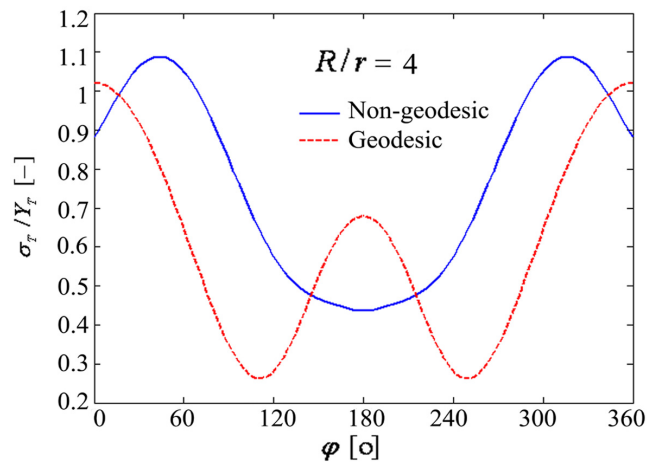
Table 1 lists the optimal values of dimensionless masses and slippage coefficients for the non-geodesics-based optimal toroidal vessels corresponding to the relative bending radii range [3, 8], compared with the masses of geodesics-based optimal toroids. The results show that the toroids determined by the present method are consistently lighter than the ones using geodesic winding. It is revealed that the filament-wound toroidal pressure vessel designed using the optimal non-geodesic trajectories has better structural efficiency and thus higher pressure carrying capacity. It should be noted that the failure criterion (9.13) corresponding to the first ply failure is true for non-geodesics-based circular toroids, because after the matrix failure the angle-ply laminate becomes a mechanism and cannot take the pressure. However, the level of longitudinal stresses in the ply, as given in Fig. 9.10, is rather low (about 0.45 of the ultimate stress). In contrast, geodesic-isotensoid vessels remain able to withstand loading up to fiber failure. Therefore the results showing that non-geodesic vessels are more efficient than geodesic ones do not always hold true, especially when fiber breakage becomes the

Chapter 9

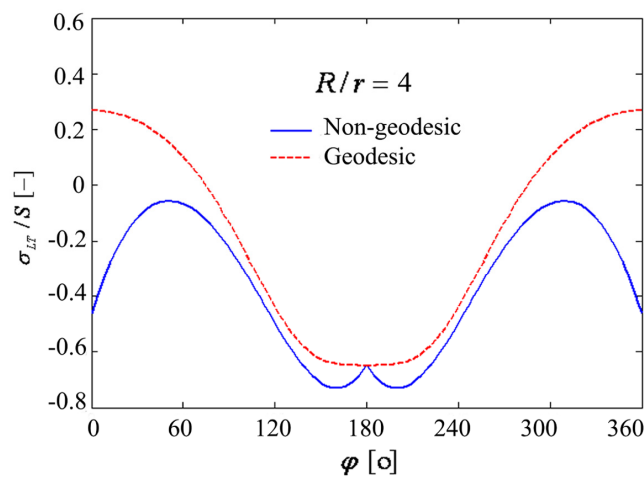
major issue for the failure of a pressure vessel. The optimal geodesic vessel is not circular and works up to fiber failure irrespective of the matrix failure predicted by equation (9.13).



(a) Longitudinal stress



(b) Transverse stress



(c) Shearing stress

Fig. 9.10: On-axis stresses for toroidal vessels ($K = 4$) obtained using the geodesics and non-geodesics: (a) longitudinal stress; (b) transverse stress and (c) shearing stress

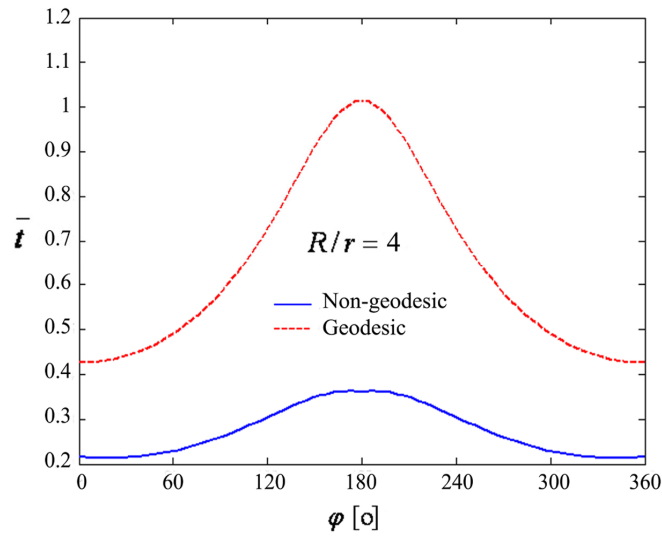


Fig. 9.11: Thickness distributions for the optimal non-geodesic and geodesic toroidal vessels

Tab. 9.1: Optimal values of dimensionless vessel mass \bar{M} and slippage coefficients λ

Relative bending Radius	$K = 3$	$K = 4$	$K = 5$	$K = 6$	$K = 7$	$K = 8$	$K = 100$
Mass for Optimal Geodesics	8.423	7.684	7.786	7.998	8.296	8.656	67.715
Mass for Optimal Non-geodesics	2.777	3.330	3.945	4.578	5.220	5.867	67.088
λ for Optimal Non-geodesics	0.211	0.157	0.136	0.116	0.106	0.097	0.012

9.6 Conclusions

The main goal of this chapter is to provide a design-oriented method for the determination of optimal non-geodesic fiber trajectories and laminate thickness distributions for filament-wound circular toroidal hydrogen storage vessels, and to evaluate the effect of the non-geodesics on the geometry and performance of toroids. The optimization procedure for the minimization of the structural mass of toroidal vessels is outlined based on the continuum theory of laminate composite materials, stability-ensuring winding conditions and the Tsai-Wu failure criterion. The classical lamination theory is employed for the stress analysis and the SQP method is utilized as a non-linear optimization algorithm. In addition, the non-geodesic winding procedure is based on a constant allowable coefficient of friction and is therefore convenient for pressure vessels manufacturing.

As a result of the design procedure, the winding angle distribution of the non-geodesic path

Chapter 9

is similar with that for the cylindrical vessel under a constant biaxial stress ratio of 2, and thus results in better structural performance of toroidal vessels. The optimization procedure is rapidly converging to stable solutions while the resulting fiber trajectories satisfy all design constraints. Compared with the optimal geodesic paths, the results also demonstrate that the non-geodesic paths determined here maximize the utilization of laminate strength and consequently minimize the mass of the circular toroid. Hence, the structural efficiency of toroidal vessels can be remarkably improved using the present design method. Furthermore, the outlined non-geodesic trajectories in combination with the optimization method provide a straightforward tool for the elaboration of winding patterns for filament-wound toroidal hydrogen storage vessels and enhance the determination of CNC data for controlling winding machines.

References

1. Marketos. Optimum toroidal pressure vessel filament wound along geodesic lines. *AIAA Journal* 1963; 1(8): 1942-5.
2. Zu L, Koussios S, Beukers A. Pattern design and optimization for filament wound toroidal pressure vessels. Proc. 23rd Annual Conference of the American Society for Composites, Memphis, TN, September 2008.
3. Zu L, He QX, Ni QQ. Pattern design for non-geodesic winding toroidal pressure vessels. Proceedings of the 16th International Conference on Composite Materials (ICCM/16), Kyoto, Japan, July 2007.
4. Li SG, Cook J. An analysis of filament overwound toroidal pressure vessels and optimum design of such structures. *J Press Vessel Technol* 2002; 124(2): 215-22.
5. Mitkevich AB, Kul'kov AA. Design optimization and forming methods for toroidal composite shells. *Mech Compo Mater* 2006; 42(2):95-108.
6. Chen RX. Design analysis on the filament-wound toroidal pressure vessel. *Journal of Solid Rocket Technology*, 2006; 29(6): 446-50.
7. Yu ZS, Yang ZT, Chu GL. Design pattern and simulation of torus for filament winding. *Mechanical and Electrical Engineering Magazine*, 2008; 25(4): 75-7.
8. Koussios S, Beukers A. Composing composites: a paradigm of reversed design. *J Design Research* 2007; 5(3): 302-16.
9. Zu L, Koussios S, Beukers A. Design of filament wound toroidal pressure vessels with circular and isotenoid-based cross sections. *Journal of Material Engineering* 2008; S1:

78-86.

10. Zwillinger, D. "Clairaut's Equation." §II.A.38 in Handbook of Differential Equations, 3rd ed. Boston, MA: Academic Press, pp. 120 and 158-160, 1997.
11. Koussios S, Beukers A, Stathis PT. Manufacturability of composite pressure vessels: application of non-geodesic winding. Proceedings of the 16th International Conference on Composite Materials, Kyoto, Japan, July 2007.
12. Koussios S, Bergsma OK, Beukers A. Isotenoid pressure vessels based on non-geodesic fiber trajectories. Proc. of 15th International Conference on Composite Materials, Durban, South Africa, June-July 2005.
13. Flügge W. Stresses in Shells. 2nd ed. New York: Springer, 1973.
14. Jorge Nocedal and Stephen J. Wright (2006). Numerical Optimization. Springer.
15. Tsai, SW, Hahn HT. Introduction to composite Materials. Westport, Conn.: Technomic Publishing Company, Inc., 1980.

Chapter 10

Continuum-based Optimal Cross

Sections of Toroidal Pressure Vessels

10.1 Introduction

Various design methods have been devoted to the design and manufacturing of filament-wound toroids. Zu et al. [1-3] proposed design approaches involving the determination of optimal fiber trajectories and winding patterns of filament-wound toroids, and developed a CAD system for their design and production. Li et al. [4] outlined a full mathematical approach to the design of overwound toroids using the membrane shell theory, considering the load-bearing capability of the wound layer and its interaction with the metallic liner. Mitkevich et al. [5] determined the winding trajectories and the profile shape of a mandrel and its transformation into given surface elements, based on the example of a toroidal membrane. Chen [6] developed a methodology to predict the burst pressure of toroidal vessels with various types of winding patterns. Yu et al. [7] have provided winding patterns for geodesically overwound toroidal vessels and carried out the computer simulation for such patterns. Jiang et al. [8] developed a novel winding machine for toroidal pressure vessels, based on the optimal design of the winding patterns. A key factor in their design process is the creation of filament-wound toroids that are mainly based on circular cross sections.

Although the toroid design is sufficiently covered in the literature, there are some deficiencies. The design for a composite toroid must take full account of the stress field as well as the material properties. Constraints imposed by the manufacturing process need to be respected, also the cross-sectional shape that may restrict the structural efficiency must be properly determined. Previous research has considered the design of fiber paths and winding

Chapter 10

parameters, but overlooked the design of adapted cross-sectional shapes (i.e. meridian profiles). One of the shortcomings of the application of circular cross sections to toroids is that the tensile strength of the filaments cannot be completely utilized, because the structural performance of a toroid is entirely governed by the cross-sectional shape. A new possibility to improve the performance of toroidal vessels has been offered by Koussios [9, 10] and Zu [11, 12] in which the adapted cross-sectional shapes of isotenoid toroids were presented and the structural efficiency of such toroid was compared with the circular one. However, these studies have not considered the continuum theory of orthotropic laminates.

An optimal shape design relies on the most efficient distribution of materials and laminate stress, in order to maximize the structural performance. As the strength-dominated and manufacturing-dominated thickness distributions do generally not match, the laminate strength cannot be maximally utilized. A well-known solution for this problem comprises netting-based geodesic-isotenoids. However, the method using the netting theory has a major defect in that the design is solely based on fiber strength and the matrix effect is not considered [13, 14]. In this chapter we determine the optimal cross-sectional shape for filament-wound toroidal pressure vessels, based on the classical lamination theory. The continuum-based meridian profile is derived with the aid of the optimality condition and the geodesic law. The influence of the theoretically required axial load on the optimal meridian shape, needed for closing the profile, is also evaluated. The comparison for the cross-sectional shapes and structural weight of equal-volume circular and continuum-based optimal toroids is then performed. In addition, for the assessment of the effect the present optimal cross-sections can have on the vessel performance, we respectively calculate and compare the performance factors of the classical vessels, the circular and the optimal toroidal vessels for various polar opening radii.

10.2 General Optimal Cross-sections

In this section we provide the governing equations for determining the continuum-based optimal profiles based on the optimality condition. The geodesically placed fibers satisfy the Clairaut's condition as given in equation (2.76):

$$r \sin \alpha = r_0 \quad (10.1)$$

where r_0 is the polar opening radius (see Fig. 2.3). We introduce now:

$$\rho = \frac{r}{R}, \quad \zeta = \frac{z}{R}, \quad a = \frac{A}{\pi p R^2} \quad (10.2)$$

Continuum-based Optimal Cross Sections of Toroidal Pressure Vessels

where R is the equatorial radius (Fig. 2.3). Substitution of equation (10.1) into (8.5), results in the differential equation which links the geometry, the roving angle and the material properties in a straightforward formulation:

$$\rho'' = \left[\frac{k\rho^2 + (1-k)\rho_0^2}{\rho^2 - (1-k)\rho_0^2} - \frac{2\rho^2}{a + \rho^2} \right] \cdot \frac{1 + \rho'^2}{\rho} \quad (10.3)$$

where ρ' and ρ'' are the first and second derivatives of ρ with respect to ζ , respectively. According to equation (10.3) the meridian shape can be adjusted to the roving orientation and the material anisotropy. However, the obtained differential equation (10.3) is of the second order, therefore it is necessary to transform it in to a first order one. Multiplication of equation (10.3) with ρ'/ρ , followed by integrating leads, after some rearrangements, to:

$$\rho' = -\sqrt{\frac{(a+1)^2(\rho^2 - \Gamma)^{1+k}}{\rho^2(a + \rho^2)^2(1-\Gamma)^{1+k}} - 1} \quad (10.4)$$

where:

$$\Gamma = (1-k)\rho_0^2 \quad (10.5)$$

where ρ_0 is the dimensionless polar opening radius. For the integration of equation (10.4), the initial set of values consists of $\rho(0) = 1$ and $\rho'(0) = 0$. The governing equation (10.4) provides the shapes of continuum-based optimal meridians for various $\{a, \rho_0, k\}$ values. This expression is only valid for the interval $[\rho_{\min}, 1]$ (selected positive real solutions by setting the argument of the numerator equal to zero), where the minimum dimensionless radius ρ_{\min} is, in most cases, slightly bigger than ρ_0 . For a given anisotropy parameter k and polar opening radius ρ_0 , the resulting meridian profile will strongly depend on the a -value (dimensionless, externally applied axial force). The $\{a, \rho_0, k\}$ -combination is able to completely determine the cross-sectional shape for a continuum-based optimal pressure vessel.

Depending on the magnitude of the axial forces as related to the internal pressure, equation (10.2), several optimal meridian profiles are obtained (see Fig. 10.1). When the axial force is sufficiently large for forcing the resulting meridian profile to be closed, the shape of the pressure vessel becomes a toroid. Fig. 10.2 outlines the sectional 3D view for a resulting toroidal pressure vessel designed using the optimal cross section ($\rho_{\min} = 0.25$, carbon-epoxy). One should note that the tensional forces of the rovings that proceed from the polar area towards the equator replace here the theoretically required external axial force A , which is applied on the polar cap. The optimal cross-sectional shapes of continuum-based (carbon-epoxy, $k = 0.0977$) and isotensoid-based ($k = 0$) toroids for various minimum radii ρ_{\min} , are shown in Fig. 10.3. It is illustrated that the aspect ratio of the optimal cross section

Chapter 10

increases with increasing anisotropy parameter. The present optimal toroid belongs to the class of doubly curved surfaces, and forms a preferable alternative for storage spaces having limited height. In addition, the optimal meridian profile of a classical pressure vessel (oblate spheroid) can also be determined by setting $a = 0$ (Fig. 10.4).

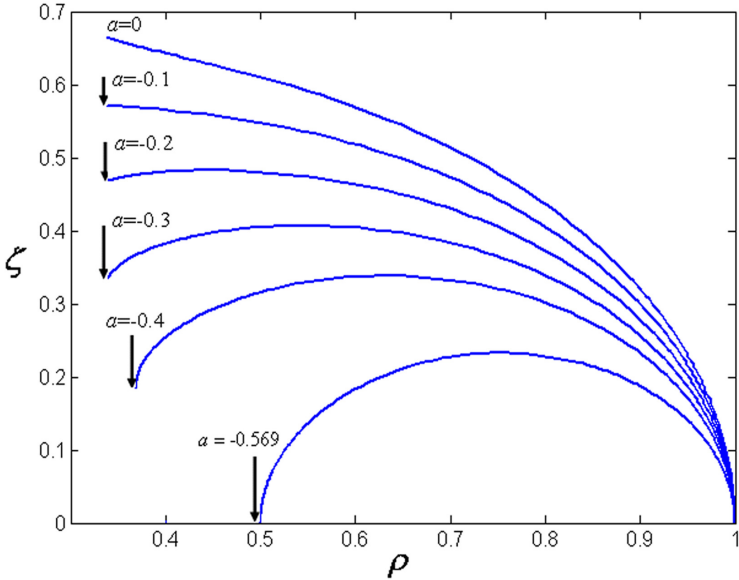


Fig. 10.1: Influence of the axial force on the resulting meridian profile

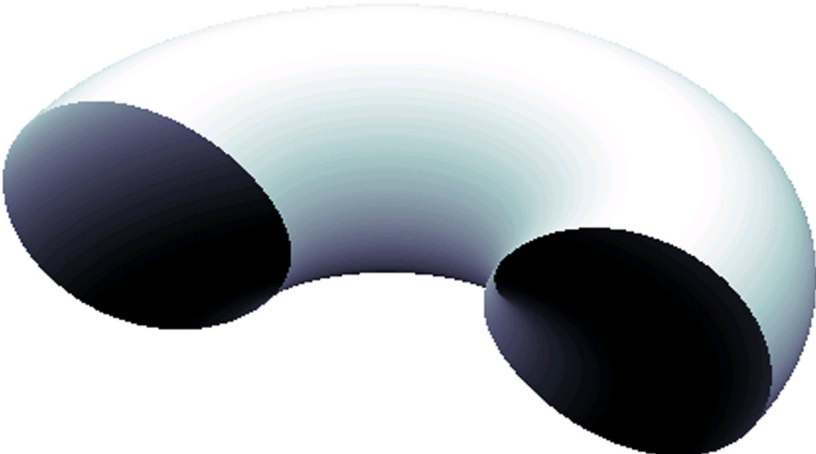


Fig. 10.2: Mandrel shape for an optimal toroids ($\rho_{\min} = 0.25$, carbon-epoxy)

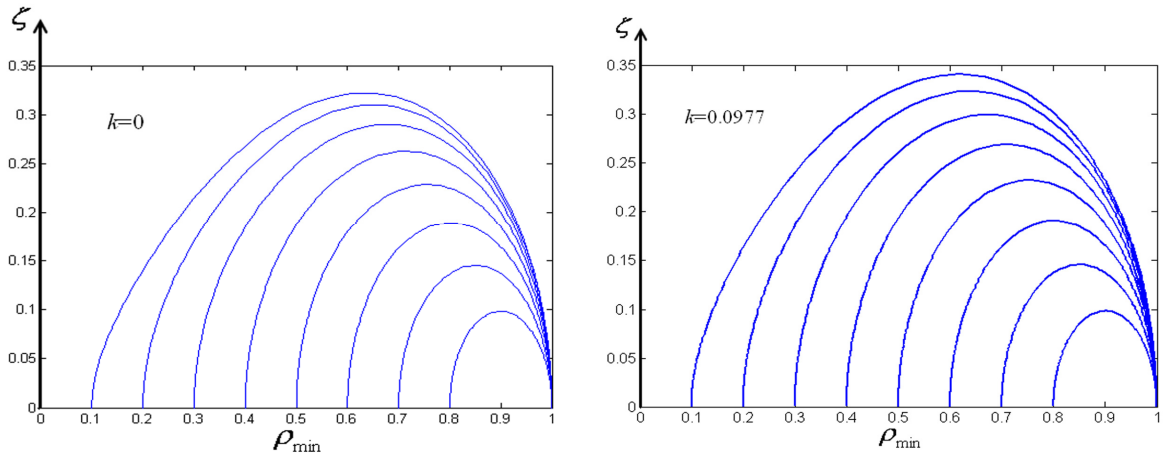


Fig. 10.3: Optimal cross-sections for isotensoids ($k=0$) and carbon-epoxy toroids ($k=0.0977$) for various ρ_{\min}

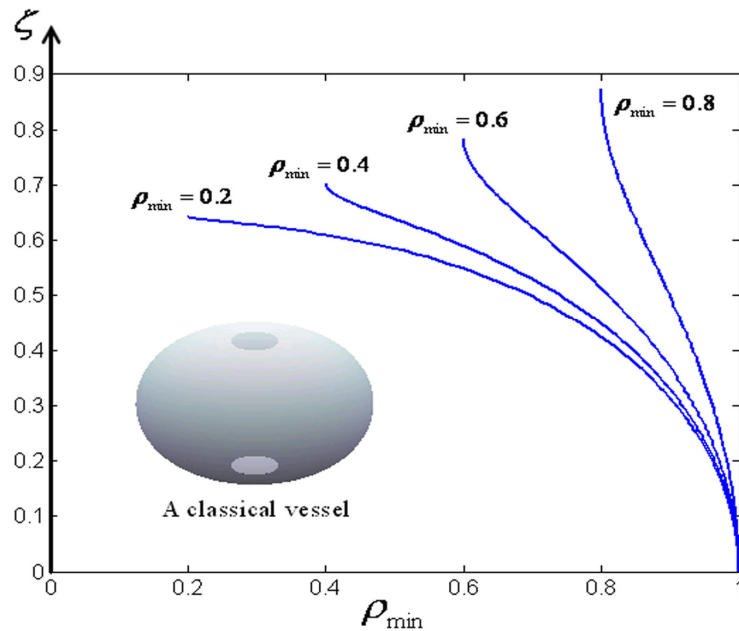


Fig. 10.4: Optimal Meridians of the classical pressure vessels corresponding to various ρ_{\min}

10.3 Volume, Weight and Thickness

In this section the cross-sectional shape, the vessel weight and performance factor of the circular and the present optimal toroid are quantified in order to demonstrate the preferable performance of toroids with the present cross sections.

The vessel volume and weight of a present optimal toroid can be given by:

$$V_{opt} = 2 \int_0^{z_m} \pi r^2 dz, \quad W_{opt} = 4\gamma \cdot \int_0^{z_m} \pi r t \sqrt{1+r'^2} dz \quad (10.6)$$

where z_m is the maximum height of the meridian profile, γ is the specific weight of the used

Chapter 10

composite material. We introduce the following dimensionless parameters:

$$\bar{V} = V / 2R^3, \quad \bar{W} = W \cdot \frac{X_T}{2\gamma\pi PR^3}, \quad \bar{t} = \frac{2X_T}{PR} \cdot t \quad (10.7)$$

where X_T is the tensile strength in the fiber direction. Substituting equations (10.2) and (10.6) into (10.7), the dimensionless volume and weight can be given by:

$$\bar{V}_{opt} = \int_0^{\zeta_m} \pi \rho^2 d\zeta, \quad (10.8)$$

$$\bar{W}_{opt} = \int_0^{\zeta_m} \rho \cdot \bar{t} \cdot \sqrt{1 + \rho'^2} d\zeta. \quad (10.9)$$

The first derivative of ρ tends to infinity at $\zeta = \zeta_m$ (the maximum height). As the result of this, the radial coordinate ρ_m of the peak point can be calculated by setting the denominator of equation (10.4) equal to zero:

$$a + \rho_m^2 = 0 \Rightarrow \rho_m = \sqrt{-a} \quad \text{where } a < 0 \quad (10.10)$$

With the aid of *Runge-Kutta* formulae, ζ_m can be further determined by equation (10.4):

$$\zeta_m = \zeta(\rho_m) \Big|_{\rho_m = \sqrt{-a}} \quad (10.11)$$

With assumptions given in section 4.2, the thickness along the meridional direction can be formulated as:

$$\frac{t}{t_{eq}} = \frac{1}{\rho} \cdot \frac{\cos \alpha_{eq}}{\cos \alpha} \quad (10.12)$$

where t_{eq} is the shell thickness at the equator.

By substitution of equations (10.1) and (10.12) into (10.9), the vessel weight (in dimensionless form) finally becomes:

$$\bar{W}_{opt} = \int_0^{\zeta_m} \rho \cdot \bar{t}_{eq} \cdot \sqrt{\frac{(1 + \rho'^2)(1 - \rho_0^2)}{\rho^2 - \rho_0^2}} d\zeta \quad (10.13)$$

The performance factor PF is used as an index for rating pressure vessels and defined as:

$$PF = \frac{pV}{W} \quad (10.14)$$

where p , V and W are the ultimate internal pressure, the vessel volume and weight, respectively. The dimensionless performance factor of an optimal toroid is given by:

$$\bar{PF}_{opt} = PF_{opt} \cdot \frac{\gamma\pi}{X_T} = \frac{pV_{opt}}{W_{opt}} \cdot \frac{\gamma\pi}{X_T} \quad (10.15)$$

Substitution of equation (10.7) into (10.15) results in:

$$\overline{PF} = \frac{\overline{V}_{opt}}{\overline{W}_{opt}} \quad (10.16)$$

Substitution of equations (10.8) and (10.9) into (10.16) leads to:

$$\overline{PF} = \frac{\int_0^{\zeta_m} \pi \rho^2 d\zeta}{\int_0^{\zeta_m} \rho \cdot \bar{t}_{eq} \cdot \sqrt{\frac{(1 + \rho'^2)(1 - \rho_0^2)}{\rho^2 - \rho_0^2}} d\zeta} \quad (10.17)$$

Substituting equation (3.29) into (7.11) results in Tsai-Wu quadratic failure criterion [15] in terms of the dimensionless thickness:

$$\begin{aligned} & \bar{t}^2 - \bar{t} X_T [F_1(m_{11}\bar{N}_\varphi + m_{12}\bar{N}_\theta) + F_2(m_{21}\bar{N}_\varphi + m_{22}\bar{N}_\theta)] \\ & - X_T^2 [F_{11}(m_{11}\bar{N}_\varphi + m_{12}\bar{N}_\theta)^2 + F_{22}(m_{21}\bar{N}_\varphi + m_{22}\bar{N}_\theta)^2 \\ & + F_{66}(m_{31}\bar{N}_\varphi + m_{31}\bar{N}_\theta)^2 + 2F_{12}(m_{11}\bar{N}_\varphi + m_{12}\bar{N}_\theta)(m_{21}\bar{N}_\varphi + m_{22}\bar{N}_\theta)] \geq 0 \end{aligned} \quad (10.18)$$

where the dimensionless shell forces are given by (refer to previous equation (8.21):

$$\bar{N}_\varphi = \left(\frac{a}{\rho} + \rho\right) \sqrt{1 + \rho'^2}, \quad \bar{N}_\theta = \left(\frac{a}{\rho} + \rho\right) \left(\frac{2\rho^2}{a + \rho^2} + \frac{\rho\rho''}{1 + \rho'^2}\right) \sqrt{1 + \rho'^2} \quad (10.19)$$

When a meridian shape and related geodesic trajectory are determined, the minimally required strength-dominated thickness $t(\rho)$ at each point assigned on the meridian is evaluated by setting equation (10.18) equal to zero and solving for t . Then, the equatorial thicknesses $t_{eq}(\rho)$ corresponding to each $t(\rho)$ are calculated using the “geometric” equation (10.12). From the obtained $t_{eq}(\rho)$ collection, the maximum value t_{eqmax} is selected as the final shell thickness at the equator:

$$\bar{t}_{eqmax} = \max_{\rho_0 \leq \rho \leq 1} \left[\frac{\rho \cos \alpha(\rho) \bar{t}(\rho)}{\cos \alpha_{eq}} \right] \quad (10.20)$$

Once t_{eqmax} is obtained, the dimensionless vessel weight W and performance factor PF can be respectively computed by equations (10.13) and (10.17) using the Gaussian quadrature rule [16].

For comparisons, the dimensionless volume and weight of an optimal toroidal vessel based on the circular cross section are given by [1, 3]:

$$\overline{V}_c = \frac{\pi^2 (1 + \rho_{min})(1 - \rho_{min})^2}{8} \quad (10.21)$$

$$\overline{W}_c = (1 - \rho_{min}) \bar{t}_{eq} \sqrt{\frac{3 + \rho_{min} - 2K}{(5 + \rho_{min})(1 - K)}} \int_0^\pi \sec \alpha d\varphi \quad (10.22)$$

where:

$$\alpha = \cos^{-1} \sqrt{\frac{(2-K)(1+\rho_{\min}) + (1-K)(1-\rho_{\min}) \cos \varphi}{(1-K)[3(1+\rho_{\min}) + 2(1-\rho_{\min}) \cos \varphi]}} \quad (10.23)$$

10.4 Evaluation and Comparison

To equalize the internal volume of a present optimal toroid with that of a circular one, the present cross-sectional shape is determined using the *Newton-Raphson* method [17]. When an internal volume is assigned, the minimum vessel radii ρ_{\min} of a circular and a present optimal meridian are respectively calculated by setting equation (10.8) equal to equation (10.21). Fig. 10.5 illustrates the distribution of dimensionless internal volumes for circular and the present optimal toroids, corresponding to various ρ_{\min} . The results indicate that the internal volumes of circular and present optimal toroids can be equal only if ρ_{\min} for the circular toroid is above 0.246. Fig. 10.6 depicts the cross-sectional shapes of circular and the present optimal toroids at equal volumes. It is shown that the aspect ratio of the present cross section is always less than that of the circular one and increases with the raise of ρ_{\min} . Additionally, the present cross section becomes identical with the circular one at small internal volumes (large ρ_{\min}).

The evaluation of the vessel weight is demonstrated by considering composite materials with various fiber-matrix combinations: glass-epoxy ($k=0.2645$), carbon-epoxy ($k=0.0977$) and aramid-epoxy ($k=0.0706$). Typical values for the mechanical properties for these composites are given in Tab. 10.1 [18]. The dimensionless weight of circular and the present optimal toroids is calculated at equal volumes and internal pressures. Fig. 10.7 shows the comparison of the dimensionless weight as a function of the dimensionless internal volume. The results reveal that the present optimal toroid is consistently lighter than the circular one at any volume and internal pressure. The weight values of the optimal aramid-epoxy toroids show about 25% maximal reduction as compared with the circular ones. It is therefore desirable to employ the present optimal cross sections for the design and production of toroidal pressure vessels. In addition, Fig. 10.8 presents the dimensionless performance factors of the classical pressure vessels, the circular and the obtained optimal toroidal pressure vessels (carbon-epoxy). It is observed that the obtained optimal toroid has better performance than the classical vessel and the circular toroid. Compared to the classical pressure vessel, the present optimal toroidal vessel is a doubly-closed body that saves on the need for materials in the end cap; in addition it reduces fiber stacking at the polar area.

Continuum-based Optimal Cross Sections of Toroidal Pressure Vessels

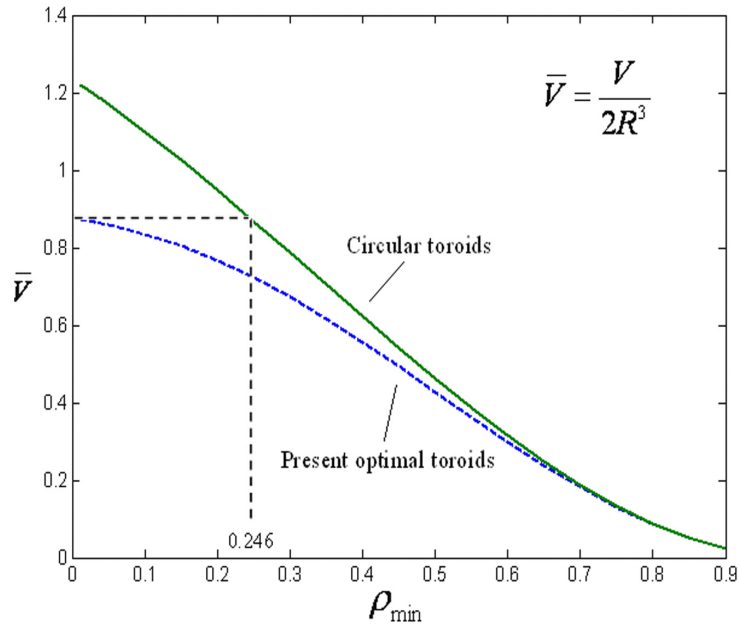
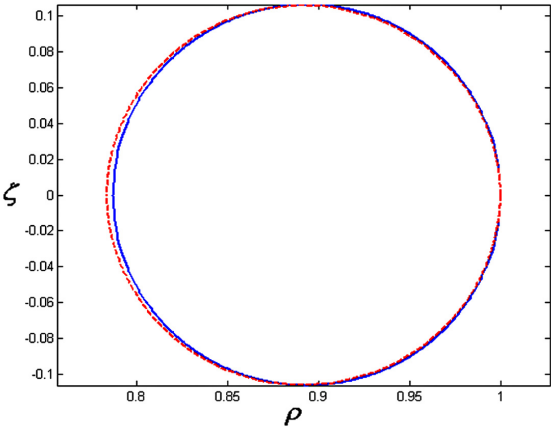


Fig. 10.5: Internal volumes of circular and the present optimal toroids with various ρ_{\min}

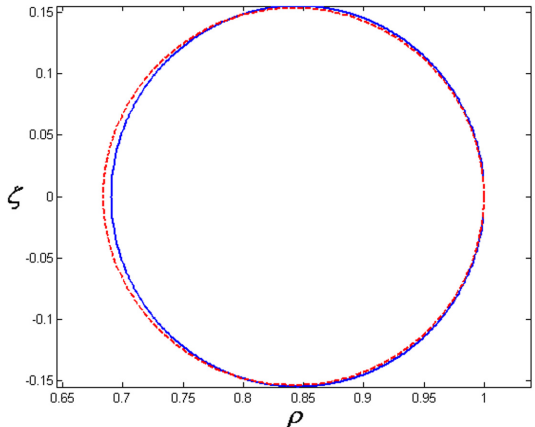
Tab. 10.1: Typical properties of unidirectional composites [18]

Properties	Carbon-epoxy	Glass-epoxy	Aramid-epoxy
Longitudinal modulus	140	60	95
Transverse modulus	11	13	5.1
Shear modulus	5.5	3.4	1.8
Poisson's ratio ν_{12}	0.27	0.3	0.34
Longitudinal tensile strength	2000	1800	2500
Transverse tensile strength	50	40	30
Longitudinal compressive strength	1200	650	300
Transverse compressive strength	170	90	130
In-plane shear strength	70	50	30

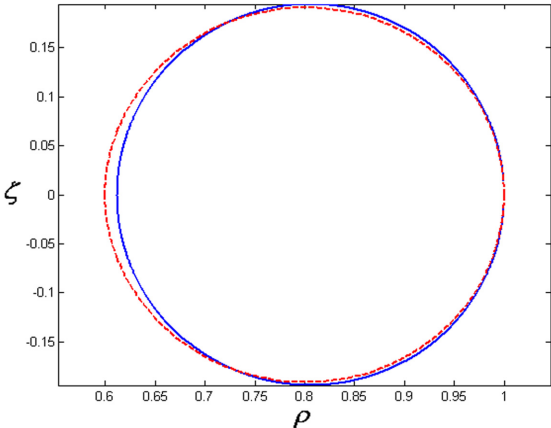
Chapter 10



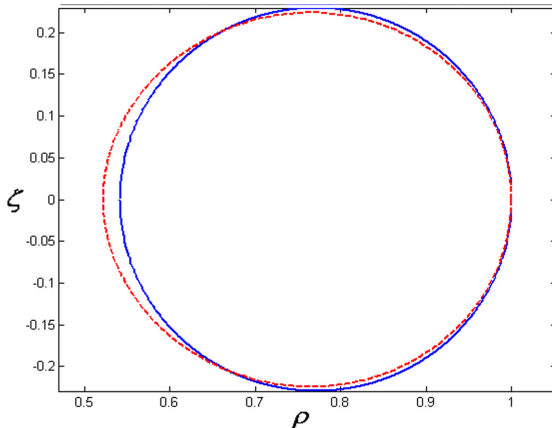
$\bar{V} = 0.1$



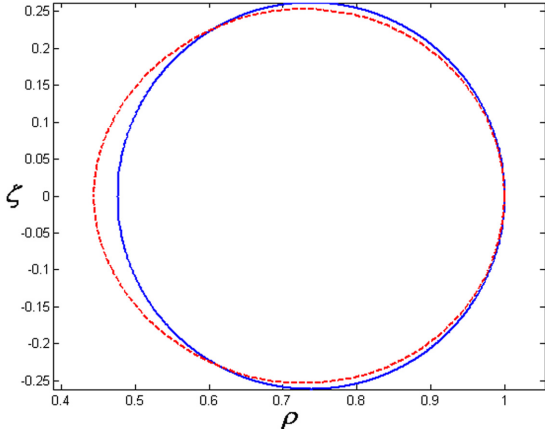
$\bar{V} = 0.2$



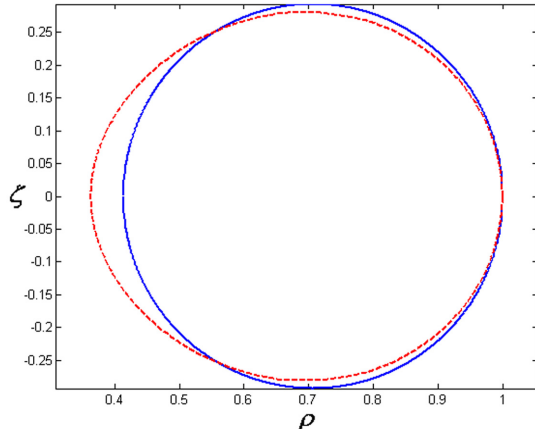
$\bar{V} = 0.3$



$\bar{V} = 0.4$



$\bar{V} = 0.5$



$\bar{V} = 0.6$

Continuum-based Optimal Cross Sections of Toroidal Pressure Vessels

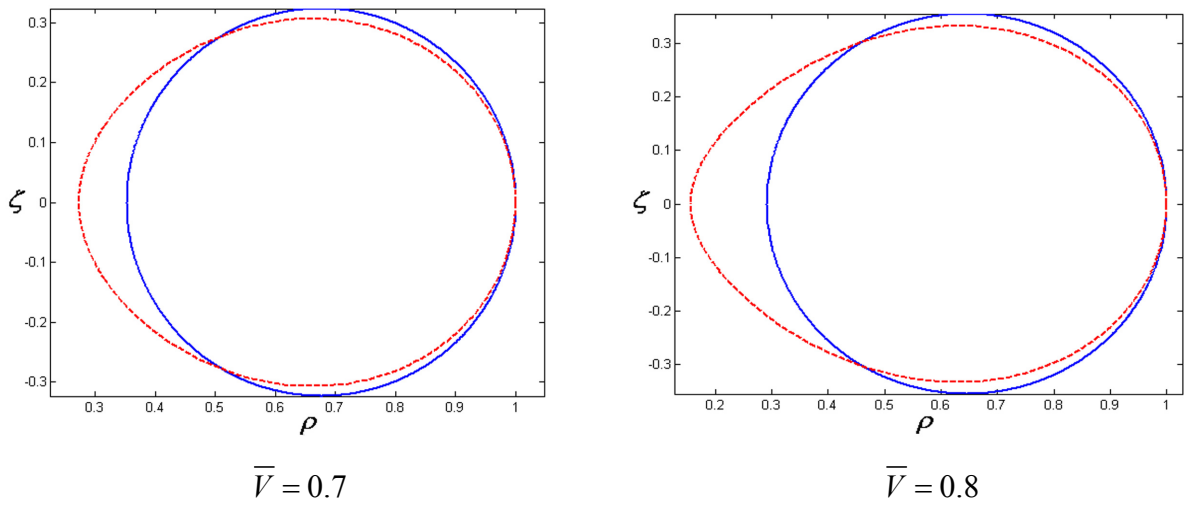


Fig. 10.6: Continued cross-sectional shapes for the circular and the present optimal toroids at equal volumes (continuous line: circular; dashed line: the present)

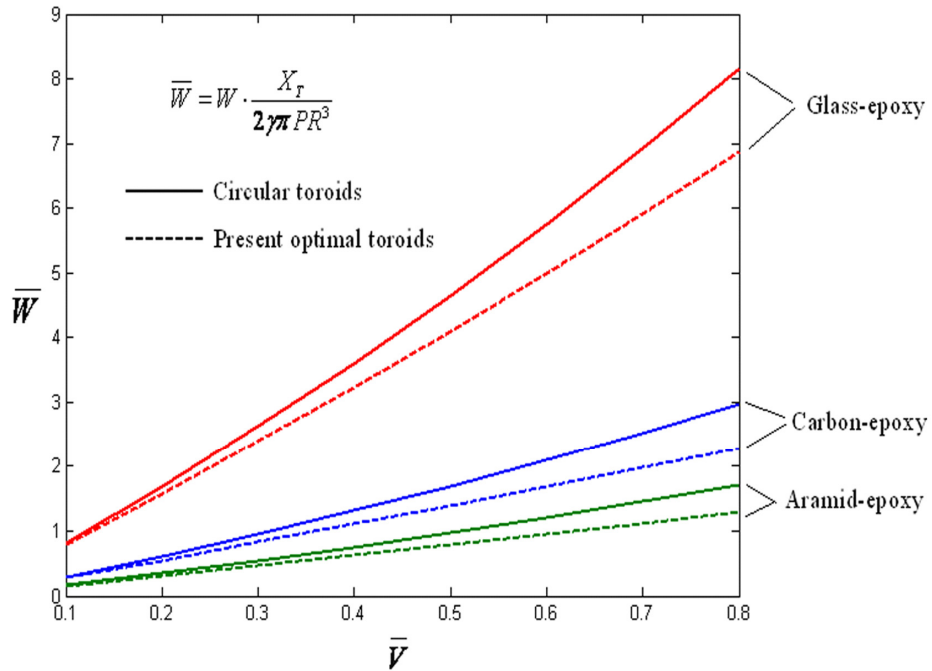


Fig. 10.7: Dimensionless weight of the circular and the present optimal toroids for various composite materials

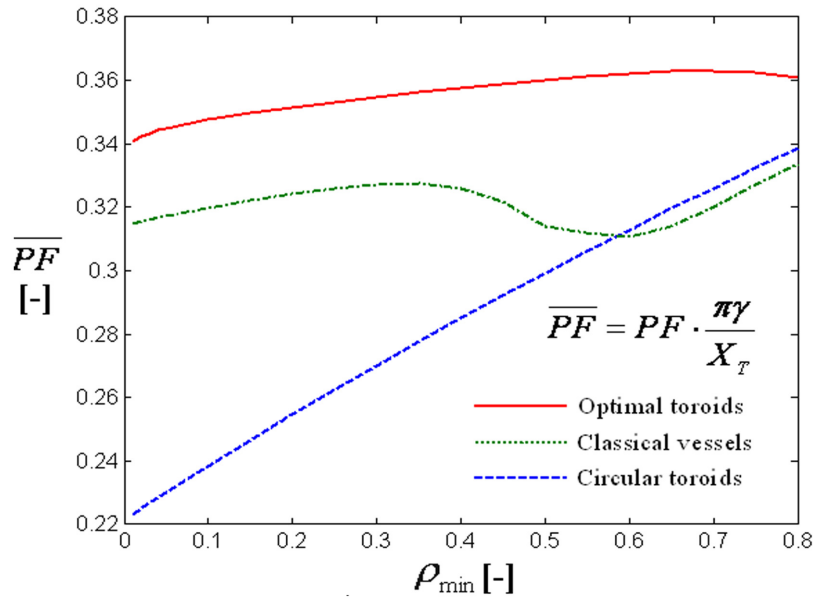


Fig. 10.8: Dimensionless performance factors of the classical vessels, the circular and the obtained optimal toroidal vessels corresponding to various ρ_{\min} (carbon-epoxy)

10.5 Conclusions

The main goal of this chapter is to provide a design-oriented method for determining the cross-sectional shapes of continuum-based optimal toroids, and to evaluate the effect of the continuum-based optimal cross sections on the geometry and structural performance of toroids. With the aid of the minimum strain energy criterion, an explicit optimality condition, e.g. equal-strains condition, which relates the roving angle and the shell stress ratio, is derived as a function of the material anisotropy parameter k . The influence of the axial load on the meridian shape is evaluated and the results indicate that the continuum-based optimal meridian curve becomes closed if the axial load reaches a particular value. The cross-sectional shapes and vessel weight of circular and continuum-based optimal toroids have been respectively determined at equal internal volumes, in order to demonstrate the reduction in structural weight that the application of the optimal cross sections can realize.

As a result of the design procedure, the present optimal toroidal vessel provides a significantly lower weight and a lower aspect ratio than the circular one at any equal volume and internal pressure, and consequently results in better performance. The structural efficiency of filament-wound toroids can be remarkably improved using the present cross sections as determined by the optimal condition of equal shell strains. The results also show

that the optimal cross sections offer an interesting alternative to spaces having limited height and volume. In addition, the optimal toroidal vessel proposed here has better structural performance than the classical vessel; this is mainly triggered by the relatively homogeneous thickness distribution over the vessel surface and the saving of materials in the end cap.

References

1. Zu L, Koussios S, Beukers A. Pattern design and optimization for filament wound toroidal pressure vessels. Proc. 23rd Annual Conference of the American Society for Composites, Memphis, TN, September 2008.
2. Zu L, He QX, Ni QQ. Pattern design for non-geodesic winding toroidal pressure vessels. Proceedings of the 16th International Conference on Composite Materials (ICCM/16), Kyoto, Japan, July 2007.
3. Zu L, Koussios S, Beukers A. Design of filament-wound circular toroidal hydrogen storage vessels based on non-geodesic fiber trajectories. *Int J Hydrogen Energy* 2010; 35(2): 660-70.
4. Li SG, Cook J. An analysis of filament overwound toroidal pressure vessels and optimum design of such structures. *J Press Vessel Technol* 2002; 124(2): 215-22.
5. Mitkevich AB, Kul'kov AA. Design optimization and forming methods for toroidal composite shells. *Mech Compo Mater* 2006; 42(2):95-108.
6. Chen RX. Design analysis on the filament-wound toroidal pressure vessel. *Journal of Solid Rocket Technology*, 2006; 29(6): 446-50.
7. Yu ZS, Yang ZT, Chu GL. Design pattern and simulation of torus for filament winding. *Mechanical and Electrical Engineering Magazine*, 2008; 25(4): 75-7.
8. Jiang XZ, Fei CD, Ma GF. Filament Winding Process of Toroidal Vessels. *Fiber compos* 2005; 41(1): 41-43.
9. Koussios S. Filament Winding: A Unified Approach. PhD Thesis report, Design and Production of Composite Structures Group, Faculty of Aerospace Engineering, Delft University of Technology, Delft, 2004.
10. Koussios S, Beukers A. Composing composites: a paradigm of reversed design. *J Des Res* 2007; 5(3): 302-16.
11. Lei Zu, Sotiris Koussios and Adriaan Beukers. New Generation of Filament Wound Toroids Based on Isotensoid Design. Proceedings of the 17th International Conference on Composite Materials, Edinburgh, UK, Jul. 2009.

Chapter 10

12. Lei Zu, Sotiris Koussios and Adriaan Beukers. Design of Filament Wound Isotenoid Toroids Based on Non-geodesic Roving Trajectories. Proceedings of the 24th Annual Technical Conference of American Society for Composites, Delaware, USA, Sept. 2009.
13. Krikanov AA. Composite pressure vessels with higher stiffness. *Compos Struct* 2000; 48: 119-27.
14. Zu L, Koussios S, Beukers A. Design of filament-wound isotenoid pressure vessels with unequal polar openings. *Compos Struct* 2010; 92(9): 2307-13.
15. Tsai SW, Wu EM. A general theory of strength for anisotropic materials. *Journal of Composite Materials* 1971; 5: 58-80.
16. Gil, Amparo; Segura, Javier; Temme, Nico M. (2007), "§5.3: Gauss quadrature", *Numerical Methods for Special Functions*, SIAM.
17. P. Deuffhard, *Newton Methods for Nonlinear Problems. Affine Invariance and Adaptive Algorithms*. Springer Series in Computational Mathematics, Vol. 35. Springer, Berlin, 2004.
18. Vasiliev VV, Morozov EV. *Advanced mechanics of composite materials*. UK: Elsevier Ltd, 2007.

Chapter 11

Integral Design and Manufacturing of Toroidal Pressure Vessels

11.1 Introduction

Various design methods have been addressed to the design and production of filament-wound toroidal pressure vessels [1-4]. However, previous investigations on toroidal vessels have only considered the structural design and optimization, and overlooked the determination of adapted winding patterns and kinematic models for involved toroidal winders. Therefore, it is desirable to provide an integral design method which links all the major design issues including structures, patterns and kinematics. Furthermore, the lack of dedicated toroidal winders is also a main drawback to permit highly automated production of toroidal pressure vessels.

In this chapter we outline a design-oriented integral method for determining the optimal fiber trajectories and related winding patterns for toroidal hydrogen storage tanks. In the second section we briefly present the model for fiber trajectories on a torus. Both geodesics and non-geodesics are considered, combined in a single theory. The governing equations for geodesic and non-geodesic trajectories on the toroidal mandrel are then given. In section **11.2** the optimal design procedure is outlined for obtaining the preferred fiber trajectories. This procedure performs a combined evaluation of the structural optimization for vessel performance and the windability for manufacturing. In section **11.3** we emphasize the importance of suitable winding patterns for obtaining an optimal pressure vessel and accordingly derive the "Diophantine" equations that produce such patterns. The main objective of the method presented here is to match the structure-dictated number of wound

Chapter 11

circuits to the solution of the Diophantine equations for determining the proper relative winding velocities of the mandrel and the feed eye. Depending on the aimed lathe machine configuration, the underlying geometric model of the new-fashioned toroidal winder is outlined and the kinematic solution for coupling the motion of the mandrel and the feed eye are derived in section 11.4. An example of the implementation of the methods for an actual toroidal hydrogen storage tank is given, as performed in the simulations for generating optimal fiber trajectories (section 11.5). Finally, some conclusions and recommendations are drawn in section 11.6.

11.2 Structural Optimization

The design of fiber trajectories is based on two criteria: optimal laminate structure and suitable winding patterns. The fiber trajectories should be able to fulfill design requirements for either strength or producibility, e.g. maximum vessel performance, maximum buckling strength, uniform stress distribution, non-slippage, non-bridging, full coverage, so that the fiber bands can precisely be positioned onto a mandrel. Providing excellent structural performance is a key issue in the design of composite hydrogen storage vessels.

A major advantage of composite materials is the large number of design variables available to the designer. To realize this potential and to maximize the structural efficiency which composites can offer, the design has to properly capture the specific requirements of the problem. Optimal design is an effective way of achieving this goal. A compromise strategy between "design for structures" and "design for windability" must be sought. A constrained optimization problem can be represented as follows:

$$\begin{aligned} & \text{Min}_{\mathbf{X}} PF(\mathbf{X}) \\ & \text{Subject to } C_i(\mathbf{X}) \leq 0 \quad i = 1, 2, \dots, m \\ & \quad \quad \quad G_k(\mathbf{X}) = 0 \quad k = 1, 2, \dots, n \\ & \quad \quad \quad \mathbf{X}_L \leq \mathbf{X} \leq \mathbf{X}_U \end{aligned}$$

where \mathbf{X} is the vector of design variables, and \mathbf{X}_L and \mathbf{X}_U are the lower and upper limits of the design variables, respectively. The meridian shape, fiber orientations, stacking sequences, slippage coefficient and layer thickness can be considered as the design variables. $PF(\mathbf{X})$ is the objective function, $C_i(\mathbf{X})$ and $G_k(\mathbf{X})$ denote the inequality and equality constraint functions, respectively. There are two classes of constraints: explicit and implicit constraints. For example, the non-bridging and non-slippage criteria are typical explicit constraints which

Integral Design and Manufacturing of Toroidal Pressure Vessels

are explicitly expressed in term of the design variables; the Tsai-Wu criterion and the full coverage condition are typical implicit constraints which cannot be explicitly expressed in term of the design variables. A number of possible indices, e.g. performance factor, vessel weight, burst pressure, strain energy density, bulking load, can be considered as the optimization objectives by which the vessel performance can be improved. According to the customers' demands and the actual manufacturing conditions, various design requirements and appropriate goals are selected as the optimization constraints and objective functions. A typical example of specific optimization for filament-wound toroidal pressure vessels can be found in [5], which the structural mass of non-geodesically overwound toroidal hydrogen storage tanks is minimized with the aid of the continuum theory and the non-geodesic law. The flow chart of structural optimization procedure is shown in Fig. 11.1.

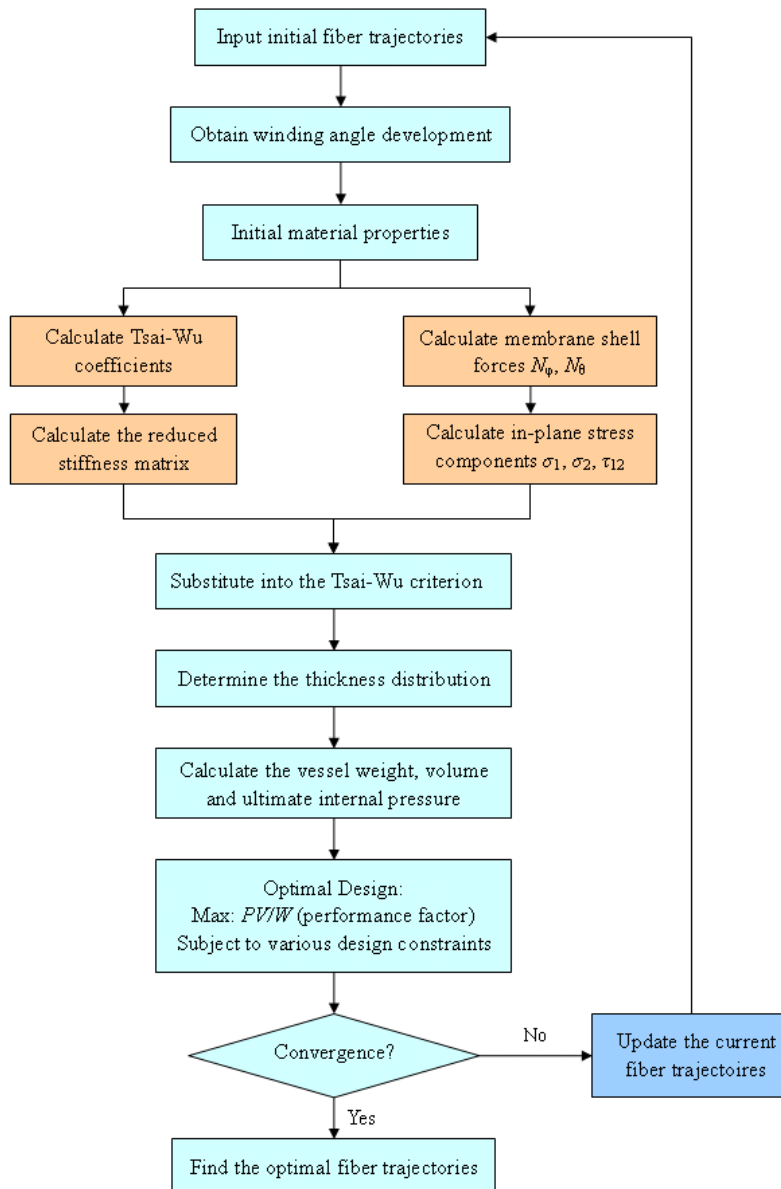


Fig. 11.1: Flow chart of structural optimization procedure

11.3 Kinematic Solutions for Toroidal Winders

Toroidal winding is in essence different from classical filament winding. The mandrel rotates in the horizontal plane and its rotation is not driven by the spindle, but some friction rollers which closely contact the outer periphery of the mandrel. The feed eye does not move parallel to the spindle nor the rotational axis of the mandrel, but at some intersecting plane perpendicular to the mandrel. The involved toroidal winder configuration is shown in Fig. 11.2. We consider here a three-dimensional model of the toroidal winder. The fiber coming from the feed eye is always tangent to the surface of the mandrel. The tangent connection point P is called the contact point between the free-hanging fiber and the mandrel surface. $O-xyz$ is the moving coordinate system which is attached to the mandrel and the z -axis is overlapping with the rotational axis (Z -axis). $O-XYZ$ is the static coordinate system and the $O-XZ$ is the plane of the motion of the feed eye. Φ is the rotation angle of the mandrel with respect to the static coordinate system.

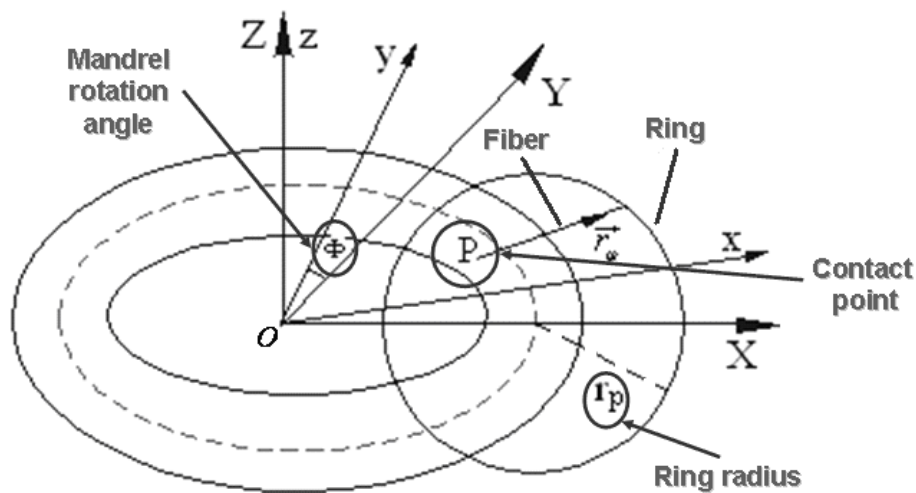


Fig. 11.2: Lay-out of a toroidal winder and its coordinate system

Assuming that the Ox - and OX -axes are overlapping initially, the relation for the moving coordinates and static coordinates can be given by:

$$\begin{Bmatrix} x \\ y \\ z \end{Bmatrix} = \begin{Bmatrix} \cos \Phi & \sin \Phi & 0 \\ -\sin \Phi & \cos \Phi & 0 \\ 0 & 0 & 1 \end{Bmatrix} \begin{Bmatrix} X \\ Y \\ Z \end{Bmatrix} \quad (11.1)$$

According to the vector representation of the torus, the coordinates of the point P are:

Integral Design and Manufacturing of Toroidal Pressure Vessels

$$\mathbf{P}(\theta, \varphi) = \{(R + r \cos \varphi) \cos \theta, (R + r \cos \varphi) \sin \theta, r \sin \varphi\} \quad (11.2)$$

The direction of the tangent line between the feed eye and the point P can be represented by the directional derivative with respect to φ :

The tangent equations connecting the point P with the feed eye are given as [9]:

$$\frac{x - (R + r \cos \varphi) \cos \theta}{\sin \theta - tg\alpha \sin \varphi \cos \theta} = \frac{y - (R + r \cos \varphi) \sin \theta}{-\cos \theta - tg\alpha \sin \varphi \sin \theta} = \frac{z - r \sin \varphi}{tg\alpha \cos \varphi}. \quad (11.3)$$

Substitution of equation (11.1) into (11.3) leads, after some arrangements, to:

$$\frac{X - (R + r \cos \varphi) \cos(\theta + \Phi)}{\sin(\theta + \Phi) - tg\alpha \sin \varphi \cos(\theta + \Phi)} = \frac{Y - (R + r \cos \varphi) \sin(\theta + \Phi)}{-\cos(\theta + \Phi) - tg\alpha \sin \varphi \sin(\theta + \Phi)} = \frac{Z - r \sin \varphi}{tg\alpha \cos \varphi} \quad (11.4)$$

One should note here that the Y -coordinate of the feed eye will always be zero. Hence equation (11.4) becomes:

$$\begin{cases} X = \frac{R + r \cos \varphi}{\cos(\theta + \Phi) + tg\alpha \sin \varphi \sin(\theta + \Phi)}, \\ Z = r \sin \varphi + \frac{(R + r \cos \varphi) tg\alpha \cos \varphi \sin(\theta + \Phi)}{\cos(\theta + \Phi) + tg\alpha \sin \varphi \sin(\theta + \Phi)}. \end{cases} \quad (11.5)$$

Equation (11.5) gives the kinematic equations of the feed eye. The eye moves along the periphery of a circle (winding ring) of radius r_e and the following relation holds:

$$X^2 + Z^2 = r_e^2. \quad (11.6)$$

Substitution of equation (11.5) into (11.6) gives the non-linear equation for the mandrel rotation angle Φ :

$$\begin{aligned} & \{r \cos \varphi + R[1 - \cos(\theta + \Phi) - tg\alpha \sin \varphi \sin(\theta + \Phi)]\}^2 \\ & + [r \sin \varphi \cos(\theta + \Phi) + (R \cos \varphi + r) tg\alpha \sin(\theta + \Phi)]^2 \\ & = \{r_p [\cos(\theta + \Phi) + tg\alpha \sin \varphi \sin(\theta + \Phi)]\}^2 \end{aligned} \quad (11.7)$$

Together with the non-geodesic equation (9.4), equation (11.7) can be solved numerically for Φ by the *Newton* method [6] with $\{\theta, \varphi\}$ -value of every step. Once Φ is obtained, the coordinates of the feed eye can then be retrieved from equation (11.5). It should be noted here the initial position of the contact point P is not located in the plane $O-XZ$ and needs to be determined by equation(11.8) with the initial value $\Phi = 0$.

The lay-out of a toroidal winder allows one or two winding rings (placed 180° apart). The machine with one winding ring places only the plus or the minus layer at a time. In contrast, the winder with two rings creates an angle-ply laminate consisting of $\pm\alpha$ layers at one go and thus has a greater manufacturing efficiency.

11.4 Uniform and Full Coverage

The fiber bands must be equally distributed, without leaving any gaps or creating excessive overlaps. Since the applied fiber band has certain dimensions (width and thickness), the winding patterns obtained by the structural optimization can generally not fully cover the mandrel surface with least fiber overlap and a minimum number of wound circuits. The result of this shortcoming is additional overwound fiber length, excessive fiber stacking and increased production time. The structure-dictated optimal trajectories need thus be adjusted according to the criterion of uniform and full coverage. Next, the required winding velocities of the toroidal mandrel and the feed eye must be determined.

Assuming that the feed eye rotates K rounds around the Y -axis in the $O-XZ$ plane while the mandrel rotates N rounds around the Z -axis, the relative winding velocity can be defined as:

$$I = \frac{\omega_m}{\omega_p} = \frac{N}{K} \quad (11.8)$$

where ω_m and ω_p are angular velocities of the mandrel and the feed eye, respectively. N and K are relative prime (have no common division factor). After completing certain number of wound circuits, the fiber band should be placed in a leading or lagging with respect to the first winding (we assume here the first winding starts from the outer periphery). Accordingly, a fine-tuning of the relative winding velocity I must be considered:

$$\Delta I = \frac{b}{2\pi K(R+r)\sin\alpha_0} \quad (11.9)$$

where b is the band width. Then the corrected relative winding velocity can be formulated as:

$$I = \frac{N}{K} \pm \frac{b}{2\pi K(R+r)\sin\alpha_0} \quad (11.10)$$

Equation (11.10) is a "Diophantine"-alike equation [7], since K , N are all integers. There is infinity of solutions to equation (11.11), and the minimum values of K and N which satisfy the equation dictate the required number of wound circuits and the fiber patterns. The ' \pm ' determines whether the final contact point leads or lags the initial point. The mandrel rotation angle corresponding to one complete rotation of the feed eye is then given by:

$$\theta_m = \frac{2\pi}{K} \left[N \pm \frac{b}{2\pi(R+r)\sin\alpha_0} \right] \quad (11.11)$$

The minimum production time and minimum fiber stacking can be achieved if the mandrel rotation angle satisfies equation (11.11). The procedure of winding pattern adjustment is outlined in Fig. 11.3.

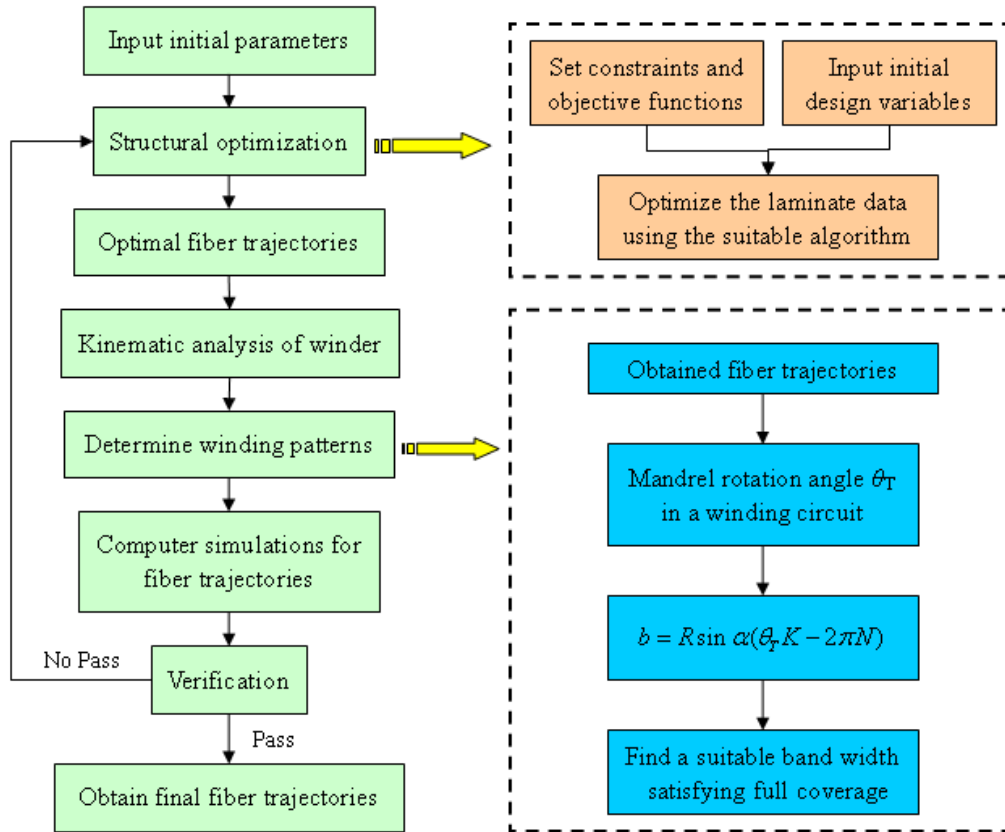


Fig. 11.3: Flow chart of winding pattern adjustment

11.5 Numerical Examples and Simulation

The integral design method of the toroidal pressure vessel is here demonstrated by considering a toroidal mandrel with $R = 540\text{mm}$, $r = 135\text{mm}$ and $b = 12\text{mm}$. The laminate is made of T300/5208 graphite/epoxy the elastic constants of which are $E_1 = 142\text{ GPa}$, $E_2 = 10.8\text{GPa}$, $G_{12} = 5.49\text{ GPa}$ and $\nu_{12} = 0.3$. The strength values are $X_T = 1568\text{ MPa}$, $Y_T = 57\text{ MPa}$, $X_C = 1341\text{ MPa}$, $Y_C = 212\text{ MPa}$, and $S = 80\text{ MPa}$. The values for the material properties are obtained from Ref. [8]. To avoid collision between the mandrel and the feed eye, the geometry of the latter has to be properly depicted. With a suitable determination for the dimensions of the feed eye and its supporting ring (winding ring), the allowed moving region of the feed eye can be obtained by checking the minimum distance between the mandrel surface and the feed eye. The ring radius r_e is here chosen as 173mm and the angular velocity of the mandrel is $\omega_m = 0.035\text{ rad/s}$. The feed eye movement during $0\sim 35\text{s}$ is outlined in Fig.11.4, in terms of the X - and Z -coordinates. To further indicate the position of the feed eye relative to the mandrel, Fig. 11.5 presents the X -coordinate corresponding to the meridional coordinate φ . The results indicates that the moving range of the feed eye varies from $X = 367\text{mm}$

Chapter 11

to $X = 713\text{mm}$ in the horizontal direction and from $Z = -173\text{mm}$ to $Z = 173\text{mm}$ in the vertical direction. Note that the errors of the winding patterns may be accumulated due to the numerical solution for the nonlinear equation (11.7).

The optimal geodesic trajectories for single and symmetrically helical winding patterns are shown in Figs. 11.6-11.7, respectively, corresponding to 10 and 30 complete rotations of the mandrel (100 and 300 winding circuits). Similarly, Figs. 11.8-11.9 illustrate the optimal non-geodesic trajectories of single and symmetrically helical winding after 10 and 40 rotations of the mandrel (40 and 160 winding circuits), respectively. The results reveal that the initial winding angle of the optimal non-geodesics is about 10 degree smaller than that of the optimal geodesics. Therefore, the resulting structure in the parallel direction can further be enhanced and the better distribution of the fiber strength in the two main directions (meridional and parallel) of the toroidal shell is achieved by using the optimal non-geodesics.

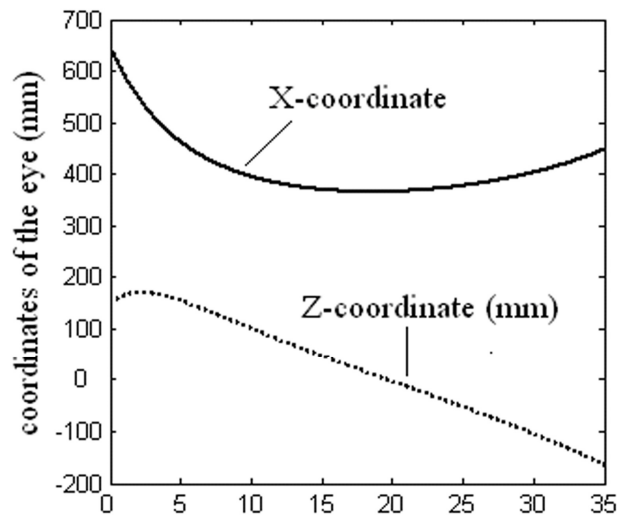


Fig. 11.4: Feed-eye movement as a function of time

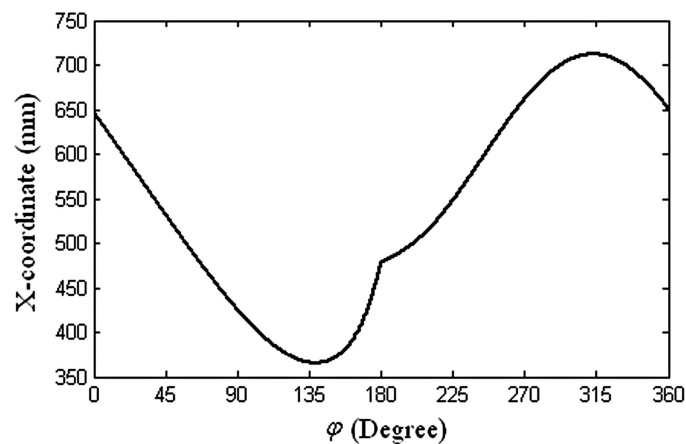
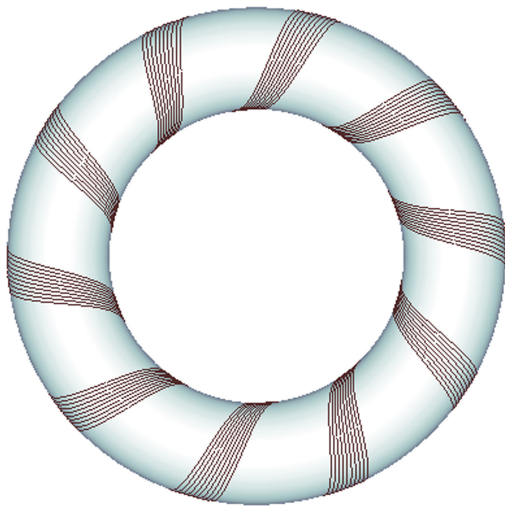
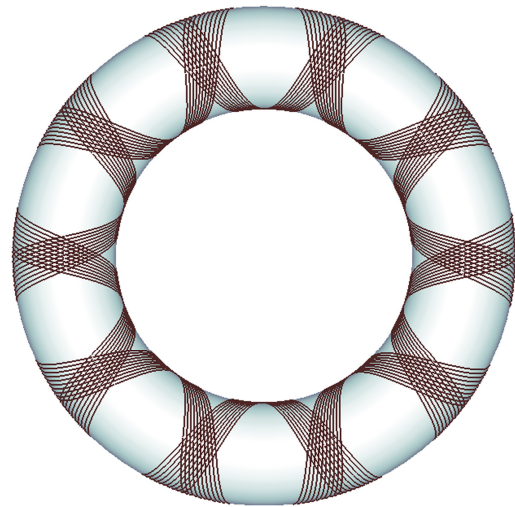


Fig. 11.5: Feed-eye movement as a function of φ

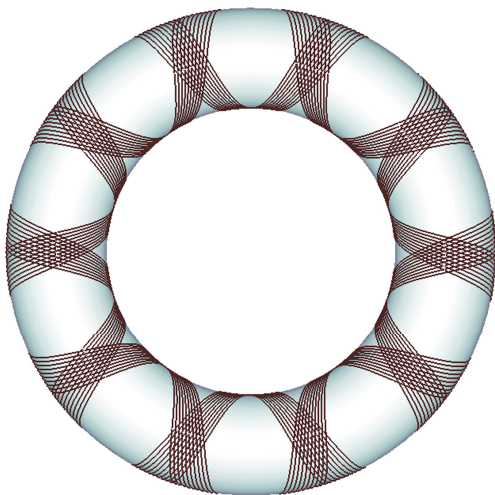


(a) Single helical winding patterns

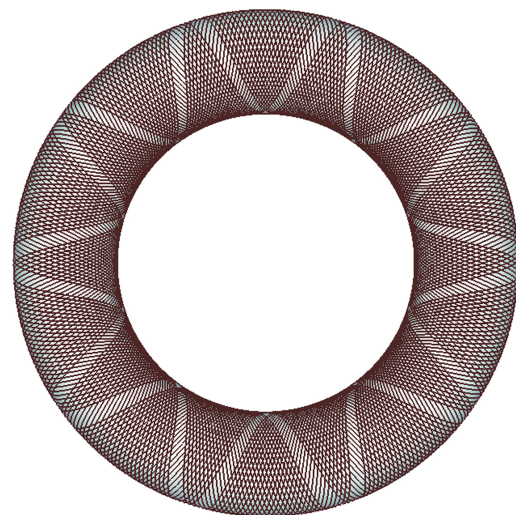


(b) Symmetrically helical winding patterns

Fig. 11.6: Optimal geodesic trajectories after 10 rotations of the mandrel (100 wound circuits)

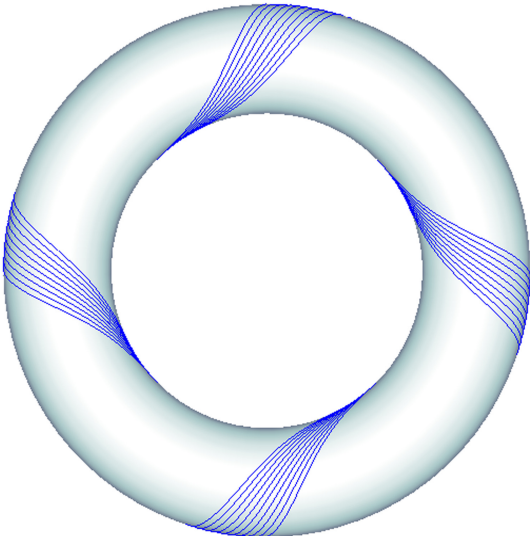


(a) Single helical winding patterns

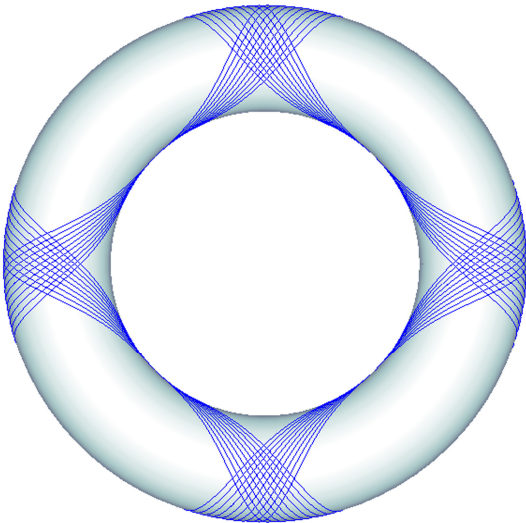


(b) Symmetrically helical winding patterns

Fig. 11.7: Optimal geodesic trajectories after 30 rotations of the mandrel (300 wound circuits)

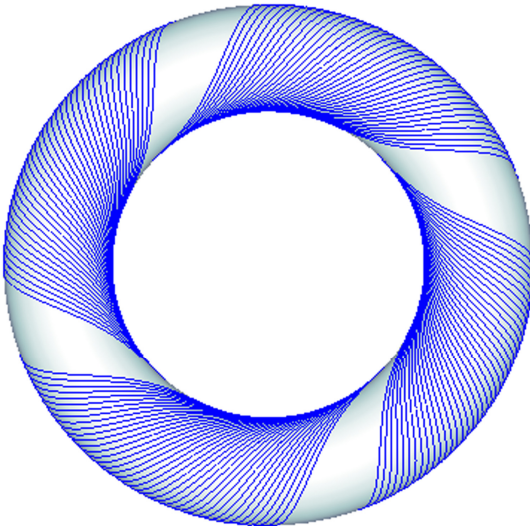


(a) Single helical winding patterns

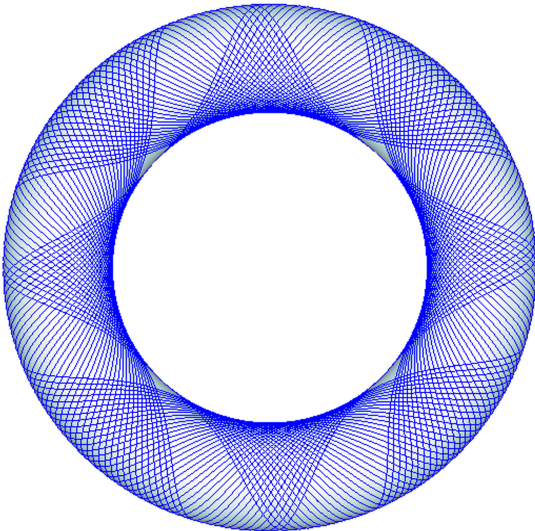


(b) Symmetrically helical winding patterns

Fig. 11.8: Optimal non-geodesics after 10 rotations of the mandrel (40 wound circuits)



(a) Single helical winding patterns



(b) Symmetrically helical winding patterns

Fig. 11.9: Optimal non-geodesics after 40 rotations of the mandrel (160 wound circuits)

11.6 Conclusions

Toroidal winding is a relatively recent development that is mostly used to produce donut shaped pressure vessels for applications that require space-saving, weight reduction and constant centre of mass. The main difference with classic filament winding is that the axis of rotational symmetry lies outside of the toroid itself and thus leads to a concave section. The goal of this paper is to match the fiber trajectories obtained by structural optimization to the winding patterns dictated by uniform and full coverage criteria. In order to achieve this, the structure-dominated parameters are indirectly introduced as variables in the pattern equation, which determines suitable winding patterns. The structural optimization procedure for achieving the maximum vessel performance factor is outlined and the resulting fiber trajectories are adjusted to uniformly and fully cover the mandrel with the minimum number of wound circuits, least fiber overlap and homogenous thickness distribution. The kinematic model of the toroidal winder is presented and the machine movement is determined by solving the kinematic equations for the mandrel and the feed eye. A practical example is applied to demonstrate the favorite performance and flexibility of the present method, where both the optimal fiber patterns and the kinematic solutions of the winder are evaluated.

As a result of the design procedure, the number of required fiber bands (dictated by structural optimization) corresponds exactly to the necessary number of wound circuits in order to create uniform and full coverage patterns. The optimal fiber trajectories suit various possible winding patterns due to their geometric flexibility and satisfy the uniform and full coverage condition well. The solution eliminates excess windings and guarantees a minimum number of wound circuits and maximum utilization of the fiber strength. Compared to the optimal geodesics, the results also show that the optimal non-geodesic patterns lead to better distribution of the fiber strength in meridional and parallel directions and consequently improve the structural efficiency of toroidal pressure vessels.

References

1. S.G. Li, J. Cook, An analysis of filament overwound toroidal pressure vessels and optimum design of such structures, *J Press Vessel Technol* 124 (2002) 215-222.
2. L. Zu, S. Koussios and A. Beukers, Design of filament-wound circular toroidal hydrogen storage vessels based on non-geodesic fiber trajectories, *Int J Hydrogen Energy* 35 (2010) 660-670.

Chapter 11

3. A.B. Mitkevich, A.A. Kul'kov, Design optimization and forming methods for toroidal composite shells, *Mech Compo Mater* 42 (2006) 95-108.
4. L. Zu, S. Koussios, A. Beukers, New generation of filament wound toroids based on isotensoid design, *Proceedings of the 17th International Conference on Composite Materials*, Edinburgh, UK, Jul. 2009.
5. Zu L, Koussios S, Beukers A. Design of filament-wound circular toroidal hydrogen storage vessels based on non-geodesic fiber trajectories. *Int J Hydrogen Energy* 2010; 35(2): 660-70.
6. P. Deuffhard, *Newton Methods for Nonlinear Problems. Affine Invariance and Adaptive Algorithms*. Springer Series in Computational Mathematics, Vol. 35. Springer, Berlin, 2004.
7. Mordell, L. J. (1969). *Diophantine equations*. Academic Press.
8. Tsai, SW, Hahn HT. *Introduction to composite Materials*. Westport, Conn.: Technomic Publishing Company, Inc., 1980.
9. Thomas GB, Finney RL. *Calculus and Analytic Geometry* (9th Ed.). Addison Wesley, 1995

IV THICK-WALLED PRESSURE VESSELS

Chapter 12

Three-dimensional Stress, Strain & Displacement Analysis

12.1 Introduction

Cylindrical composite pressure vessels made of fiber-reinforced materials have many potential advantages over their steel counterparts, such as high specific stiffness and strength, convenient designability, good corrosion resistance and thermal insulation. Fuel tanks, rocket motors, breathing apparatus and pipes are some examples of composite pressure vessels. This chapter outlines a 3D elastic solution for stresses and deformations of thick-walled anisotropic cylinders. Each cylindrical lamina is made from an orthotropic material with a given filament winding angle, which can be varied for each layer. This study is limited to linear elastic relations between stress/strain and strain/displacements and neglects the transition regions near end closures of a cylinder. The design and analysis approaches pertaining to the elastic stress solution and the general stress-strain, strain-displacement and shell equilibrium

Chapter 12

equations for an element within a thick cylindrical lamina are here documented and presented. A review is devoted to 3D elasticity approaches for obtaining the exact solution of the stresses and strains induced by internal pressure, and to the effects of hygrothermal loading and twisting. A thick-walled cylindrical pressure vessel, which comprises four CFRP layers and an aluminum liner, is analyzed to demonstrate the effects of the liner and its thickness variation on the stress distribution of the composite overwrap. In addition, the Von Mises stress of the metal liner and the Tsai-Wu strength ratio of the composite overwrap are calculated for various liner/fiber/resin materials to find the best combination.

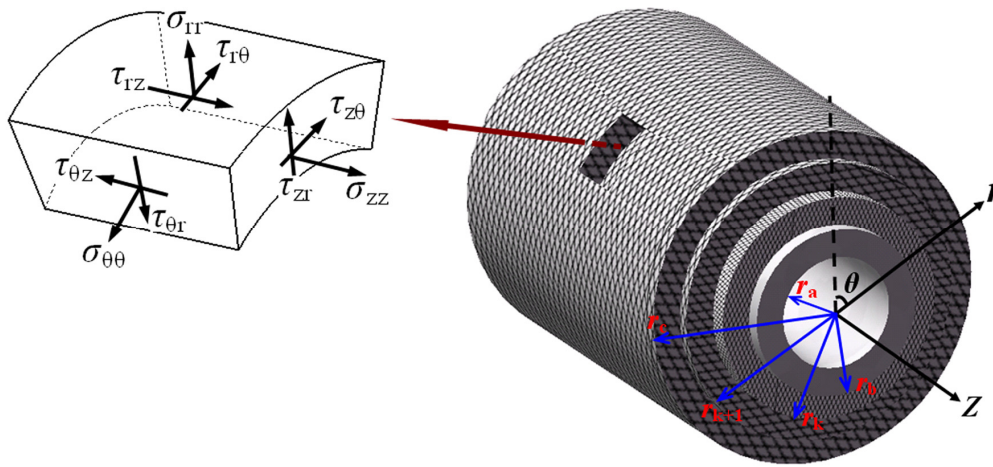


Fig. 12.1: Illustration of the cylindrical coordinate system and the stress components

12.2 Three-dimensional Stress and Strain

In the following analysis, the attention is addressed on the cylindrical section of a filament-wound pressure vessel with an isotropic liner. A standard cylindrical coordinate system is used in the analysis, the axial, hoop (circumferential), and radial coordinates being denoted as z , θ and r , respectively. The inner and outer radii of the isotropic liner are denoted as r_a and r_b while the outer radius of the laminated orthotropic shell is r_c . The interface between the k^{th} and $(k+1)^{\text{th}}$ lamina is denoted as r_k . The innermost lamina is referred to as the lamina 1 while the outermost lamina is referred to as lamina N . The orientation of the fibers in a given lamina is denoted by the angle α . This angle is measured relative to the cylindrical axis of symmetry (Z -axis). The inner radius of the metal liner and its thickness are constant throughout the cylinder. The internal pressure is supported by fiber overwrapped laminae as well as the liner. The state of stress or strain in the thick-walled cylinder is three-dimensional.

Three-dimensional Stress, Strain & Displacement Analysis

The stresses on a small infinitesimal element taken from the shell are illustrated in Fig. 12.1. Standard notation is here used and the six components of stress are σ_{zz} , $\sigma_{\theta\theta}$, σ_{rr} , $\tau_{\theta r}$, τ_{zr} , and $\tau_{z\theta}$, while the six components of strain are ε_{zz} , $\varepsilon_{\theta\theta}$, ε_{rr} , $\gamma_{\theta r}$, γ_{zr} , and $\gamma_{z\theta}$.

Linear elasticity requires that the equations defining strains and displacements must simultaneously be satisfied. It is necessary that in the process of deformation no voids or dislocations are created. This condition (referring to a monolithic material or elastic continuum) possesses limitations upon the strains and the displacements. Such restrictions are mathematically defined as compatibility equations. For the general case, six compatibility equations exist; however when one condenses a problem to either plane stress or strain, a single compatibility condition emerges. For generalized plane strain along the axis of a cylinder, the compatibility equation can be derived by taking appropriate partial derivatives of the stress-strain relations and making substitutions to eliminate displacements. The general theory of the anisotropic cylinders is given by Lekhnitskii [1]. He investigated the plane stresses in a cylindrical shell subjected to internal and external pressures, which is cylindrically orthotropic. By layering a number of such shells and by matching the radial stresses and deformations of adjacent shells at their interfaces, he developed relations describing the stresses and strains in a multi-layer cylindrical shell [2]. Tsai [3] has extended Lekhnitskii's work to the case of generalized plane strain, in which the axial strain of the cylinder is a constant rather than zero ($\varepsilon_z = \varepsilon_0$), and applied it to a filament-wound cylinder where each layer of Lekhnitskii's model corresponds to a 'winding layer' of the cylindrical pressure vessel. The assumption based on the generalized plane strain can introduce small errors because the restraint condition itself superposes its own stresses due to internal Poisson's action [4]. Witherell [5] presented a three step axial strain equilibrating correction procedure for the plane-strain analysis method. First the conventional ($\varepsilon_z = 0$) plane-strain axial procedure is used to determine laminate stresses due to the applied pressure. Then, in the correction, axial forces are applied to the individual lamina such that each lamina sees the same common axial strain that has initially been assumed ($\varepsilon_z = \varepsilon_0$). In the third step, the gaps and overlaps resulting in the radial direction from the equilibrium lamina stresses are used to compute additional inter-ply stresses which are finally added to the original pressure solution. Roy and Tsai [6] proposed a simple and efficient design method for thick composite cylinders; the stress analysis is based on 3-dimensional elasticity by considering the cylinder in the state of generalized plane strain for both open-ended (pipes) and closed-ended (pressure vessel) cases. Based on the three-dimensional anisotropic elasticity, an exact elastic solution for stresses and strains of the pipes under internal pressure is presented by Xia et al. [7]. A

Chapter 12

computer model [8] has been developed to investigate stresses and strains of thick-walled, orthotropic sandwich pipes under internal pressure. Noor and Burton [9] have systematically evaluated the effects of variation in the lamination and the geometric parameters of multilayered composite cylinders on the accuracy of the static and vibrational responses predicted by eight modeling approaches. Mackerle [10] presented a bibliographical review of finite element methods applied in thick-walled pressure vessels and piping. Tabakovin [11] presented an exact analytical solution for closed-ended laminated cylinders limited to five layers. Wild and Vickers [12] developed an analytical procedure to assess the stresses and deformations of filament-wound structures under combined centrifugal loading, internal pressure, and axial loading. Hyer [13] discussed the results of a layer-by-layer analysis of a thick-walled cross-ply graphite-epoxy cylinder subjected to external hydrostatic pressure. The analysis, which is valid away from the ends of the cylinder and is based on a generalized plane deformation elasticity solution for each layer, considers inter- and intra-laminar stresses. Mirza et al. [14] studied composite cylindrical vessels under concentrated moments applied at discrete lug positions by using the finite element method. The first-ply failure in composite pressure vessels were investigated by some authors [15, 16] by using acoustic emission technique. Their results showed good agreement between FEM and experiments. Ruddock and Spencer [17] proposed a new numerical method for the determination of stress and deformation in laminated and inhomogeneous, anisotropic, elastic and thermo-elastic plates and shells, without recourse to any thin plate or shell approximations. Kokan and Gramoll [18] described techniques for calculating the elastic stresses and strains that would be encountered as a result of manufacture and utilization. Optimization of the stress-strain state of a thick-walled pipe on the basis of Young's modulus of the material has been made by Kalinnikov and Korlyakov [19]. Ren [20] presented a 3-D elasticity solution for an anisotropic laminated circular cylindrical shell, simply supported under axisymmetric loads and used the power series method for the analysis of anisotropic laminated circular cylindrical shells under axisymmetric loading. He also obtained exact solutions for cross-ply laminated cylindrical shells [21]. Chandrashekhara and Gopalakrishnan [22] presented an elasticity solution for a long transversely isotropic multilayered circular shell. An approximate 3-D elasticity solution has been presented for an infinite, thick, orthotropic laminated circular cylindrical shell of revolution subjected to a distributed pinch load [23]. A three-dimensional analysis of cylindrical shells can be also found in works of Noor and Rarig [24], Grigorenko et al. [25], Noor and Peters [26], Roy [27], and others. More complex 3-D analytical approaches can be found in works of Dotvc and Tso [28], Whitney and Sun [29], Lee and

Springer [30], Ding and Tang [31], Spencer et al. [32], Chandrashekhara [33, 34], Kollar et al. [35], where an arbitrary lay-up and/or more complex loading conditions were considered.

A thick-walled multi-layered filament-wound cylindrical shell is here considered based on Lekhnitskii's theory [1, 2] which assumes that the axis of cylindrical anisotropy coincides with the geometrical axis of the cylinder (Z -axis). In most previous work, the following hypotheses have been proposed for the formulation of stresses and deformations:

- (1) The cylinder is subjected to axisymmetric loading and keeps symmetry before and after deformation. The stresses and strains are independent of the hoop coordinate θ ($\partial/\partial\theta = 0$);
- (2) The shell is assumed to consist of several helically wound laminae, each of which forms an angle-ply anisotropic configuration of $\pm\alpha$ lamina acting as a homogeneous and orthotropic unit, as shown in Fig. 12.2;
- (3) For an axially symmetric case, the shear stresses τ_{rz} , $\tau_{r\theta}$ are equal to zero. $\tau_{z\theta}$ is also assumed to be zero since the twisting moment can be considered negligible for moderate and low pressure vessels;
- (4) Since the interlaminar shear modulus can be considered negligible in comparison to the elastic moduli of the laminae in the fiber direction, the interlaminar shear or tensile stress will not lead to delamination failure and is not here considered;
- (5) The end cap effects are limited to only small end portions of the pressure vessel. The cylinder is assumed to be in a state of generalized plane strain ($\varepsilon_z = \varepsilon_0$), since the plane sections remain plane at distant sections from the closed-ends (Saint-Venant's principle).

The design and analysis are primarily based on the direct solution method or the stress function method. These two approaches are elaborated as follows:

12.2.1 Direct solution method

The equilibrium equation of the element in the radial direction can be written as:

$$\begin{aligned} & \left(\sigma_r + \frac{\partial\sigma_r}{\partial r} dr\right)(r + dr)d\theta dz - \sigma_r r d\theta dz - \left(\sigma_\theta + \frac{\partial\sigma_\theta}{\partial\theta} d\theta\right)dr dz \sin\frac{d\theta}{2} - \sigma_\theta dr dz \sin\frac{d\theta}{2} \\ & - \tau_{r\theta} dr dz + \left(\tau_{r\theta} + \frac{\partial\tau_{r\theta}}{\partial\theta} d\theta\right)dr dz - \tau_{rz} r dr d\theta + \left(\tau_{rz} + \frac{\partial\tau_{rz}}{\partial z} dz\right)r dr d\theta = 0 \end{aligned} \quad (12.1)$$

Since $\sin A \approx A$ and $\cos A \approx 0$ for $A \rightarrow 0$, neglecting 2nd order terms and then dividing both sides of equation (12.1) by $(dzd\theta dr)$ yields [36]:

$$\frac{\partial\sigma_r}{\partial r} + \frac{\sigma_r - \sigma_\theta}{r} + \frac{\partial\tau_{rz}}{\partial z} + \frac{1}{r} \frac{\partial\tau_{r\theta}}{\partial\theta} = 0 \quad (12.2)$$

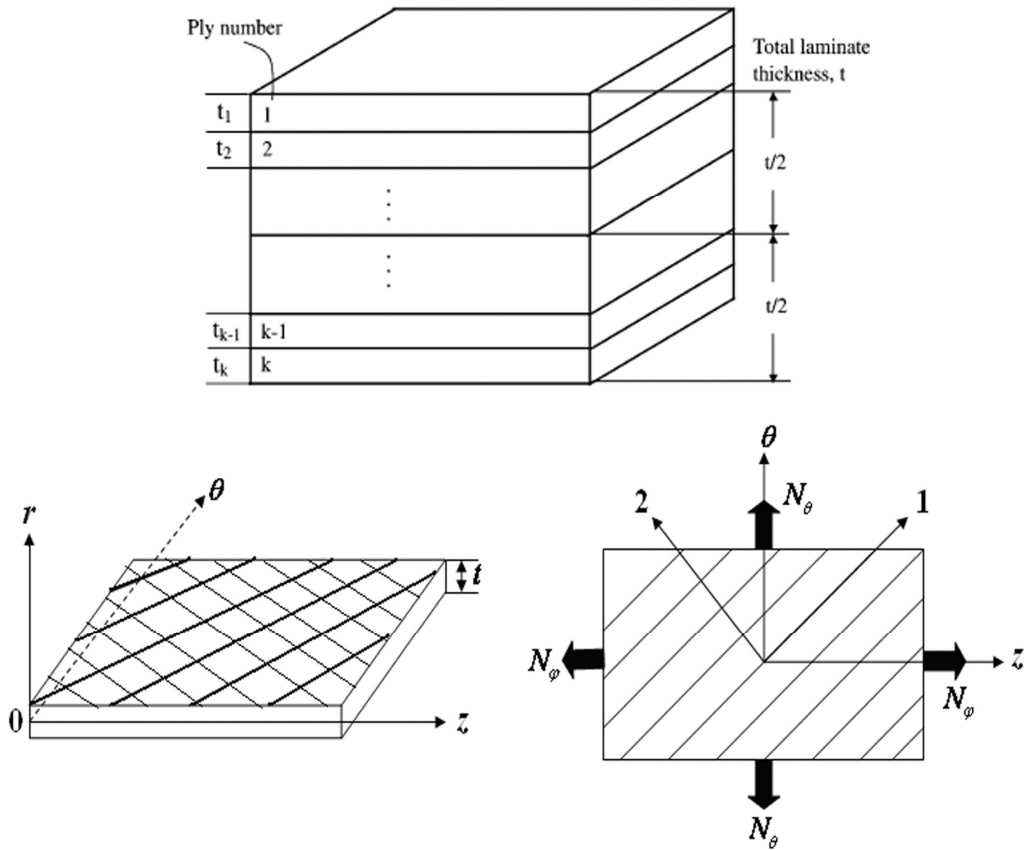


Fig. 12.2: Anisotropic configuration of $\pm\alpha$ laminae

A similar procedure can be followed for the derivation of equilibrium equations in the hoop and axial directions, respectively:

$$\text{Hoop direction: } \frac{1}{r} \frac{\partial \sigma_\theta}{\partial \theta} + \frac{2\tau_{r\theta}}{r} + \frac{\partial \tau_{r\theta}}{\partial r} + \frac{\partial \tau_{z\theta}}{\partial z} = 0 \quad (12.3)$$

$$\text{Axial direction: } \frac{\partial \sigma_z}{\partial z} + \frac{\partial \tau_{rz}}{\partial r} + \frac{\tau_{rz}}{r} + \frac{1}{r} \frac{\partial \tau_{z\theta}}{\partial \theta} = 0 \quad (12.4)$$

The strain-displacement relations are written as [1]:

$$\begin{aligned} \varepsilon_r &= \frac{\partial u_r}{\partial r}, \quad \varepsilon_\theta = \frac{u_r}{r} + \frac{\partial u_\theta}{r \partial \theta}, \quad \varepsilon_z = \frac{\partial u_z}{\partial z}, \\ \gamma_{\theta z} &= \frac{\partial u_z}{r \partial \theta} + \frac{\partial u_\theta}{\partial z}, \quad \gamma_{rz} = \frac{\partial u_r}{\partial z} + \frac{\partial u_z}{\partial r}, \quad \gamma_{r\theta} = \frac{\partial u_r}{r \partial \theta} + \frac{\partial u_\theta}{\partial r} - \frac{u_\theta}{r} \end{aligned} \quad (12.5)$$

where u_r , u_θ , and u_z represent radial, hoop and axial displacements, respectively. It should be stated that these equations are restricted to small displacements since they comprise only the linear terms of the full set.

Using the preceding hypotheses ($\partial/\partial\theta=0$, $\tau_{rz} = \tau_{r\theta} = \tau_{z\theta} = 0$), only equation (2) remains for equilibrium of the cylindrical shell element and simplifies to:

Three-dimensional Stress, Strain & Displacement Analysis

$$\frac{\partial \sigma_r}{\partial r} + \frac{\sigma_r - \sigma_\theta}{r} = 0 \quad (12.6)$$

In addition, the strain-displacement relations can be rewritten as:

$$\varepsilon_r = \frac{\partial u_r}{\partial r}, \quad \varepsilon_\theta = \frac{u_r}{r}, \quad \varepsilon_z = \varepsilon_0 \quad (12.7)$$

For thick-walled filament-wound pressure vessels, the relations for stresses and strains become more complicated because of their anisotropic character. A single orthotropic lamina of fiber-reinforced composite material is here considered, as shown in Fig. 12.3. In this lamina, the {1-2-3} principle material coordinate system is used where 1, 2, 3 denote the fiber, transverse and normal (through-thickness) directions, respectively.

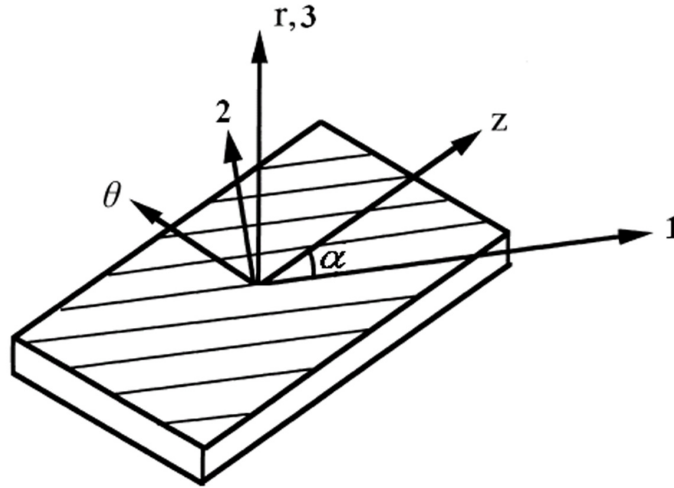


Fig. 12.3: Relation of coordinate system between principle material axes and cylindrical axes

The stress-strain relations for the k^{th} lamina in the material coordinate axes are given by:

$$\begin{bmatrix} \sigma_{11} \\ \sigma_{22} \\ \sigma_{33} \\ \tau_{23} \\ \tau_{13} \\ \tau_{12} \end{bmatrix}^{(k)} = \begin{bmatrix} Q_{11} & Q_{12} & Q_{13} & 0 & 0 & 0 \\ Q_{21} & Q_{22} & Q_{23} & 0 & 0 & 0 \\ Q_{31} & Q_{32} & Q_{33} & 0 & 0 & 0 \\ 0 & 0 & 0 & Q_{44} & 0 & 0 \\ 0 & 0 & 0 & 0 & Q_{55} & 0 \\ 0 & 0 & 0 & 0 & 0 & Q_{66} \end{bmatrix}^{(k)} \begin{bmatrix} \varepsilon_{11} \\ \varepsilon_{22} \\ \varepsilon_{33} \\ \gamma_{23} \\ \gamma_{13} \\ \gamma_{12} \end{bmatrix}^{(k)} \quad (12.8)$$

where subscripts 1 and 2 denote the in-plane longitudinal and transverse directions referred to as the material axes; 3 is the direction perpendicular to the 1-2 plane. The on-axis stiffness components Q_{ij} ($i, j = 1 \sim 6$) are stated by engineering constants [3]:

$$\begin{aligned}
 Q_{11} &= \frac{1 - \nu_{23}\nu_{32}}{E_2 E_3 \Delta}, & Q_{12} &= \frac{\nu_{21} + \nu_{23}\nu_{31}}{E_2 E_3 \Delta}, & Q_{13} &= \frac{\nu_{31} + \nu_{21}\nu_{32}}{E_2 E_3 \Delta}, \\
 Q_{22} &= \frac{1 - \nu_{13}\nu_{31}}{E_1 E_3 \Delta}, & Q_{23} &= \frac{\nu_{32} + \nu_{12}\nu_{31}}{E_1 E_3 \Delta}, & Q_{33} &= \frac{1 - \nu_{12}\nu_{21}}{E_1 E_2 \Delta}, \\
 Q_{44} &= G_{23}, & Q_{55} &= G_{31}, & Q_{66} &= G_{12}.
 \end{aligned} \tag{12.9}$$

where

$$\Delta = \frac{1 - \nu_{12}\nu_{21} - \nu_{23}\nu_{32} - \nu_{31}\nu_{13} - 2\nu_{21}\nu_{32}\nu_{13}}{E_1 E_2 E_3}$$

$E_1, E_2,$ and E_3 are Young's elastic moduli along the 1, 2, and 3 directions, respectively; ν_{ij} ($i, j = 1, 2, 3$) are the Poisson's ratios; $G_{12}, G_{23},$ and G_{13} are the shear moduli.

The stresses in the principal material coordinate system (1-2-3 system) can be transformed into the z - θ - r global coordinate system as shown in Fig. 12.3. The fibers are oriented at angle α with respect to the $+z$ axis of the global system. The fibers are parallel to the z - θ plane and the 3 and z axes coincide with each other. The winding angle α will be considered positive when the fibers rotate counterclockwise from the $+z$ axis toward the $+\theta$ axis. The stresses on an infinitesimal element are now identified with respect to the z - θ - r system. The stress-strain relations in the z - θ - r coordinate system are given as follows [1]:

$$\begin{bmatrix} \sigma_z \\ \sigma_\theta \\ \sigma_r \\ \tau_{\theta r} \\ \tau_{zr} \\ \tau_{z\theta} \end{bmatrix}^{(k)} = \begin{bmatrix} \bar{Q}_{11} & \bar{Q}_{12} & \bar{Q}_{13} & 0 & 0 & \bar{Q}_{16} \\ \bar{Q}_{12} & \bar{Q}_{22} & \bar{Q}_{23} & 0 & 0 & \bar{Q}_{26} \\ \bar{Q}_{13} & \bar{Q}_{23} & \bar{Q}_{33} & 0 & 0 & \bar{Q}_{36} \\ 0 & 0 & 0 & \bar{Q}_{44} & \bar{Q}_{45} & 0 \\ 0 & 0 & 0 & \bar{Q}_{45} & \bar{Q}_{55} & 0 \\ \bar{Q}_{16} & \bar{Q}_{26} & \bar{Q}_{36} & 0 & 0 & \bar{Q}_{66} \end{bmatrix}^{(k)} \begin{bmatrix} \varepsilon_z \\ \varepsilon_\theta \\ \varepsilon_r \\ \gamma_{\theta r} \\ \gamma_{zr} \\ \gamma_{z\theta} \end{bmatrix}^{(k)} \tag{12.10}$$

\bar{Q}_{ij} ($i, j = 1 \sim 6$) are the off-axis stiffness components related to the on-axis stiffness Q_{ij} :

$$\begin{aligned}
 \bar{Q}_{11} &= Q_{11}c^4 + 2(Q_{12} + 2Q_{66})c^2s^2 + Q_{22}s^4, \\
 \bar{Q}_{12} &= (Q_{11} + Q_{22} - 4Q_{66})c^2s^2 + Q_{12}(c^4 + s^4), \\
 \bar{Q}_{13} &= Q_{13}c^2 + Q_{23}s^2, \\
 \bar{Q}_{16} &= (Q_{11} - Q_{12} - 2Q_{66})sc^3 + (Q_{12} - Q_{22} + 2Q_{66})cs^3, \\
 \bar{Q}_{22} &= Q_{11}s^4 + 2(Q_{12} + 2Q_{66})c^2s^2 + Q_{22}c^4, \\
 \bar{Q}_{23} &= Q_{23}c^2 + Q_{13}s^2,
 \end{aligned}$$

Three-dimensional Stress, Strain & Displacement Analysis

$$\begin{aligned}
 \bar{Q}_{26} &= (Q_{11} - Q_{12} - 2Q_{66})cs^3 + (Q_{12} - Q_{22} + 2Q_{66})sc^3, \\
 \bar{Q}_{33} &= Q_{33}, \\
 \bar{Q}_{36} &= (Q_{13} - Q_{23})cs, \\
 \bar{Q}_{44} &= Q_{44}c^2 + Q_{55}s^2, \\
 \bar{Q}_{45} &= (Q_{55} - Q_{44})cs, \\
 \bar{Q}_{55} &= Q_{55}c^2 + Q_{44}s^2, \\
 \bar{Q}_{66} &= (Q_{11} + Q_{22} - 2Q_{12} - 2Q_{66})c^2s^2 + Q_{66}(c^4 + s^4). \tag{12.11}
 \end{aligned}$$

where $c = \cos\alpha$, $s = \sin\alpha$. Substituting the stress-strain relation of equation (12.10) into (12.6), and using equation (12.7), the governing equation for the radial displacement of the k^{th} lamina is now given by:

$$\frac{d^2 u_r^{(k)}}{dr^2} + \frac{1}{r} \frac{du_r^{(k)}}{dr} - \frac{\bar{Q}_{22}^{(k)}}{\bar{Q}_{33}^{(k)}} \frac{u_r^{(k)}}{r^2} - \frac{\bar{Q}_{12}^{(k)} - \bar{Q}_{13}^{(k)}}{\bar{Q}_{33}^{(k)}} \frac{\varepsilon_0}{r} = 0 \tag{12.12}$$

Please note here for anisotropic materials the following conditions holds: $\bar{Q}_{22}^{(k)} / \bar{Q}_{33}^{(k)} > 0$ and

$\bar{Q}_{22}^{(k)} / \bar{Q}_{33}^{(k)} \neq 1$. With $\beta^{(k)} = \sqrt{\frac{\bar{Q}_{22}^{(k)}}{\bar{Q}_{33}^{(k)}}}$, $\eta^{(k)} = \frac{\bar{Q}_{12}^{(k)} - \bar{Q}_{13}^{(k)}}{\bar{Q}_{33}^{(k)} - \bar{Q}_{22}^{(k)}}$, the general solution for equation (12.12)

can be given by:

$$u_r^{(k)}(r) = D_1^{(k)} r^{\beta^{(k)}} + D_2^{(k)} r^{-\beta^{(k)}} + \eta^{(k)} \varepsilon_0 r \tag{12.13}$$

where $D_1^{(k)}$ and $D_2^{(k)}$ are the unknown constants of integration which can be determined by the boundary conditions and the interface continuity conditions that apply between adjacent laminae. Substituting equation (12.13) into (12.7) and plugging the result into equation (12.10), gives:

$$\begin{Bmatrix} \sigma_z^{(k)}(r) \\ \sigma_\theta^{(k)}(r) \\ \sigma_r^{(k)}(r) \end{Bmatrix} = \begin{bmatrix} H_z^{(k)} & I_z^{(k)} & J_z^{(k)} \\ H_\theta^{(k)} & I_\theta^{(k)} & J_\theta^{(k)} \\ H_r^{(k)} & I_r^{(k)} & J_r^{(k)} \end{bmatrix} \begin{Bmatrix} \varepsilon_0 \\ D_1^{(k)} r^{(\beta^{(k)}-1)} \\ D_2^{(k)} r^{-(\beta^{(k)}+1)} \end{Bmatrix} \tag{12.14}$$

where:

$$\begin{aligned}
 H_z^{(k)} &= \bar{Q}_{11}^{(k)} + \eta^{(k)}(\bar{Q}_{12}^{(k)} + \bar{Q}_{13}^{(k)}), & I_z^{(k)} &= \bar{Q}_{12}^{(k)} + \beta^{(k)}\bar{Q}_{13}^{(k)}, & J_z^{(k)} &= \bar{Q}_{12}^{(k)} - \beta^{(k)}\bar{Q}_{13}^{(k)}, \\
 H_\theta^{(k)} &= \bar{Q}_{12}^{(k)} + \eta^{(k)}(\bar{Q}_{22}^{(k)} + \bar{Q}_{23}^{(k)}), & I_\theta^{(k)} &= \bar{Q}_{22}^{(k)} + \beta^{(k)}\bar{Q}_{23}^{(k)}, & J_\theta^{(k)} &= \bar{Q}_{22}^{(k)} - \beta^{(k)}\bar{Q}_{23}^{(k)}, \\
 H_r^{(k)} &= \bar{Q}_{13}^{(k)} + \eta^{(k)}(\bar{Q}_{23}^{(k)} + \bar{Q}_{33}^{(k)}), & I_r^{(k)} &= \bar{Q}_{23}^{(k)} + \beta^{(k)}\bar{Q}_{33}^{(k)}, & J_r^{(k)} &= \bar{Q}_{23}^{(k)} - \beta^{(k)}\bar{Q}_{33}^{(k)}.
 \end{aligned} \tag{12.15}$$

Chapter 12

The design of composite pressure vessels usually involves placing FRP laminae over an inner liner made of some isotropic material [17]. The use of the liner is preferred for several reasons. The liner serves as a protective layer for the composite overwraps while preventing leakage of the stored gas or liquid. Furthermore, the isotropic liner typically has better elastic properties in the radial direction for transferring load. In this case, the following relations for the stiffness components are given:

$$Q_{11}^L = Q_{22}^L = Q_{33}^L, \quad Q_{12}^L = Q_{13}^L = Q_{23}^L, \quad Q_{44}^L = Q_{55}^L = Q_{66}^L, \quad Q_{16}^L = Q_{26}^L = Q_{36}^L = 0 \quad (12.16)$$

where the superscript L denotes the isotropic liner. The governing equation (12.12) thus reduces to:

$$\frac{d^2 u_r^L}{dr^2} + \frac{1}{r} \frac{du_r^L}{dr} - \frac{u_r^L}{r^2} = 0 \quad (12.17)$$

The general solution for equation (12.17) is:

$$u_r^L(r) = D_1^L r + D_2^L / r \quad (12.18)$$

where D_1^L and D_2^L are the unknown integration constants. The stress-strain relations for an isotropic material liner can be formulated as:

$$\begin{Bmatrix} \sigma_z \\ \sigma_\theta \\ \sigma_r \\ \tau_{\theta r} \\ \tau_{zr} \\ \tau_{z\theta} \end{Bmatrix}^L = \lambda \begin{bmatrix} 1-\mu & \mu & \mu & 0 & 0 & 0 \\ \mu & 1-\mu & \mu & 0 & 0 & 0 \\ \mu & \mu & 1-\mu & 0 & 0 & 0 \\ 0 & 0 & 0 & 1-2\mu & 0 & 0 \\ 0 & 0 & 0 & 0 & 1-2\mu & 0 \\ 0 & 0 & 0 & 0 & 0 & 1-2\mu \end{bmatrix} \begin{Bmatrix} \varepsilon_z \\ \varepsilon_\theta \\ \varepsilon_r \\ \frac{\gamma_{\theta r}}{2} \\ \frac{\gamma_{zr}}{2} \\ \frac{\gamma_{z\theta}}{2} \end{Bmatrix}^L \quad (12.19)$$

where $\lambda = \frac{E}{(1-2\mu)(1+\mu)}$; E and μ are the Young's modulus of elasticity and the Poisson's

ratio of the used isotropic material, respectively. Substituting equation (12.18) into (12.7) and plugging the result into equation (12.10), leads to the well-known Lamé's equations for thick-walled cylinders of isotropic materials:

$$\begin{Bmatrix} \sigma_z^L(r) \\ \sigma_\theta^L(r) \\ \sigma_r^L(r) \end{Bmatrix} = \lambda \begin{bmatrix} 1-\mu & 2\mu & 0 \\ \mu & 1 & 1-2\mu \\ \mu & 1 & 2\mu-1 \end{bmatrix} \begin{Bmatrix} \varepsilon_0 \\ D_1^L \\ D_2^L / r^2 \end{Bmatrix} \quad (12.20)$$

If the number of laminae is n , the total number of the unknown integration constants will be $2n+3$ (D_1^L , D_2^L , $D_1^{(k)}$, $D_2^{(k)}$, ε_0). In addition, since the vessel is only subjected to uniform

Three-dimensional Stress, Strain & Displacement Analysis

internal pressure, the radial normal stress at the inner liner surface is equal to the pressure p , while at the outer surface of the n^{th} lamina the radial stress is zero. Assuming that the interfaces between adjacent laminae and between the metal liner and the first lamina are perfectly bonded, the boundary conditions, which ensure continuity for the displacements and stresses at each interface, can be summarized as follows:

Displacement continuity:

$$u_r^{(k)}(r = r_k) = u_r^{(k+1)}(r = r_k) \quad (12.21)$$

$$u_r^{(1)}(r = r_b) = u_r^L(r = r_b) \quad (12.22)$$

Radial stress continuity (traction boundary conditions):

$$\sigma_r^{(k)}(r = r_k) = \sigma_r^{(k+1)}(r = r_k) \quad (12.23)$$

$$\sigma_r^{(1)}(r = r_b) = \sigma_r^L(r = r_b) \quad (12.24)$$

$$\sigma_r^L(r = r_a) = -p \quad \text{for the inner liner surface} \quad (12.25)$$

$$\sigma_r^{(n)}(r = r_c) = 0 \quad \text{for the outer composites surface} \quad (12.26)$$

Axial equilibrium:

Closed-end condition (Pressure vessels):

For a cylindrical pressure vessel with closed ends, the axial equilibrium should be satisfied by the following relation:

$$2\pi \left(\int_{r_a}^{r_b} \sigma_z^L(r) r dr + \sum_{k=1}^n \int_{r_{k-1}}^{r_k} \sigma_z^{(k)}(r) r dr \right) = \pi p r_a^2 \quad (12.27)$$

Open-end condition (Pipes):

When both ends of the cylinder are free, the resultant of σ_z for an open-end condition is equal to the axial force at the ends:

$$2\pi \left(\int_{r_a}^{r_b} \sigma_z^L(r) r dr + \sum_{k=1}^n \int_{r_{k-1}}^{r_k} \sigma_z^{(k)}(r) r dr \right) = A \quad (12.28)$$

where A is the resultant axial force acting on the ends of the cylinder. It should be mentioned that the axial equilibrium equation with closed-end condition is generally used for pressure vessels.

A $2n+3$ order linear system of equations can be formulated by substitution of equations (12.13), (12.14), (12.18) and (12.20) into preceding boundary conditions. The simultaneous solution of these equations will finally determine the $2n+3$ unknown integration constants:

$$\begin{Bmatrix} D_1^L \\ D_2^L \\ D_1^{(k)} \\ D_2^{(k)} \\ D_1^{(2)} \\ D_2^{(2)} \\ \varepsilon_0 \end{Bmatrix} = \begin{bmatrix} \lambda & \lambda(2\mu-1)/r_a^2 & 0 & 0 & 0 & 0 & \lambda\mu \\ \lambda & \lambda(2\mu-1)/r_b^2 & -I_r^{(1)}r_b^{-(\beta^{(1)+1})} & -J_r^{(1)}r_b^{-(\beta^{(1)+1})} & 0 & 0 & \lambda\mu-H_r^{(1)} \\ r_b & 1/r_b & -r_b^{\beta^{(1)}} & -r_b^{-\beta^{(1)}} & 0 & 0 & -\eta^{(1)}r_b \\ 0 & 0 & I_r^{(1)}r_1^{-(\beta^{(1)-1})} & J_r^{(1)}r_1^{-(\beta^{(1)+1})} & -I_r^{(2)}r_1^{-(\beta^{(2)-1})} & -J_r^{(2)}r_1^{-(\beta^{(2)+1})} & H_r^{(1)}-H_r^{(2)} \\ 0 & 0 & r_1^{\beta^{(1)}} & r_1^{-\beta^{(1)}} & -r_1^{\beta^{(2)}} & -r_1^{-\beta^{(2)}} & (\eta^{(1)}-\eta^{(2)})r_1 \\ 0 & 0 & I_r^{(2)}r_1^{-(\beta^{(2)-1})} & J_r^{(2)}r_1^{-(\beta^{(2)+1})} & 0 & 0 & H_r^{(2)} \\ \lambda\mu\chi_1 & 0 & I_z^{(1)}\chi_4 & J_z^{(1)}\chi_5 & I_z^{(2)}\chi_6 & J_z^{(2)}\chi_7 & \frac{\lambda(1-\mu)\chi_1+H_z^{(1)}\chi_2+H_z^{(2)}\chi_3}{2} \end{bmatrix}^{-1} \begin{Bmatrix} -p \\ 0 \\ 0 \\ 0 \\ 0 \\ 0 \\ \frac{pr_a^2}{2} \end{Bmatrix} \quad (12.29)$$

where:

$$\begin{aligned} \chi_1 &= (r_b^2 - r_a^2), \quad \chi_2 = (r_1^2 - r_b^2), \quad \chi_3 = (r_c^2 - r_1^2), \quad \chi_4 = \frac{r_1^{(\beta^{(1)+1})} - r_b^{(\beta^{(1)+1})}}{\beta^{(1)} + 1}, \\ \chi_5 &= \frac{r_1^{(1-\beta^{(1)})} - r_b^{(1-\beta^{(1)})}}{1 - \beta^{(1)}}, \quad \chi_6 = \frac{r_c^{(\beta^{(2)+1})} - r_1^{(\beta^{(2)+1})}}{\beta^{(2)} + 1}, \quad \chi_7 = \frac{r_c^{(1-\beta^{(2)})} - r_1^{(1-\beta^{(2)})}}{1 - \beta^{(2)}} \end{aligned} \quad (12.30)$$

Once the integration constants $D_1^L, D_2^L, D_1^{(k)}, D_2^{(k)}, \varepsilon_0$ are determined by solving equation (12.29), the stresses and deformations of the liner and each lamina can be evaluated by substitution of these constants into equations (12.13), (12.14), (12.18) and (12.20).

12.2.2 Stress function approach

The foundation of the present approach is an exact three-dimensional solution obtained by Lekhnitskii [1, 2] for a single-layered anisotropic cylinder with uniformly distributed pressure. This solution has been extended for multilayered cylinders with open and closed ends by deriving the governing differential equations in terms of stress functions proposed by Lekhnitskii [2]. The strain-stress relations of the k^{th} lamina can be written as the inverse form of equation (12.10):

$$\begin{bmatrix} \varepsilon_z \\ \varepsilon_\theta \\ \varepsilon_r \\ \gamma_{\theta r} \\ \gamma_{zr} \\ \gamma_{z\theta} \end{bmatrix}^k = \begin{bmatrix} a_{11} & a_{12} & a_{13} & a_{14} & a_{15} & a_{16} \\ a_{21} & a_{22} & a_{23} & a_{24} & a_{25} & a_{26} \\ a_{31} & a_{32} & a_{33} & a_{34} & a_{35} & a_{36} \\ a_{41} & a_{42} & a_{43} & a_{44} & a_{45} & a_{46} \\ a_{51} & a_{52} & a_{53} & a_{54} & a_{55} & a_{56} \\ a_{61} & a_{62} & a_{63} & a_{64} & a_{65} & a_{66} \end{bmatrix}^k \begin{bmatrix} \sigma_z \\ \sigma_\theta \\ \sigma_r \\ \tau_{\theta r} \\ \tau_{zr} \\ \tau_{z\theta} \end{bmatrix}^k \quad (12.31)$$

Three-dimensional Stress, Strain & Displacement Analysis

According to the hypotheses that have been proposed for the formulation of stresses and deformations, the stress-strain relations for the k^{th} lamina can be expressed in terms of the compliance components:

$$\begin{bmatrix} \varepsilon_z \\ \varepsilon_\theta \\ \varepsilon_r \end{bmatrix}^{(k)} = \begin{bmatrix} a_{zz} & a_{z\theta} & a_{zr} \\ a_{z\theta} & a_{\theta\theta} & a_{\theta r} \\ a_{zr} & a_{\theta r} & a_{rr} \end{bmatrix}^{(k)} \begin{bmatrix} \sigma_z \\ \sigma_\theta \\ \sigma_r \end{bmatrix}^{(k)} \quad (12.32)$$

Since $\varepsilon_z = \varepsilon_0$, we have:

$$\varepsilon_z^{(k)} = a_{zz}^{(k)} \sigma_z^{(k)} + a_{z\theta}^{(k)} \sigma_\theta^{(k)} + a_{zr}^{(k)} \sigma_r^{(k)} = \varepsilon_0 \quad (12.33)$$

If ε_z is taken out from the above equation and then substituted into equation (12.32), the following equations are obtained for the radial and hoop strains:

$$\begin{Bmatrix} \varepsilon_\theta \\ \varepsilon_r \end{Bmatrix}^{(k)} = \begin{bmatrix} \beta_{\theta\theta} & \beta_{\theta r} & a_{\theta z} / a_{zz} \\ \beta_{\theta r} & \beta_{rr} & a_{rz} / a_{zz} \end{bmatrix}^{(k)} \begin{Bmatrix} \sigma_\theta \\ \sigma_r \\ \varepsilon_0 \end{Bmatrix}^{(k)} \quad (12.34)$$

where

$$\beta_{rr}^{(k)} = a_{rr}^{(k)} - \frac{a_{zr}^{(k)2}}{a_{zz}^{(k)}}, \quad \beta_{r\theta}^{(k)} = a_{r\theta}^{(k)} - \frac{a_{z\theta}^{(k)} a_{zr}^{(k)}}{a_{zz}^{(k)}}, \quad \beta_{\theta\theta}^{(k)} = a_{\theta\theta}^{(k)} - \frac{a_{z\theta}^{(k)2}}{a_{zz}^{(k)}}. \quad (12.35)$$

Using Lekhnitskii's theory in a cylindrical coordinate system, the stress functions F and Ψ are related to the stress components by the equations [2]:

$$\begin{aligned} \sigma_r^{(k)} &= \frac{1}{r} \frac{\partial F^{(k)}}{\partial r} + \frac{1}{r^2} \frac{\partial^2 F^{(k)}}{\partial \theta^2} + \bar{U}^{(k)}, \quad \sigma_\theta^{(k)} = \frac{\partial^2 F^{(k)}}{\partial r^2} + \bar{U}^{(k)}, \quad \tau_{\theta r}^{(k)} = -\frac{\partial^2}{\partial \theta \partial r} \left(\frac{F^{(k)}}{r} \right), \\ \tau_{zr}^{(k)} &= \frac{1}{r} \frac{\partial \Psi^{(k)}}{\partial r}, \quad \tau_{z\theta}^{(k)} = -\frac{\partial \Psi^{(k)}}{\partial r}. \end{aligned} \quad (12.36)$$

Since the body force \bar{U} is not considered, the preceding equations are here simplified for the axisymmetric problem:

$$\sigma_\theta^{(k)} = \frac{\partial^2 F^{(k)}}{\partial r^2} = \frac{d^2 F^{(k)}}{dr^2}, \quad \sigma_r^{(k)} = \frac{1}{r} \frac{\partial F^{(k)}}{\partial r} = \frac{1}{r} \frac{dF^{(k)}}{dr} \quad (12.37)$$

The compatibility equation which relates the radial and hoop strain components is:

$$\varepsilon_r^{(k)} = \varepsilon_\theta^{(k)} + r \frac{d\varepsilon_\theta^{(k)}}{dr} \quad (12.38)$$

Substituting equation (12.37) into (12.34) and plugging the results into (12.38) gives an ordinary differential equation of the stress function F as:

$$r^3 \beta_{\theta\theta}^{(k)} \frac{d^3 F^{(k)}}{dr^3} + r^2 \beta_{\theta\theta}^{(k)} \frac{d^2 F^{(k)}}{dr^2} - r \beta_{rr}^{(k)} \frac{dF^{(k)}}{dr} = \varepsilon_0 r^2 \beta_\varepsilon^{(k)} \quad (12.39)$$

Chapter 12

where $\beta_\varepsilon^{(k)} = \frac{a_{zr}^{(k)} - a_{z\theta}^{(k)}}{a_{zz}^{(k)}}$. The solution for the stress function $F^{(k)}$ can then be given as:

$$F^{(k)} = C_0^{(k)} + C_1^{(k)}r^{1+\Gamma^{(k)}} + C_2^{(k)}r^{1-\Gamma^{(k)}} + \frac{c^{(k)}\varepsilon_0 r^2}{2} \quad (12.40)$$

where

$$\Gamma^{(k)} = \sqrt{\beta_{rr}^{(k)} / \beta_{\theta\theta}^{(k)}}, \quad c^{(k)} = \frac{\beta_\varepsilon^{(k)}}{(1-\Gamma^{(k)2})\beta_{\theta\theta}^{(k)}}$$

Substituting equation (12.40) into (12.37) gives the expression for normal stress components:

$$\begin{Bmatrix} \sigma_z(r) \\ \sigma_\theta(r) \\ \sigma_r(r) \end{Bmatrix}^{(k)} = \begin{bmatrix} -\frac{a_{rz} + \Gamma a_{\theta z}}{a_{zz}}(1+\Gamma) & -\frac{a_{rz} - \Gamma a_{\theta z}}{a_{zz}}(1-\Gamma) & -\frac{1+c(a_{rz} + a_{\theta z})}{a_{zz}} \\ \Gamma(1+\Gamma) & -\Gamma(1-\Gamma) & c \\ 1+\Gamma & 1-\Gamma & c \end{bmatrix}^{(k)} \begin{Bmatrix} C_1 r^{\Gamma-1} \\ C_2 r^{-\Gamma-1} \\ \varepsilon_0 \end{Bmatrix}^{(k)} \quad (12.41)$$

Substituting equation (12.41) into (12.32) and using the relation $u_r^{(k)} = \varepsilon_\theta^{(k)}r$, leads to:

$$u_r^{(k)} = (\beta_{\theta r}^{(k)} + \Gamma^{(k)}\beta_{\theta\theta}^{(k)})(1+\Gamma^{(k)})C_1^{(k)}r^{\Gamma^{(k)}} + (\beta_{\theta r}^{(k)} - \Gamma^{(k)}\beta_{\theta\theta}^{(k)})(1-\Gamma^{(k)})C_2^{(k)}r^{-\Gamma^{(k)}} + [(\beta_{\theta r}^{(k)} + \beta_{\theta\theta}^{(k)})c^{(k)} + \frac{a_{z\theta}^{(k)}}{a_{zz}^{(k)}}]\varepsilon_0 r \quad (12.42)$$

where $C_1^{(k)}$ and $C_2^{(k)}$ are unknown constants of integration which can be determined by the boundary conditions presented in equations (12.21) ~ (12.28). The stresses and strains can then be determined by substituting the obtained constants into equations (12.32) and (12.41).

12.3 Hygrothermal Effects

It is well known that material properties as well as the structural behavior are affected by environmental factors, such as elevated or reduced temperature, humidity and corrosive fluids. These factors must be taken into consideration since they affect the mechanical and physical properties of composite materials, resulting in a reduced performance. The effect of elevated temperature can be observed in the mechanical properties as a decrease in the modulus and strength because of thermal softening. Especially in polymer-based composites, the matrix-dominated properties are more affected than the fiber-dominated properties. For example, the longitudinal strength and modulus of a unidirectional composite lamina remain almost constant but the off-axis properties of the same lamina are significantly reduced as the temperature approaches the glass transition temperature of the polymer. When exposed to humid air or sea water environment, many polymeric matrix composites absorb moisture by

Three-dimensional Stress, Strain & Displacement Analysis

instantaneous surface absorption followed by diffusion through the matrix. Analysis of moisture absorption shows that for epoxy and polyester matrix composites, the moisture concentration increases initially with time and approaches an equilibrium (saturation) level after several days of exposure to humid environments [3].

Roy [37] presented the thermal stress analysis of a thick laminated ring, which was assumed to be cylindrically orthotropic. The analysis was based on considering the ring with orthotropic materials in the state of plane stress in the hoop and axial plane. Ben [38] has reported an accurate, finite-cylindrical element method to obtain the thermal stresses and deformation for thick-walled cylinders and evaluated the effects of thermal residual stresses on thick-walled FRP cylindrical pipes. Parnas and Katirci [39] developed an analytical procedure to design and predict the behavior of fiber reinforced composite pressure vessels. Internal pressure, axial force and body force due to rotation, in addition to temperature and moisture variation throughout the body are here considered. Jacquemin and Vautrin [40] examined the moisture concentration and the hygrothermal internal stress fields for evaluating the durability of thick composite pipes subjected to cyclic environmental conditions. Hyer et al. [41, 42] investigated the effects of a uniform temperature change on the stresses and deformations of angle-ply and cross-ply composite tubes, and determined the accuracy of an approximate solution based on the principle of complementary virtual work. Xia et al. [43] presented a solution based on the classical cylindrically anisotropic theory for the thermal stress and strain in a filament-wound fiber-reinforced sandwich pipe subjected to internal pressure and temperature change. Khdeir [44] investigated thermal deformations and stresses in cross-ply laminated circular cylindrical shells based on the state space approach which is used to solve exactly the thermoelastic governing equations. Sayman [45] investigated multilayered closed composite cylinders under hygrothermal loading by using analytical and finite element methods. Akcay and Kaynak [46] performed a failure analysis on the basis of analytical expressions of multilayered filament wound structures in composite cylinders for the plane-strain and closed-end condition cases, under internal pressure and uniform thermal loading.

The assumptions used in the majority of the aforementioned investigations are:

- (1) Temperature and moisture content inside the material vary only in the thickness direction;
- (2) thermal conductivity of the material is independent of temperature and moisture level;
- (3) the environmental conditions (temperature and moisture level) are constant.

Similar to chapter 3, the cylinder is assumed to be under a plane-strain state, and all shear strain components vanish. Using the cylindrical coordinate system shown in Fig. 12.1, the

Chapter 12

stress-strain relations of the k^{th} layer considering the thermal expansion and chemical changes ("shrinkage") are given by:

$$\begin{Bmatrix} \sigma_z(r) \\ \sigma_\theta(r) \\ \sigma_r(r) \end{Bmatrix}^{(k)} = \begin{bmatrix} \bar{Q}_{11} & \bar{Q}_{12} & \bar{Q}_{13} \\ \bar{Q}_{21} & \bar{Q}_{22} & \bar{Q}_{23} \\ \bar{Q}_{31} & \bar{Q}_{32} & \bar{Q}_{33} \end{bmatrix}^{(k)} \begin{Bmatrix} \varepsilon_z - \alpha_z \Delta T - \beta_z c \\ \varepsilon_\theta - \alpha_\theta \Delta T - \beta_\theta c \\ \varepsilon_r - \alpha_r \Delta T - \beta_r c \end{Bmatrix}^{(k)} \quad (12.43)$$

where α_z , α_θ and α_r are the thermal expansion coefficients, respectively; β_z , β_θ , β_r and c are the hygroscopic expansion coefficients and moisture concentration, respectively.

Since the temperature is assumed to be spatially uniform and the cylinder is long enough, none of the tube responses are dependent on the circumferential and axial coordinate, θ and z . As a result of this, the equilibrium conditions take a form similar to equation (12.6). Consideration of only the thermal effect, followed by substitution of equation (12.43) into (12.6) in combination with the strain-displacement relations (12.10), gives:

$$\frac{d^2 u_r^{(k)}}{dr^2} + \frac{1}{r} \frac{du_r^{(k)}}{dr} - \frac{\bar{Q}_{22}^{(k)}}{\bar{Q}_{33}^{(k)}} \frac{u_r^{(k)}}{r^2} - \frac{\bar{Q}_{12}^{(k)} - \bar{Q}_{13}^{(k)}}{\bar{Q}_{33}^{(k)}} \frac{\varepsilon_0}{r} - \frac{\xi_r^{(k)} - \xi_\theta^{(k)}}{\bar{Q}_{33}^{(k)}} \frac{\Delta T}{r} = 0 \quad (12.44)$$

where:

$$\begin{Bmatrix} \xi_\theta^{(k)} \\ \xi_r^{(k)} \end{Bmatrix} = \begin{bmatrix} \bar{Q}_{12}^{(k)} & \bar{Q}_{22}^{(k)} & \bar{Q}_{23}^{(k)} \\ \bar{Q}_{13}^{(k)} & \bar{Q}_{23}^{(k)} & \bar{Q}_{33}^{(k)} \end{bmatrix} \begin{Bmatrix} \alpha_z^{(k)} \\ \alpha_\theta^{(k)} \\ \alpha_r^{(k)} \end{Bmatrix} \quad (12.45)$$

With $\delta^{(k)} = \frac{\bar{Q}_{12}^{(k)} - \bar{Q}_{13}^{(k)}}{\bar{Q}_{33}^{(k)}}$, $\eta^{(k)} = \frac{\xi_r^{(k)} - \xi_\theta^{(k)}}{\bar{Q}_{33}^{(k)}}$, $\omega^{(k)} = \sqrt{\frac{\bar{Q}_{22}^{(k)}}{\bar{Q}_{33}^{(k)}}}$, the general solution for equation

(12.45) takes the following form:

$$u_r^{(k)}(r) = D_1^{(k)} r^{\omega^{(k)}} + D_2^{(k)} r^{-\omega^{(k)}} + \frac{(\delta^{(k)} \varepsilon_0 + \eta^{(k)} \Delta T) r}{1 - \omega^{(k)2}} \quad \text{for } \omega^{(k)} \neq 1 \text{ (anisotropic laminae)} \quad (12.46)$$

$$u_r^{(L)}(r) = D_1^{(L)} r + D_2^{(L)} r + \frac{(\delta^{(L)} \varepsilon_0 + \eta^{(L)} \Delta T)}{2} r \ln r \quad \text{for } \omega^{(k)} = 1 \text{ (isotropic liner)} \quad (12.47)$$

where D_1 and D_2 are unknown constants of integration which can be determined by the boundary conditions presented in equations (12.21)~(12.28). The stresses can then be determined by substituting the obtained constants into equation (12.43).

12.4 Twisting

Twisting, due to lack of exact symmetry in ply stacking, can be calculated on an individual lamina basis using the methods presented by Sherrer [47]. It has theoretically been shown [48, 49] that filament-wound cylinders under internal pressure exhibit twisting even though the lay-up is of a symmetric angle-ply, i.e., $[\pm\alpha]_n$. This is because the off-axis laminate causes a non-zero resultant in the coupling terms of the transformed reduced stiffness matrix. This twisting gives in-plane shear strains of the cylindrical shell. Hoa and Mannarino [49] investigated twisting in filament-wound cylinders subjected to internal pressure and used two approaches to give a rigorous proof for the existence thereof. The twisting effect has also been taken into account by other researchers [4, 6, 7, 13, 30, 37, 41, 42].

Considering the twisting moment, located in the z - θ plane of the cylinder, the shear strain $\gamma_{z\theta}$ of the k^{th} lamina can be expressed as [7]:

$$\gamma_{z\theta}^{(k)} = \gamma_0 r \quad (12.48)$$

where γ_0 represents the twisting rate of pipe (angle/unit length). The off-axis hoop and radial stress-strain relations of the k^{th} lamina are thus written as:

$$\begin{Bmatrix} \sigma_\theta \\ \sigma_r \end{Bmatrix} = \begin{bmatrix} \bar{Q}_{21} & \bar{Q}_{22} & \bar{Q}_{23} & \bar{Q}_{26} \\ \bar{Q}_{31} & \bar{Q}_{32} & \bar{Q}_{33} & \bar{Q}_{36} \end{bmatrix} \begin{Bmatrix} \varepsilon_z \\ \varepsilon_\theta \\ \varepsilon_r \\ \gamma_{z\theta} \end{Bmatrix} \quad (12.49)$$

Substituting equations (12.48) and (12.49) into (12.6), the governing equation for the radial displacement becomes:

$$\frac{d^2 u_r^{(k)}}{dr^2} + \frac{1}{r} \frac{du_r^{(k)}}{dr} - \frac{\bar{Q}_{22}^{(k)}}{\bar{Q}_{33}^{(k)}} \frac{u_r^{(k)}}{r^2} - \frac{\bar{Q}_{12}^{(k)} - \bar{Q}_{13}^{(k)}}{\bar{Q}_{33}^{(k)}} \frac{\varepsilon_0}{r} - \frac{\bar{Q}_{26}^{(k)} - 2\bar{Q}_{36}^{(k)}}{\bar{Q}_{33}^{(k)}} \gamma_0 = 0 \quad (12.50)$$

Let $\zeta^{(k)} = \frac{\bar{Q}_{26}^{(k)} - 2\bar{Q}_{36}^{(k)}}{4\bar{Q}_{33}^{(k)} - \bar{Q}_{22}^{(k)}}$. The general solution for equation (12.50) can now be derived as:

$$u_r^{(k)}(r) = D_1^{(k)} r^{\beta^{(k)}} + D_2^{(k)} r^{-\beta^{(k)}} + \eta^{(k)} \varepsilon_0 r + \zeta^{(k)} \gamma_0 r^2 \quad (12.51)$$

where $D_1^{(k)}$ and $D_2^{(k)}$ are constants of integration. Substituting equation (12.51) into (12.7) and plugging the result into equation (12.10), gives:

$$\begin{Bmatrix} \sigma_z^{(k)}(r) \\ \sigma_\theta^{(k)}(r) \\ \sigma_r^{(k)}(r) \\ \tau_{z\theta}^{(k)}(r) \end{Bmatrix} = \begin{bmatrix} H_z^{(k)} & I_z^{(k)} & J_z^{(k)} & K_z^{(k)} \\ H_\theta^{(k)} & I_\theta^{(k)} & J_\theta^{(k)} & K_\theta^{(k)} \\ H_r^{(k)} & I_r^{(k)} & J_r^{(k)} & K_r^{(k)} \\ H_{z\theta}^{(k)} & I_{z\theta}^{(k)} & J_{z\theta}^{(k)} & K_{z\theta}^{(k)} \end{bmatrix} \begin{Bmatrix} \varepsilon_0 \\ D_1^{(k)} r^{(\beta^{(k)}-1)} \\ D_2^{(k)} r^{-(\beta^{(k)}+1)} \\ \gamma_0 r \end{Bmatrix} \quad (12.52)$$

where:

$$\begin{bmatrix} H_z^{(k)} & I_z^{(k)} & J_z^{(k)} & K_z^{(k)} \\ H_\theta^{(k)} & I_\theta^{(k)} & J_\theta^{(k)} & K_\theta^{(k)} \\ H_r^{(k)} & I_r^{(k)} & J_r^{(k)} & K_r^{(k)} \\ H_{z\theta}^{(k)} & I_{z\theta}^{(k)} & J_{z\theta}^{(k)} & K_{z\theta}^{(k)} \end{bmatrix} = \begin{bmatrix} \bar{Q}_{11} & \bar{Q}_{12} & \bar{Q}_{13} & \bar{Q}_{16} \\ \bar{Q}_{21} & \bar{Q}_{22} & \bar{Q}_{23} & \bar{Q}_{26} \\ \bar{Q}_{31} & \bar{Q}_{32} & \bar{Q}_{33} & \bar{Q}_{36} \\ \bar{Q}_{16} & \bar{Q}_{26} & \bar{Q}_{36} & \bar{Q}_{66} \end{bmatrix}^{(k)} \begin{bmatrix} 1 & 0 & 0 & 0 \\ \eta^{(k)} & 1 & 1 & \zeta^{(k)} \\ \eta^{(k)} & \beta^{(k)} - \beta^{(k)} & 2\zeta^{(k)} & \\ 0 & 0 & 0 & 1 \end{bmatrix} \quad (12.53)$$

Substitution of equations (12.51) and (12.52) into the boundary conditions given in equations (10.21) ~ (10.28) leads to an algebraic system of equations for the unknown constants $C_1, C_2, D_1^{(k)}, D_2^{(k)}, \varepsilon_0, \gamma_0$. It should be noted that there is one more unknown constant, i.e., the twisting coefficient γ_0 . Therefore, the following boundary condition needs to be added for satisfying the zero-torsion criterion:

$$2\pi \sum_{k=1}^n \int_{r_{k-1}}^{r_k} \tau_{z\theta}^{(k)}(r) r^2 dr = 0 \quad (12.54)$$

The stresses and displacements can then be calculated by using the obtained integration constants.

Hoa and Mannarino [49] also stated that there are a few situations where twist disappears:

- (1) Symmetric laminate: If the filament winding process creates a perfectly symmetric laminate about its midplane, the coupling terms B_{16}, B_{26} vanish and twisting will not occur;
- (2) Winding at 0° (polar winding) or 90° (hoop winding) or combination of both. In these cases, $Q_{16} = Q_{26} = 0$;
- (3) There are intermediate angles between 0° and 90° where twist vanishes, depending on material constants, the radius of the cylinder as well as lamina thickness (Refer to [59] for the governing equation).

12.5 Effective Elastic Properties

For most composite materials, the engineering constants $E_{11}, E_{22}, E_{33}, G_{12}, G_{13}, G_{23}, \nu_{12}, \nu_{13}, \nu_{23}$ are required for the 1-2-3 principal material coordinate system. These engineering properties are indirectly involved in the transformed reduced stiffness and compliance matrices. Engineering properties can also be defined in the z - θ - r global coordinate system;

Three-dimensional Stress, Strain & Displacement Analysis

they are much more often used and mean considerably more to many designers and engineers because the physical interpretation of these quantities is well established and understood. There is plenty of information on the elastic constants for unidirectional fiber-reinforced composites and in-plane elastic constants for thin laminates, but a limited number of studies aimed at determining the effective material properties of laminates in three dimensions, thus including the through-thickness direction.

Enie and Rizzo [50] estimated all the elastic constants needed for three-dimensional stress analysis. They assumed uniform in-plane strains and used a "heuristic parallel model" for determining through-thickness Poisson ratios. Chou et al. [51] considered laminates consisting of an assembly of identical repeated sub-laminates and determined the effective elastic constants in three dimensions by assuming that all layers in any given sub-laminate experienced constant in-plane strains and through-thickness normal and shear stresses. Sun and Li [52] predicted negative through-thickness Poisson ratios for angle-ply laminates and showed that the magnitude of the Poisson ratio depends greatly upon the degree of anisotropy of the material and the orientation of the layers. Pagano [53] conducted a more rigorous theoretical analysis for thin laminates allowing for bending and twisting and assuming constant through-thickness normal and shear stresses and derived expressions for the effective elastic constants in three dimensions. Roy and Tsai [54] employed a numerical approach to analyze orthotropic and symmetric laminates without the assumption of constant through-thickness stresses. Herakovich [55] presented a theoretical analysis to calculate the effective Poisson ratios for angle-ply laminates. In his analysis, he assumed that through-thickness stresses were zero and he predicted negative Poisson ratios in the through-thickness direction for angle-ply laminates made from graphite/epoxy.

A laminated composite with its own effective elastic properties, contains a number of anisotropic plates. When these effective elastic properties of the laminate are used, the body is considered to as responding to the applied loads as a single unit. The effective elastic properties of the laminate can be determined by using the theory of the laminated plates. In this study filament wound structures are assumed to be made of angle-ply laminates. An angle-ply laminate has alternating lamina having $+\alpha$ and $-\alpha$ winding angles. Therefore, a filament-wound cylindrical shell can macroscopically be considered as an angle-ply laminate. For multi-layered cylinders, each layer is an angle-ply laminate with its own winding angle. Neglecting the effect of curvature, the effective elastic properties of each of these layers can be formulated as follows:

The average (effective) through-thickness normal stress $\bar{\sigma}_r$ is taken into account and is

Chapter 12

treated as constant throughout the thickness. From row 3 of matrix equation (12.10), ε_r can be expressed as:

$$\varepsilon_r = \frac{\bar{\sigma}_r - \bar{Q}_{31}\varepsilon_z - \bar{Q}_{32}\varepsilon_\theta - \bar{Q}_{36}\gamma_{z\theta}}{\bar{Q}_{33}} \quad (12.55)$$

Substituting equation (12.55) into row 1, 2, 6 of matrix equation (12.10), respectively, leads to:

$$\begin{Bmatrix} \sigma_z \\ \sigma_\theta \\ \tau_{z\theta} \end{Bmatrix} = \begin{bmatrix} \bar{Q}_{11} - \frac{\bar{Q}_{13}^2}{\bar{Q}_{33}} & \bar{Q}_{12} - \frac{\bar{Q}_{23}\bar{Q}_{13}}{\bar{Q}_{33}} & \bar{Q}_{16} - \frac{\bar{Q}_{36}\bar{Q}_{13}}{\bar{Q}_{33}} \\ \bar{Q}_{12} - \frac{\bar{Q}_{13}\bar{Q}_{23}}{\bar{Q}_{33}} & \bar{Q}_{22} - \frac{\bar{Q}_{23}^2}{\bar{Q}_{33}} & \bar{Q}_{26} - \frac{\bar{Q}_{36}\bar{Q}_{23}}{\bar{Q}_{33}} \\ \bar{Q}_{16} - \frac{\bar{Q}_{36}\bar{Q}_{13}}{\bar{Q}_{33}} & \bar{Q}_{26} - \frac{\bar{Q}_{36}\bar{Q}_{23}}{\bar{Q}_{33}} & \bar{Q}_{66} - \frac{\bar{Q}_{36}^2}{\bar{Q}_{33}} \end{bmatrix} \begin{Bmatrix} \varepsilon_z \\ \varepsilon_\theta \\ \gamma_{z\theta} \end{Bmatrix} + \begin{bmatrix} \frac{\bar{Q}_{13}}{\bar{Q}_{33}} \\ \frac{\bar{Q}_{23}}{\bar{Q}_{33}} \\ \frac{\bar{Q}_{26}}{\bar{Q}_{33}} \end{bmatrix} \bar{\sigma}_r \quad (12.56)$$

If the filament-wound cylinder is modeled with a balanced and symmetric arrangement of layers $(\pm\alpha)_n$ as shown in Fig. 11.2 with the same materials, fiber orientations, and the same thickness of layers, we have:

$$\begin{Bmatrix} N_z \\ N_\theta \\ N_{\theta r} \\ N_{zr} \\ N_{z\theta} \end{Bmatrix} = \begin{bmatrix} A_{11} & A_{12} & 0 & 0 & 0 \\ A_{21} & A_{22} & 0 & 0 & 0 \\ 0 & 0 & A_{44} & 0 & 0 \\ 0 & 0 & 0 & A_{55} & 0 \\ 0 & 0 & 0 & 0 & A_{66} \end{bmatrix} \begin{Bmatrix} \varepsilon_z \\ \varepsilon_\theta \\ \gamma_{\theta r} \\ \gamma_{zr} \\ \gamma_{z\theta} \end{Bmatrix} + \begin{bmatrix} H_1 \\ H_2 \\ 0 \\ 0 \\ 0 \end{bmatrix} \bar{\sigma}_r \quad (12.57)$$

where N_z , N_θ , $N_{\theta r}$, N_{zr} and $N_{z\theta}$ are the force resultants per unit length acting on the edges of an elementary sheet of thickness. A_{ij} ($i, j = 1, 2, 4, 5, 6$) and H_{ij} ($i, j = 1, 2$) can be defined as:

$$A_{ij} = \begin{cases} \sum_{k=1}^n (W_{ij})^{(k)} t^{(k)} & (i, j = 1, 2, 6) \\ \sum_{k=1}^n (\bar{Q}_{ij})^{(k)} t^{(k)} & (i, j = 4, 5) \end{cases}, \quad H_i = \sum_{k=1}^n \left(\frac{\bar{Q}_{i3}}{\bar{Q}_{33}} \right)^{(k)} t^{(k)} \quad (i = 1, 2) \quad (12.58)$$

where

$$W_{ij} = \bar{Q}_{ij} - \frac{\bar{Q}_{i3}\bar{Q}_{j3}}{\bar{Q}_{33}} \quad (i, j = 1, 2, 6) \quad (12.59)$$

Because an equal number of $\pm\alpha$ laminae have the same thickness, equation (12.58) can be rewritten as:

$$A_{ij} = \begin{cases} ntW_{ij} & (i, j = 1, 2, 6) \\ nt\bar{Q}_{ij} & (i, j = 4, 5) \end{cases}, \quad H_i = nt \frac{\bar{Q}_{i3}}{\bar{Q}_{33}} \quad (i = 1, 2) \quad (12.60)$$

Substituting expressions (equation (12.60)) for A_{ij} and H_i into equation (12.57) yields:

$$\begin{Bmatrix} \frac{N_z}{nt} \\ \frac{N_\theta}{nt} \\ \frac{N_{\theta r}}{nt} \\ \frac{N_{zr}}{nt} \\ \frac{N_{z\theta}}{nt} \end{Bmatrix} = \begin{bmatrix} W_{11} & W_{12} & 0 & 0 & 0 \\ W_{12} & W_{22} & 0 & 0 & 0 \\ 0 & 0 & \bar{Q}_{44} & 0 & 0 \\ 0 & 0 & 0 & \bar{Q}_{55} & 0 \\ 0 & 0 & 0 & 0 & W_{66} \end{bmatrix} \begin{Bmatrix} \varepsilon_z \\ \varepsilon_\theta \\ \gamma_{\theta r} \\ \gamma_{zr} \\ \gamma_{z\theta} \end{Bmatrix} + \begin{Bmatrix} \bar{Q}_{13} \\ \bar{Q}_{33} \\ \bar{Q}_{23} \\ \bar{Q}_{33} \\ 0 \\ 0 \\ 0 \end{Bmatrix} \bar{\sigma}_r \quad (12.61)$$

Now assume that a uniaxial direct stress (σ_r) is applied in the through-thickness direction and no external load is exerted in the x-y plane (i.e. the in-plane stress resultants N_x, N_y, N_{xy} are all zero). The simultaneous solution of the row 1, 2, 6 of matrix equation (12.61) provides:

$$\varepsilon_z = \frac{(H_2 W_{12} - H_1 W_{22})}{W_{11} W_{22} - W_{12}^2} \sigma_r, \quad \varepsilon_\theta = \frac{(H_1 W_{12} - H_2 W_{11})}{W_{11} W_{22} - W_{12}^2} \sigma_r, \quad \tau_{z\theta} = 0. \quad (12.62)$$

From row 3 of matrix (12.10), the radial normal stress can be given by ($\gamma_{z\theta} = 0$):

$$\sigma_r = \bar{Q}_{31} \varepsilon_z + \bar{Q}_{32} \varepsilon_\theta + \bar{Q}_{33} \varepsilon_r \quad (12.63)$$

Substitution of ε_z and ε_θ from equation (12.62) into (12.63) gives a direct relation for σ_r and ε_r . All layers are of the same material; therefore, the effective constants in the through-thickness direction E_r, ν_{zr} and $\nu_{\theta r}$ can be found:

$$E_r = \frac{\sigma_r}{\varepsilon_r} = \frac{\bar{Q}_{11} \bar{Q}_{22} \bar{Q}_{33} - \bar{Q}_{11} \bar{Q}_{23}^2 - \bar{Q}_{22} \bar{Q}_{13}^2 - \bar{Q}_{33} \bar{Q}_{12}^2 + 2 \bar{Q}_{23} \bar{Q}_{31} \bar{Q}_{12}}{\bar{Q}_{11} \bar{Q}_{22} - \bar{Q}_{12}^2},$$

$$\nu_{rz} = -\frac{\varepsilon_z}{\varepsilon_r} = \frac{\bar{Q}_{13} \bar{Q}_{22} - \bar{Q}_{12} \bar{Q}_{23}}{\bar{Q}_{11} \bar{Q}_{22} - \bar{Q}_{12}^2}, \quad \nu_{r\theta} = -\frac{\varepsilon_\theta}{\varepsilon_r} = \frac{\bar{Q}_{11} \bar{Q}_{23} - \bar{Q}_{12} \bar{Q}_{13}}{\bar{Q}_{11} \bar{Q}_{22} - \bar{Q}_{12}^2}. \quad (12.64)$$

Similarly, other effective elastic constants can be obtained by considering uniaxial tension or shear loading applied in the x-y, x-z, y-z planes, respectively:

$$E_z = \frac{\bar{Q}_{11} \bar{Q}_{22} \bar{Q}_{33} - \bar{Q}_{11} \bar{Q}_{23}^2 - \bar{Q}_{22} \bar{Q}_{13}^2 - \bar{Q}_{33} \bar{Q}_{12}^2 + 2 \bar{Q}_{23} \bar{Q}_{31} \bar{Q}_{12}}{\bar{Q}_{22} \bar{Q}_{33} - \bar{Q}_{23}^2},$$

$$E_\theta = \frac{\bar{Q}_{11} \bar{Q}_{22} \bar{Q}_{33} - \bar{Q}_{11} \bar{Q}_{23}^2 - \bar{Q}_{22} \bar{Q}_{13}^2 - \bar{Q}_{33} \bar{Q}_{12}^2 + 2 \bar{Q}_{23} \bar{Q}_{31} \bar{Q}_{12}}{\bar{Q}_{11} \bar{Q}_{33} - \bar{Q}_{13}^2},$$

$$G_{z\theta} = \frac{\bar{Q}_{33} \bar{Q}_{66} - \bar{Q}_{36}^2}{\bar{Q}_{33}}, \quad G_{\theta r} = \bar{Q}_{44}, \quad G_{zr} = \bar{Q}_{55},$$

Chapter 12

$$\begin{aligned}
 v_{z\theta} &= \frac{\bar{Q}_{12}\bar{Q}_{33} - \bar{Q}_{13}\bar{Q}_{23}}{\bar{Q}_{22}\bar{Q}_{33} - \bar{Q}_{23}^2}, & v_{\theta z} &= \frac{\bar{Q}_{12}\bar{Q}_{33} - \bar{Q}_{13}\bar{Q}_{23}}{\bar{Q}_{11}\bar{Q}_{33} - \bar{Q}_{13}^2}, \\
 v_{zr} &= \frac{\bar{Q}_{13}\bar{Q}_{22} - \bar{Q}_{12}\bar{Q}_{23}}{\bar{Q}_{22}\bar{Q}_{33} - \bar{Q}_{23}^2}, & v_{\theta r} &= \frac{\bar{Q}_{11}\bar{Q}_{23} - \bar{Q}_{12}\bar{Q}_{13}}{\bar{Q}_{11}\bar{Q}_{33} - \bar{Q}_{13}^2}.
 \end{aligned} \tag{12.65}$$

The generalized Hooke's law for a transversely isotropic cylinder can be written in terms of the effective elastic constants:

$$\begin{bmatrix} \varepsilon_z \\ \varepsilon_\theta \\ \varepsilon_r \\ \gamma_{\theta r} \\ \gamma_{zr} \\ \gamma_{z\theta} \end{bmatrix} = \begin{bmatrix} \frac{1}{E_z} & -\frac{\nu_{\theta z}}{E_\theta} & -\frac{\nu_{rz}}{E_r} & 0 & 0 & 0 \\ -\frac{\nu_{z\theta}}{E_z} & \frac{1}{E_\theta} & -\frac{\nu_{r\theta}}{E_r} & 0 & 0 & 0 \\ -\frac{\nu_{zr}}{E_z} & -\frac{\nu_{\theta r}}{E_\theta} & \frac{1}{E_r} & 0 & 0 & 0 \\ 0 & 0 & 0 & \frac{1}{G_{\theta r}} & 0 & 0 \\ 0 & 0 & 0 & 0 & \frac{1}{G_{zr}} & 0 \\ 0 & 0 & 0 & 0 & 0 & \frac{1}{G_{z\theta}} \end{bmatrix} \begin{bmatrix} \sigma_z \\ \sigma_\theta \\ \sigma_r \\ \sigma_{\theta r} \\ \sigma_{zr} \\ \sigma_{z\theta} \end{bmatrix} \tag{12.66}$$

Recalling the compatibility equation (12.38) for linking the radial and hoop strains and substituting equation (12.66) into (12.38) gives ($\varepsilon_z = \varepsilon_0$):

$$r^2 \left[\frac{1}{E_\theta} - \frac{\nu_{z\theta}^2}{E_z} \right] \left[\frac{d^2 \sigma_r}{dr^2} + \frac{3}{r} \frac{d\sigma_r}{dr} \right] + \sigma_r \left[\frac{1}{E_\theta} (1 - \nu_{z\theta} \nu_{\theta z}) - \frac{1}{E_r} (1 - \nu_{zr} \nu_{rz}) \right] + \varepsilon_0 (\nu_{zr} - \nu_{z\theta}) = 0 \tag{12.67}$$

The solution of the above equation is:

$$\begin{aligned}
 \sigma_r(r) &= C_1 r^{\beta-1} + C_2 r^{-\beta-1} + K \varepsilon_0, \\
 \sigma_\theta(r) &= \beta C_1 r^{\beta-1} - \beta C_2 r^{-\beta-1} + K \varepsilon_0, \\
 \sigma_z(r) &= E_z \varepsilon_0 + \nu_{z\theta} \sigma_\theta(r) + \nu_{zr} \sigma_r(r).
 \end{aligned} \tag{12.68}$$

where

$$\beta = \sqrt{\frac{E_\theta (1 - \nu_{rz} \nu_{zr})}{E_r (1 - \nu_{z\theta} \nu_{\theta z})}}, \quad K = \frac{E_\theta E_r (\nu_{z\theta} - \nu_{zr})}{E_r (1 - \nu_{z\theta} \nu_{\theta z}) - E_\theta (1 - \nu_{zr} \nu_{rz})}. \tag{12.69}$$

C_1 and C_2 are constants of integration which can be determined by the boundary conditions for stress continuity and axial equilibrium (see equations (12.21) ~ (12.28)):

$$C_1 = \frac{-pr_c^{-\beta-1} - K \varepsilon_0 (r_c^{-\beta-1} - r_a^{-\beta-1})}{r_a^{\beta-1} r_c^{-\beta-1} - r_c^{\beta-1} r_a^{-\beta-1}}, \quad C_2 = r_c^{2\beta} \frac{pr_c^{-\beta-1} + K \varepsilon_0 (r_c^{-\beta-1} - r_a^{-\beta-1})}{r_a^{\beta-1} r_c^{-\beta-1} - r_c^{\beta-1} r_a^{-\beta-1}} - K \varepsilon_0 r_c^{\beta+1} \tag{12.70}$$

It should be noted that these results for the stresses and strains under internal pressure are

equivalent to those determined by the direct solution approach and stress function approach (see section 12.2.1 and 12.2.2) for an anisotropic cylinder.

12.6 Three-dimensional Failure Criteria

For strength-dominated structures, the dimensioning process is performed by comparing stresses (or strains) created by the applied loads with the allowable strength (or strain) values of the material. The failure of a composite pressure vessel generally includes two main steps: firstly, cracks appear in the matrix, and then the pressure is taken up by the fibers until they fail [56]. However, in a commercial storage vessel the matrix failure becomes a major issue for the leak-before-break safety of a pressure vessel.

Kitao and Akiyama [57] analyzed and evaluated the progress of failure in thick-walled FW pipes with different winding-angles under internal pressure. Roy and Massard [58] studied the design of thick multi-layered composite spherical pressure vessels based on a 3-D linear elastic solution. They found that the Tsai-Wu failure criterion [59] is suitable for strength analysis. One of the important contributions of Roy's investigation is that hybrid spheres made from two different materials showed an opportunity to increase the burst pressure. Adali et al. [60] proposed another method on the optimization of multi-layered composite pressure vessels using a 3-D exact elasticity solution, subjected to axisymmetrical loading conditions. In his study, the three dimensional interactive Tsai-Wu failure criterion was employed to predict the maximum burst pressure. Sun et al. [61] calculated the stresses and the burst pressure of filament wound solid-rocket motor cases, which are a type of thick-walled filament-wound pressure vessel. The maximum stress criteria and the stiffness-degradation models were introduced in their failure analysis. Onder et al. [62] used an analytical elastic solution and finite element method to determine the burst pressure of multi-layered angle-ply composite pressure vessels under internal pressure and hygrothermal forces. The Tsai-Wu criterion, the maximum stress and maximum strain theories were used to compute the failure loads of the composite layers in a simple form.

Composite pressure vessels, where aligned fiber bands are laid down in the filament winding process, can usually be regarded as having a transversely isotropic character at the macroscopic lamina level. There have been a great number of papers covering a variety of failure criteria for transversely isotropic fiber composites. Ref. [63] reviews the results of a 12-year "World Wide Failure Exercise" where 19 failure criteria were outlined and evaluated, aimed at providing a comprehensive description of the foremost failure theories available at

Chapter 12

the present time. However, with improved manufacturing technology, fiber reinforced composite materials are used in thicker structures with significant out of plane stresses, for which the plane stress assumption is no longer valid and thus, 2D failure criteria are no longer reliable. Therefore, a reliable 3D failure criterion, which does not assume a state of plane stress, is needed for thick cylinders. The strength of filament-wound composite pressure vessels is determined by the tensile and compressive strengths in the fiber and transverse directions and by the in-plane shear strength of the composite material.

Failure in tension usually occurs when the fibers break, whereas failure in compression involves debonding of the fibers and the matrix material as a result of micro-buckling. Failure in shear is usually characterized by crack propagation through the composite material. In composite structures, tensile, compressive and shear stresses may result even from simple loading conditions, and therefore the failure mode of composite structures is rather complicated. There exists a number of criteria to predict failure of composite pressure vessels, ranging from the simplest non-interactive ones to highly interactive ones. The most frequently used criteria can be divided into two groups:

12.6.1 Tensor polynomial interactive criteria

These criteria are extensions of similar criteria for isotropic materials, which include the maximum stress/strain conditions and quadratic failure criteria (Tsai-Wu / Tsai-Hill / Hoffman / Chamis), and employ mathematical formulations to describe the failure surface as a function of the material strength parameters. Generally, these formulations are based on the process of adjusting the strength parameters to curve-fit experimental test data. The most general polynomial failure criterion for composite materials has been first proposed by Gol'denblat and Kopnov [64]:

$$F_i \sigma_i + F_{ij} \sigma_i \sigma_j + F_{ijk} \sigma_i \sigma_j \sigma_k + \dots = 1 \quad (i, j, k = 1, 2, \dots, 6) \quad (12.71)$$

where the stresses σ_i , σ_j , σ_k are the components of the stress tensor referred to the principle material coordinates; F_i , F_{ij} and F_{ijk} are strength parameters related to the unidirectional lamina strengths in the material axes. For practical application to anisotropic materials, the third-order tensor F_{ijk} can generally be neglected [65]. Accordingly, the general form equation (12.71) reduces to the most widely used quadratic criterion (Tsai-Wu criterion [69]), given by:

$$F_i \sigma_i + F_{ij} \sigma_i \sigma_j \leq 1 \quad (i, j = 1, 2, \dots, 6) \quad (12.72)$$

In equation (12.72) the coefficients F_i and F_{ij} are strength tensors of the second and fourth

Three-dimensional Stress, Strain & Displacement Analysis

rank, respectively; they can be evaluated by uniaxial tensile, compressive, and shear tests, except for the interactive coupling terms F_{ij} ($i \neq j$) which must be obtained by biaxial tension tests. Considering that the change in the sign of shear stress does not change the failure stress, all terms containing a shear stress to first power must vanish:

$$F_4 = F_5 = F_6 = F_{45} = F_{56} = F_{46} = F_{14} = F_{15} = F_{16} = F_{24} = F_{25} = F_{26} = F_{34} = F_{35} = F_{36} = 0. \quad (12.73)$$

Then the Tsai-Wu quadratic tensor form equation (12.72) is rewritten in the following expanded form:

$$F_1\sigma_{11} + F_2\sigma_{22} + F_3\sigma_{33} + 2F_{12}\sigma_{11}\sigma_{22} + 2F_{13}\sigma_{11}\sigma_{33} + 2F_{23}\sigma_{22}\sigma_{33} + F_{11}\sigma_{11}^2 + F_{22}\sigma_{22}^2 + F_{33}\sigma_{33}^2 + F_{44}\tau_{23}^2 + F_{55}\tau_{13}^2 + F_{66}\tau_{12}^2 = 1 \quad (12.74)$$

where the strength tensors $F_1, F_2, F_3, F_{11}, F_{22}, F_{33}, F_{12}, F_{13}, F_{23}, F_{44}, F_{55}$ and F_{66} are given by:

$$F_1 = \frac{1}{X^T} - \frac{1}{X^C}, \quad F_2 = \frac{1}{Y^T} - \frac{1}{Y^C}, \quad F_3 = \frac{1}{Z^T} - \frac{1}{Z^C}, \quad F_{11} = \frac{1}{X^T X^C}, \quad F_{22} = \frac{1}{Y^T Y^C}, \quad F_{33} = \frac{1}{Z^T Z^C},$$

$$F_{44} = \frac{1}{S_{23}^2}, \quad F_{55} = \frac{1}{S_{13}^2}, \quad F_{66} = \frac{1}{S_{12}^2}, \quad F_{12} = -\frac{1}{2\sqrt{X^T X^C Y^T Y^C}}, \quad F_{13} = -\frac{1}{2\sqrt{X^T X^C Z^T Z^C}},$$

$$F_{23} = -\frac{1}{2\sqrt{Y^T Y^C Z^T Z^C}}, \quad (12.75)$$

in which X^T, Y^T, Z^T denote the tensile strengths of the unidirectional lamina in the fiber, transverse and normal (through-thickness) directions, respectively. Similarly, X^C, Y^C, Z^C denote the compressive strengths in the three principal material directions. Further, S_{12}, S_{13} and S_{23} denote the shear strengths in the three orthogonal planes. equation (12.74) represents the general 3D quadratic failure criterion for the k^{th} lamina in material symmetry coordinates.

Various other quadratic criteria have been proposed to determine the strength parameters and differ solely on the approximation used to compute the strength tensors F_i and F_{ij} . They show identical tensor forms with the general Tsai-Wu quadratic criterion, where only the expressions for parameters F_i and F_{ij} are varied in order to give a good fit of the failure surface to the experimental data. The most popular and well-known quadratic criteria include:

(1) Tsai-Hill 3D criterion [66]:

$$F_1 = F_2 = F_3 = 0, \quad F_{11} = \frac{1}{X^{T2}}, \quad F_{22} = \frac{1}{Y^{T2}}, \quad F_{33} = \frac{1}{Z^{T2}}, \quad F_{44} = \frac{1}{S_{23}^2}, \quad F_{55} = \frac{1}{S_{13}^2}, \quad F_{66} = \frac{1}{S_{12}^2},$$

$$F_{12} = -\frac{1}{2}\left(\frac{1}{X^{T2}} + \frac{1}{Y^{T2}} - \frac{1}{Z^{T2}}\right), \quad F_{13} = -\frac{1}{2}\left(\frac{1}{Z^{T2}} + \frac{1}{X^{T2}} - \frac{1}{Y^{T2}}\right), \quad F_{23} = -\frac{1}{2}\left(\frac{1}{Y^{T2}} + \frac{1}{Z^{T2}} - \frac{1}{X^{T2}}\right). \quad (12.76)$$

(2) Hoffman 3D criterion [67]:

$$\begin{aligned}
 F_1 &= \frac{1}{X^T} - \frac{1}{X^C}, \quad F_2 = \frac{1}{Y^T} - \frac{1}{Y^C}, \quad F_3 = \frac{1}{Z^T} - \frac{1}{Z^C}, \quad F_{11} = \frac{1}{X^T X^C}, \quad F_{22} = \frac{1}{Y^T Y^C}, \quad F_{33} = \frac{1}{Z^T Z^C}, \\
 F_{44} &= \frac{1}{S_{23}^2}, \quad F_{55} = \frac{1}{S_{13}^2}, \quad F_{66} = \frac{1}{S_{12}^2}, \quad F_{12} = -\frac{1}{2} \left(\frac{1}{X^T X^C} + \frac{1}{Y^T Y^C} - \frac{1}{Z^T Z^C} \right), \\
 F_{13} &= -\frac{1}{2} \left(\frac{1}{Z^T Z^C} + \frac{1}{X^T X^C} - \frac{1}{Y^T Y^C} \right), \quad F_{23} = -\frac{1}{2} \left(\frac{1}{Y^T Y^C} + \frac{1}{Z^T Z^C} - \frac{1}{X^T X^C} \right). \quad (12.77)
 \end{aligned}$$

(3) Chamis 3D criterion [68]:

$$\begin{aligned}
 F_1 = F_2 = F_3 = 0, \quad F_{11} &= \frac{1}{X^{T2}}, \quad F_{22} = \frac{1}{Y^{T2}}, \quad F_{33} = \frac{1}{Z^{T2}}, \quad F_{44} = \frac{1}{S_{23}^2}, \quad F_{55} = \frac{1}{S_{13}^2}, \quad F_{66} = \frac{1}{S_{12}^2}, \\
 F_{12} &= -\frac{K_{12}}{X^T Y^T}, \quad F_{13} = -\frac{K_{13}}{X^T Z^T}, \quad F_{23} = -\frac{K_{23}}{Y^T Z^T}. \quad (12.78)
 \end{aligned}$$

where K_{12} , K_{13} and K_{23} are the strength coefficients that depend on the material.

Among these failure theories, the Tsai-Wu criterion is a relatively new multi-axial strength theory and gives the most conservative results for strength in many problems. Specific merits of the Tsai-Wu criterion include (1) invariance under rotation or redefinition of coordinates; (2) transformation via known tensor transformation laws; and (3) symmetry properties similar to those of the stiffness and compliances [69].

For transversely isotropic materials with plane 2-3 as the isotropic plane, the indices associated with this plane are identical. Thus the following 5 relations hold:

$$F_2 = F_3, \quad F_{12} = F_{13}, \quad F_{22} = F_{33}, \quad F_{55} = F_{66}, \quad F_{44} = 2(F_{22} - F_{23}). \quad (12.79)$$

Hence the 12 strength parameters in equation (12.74) reduce to 7 independent parameters (F_1 , F_2 , F_{11} , F_{22} , F_{12} , F_{23} and F_{66}) for transverse isotropy. Then the 3D Tsai-Wu criterion for the k^{th} lamina becomes:

$$\begin{aligned}
 F_1^{(k)} \sigma_{11}^{(k)} + F_2^{(k)} (\sigma_{22}^{(k)} + \sigma_{33}^{(k)}) + F_{11}^{(k)} \sigma_{11}^{(k)2} + F_{22}^{(k)} (\sigma_{22}^{(k)2} + \sigma_{33}^{(k)2}) + 2F_{12}^{(k)} \sigma_{11}^{(k)} (\sigma_{22}^{(k)} + \sigma_{33}^{(k)}) \\
 + 2F_{23}^{(k)} \sigma_{22}^{(k)} \sigma_{33}^{(k)} + 2(F_{22}^{(k)} - F_{23}^{(k)}) \tau_{23}^{(k)2} + F_{66}^{(k)} (\tau_{13}^{(k)2} + \tau_{12}^{(k)2}) = 1 \quad (12.80)
 \end{aligned}$$

where the strength parameters $F_1^{(k)}$, $F_2^{(k)}$, $F_{11}^{(k)}$, $F_{22}^{(k)}$, $F_{12}^{(k)}$, $F_{23}^{(k)}$ and $F_{66}^{(k)}$ are given by:

$$\begin{aligned}
 F_1^{(k)} &= \frac{1}{X^{T(k)}} - \frac{1}{X^{C(k)}}, \quad F_2^{(k)} = \frac{1}{Y^{T(k)}} - \frac{1}{Y^{C(k)}}, \quad F_{11}^{(k)} = \frac{1}{X^{T(k)} X^{C(k)}}, \quad F_{22}^{(k)} = \frac{1}{Y^{T(k)} Y^{C(k)}}, \\
 F_{12}^{(k)} &= -\frac{1}{2\sqrt{X^{T(k)} X^{C(k)} Y^{T(k)} Y^{C(k)}}}, \quad F_{23}^{(k)} = -\frac{1}{2Y^{T(k)} Y^{C(k)}}, \quad F_{66}^{(k)} = \frac{1}{S_{12}^{(k)2}}. \quad (12.81)
 \end{aligned}$$

It should be noted here that failure in cylindrical pressure vessels due to uniformly

distributed pressure is normally intra-laminar (due to fiber fracture, matrix cracking, etc) [3]. Therefore, the transverse shear stresses are not here considered and the Tsai-Wu criterion is applied to each individual lamina to check for failure or otherwise. Equation (12.80) is accordingly rewritten as:

$$F_1^{(k)} \sigma_{11}^{(k)} + F_2^{(k)} (\sigma_{22}^{(k)} + \sigma_{33}^{(k)}) + F_{11}^{(k)} \sigma_{11}^{(k)2} + F_{22}^{(k)} (\sigma_{22}^{(k)2} + \sigma_{33}^{(k)2}) + 2F_{12}^{(k)} \sigma_{11}^{(k)} (\sigma_{22}^{(k)} + \sigma_{33}^{(k)}) + 2F_{23}^{(k)} \sigma_{22}^{(k)} \sigma_{33}^{(k)} + F_{66}^{(k)} \tau_{12}^{(k)2} = 1 \quad (12.82)$$

Equation (12.80) can be used to predict the intra-laminar failure for the k^{th} layer of filament-wound multilayered pressure vessels. The normal stresses components σ_{11} , σ_{22} , σ_{33} and in-plane shear stress τ_{12} are referred to the principal material coordinates and are related to the shell stresses by:

$$\begin{Bmatrix} \sigma_{11}^{(k)} \\ \sigma_{22}^{(k)} \\ \sigma_{33}^{(k)} \\ \tau_{12}^{(k)} \end{Bmatrix} = \begin{bmatrix} \cos^2 \alpha & \sin^2 \alpha & \sin 2\alpha \\ \sin^2 \alpha & \cos^2 \alpha & -\sin 2\alpha \\ 0 & 0 & 1 \\ -\sin \alpha \cos \alpha & \sin \alpha \cos \alpha & \cos 2\alpha \end{bmatrix} \begin{Bmatrix} \sigma_{zz}^{(k)} \\ \sigma_{\theta\theta}^{(k)} \\ \sigma_{rr}^{(k)} \\ \tau_{z\theta}^{(k)} \end{Bmatrix} \quad (12.83)$$

The design objective is usually to maximize the burst pressure P_b subjected to a failure criterion like equation (12.82). The design problem for a multilayered pressure vessel of a given inner-to-outer radius ratio r_c/r_a , number of layers n and (possible) axial force F , can be stated as (First-Ply-Failure):

$$P_{\max} = \underset{\alpha}{\text{Max}} P_b(\bar{\alpha}, r) = \underset{\alpha}{\text{Max}} \underset{r}{\text{Min}} P_b \quad (12.84)$$

where $\bar{\alpha} = (\alpha_1, \alpha_2, \dots, \alpha_n)$.

12.6.2 Failure modes based failure theories

The disadvantage of the tensor polynomial failure theories is that they are not directly related to damage mechanisms and do not explicitly differentiate matrix failure and fiber failure. Some modern failure theories have emerged which distinguish between failure modes, including: Hashin-Rotem [70, 71], Puck [72, 73], Dávila-Pinho [74, 75], Christensen [76, 77], Hinton [78], Daniel [79-83], Sun-Tao [84], Cuntze [85], Yamada-Sun [86], Koop-Michaeli [87], Kroll-Hufenbach [88], Zinoviev [89], Gosse [90], Hart-Smith [91], etc. Hashin and Puck are credited for establishing the need for failure criteria that are based on failure mechanisms. The historical importance of these proposals is that they initiate a different way of approaching the formulation of composites failure criteria. To our knowledge, these are the first to recognize different modes of failure, followed by the recognition of the variables that

Chapter 12

correspond to these modes and the interactions between them. The most general 3D criteria which probably received the most attention, are here outlined:

Hashin's 3D criteria [71]

Hashin's criteria have been usually implemented within the two dimensional classical lamination approach for point stress calculations with ply discounting as the material degradation model. These criteria are extended to three-dimensional problems where the transverse normal and shearing stress components are taken into account. Furthermore, the effect of the shear stress is now taken into account in the tensile fiber mode. The in total six failure modes are:

(1) Tensile fiber failure mode ($\sigma_{11} \geq 0$):

$$\left(\frac{\sigma_{11}}{X^T}\right)^2 + \frac{\sigma_{12}^2 + \sigma_{13}^2}{S^2} = \begin{cases} \geq 1 & \text{failure} \\ < 1 & \text{no failure} \end{cases} \quad (12.85)$$

(2) Compressive fiber failure mode ($\sigma_{11} < 0$):

$$\left(\frac{\sigma_{11}}{X^C}\right)^2 = \begin{cases} \geq 1 & \text{failure} \\ < 1 & \text{no failure} \end{cases} \quad (12.86)$$

(3) Tensile matrix failure mode ($\sigma_{22} + \sigma_{33} > 0$):

$$\frac{(\sigma_{22} + \sigma_{33})^2}{Y^{T2}} + \frac{\sigma_{23}^2 - \sigma_{22}\sigma_{33}}{S^{T2}} + \frac{\sigma_{12}^2 + \sigma_{13}^2}{S^2} = \begin{cases} \geq 1 & \text{failure} \\ < 1 & \text{no failure} \end{cases} \quad (12.87)$$

(4) Compressive matrix failure mode ($\sigma_{22} + \sigma_{33} < 0$):

$$\left[\left(\frac{Y^C}{2S^T}\right)^2 - 1\right] \left(\frac{\sigma_{22} + \sigma_{33}}{Y^C}\right) + \frac{(\sigma_{22} + \sigma_{33})^2}{4S^{T2}} + \frac{\sigma_{23}^2 - \sigma_{22}\sigma_{33}}{S^{T2}} + \frac{\sigma_{12}^2 + \sigma_{13}^2}{S^2} = \begin{cases} \geq 1 & \text{failure} \\ < 1 & \text{no failure} \end{cases} \quad (12.88)$$

(5) Interlaminar tensile failure mode ($\sigma_{33} > 0$):

$$\left(\frac{\sigma_{33}}{Z^T}\right)^2 = \begin{cases} \geq 1 & \text{failure} \\ < 1 & \text{no failure} \end{cases} \quad (12.89)$$

(6) Interlaminar compression failure mode ($\sigma_{33} < 0$):

$$\left(\frac{\sigma_{33}}{Z^C}\right)^2 = \begin{cases} \geq 1 & \text{failure} \\ < 1 & \text{no failure} \end{cases} \quad (12.90)$$

where σ_{ij} are the stress components; the tensile and compressive strengths for the lamina are denoted by superscripts T and C , respectively; S and S^T represent the in-plane and transverse shear strengths, respectively.

Failure indices for Hashin's criteria refer to fiber and matrix failures and involve different failure modes. For the matrix failure mode, a quadratic criterion was used since a linear

Three-dimensional Stress, Strain & Displacement Analysis

approximation usually underestimates the material strength, and a higher degree would be too complicated for this formulation.

Puck's criteria [73]

These criteria avoid the deficiencies of both non-interactive and interactive criteria. Puck's theory consists of in total five failure modes, two for fiber failure (tensile and compressive) and three for matrix failure. The physically-based inter-fiber fracture conditions with their corresponding mechanisms are summarized in Tab. 12.1. This theory, which is extracted from the brittle failure behavior of composites, makes failure analysis even more realistic than it has been with the methods described previously. In addition, it makes the distinction between different failure modes (A, B and C) possible.

LaRC04 criteria [75]

The domain determination of elastic response under complex stress states is an essential component for an accurate damage model. A set of 3D failure criteria denoted LaRC04, which is formulated by damage activation functions, can be also applied to a 3D state of stress and predict fiber and matrix failure accurately, without any curve-fitting. This approach assumes that the elastic domain is enclosed by four surfaces, each of which accounts for one failure mechanism: longitudinal and transverse fracture under tension and compression. Furthermore, it contains a correction for considering shear-induced non-linear behavior and fiber kinking triggered by an initial fiber misalignment angle and by the rotation of the fibers during compressive loading. However, the improvement in accuracy of the LaRC04 criteria is associated with a significant increase in computational effort. The total of six failure modes (LaRC04 #1~#6), which represent two fiber failure modes, three matrix failure modes and a combined mode (when fiber and matrix failures occur simultaneously), are presented in Tab. 12.2. The meanings of the symbols and the full details on the derivation and validation of the LaRC04 failure criteria can be found in Ref. [84].

Christensen's criteria [76]

Christensen developed a 3D stress-strain relation for a transversely isotropic material that can be expressed in a regular part, plus a term that only includes the effect of deformation in the direction of the fiber, a term that the author relates to a particular reinforcement effect. This theory considers two modes of yield/failure, one being matrix dominated, the other being fiber dominated. The resulting criteria are quadratic in the components of the average stress

Chapter 12

tensor with two material parameters for each mode of yield/failure. A balance is sought between achieving the maximum generality and minimizing the number of material parameters (that must be experimentally evaluated) for application to any particular material system. The failure criterion can be expressed in terms of two failure modes:

(1) Matrix mode:

$$\left(\frac{1}{Y^T} - \frac{1}{Y^C}\right)(\sigma_{22} + \sigma_{33}) + \frac{(\sigma_{22} - \sigma_{33})^2 + 4\sigma_{23}^2}{Y^T Y^C} + \frac{(\sigma_{12}^2 + \sigma_{13}^2)}{S^2} = \begin{cases} \geq 1 & \text{failure} \\ < 1 & \text{no failure} \end{cases} \quad (12.91)$$

(2) Fiber mode:

$$\left(\frac{1}{X^T} - \frac{1}{X^C}\right)\sigma_{11} + \frac{\sigma_{11}^2}{X^T X^C} - \frac{1}{4}\left(\frac{1}{X^T} + \frac{1}{X^C}\right)^2 \sigma_{11}(\sigma_{22} + \sigma_{33}) = \begin{cases} \geq 1 & \text{failure} \\ < 1 & \text{no failure} \end{cases} \quad (12.92)$$

NU criteria [80]

This is a recently developed interfiber/interlaminar failure theory at Northwestern University (NU) based on interlaminar matrix strain criteria. It was found [89, 91] that the NU theory was in better agreement with experimental results than all other theories for off-axis compressive behavior, i.e., under combined transverse compression and shear parallel to the fibers. Depending on different failure modes (compression/shear/tension), the failure criterion is governed by the maximum shear strain, the maximum tensile strain (set by pure shear) and the maximum tensile strain (set by transverse tension), respectively, all situated in the interlaminar region. The theory is expressed in the form of three sub-criteria:

(1) Compression-dominated failure:

$$\left(\frac{\sigma_{33}}{Z^C}\right)^2 + \left(\frac{\tau_{13}}{Z^C}\right)^2 \left(\frac{E_3}{G_{13}}\right)^2 = 1 \quad (\text{NUa criterion}) \quad (12.93)$$

(2) Shear-dominated failure:

$$\left(\frac{\tau_{13}}{S_{13}}\right)^2 + 2\frac{\sigma_{33}}{S_{13}} \frac{G_{13}}{E_3} = 1 \quad (\text{NUb criterion}) \quad (12.94)$$

(3) Tension-dominated failure:

$$\frac{\sigma_{33}}{Z^T} + \left(\frac{\tau_{13}}{Z^T}\right)^2 \left(\frac{E_3}{2G_{13}}\right)^2 = 1 \quad (\text{NUc criterion}) \quad (12.95)$$

For loading on the 1-2 plane, results are simply obtained by changing the through-thickness stresses and strength tensors to the corresponding in-plane tensors in the above criteria [89].

Tab. 12.1: Puck's criteria failure modes with corresponding mechanisms [73]

Type of failure	Failure mode	Failure condition	Condition for validity
Fiber failure (FF)	Tensile	$\frac{1}{\varepsilon_{1T}} \left(\varepsilon_{11} + \frac{\nu_{f12}}{E_{f1}} m_{\sigma f} \sigma_{22} \right)$	$(\dots) \geq 0$
	Compression (kinking)	$\frac{1}{\varepsilon_{1C}} \left \varepsilon_{11} + \frac{\nu_{f12}}{E_{f1}} m_{\sigma f} \sigma_{22} \right = 1 - (10\gamma_{12})^2$	$(\dots) < 0$
Inter-fiber fracture (IFF)	Mode A, $\theta_{fp} = 0^\circ$	$\sqrt{\left(\frac{\tau_{12}}{S}\right)^2 + \left(1 - P_{\perp\parallel}^{(+)} \frac{Y^T}{S}\right)^2 \left(\frac{\sigma_{22}}{Y^T}\right)^2} + P_{\perp\parallel}^{(+)} \frac{\sigma_{22}}{S} = 1 - \left \frac{\sigma_{11}}{\sigma_{11D}} \right $	$\sigma_{22} \geq 0$
	Mode B, $\theta_{fp} = 0^\circ$	$\frac{1}{S} \left(\sqrt{\tau_{12}^2 + (p_{\perp\parallel}^{(-)} \sigma_{22})^2} + p_{\perp\parallel}^{(-)} \sigma_{22} \right) = 1 - \left \frac{\sigma_{11}}{\sigma_{11D}} \right $	$\sigma_{22} < 0$ and $0 \leq \left \frac{\sigma_{22}}{\tau_{12}} \right \leq \frac{R_{\perp\parallel}^A}{ \tau_{12c} }$
	Mode C, $\cos \theta_{fp} = \sqrt{\frac{f_w R_{\perp\parallel}^A}{(-\sigma_2)}}$	$\left[\left(\frac{\tau_{12}}{2(1 + p_{\perp\parallel}^{(-)})S} \right)^2 + \left(\frac{\sigma_{22}}{Y^C} \right)^2 \right] \frac{Y^C}{-\sigma_{22}} = 1 - \left \frac{\sigma_{11}}{\sigma_{11D}} \right $	$\sigma_{22} < 0$ and $0 \leq \left \frac{\tau_{12}}{\sigma_{22}} \right \leq \frac{ \tau_{12c} }{R_{\perp\parallel}^A}$
Definitions	$P_{\perp\parallel}^{(+)} = -\left(\frac{d\tau_{12}}{d\sigma_{22}}\right)_{\sigma_{22}=0}$ of (σ_2, τ_{12}) curve, $\sigma_2 > 0$	$P_{\perp\parallel}^{(+)} = -\left(\frac{d\tau_{12}}{d\sigma_{22}}\right)_{\sigma_{22}=0}$ of (σ_{22}, τ_{12}) curve, $\sigma_{22} > 0$	
Parameter relationships	$R_{\perp\parallel}^A = \frac{Y^C}{2(1 + p_{\perp\parallel}^{(-)})} = \frac{S}{2p_{\perp\parallel}^{(-)}} \left(\sqrt{1 + 2p_{\perp\parallel}^{(-)} \frac{Y^C}{S}} - 1 \right)$	$p_{\perp\parallel}^{(-)} = p_{\perp\parallel}^{(-)} \frac{R_{\perp\parallel}^A}{S}$	$\tau_{12} = S \sqrt{1 + 2p_{\perp\parallel}^{(-)}}$

Tab. 12.2: Summary of the LaRC04 criteria [75]

MATRIX FAILURE

Matrix compressive failure $\sigma_{22} < 0$

Matrix tensile failure $\sigma_{22} \geq 0$ (LaRC04 #1)

$$\sigma_{11} < -Y^C \quad (\text{LaRC04 \#5})$$

$$\sigma_{11} \geq -Y^C \quad (\text{LaRC04 \#2})$$

$$FI_M = (1-g) \frac{\sigma_2}{Y_{is}^T} + g \left(\frac{\sigma_2}{Y_{is}^T} \right)^2 + \frac{\Lambda_{23}^0 \tau_{23}^2 + \chi(\gamma_{12})}{\chi(\gamma_{12|is}^u)}$$

$$FI_M = \left(\frac{\tau^{Tm}}{S^T - \eta^T \sigma_n^m} \right)^2 + \left(\frac{\tau^{Lm}}{S_{is}^L - \eta^L \sigma_n^m} \right)^2$$

$$FI_M = \left(\frac{\tau^T}{S^T - \eta^T \sigma_n} \right)^2 + \left(\frac{\tau^L}{S_{is}^L - \eta^L \sigma_n} \right)^2$$

FIBER FAILURE

Fiber tensile failure $\sigma_{11} \geq 0$ (LaRC04 #3)

Fiber compressive failure $\sigma_{11} < 0$ (LaRC04 #3)

$$\sigma_{2m2m} < 0 \quad (\text{LaRC04 \#4})$$

$$\sigma_{2m2m} \geq 0 \quad (\text{LaRC04 \#6})$$

$$FI_F = \frac{\sigma_{11}}{X^T}$$

$$FI_F = \left(\frac{\tau_{1m2m}}{S_{is}^L - \eta^L \sigma_{2m2m}} \right)^2$$

$$FI_{M/F} = (1-g) \frac{\sigma_{2m2m}}{Y_{is}^T} + g \left(\frac{\sigma_{2m2m}}{Y_{is}^T} \right)^2 + \frac{\Lambda_{23}^0 \tau_{2m3w}^2 + \chi(\gamma_{1m2m})}{\chi(\gamma_{12|is}^u)}$$

12.6.3 Reviews of failure criteria

Daniel [83] reviewed the major laminate failure analyses and the primary divergence observed in the prediction of laminate failures. A practical approach for laminate failure analysis, which considered the validity and applicability of various failure theories, has also been recommended. Sun et al. [84] reviewed six failure theories which appear representative of those that have been proposed over the years and showed comparisons of theoretical predictions with experimental results for six different composite material systems and various loading conditions. Echaabi et al. [92] briefly reviewed the formalisms of most recent and widely used failure models and discussed their applications to capture failure of composite laminates by comparing the advantages and limitations of each criterion.

12.7 Numerical Examples and Discussion

In this section, the previously presented 3D elasticity solution is applied to the cylindrical section of thick-walled filament-wound pressure vessels. With the aid of the anisotropic elasticity theory, the exact solutions for the stress and deformation fields are given, taking the through-thickness stress gradients into account. The assumption of generalized plane strain, which states that the axial strain of the cylinder is a non-zero constant, is here applied. The in-plane twisting moment and shear stress are also considered and assumed to be a linear function of the radial coordinate.

Substitution of equations (12.18), (12.20), (12.51) and (12.52) into the boundary conditions given in equations (21)~(28) and (54), leads to a system of linear algebraic equations for the unknown constants $D_1^L, D_2^L, D_1^{(k)}, D_2^{(k)}, \varepsilon_0, \gamma_0$:

$$\begin{bmatrix}
 d_{11} & 0 & 0 & 0 & 0 & e_{11} & 0 & 0 & 0 & 0 & a_{11} & 0 \\
 d_{12} & d_{22} & 0 & 0 & 0 & e_{21} & e_{22} & 0 & 0 & 0 & a_{21} & a_{22} \\
 0 & d_{32} & d_{33} & 0 & 0 & 0 & e_{32} & e_{33} & 0 & 0 & a_{31} & a_{32} \\
 0 & 0 & d_{43} & d_{44} & 0 & 0 & 0 & e_{43} & e_{44} & 0 & a_{41} & a_{42} \\
 0 & 0 & 0 & d_{54} & d_{55} & 0 & 0 & 0 & e_{54} & e_{55} & a_{51} & a_{52} \\
 d_{61} & d_{62} & 0 & 0 & 0 & e_{61} & e_{62} & 0 & 0 & 0 & a_{61} & a_{62} \\
 0 & d_{72} & d_{73} & 0 & 0 & 0 & e_{72} & e_{73} & 0 & 0 & a_{71} & a_{72} \\
 0 & 0 & d_{83} & d_{84} & 0 & 0 & 0 & e_{83} & e_{84} & 0 & a_{81} & a_{82} \\
 0 & 0 & 0 & d_{94} & d_{95} & 0 & 0 & 0 & e_{94} & e_{95} & a_{91} & a_{92} \\
 0 & 0 & 0 & 0 & d_{05} & 0 & 0 & 0 & 0 & e_{05} & a_{01} & a_{02} \\
 f_{01} & f_{02} & f_{03} & f_{04} & f_{05} & 0 & f_{07} & f_{08} & f_{09} & f_{10} & f_{11} & f_{12} \\
 0 & g_{02} & g_{03} & g_{04} & g_{05} & 0 & g_{07} & g_{08} & g_{09} & g_{10} & g_{11} & g_{12}
 \end{bmatrix}
 \begin{bmatrix}
 D_1^L \\
 D_1^{(1)} \\
 D_1^{(2)} \\
 D_1^{(3)} \\
 D_1^{(4)} \\
 D_2^L \\
 D_2^{(1)} \\
 D_2^{(2)} \\
 D_2^{(3)} \\
 D_2^{(4)} \\
 \varepsilon_0 \\
 \gamma_0
 \end{bmatrix}
 =
 \begin{bmatrix}
 -p \\
 0 \\
 0 \\
 0 \\
 0 \\
 0 \\
 0 \\
 0 \\
 0 \\
 0 \\
 pr_a^2/2 \\
 0
 \end{bmatrix}
 \quad (12.96)$$

Chapter 12

where the expressions for parameters a_{ij} , d_{ij} , e_{ij} , f_{ij} , g_{ij} in the coefficient matrix are given by:

$$d_{11} = \lambda$$

$$e_{11} = \lambda(2\mu - 1) / r_a^2$$

$$a_{11} = \lambda\mu$$

$$d_{12} = r_b$$

$$d_{22} = -r_b^{\beta^{(1)}}$$

$$e_{21} = 1 / r_b$$

$$e_{22} = -r_b^{-\beta^{(1)}}$$

$$a_{21} = -\eta^{(1)} r_b$$

$$a_{22} = -\zeta^{(1)} r_b^2$$

$$d_{32} = r_1^{\beta^{(1)}}$$

$$d_{33} = -r_1^{\beta^{(2)}}$$

$$e_{32} = r_1^{-\beta^{(1)}}$$

$$e_{33} = -r_1^{-\beta^{(2)}}$$

$$a_{31} = (\eta^{(1)} - \eta^{(2)}) r_1$$

$$a_{32} = (\zeta^{(1)} - \zeta^{(2)}) r_1^2$$

$$d_{43} = r_2^{\beta^{(2)}}$$

$$d_{44} = -r_2^{\beta^{(3)}}$$

$$e_{43} = r_2^{-\beta^{(2)}}$$

$$e_{44} = -r_2^{-\beta^{(3)}}$$

$$a_{41} = (\eta^{(2)} - \eta^{(3)}) r_2$$

$$a_{42} = (\zeta^{(2)} - \zeta^{(3)}) r_2^2$$

$$d_{54} = r_3^{\beta^{(3)}}$$

$$d_{55} = -r_3^{\beta^{(4)}}$$

$$e_{54} = r_3^{-\beta^{(3)}}$$

$$e_{55} = -r_3^{-\beta^{(4)}}$$

$$a_{51} = (\eta^{(3)} - \eta^{(4)})r_3$$

$$a_{52} = (\zeta^{(3)} - \zeta^{(4)})r_3^2$$

$$d_{61} = \lambda$$

$$d_{62} = -(\bar{Q}_{23}^{(1)} + \beta^{(1)}\bar{Q}_{33}^{(1)})r_b^{\beta^{(1)}-1}$$

$$e_{61} = \lambda(2\mu - 1)/r_b^2$$

$$e_{62} = -(\bar{Q}_{23}^{(1)} - \beta^{(1)}\bar{Q}_{33}^{(1)})r_b^{-\beta^{(1)}-1}$$

$$a_{61} = \lambda\mu - [\bar{Q}_{13}^{(1)} + \eta^{(1)}(\bar{Q}_{23}^{(1)} + \bar{Q}_{33}^{(1)})]$$

$$a_{62} = -[\bar{Q}_{36}^{(1)} + \zeta^{(1)}(\bar{Q}_{23}^{(1)} + 2\bar{Q}_{33}^{(1)})]r_b$$

$$d_{72} = (\bar{Q}_{23}^{(1)} + \beta^{(1)}\bar{Q}_{33}^{(1)})r_1^{\beta^{(1)}-1}$$

$$d_{73} = -(\bar{Q}_{23}^{(2)} + \beta^{(2)}\bar{Q}_{33}^{(2)})r_1^{\beta^{(2)}-1}$$

$$e_{72} = (\bar{Q}_{23}^{(1)} - \beta^{(1)}\bar{Q}_{33}^{(1)})r_1^{-\beta^{(1)}-1}$$

$$e_{73} = -(\bar{Q}_{23}^{(2)} - \beta^{(2)}\bar{Q}_{33}^{(2)})r_1^{-\beta^{(2)}-1}$$

$$a_{71} = \bar{Q}_{13}^{(1)} - \bar{Q}_{13}^{(2)} + \eta^{(1)}(\bar{Q}_{23}^{(1)} + \bar{Q}_{33}^{(1)}) - \eta^{(2)}(\bar{Q}_{23}^{(2)} + \bar{Q}_{33}^{(2)})$$

$$a_{72} = [\bar{Q}_{36}^{(1)} - \bar{Q}_{36}^{(2)} + \zeta^{(1)}(\bar{Q}_{23}^{(1)} + 2\bar{Q}_{33}^{(1)}) - \zeta^{(2)}(\bar{Q}_{23}^{(2)} + 2\bar{Q}_{33}^{(2)})]r_1$$

$$d_{83} = (\bar{Q}_{23}^{(2)} + \beta^{(2)}\bar{Q}_{33}^{(2)})r_2^{\beta^{(2)}-1}$$

$$d_{84} = -(\bar{Q}_{23}^{(3)} + \beta^{(3)}\bar{Q}_{33}^{(3)})r_2^{\beta^{(3)}-1}$$

$$e_{83} = (\bar{Q}_{23}^{(2)} - \beta^{(2)}\bar{Q}_{33}^{(2)})r_2^{-\beta^{(2)}-1}$$

$$e_{84} = -(\bar{Q}_{23}^{(3)} - \beta^{(3)}\bar{Q}_{33}^{(3)})r_2^{-\beta^{(3)}-1}$$

$$a_{81} = \bar{Q}_{13}^{(2)} - \bar{Q}_{13}^{(3)} + \eta^{(2)}(\bar{Q}_{23}^{(2)} + \bar{Q}_{33}^{(2)}) - \eta^{(3)}(\bar{Q}_{23}^{(3)} + \bar{Q}_{33}^{(3)})$$

$$a_{82} = [\bar{Q}_{36}^{(2)} - \bar{Q}_{36}^{(3)} + \zeta^{(2)}(\bar{Q}_{23}^{(2)} + 2\bar{Q}_{33}^{(2)}) - \zeta^{(3)}(\bar{Q}_{23}^{(3)} + 2\bar{Q}_{33}^{(3)})]r_2$$

$$d_{94} = (\bar{Q}_{23}^{(3)} + \beta^{(3)}\bar{Q}_{33}^{(3)})r_3^{\beta^{(3)}-1}$$

$$d_{95} = -(\bar{Q}_{23}^{(4)} + \beta^{(4)}\bar{Q}_{33}^{(4)})r_3^{\beta^{(4)}-1}$$

$$e_{94} = (\bar{Q}_{23}^{(3)} - \beta^{(3)}\bar{Q}_{33}^{(3)})r_3^{-\beta^{(3)}-1}$$

$$e_{95} = -(\bar{Q}_{23}^{(4)} - \beta^{(4)}\bar{Q}_{33}^{(4)})r_3^{-\beta^{(4)}-1}$$

Chapter 12

$$a_{91} = \bar{Q}_{13}^{(3)} - \bar{Q}_{13}^{(4)} + \eta^{(3)}(\bar{Q}_{23}^{(3)} + \bar{Q}_{33}^{(3)}) - \eta^{(4)}(\bar{Q}_{23}^{(4)} + \bar{Q}_{33}^{(4)})$$

$$a_{92} = [\bar{Q}_{36}^{(3)} - \bar{Q}_{36}^{(4)} + \zeta^{(3)}(\bar{Q}_{23}^{(3)} + 2\bar{Q}_{33}^{(3)}) - \zeta^{(4)}(\bar{Q}_{23}^{(4)} + 2\bar{Q}_{33}^{(4)})]r_3$$

$$d_{05} = (\bar{Q}_{23}^{(4)} + \beta^{(4)}\bar{Q}_{33}^{(4)})r_c^{\beta^{(4)}-1}$$

$$e_{05} = (\bar{Q}_{23}^{(4)} - \beta^{(4)}\bar{Q}_{33}^{(4)})r_c^{-\beta^{(4)}-1}$$

$$a_{01} = \bar{Q}_{13}^{(4)} + \eta^{(4)}(\bar{Q}_{23}^{(4)} + \bar{Q}_{33}^{(4)})$$

$$a_{02} = [\bar{Q}_{36}^{(4)} + \zeta^{(4)}(\bar{Q}_{23}^{(4)} + 2\bar{Q}_{33}^{(4)})]r_c$$

$$f_{01} = \lambda\mu(r_b^2 - r_a^2)$$

$$f_{02} = \frac{(\bar{Q}_{12}^{(1)} + \beta^{(1)}\bar{Q}_{13}^{(1)})(r_1^{\beta^{(1)}+1} - r_b^{\beta^{(1)}+1})}{1 + \beta^{(1)}}$$

$$f_{03} = \frac{(\bar{Q}_{12}^{(2)} + \beta^{(2)}\bar{Q}_{13}^{(2)})(r_2^{\beta^{(2)}+1} - r_1^{\beta^{(2)}+1})}{1 + \beta^{(2)}}$$

$$f_{04} = \frac{(\bar{Q}_{12}^{(3)} + \beta^{(3)}\bar{Q}_{13}^{(3)})(r_3^{\beta^{(3)}+1} - r_2^{\beta^{(3)}+1})}{1 + \beta^{(1)}}$$

$$f_{05} = \frac{(\bar{Q}_{12}^{(4)} + \beta^{(4)}\bar{Q}_{13}^{(4)})(r_c^{\beta^{(4)}+1} - r_3^{\beta^{(4)}+1})}{1 + \beta^{(4)}}$$

$$f_{07} = \frac{(\bar{Q}_{12}^{(1)} - \beta^{(1)}\bar{Q}_{13}^{(1)})(r_1^{1-\beta^{(1)}} - r_b^{1-\beta^{(1)}})}{1 - \beta^{(1)}}$$

$$f_{08} = \frac{(\bar{Q}_{12}^{(2)} - \beta^{(2)}\bar{Q}_{13}^{(2)})(r_2^{1-\beta^{(2)}} - r_1^{1-\beta^{(2)}})}{1 - \beta^{(2)}}$$

$$f_{09} = \frac{(\bar{Q}_{12}^{(3)} - \beta^{(3)}\bar{Q}_{13}^{(3)})(r_3^{1-\beta^{(3)}} - r_2^{1-\beta^{(3)}})}{1 - \beta^{(3)}}$$

$$f_{10} = \frac{(\bar{Q}_{12}^{(4)} - \beta^{(4)}\bar{Q}_{13}^{(4)})(r_c^{1-\beta^{(4)}} - r_3^{1-\beta^{(4)}})}{1 - \beta^{(4)}}$$

$$f_{11} = \frac{\lambda(1-\mu)(r_b^2 - r_a^2)}{2} + \sum_{k=1}^4 \frac{[\bar{Q}_{11}^{(k)} + \eta^{(k)}(\bar{Q}_{12}^{(k)} + \bar{Q}_{13}^{(k)})](r_k^2 - r_{k-1}^2)}{2}$$

$$f_{12} = \sum_{k=1}^4 \frac{[\bar{Q}_{16}^{(k)} + \zeta^{(k)}(\bar{Q}_{12}^{(k)} + 2\bar{Q}_{13}^{(k)})](r_k^3 - r_{k-1}^3)}{3}$$

$$g_{02} = \frac{(\bar{Q}_{26}^{(1)} + \beta^{(1)}\bar{Q}_{36}^{(1)})(r_1^{\beta^{(1)}+2} - r_b^{\beta^{(1)}+2})}{2 + \beta^{(1)}}$$

$$g_{03} = \frac{(\bar{Q}_{26}^{(2)} + \beta^{(2)} \bar{Q}_{36}^{(2)})(r_2^{\beta^{(2)+2}} - r_1^{\beta^{(2)+2}})}{2 + \beta^{(2)}}$$

$$g_{04} = \frac{(\bar{Q}_{26}^{(3)} + \beta^{(3)} \bar{Q}_{36}^{(3)})(r_3^{\beta^{(3)+2}} - r_2^{\beta^{(3)+2}})}{2 + \beta^{(3)}}$$

$$g_{05} = \frac{(\bar{Q}_{26}^{(4)} + \beta^{(4)} \bar{Q}_{36}^{(4)})(r_c^{\beta^{(4)+2}} - r_3^{\beta^{(4)+2}})}{2 + \beta^{(4)}}$$

$$g_{07} = \frac{(\bar{Q}_{26}^{(1)} - \beta^{(1)} \bar{Q}_{36}^{(1)})(r_1^{2-\beta^{(1)}} - r_b^{2-\beta^{(1)}})}{2 - \beta^{(1)}}$$

$$g_{08} = \frac{(\bar{Q}_{26}^{(2)} - \beta^{(2)} \bar{Q}_{36}^{(2)})(r_1^{2-\beta^{(2)}} - r_b^{2-\beta^{(2)}})}{2 - \beta^{(2)}}$$

$$g_{09} = \frac{(\bar{Q}_{26}^{(3)} - \beta^{(3)} \bar{Q}_{36}^{(3)})(r_1^{2-\beta^{(3)}} - r_b^{2-\beta^{(3)}})}{2 - \beta^{(3)}}$$

$$g_{10} = \frac{(\bar{Q}_{26}^{(4)} - \beta^{(4)} \bar{Q}_{36}^{(4)})(r_1^{2-\beta^{(4)}} - r_b^{2-\beta^{(4)}})}{2 - \beta^{(4)}}$$

$$g_{11} = \sum_{k=1}^4 \frac{[\bar{Q}_{16}^{(k)} + \eta^{(k)}(\bar{Q}_{26}^{(k)} + \bar{Q}_{36}^{(k)})](r_k^3 - r_{k-1}^3)}{3}$$

$$g_{12} = \frac{E(r_b^4 - r_a^4)}{8(1 + \mu)} + \sum_{k=1}^4 \frac{[\bar{Q}_{66}^{(k)} + \zeta^{(k)}(\bar{Q}_{26}^{(k)} + 2\bar{Q}_{36}^{(k)})](r_k^4 - r_{k-1}^4)}{4}$$

Once the integration constants are determined by solving equation (12.96), the stresses and displacements of the isotropic liner and each anisotropic layer can then be recovered by substitution of these constants into equations (12.31), (12.48), (12.51) and (12.52).

A computerized procedure based on the above multi-layered anisotropic analysis has been incorporated into a MATLAB program that allows the user to input material properties, boundary/interface conditions, internal pressure load and winding angle distributions. The program can calculate stress, strain, and deformation of multi-layered composite pressure vessels. A numerical example, which was previously described by Xia et al. [7], is investigated herein with the addition of an aluminum alloy (A6063-T6) liner. In this example (see Fig. 12.4), a thick-walled anisotropic cylindrical vessel comprises four CFRP (T300/934 carbon fiber/epoxy) layers and an aluminum alloy (A6063-T6) seamless liner, which has an inner radius $r_a = 50$ mm and a thickness 0.5 mm for each CFRP layer. The four layers are oriented symmetrically as $[55^\circ/-55^\circ/55^\circ/-55^\circ]$ and the vessel is subjected to the internal

Chapter 12

pressure of 10 MPa. To assess the influence of the liner thickness on stress distribution of the multilayered anisotropic shell, the stress components in the cylindrical coordinates (σ_{zz} , $\sigma_{\theta\theta}$, σ_{rr} and $\tau_{z\theta}$) are evaluated with various thicknesses of the aluminum liner ($t_L = 1\text{mm}$, 2mm , 3mm and 4mm), and the results are compared to those obtained by Xia et al. [7] ($t_L = 0$, no liner).

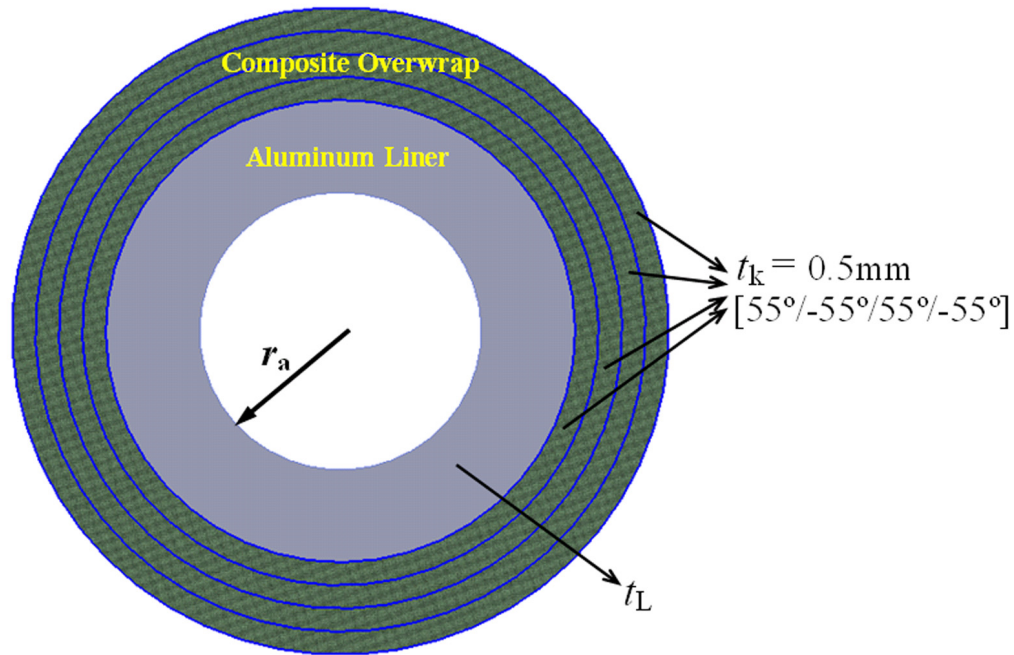


Fig. 12.4: An aluminum-lined cylindrical pressure vessel with 4 composite layers

Figs. 12.5-12.8 represent the axial, hoop, radial and in-plane shear stress distributions along the multilayered anisotropic wall, respectively. The results show that the magnitude of all the stress components rapidly decrease as the liner thickness is increased. For instance, the axial stresses of the cylindrical vessel with the liner thicknesses of 1 mm, 2 mm, 3 mm and 4 mm show about 34.7%, 51.8%, 61.9% and 68.6% reduction, respectively, as compared to that without liner ($t_L = 0$ as presented by Xia et al. [7]). Figs. 12.5 and 12.6 show that the composite overwrap has a nearly constant axial stress and a reduced hoop stress through the wall thickness; moreover, the hoop stress is decreased by a greater slope than the axial stress. This indicates that the ratio of hoop-to-axial stress is no longer a constant through the cylinder wall and varies with the wall thickness. From Fig. 12.7, it can be seen that the radial stress is compressive under the uniform internal pressure and shows a nearly linear distribution through the wall of the cylinder. The magnitude of the radial stress is much smaller than that of the axial and hoop stresses. Fig. 12.8 illustrates that the shear stress $\tau_{z\theta}$ has a piecewise

Three-dimensional Stress, Strain & Displacement Analysis

distribution and alternates between positive and negative values that are identical with the sign of the winding angle. From Figs. 12.5~12.8, it is also demonstrated that the addition of the liner leads to more homogenous stress distributions through the wall thickness, and that the difference of stress between the inner and outer layers diminishes while increasing the liner thickness.

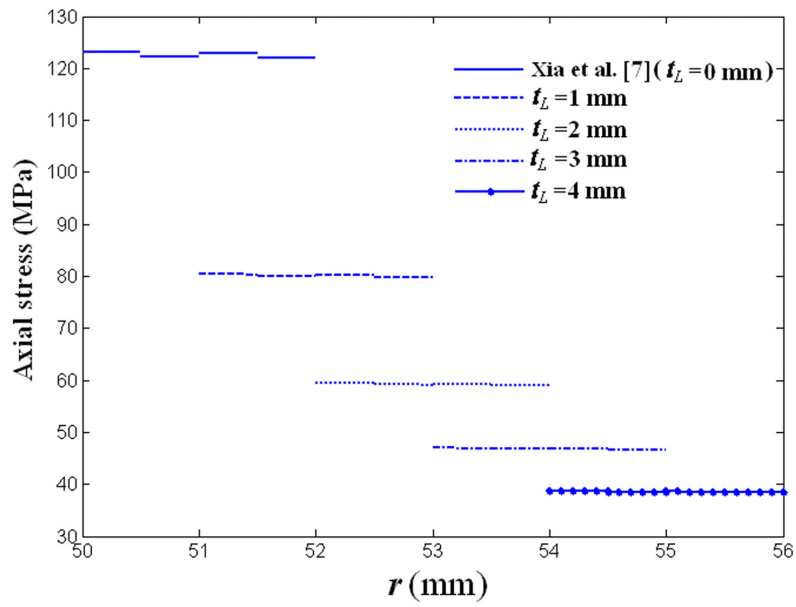


Fig. 12.5: Distributions of the axial stress through the wall of the composite overwrap

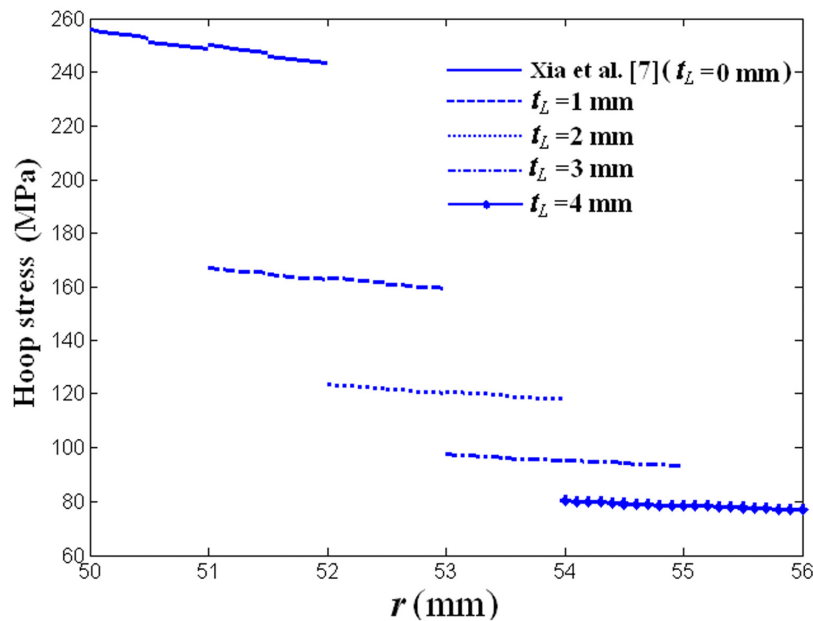


Fig. 12.6: Distributions of the hoop stress through the wall of the composite overwrap

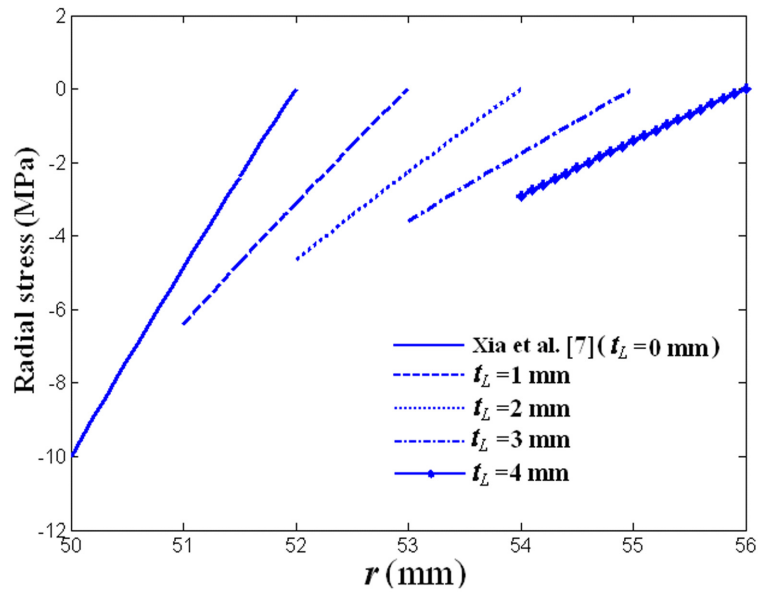


Fig. 12.7: Distributions of the radial stress through the wall of the composite overwrap

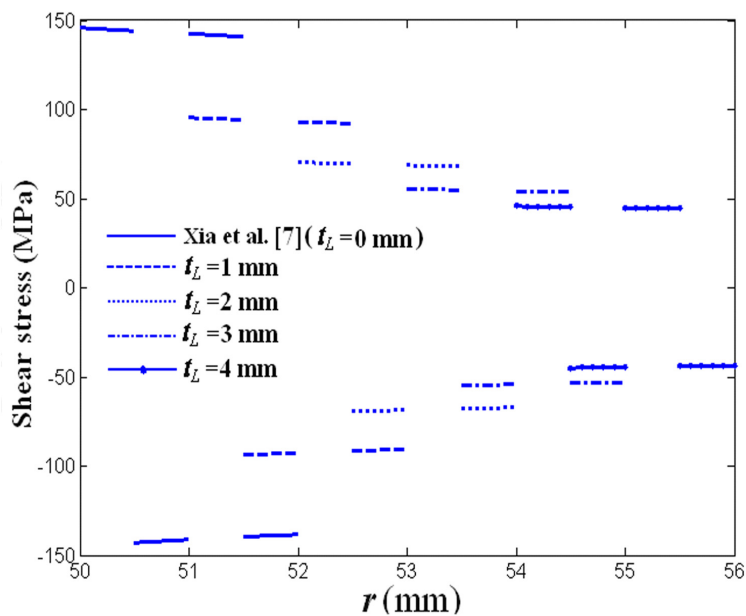


Fig. 12.8: Distributions of the shear stress through the wall of the composite overwrap

Fig. 12.9 gives the twisting rates γ_0 of the cylindrical shells with various liner thicknesses, as compared to that calculated by Xia et al. [7] (no liner). It is shown that the addition of the aluminum liner does considerably reduce the twisting of the cylinder; with a thicker liner it exhibits a smaller twisting rate. However, it is also observed that the twisting is fairly small as compared to the dimensions of the cylinder.

Fig. 12.10 shows the Tsai-Wu strength ratios R through the wall of the anisotropic laminated shell. It is revealed that the strength reserve of the laminate is considerably

Three-dimensional Stress, Strain & Displacement Analysis

improved by the addition of the liner; it is also increased with increasing the liner thickness. In addition, the strength ratio increases from the inner layer to the outer layer; this implies that the inner layer withstands the highest stress levels and is the most critical location in regard to structural failure.

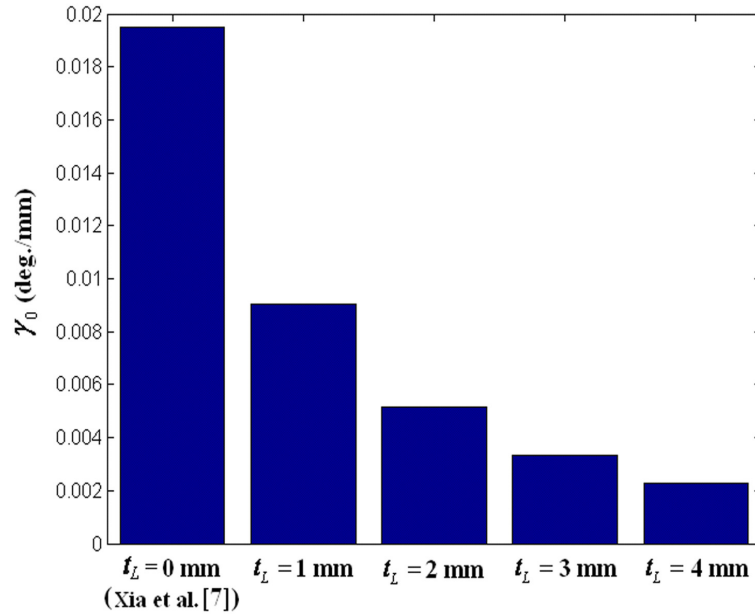


Fig. 12.9: Comparison of the twisting rates for various liner thicknesses

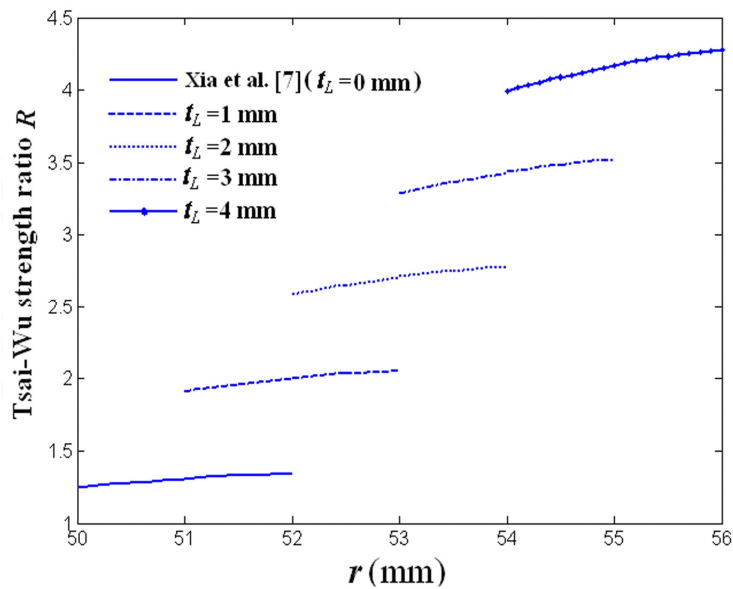


Fig. 12.10: Tsai-Wu strength ratios through the wall of the composite overwrap

The effect of liner material selection on the stress distributions of anisotropic composite overwrap layers is demonstrated by considering three liner materials with the same thickness

Chapter 12

($t_L = 2$ mm): Aluminum 6063-T6 ($E = 68.9$ GPa, $\mu = 0.34$), Titanium B-120VCA ($E = 120$ GPa, $\mu = 0.33$) and Strainless Steel 301 ($E = 193$ GPa, $\mu = 0.3$) [93]. Figs. 12.11~12.13 describe the stress distributions through the wall of the composite overwrap layers in the axial, hoop and radial directions, respectively. In Fig. 12.14 the twisting rates of the cylinders are determined for the above given materials. The results show that the isotropic metal liner with a higher elastic modulus yields a lower stress level as well as a smaller twisting rate of the anisotropic composite shell.

Various combinations among three composite materials (T300/934, B(4)/5505, E-glass/epoxy) and three liner materials (A6063-T6, B-120VCA, Steel 301) are evaluated by calculating the equivalent Von Mises stress through the wall of the metal liner (Fig.12.15) and the Tsai-Wu strength ratio R through the wall of the anisotropic composite laminate (Fig. 12.16). Typical values of the mechanical properties for the three composite materials are given in Tab. 12.3 [94-96]. A material anisotropy parameter k is here adopted to represent the degree of laminate anisotropy; k is defined as [97-101]:

$$k = \frac{E_2(1+\nu_{12})}{E_1(1+\nu_{21})} \quad (12.97)$$

where the involved engineering parameters refer to the individual UD layer of the used composite material. For $k = 1$ the engineering constants are identical, hence the considered material will be isotropic; $k = 0$ represents the netting case where the contribution of the matrix to the mechanical properties of the layer is considered negligible. The anisotropy parameters of the considered three composite materials are $k=0.0939$ for T300/934, $k=0.1093$ for B(4)/5505 and $k = 0.4101$ for E-glass/epoxy. It should be noted here that a composite layer with a higher anisotropy has a lower k .

Fig. 12.15 illustrates that a composite wall with higher anisotropy results in a lower Von Mises stress for a given liner material, and that for a given composite material a low-modulus metal liner exhibits a lower Von Mises stress. Fig. 12.16 reveals that for a given liner material the Tsai-Wu strength ratios as obtained using high-anisotropy composite materials are higher than those using composites with low anisotropy; in addition, for the same composite material a high-modulus metal liner leads to a higher strength ratio.

It can be concluded that the combination of a high-anisotropy composite and a low-modulus metal liner produces a lower Von Mises stress level of the liner; on the other hand, the combination of a high-anisotropy composites and a high-modulus metal liner provides larger strength reserve of the composite overwrap laminate.

Three-dimensional Stress, Strain & Displacement Analysis

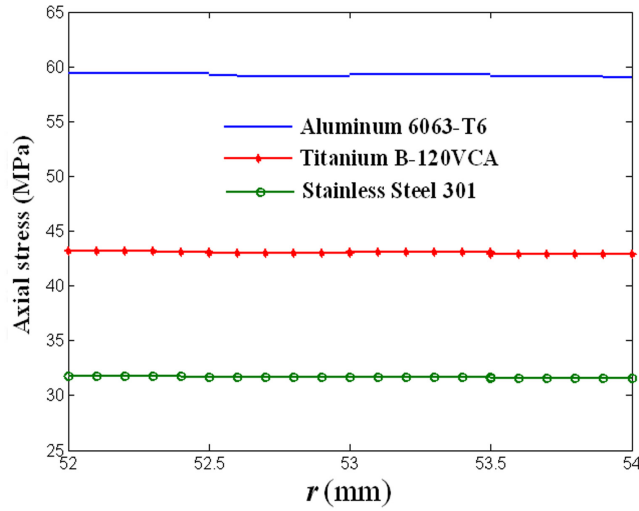


Fig. 12.11: The axial stress of the composite overwrap with various liner materials

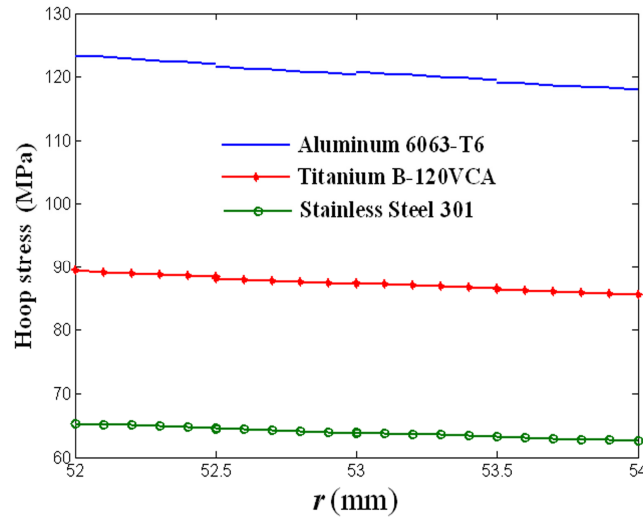


Fig. 12.12: The hoop stress of the composite overwrap with various liner materials

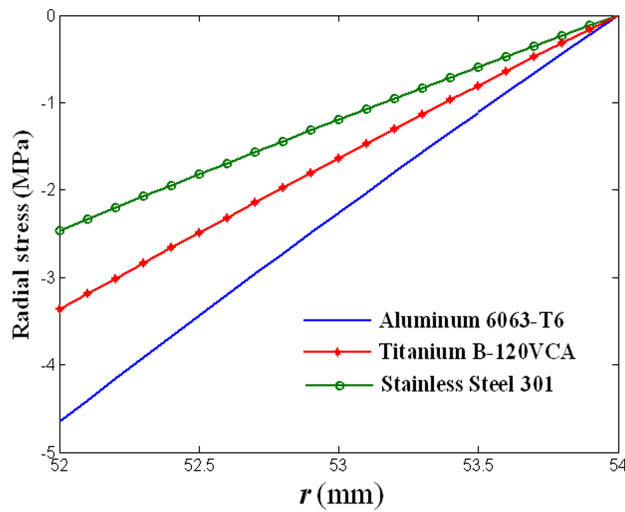


Fig. 12.13: The radial stress of the composite overwrap with various liner materials

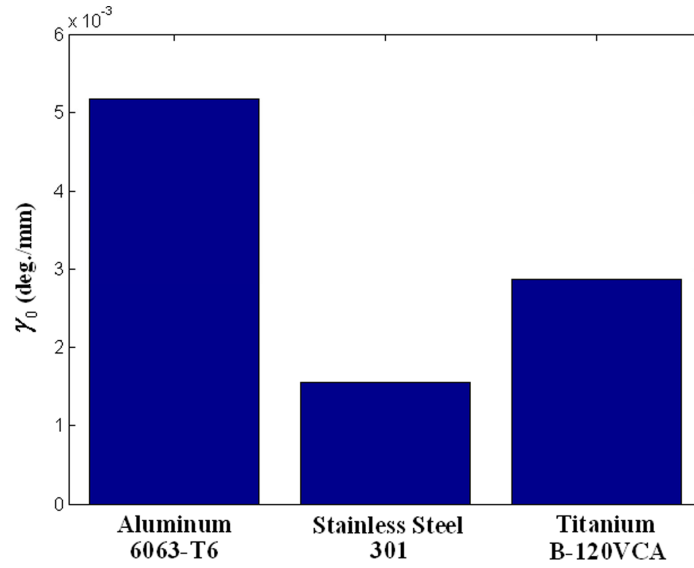


Fig. 12.14: Twisting rates of the composite overwrap with various liner materials

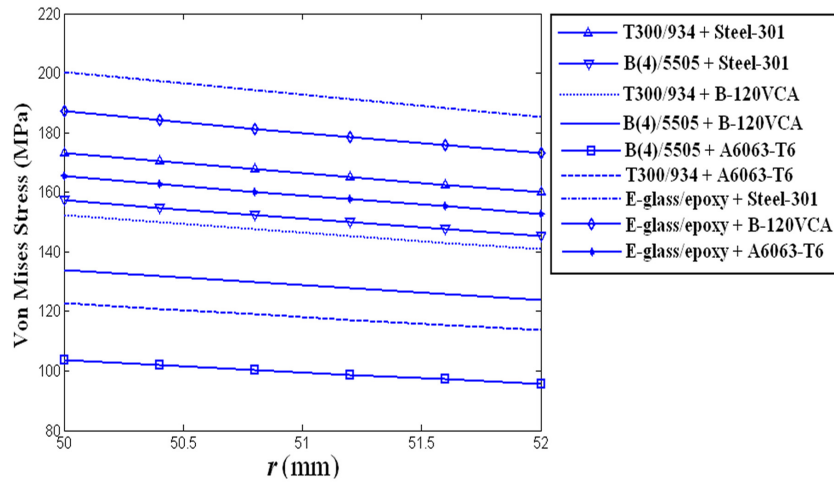


Fig. 12.15: Von Mises stress distributions through the wall of the metal liner

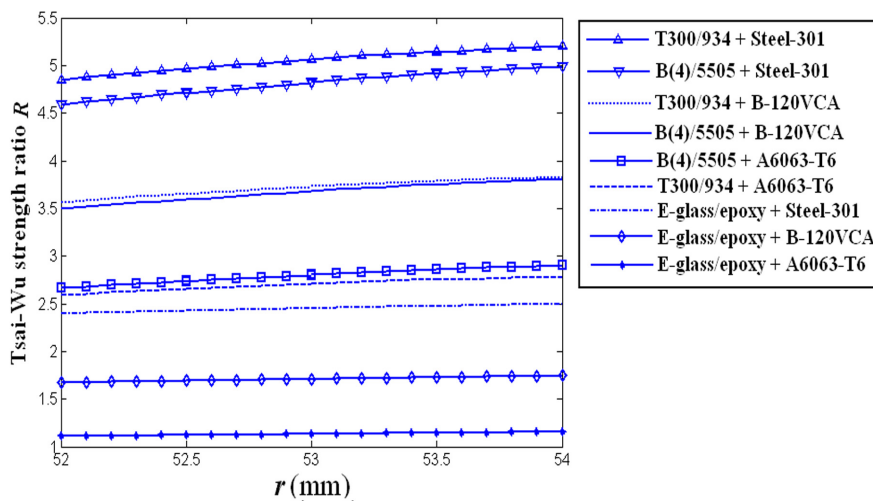


Fig. 12.16: Distributions of Tsai-Wu strength ratios through the composite wall

Three-dimensional Stress, Strain & Displacement Analysis

Tab. 12.3: Typical mechanical properties of unidirectional composites [94-96]

Properties	T300/F934	E-glass/epoxy	B(4)/5505
Longitudinal modulus, E_1 (GPa)	141.6	43.4	204
Transverse modulus, E_2 (GPa)	10.7	15.2	18.5
In-plane shear modulus, G_{12} (GPa)	3.88	6.14	5.59
Major poisson's ratio, ν_{12}	0.268	0.29	0.23
Through thickness poisson's ratio, ν_{23}	0.495	0.38	0.3
Longitudinal tensile strength, X_T (MPa)	1314	1062	1260
Transverse tensile strength, Y_T (MPa)	43	31	61
Longitudinal compressive strength, X_c (MPa)	1220	610	2500
Transverse compressive Strength, Y_c (MPa)	168	118	202
In-plane shear strength, S (MPa)	48	72	67

12.8 Conclusions

In order to increase the applicability and efficiency of high-pressure filament-wound pressure vessels, it was concluded already several years ago that more knowledge regarding stress analysis and structural optimization of thick-walled multilayered anisotropic shells needed to be generated.

It is shown that for composite pressure vessels with a ratio of outer to inner radius, up to 1.1, thin and thick wall solutions give similar results in terms of the optimal winding angle, stress/strain distribution, the burst pressure, etc. As the ratio increases, a thick-walled shell analysis is imperatively required. This chapter is a preliminary investigation aimed at improving the understanding of engineering design and analysis for thick-walled filament-wound cylindrical pressure vessels.

In the last few years, much effort is dedicated towards understanding the mechanisms of stress and strain distributions of thick-walled composite pressure vessels subjected to internal

Chapter 12

and external pressure, axial force, centrifugal force, temperature and moisture variation, etc. Because of the anisotropy in composites and the presence of curvature in shell structures, obtaining exact three-dimensional elasticity solutions for laminated cylinders imposes considerable mathematical complexity. However, in some cases a three-dimensional approach can still be used. For example, load conditions specified as axisymmetrically distributed load (internal or external pressure), will considerably simplify the equations of the exact three-dimensional theory. It has been shown that the stresses and deformations of thick-walled multilayer cylinders depend strongly on the stacking sequence. For cylindrical pressure vessels with different angle-ply laminae, the ratio of hoop-to-axial stress varies with each lamina and is no longer a constant of 2. The through-thickness normal stress distributions show nearly linear variations that are relatively smaller compared to those in hoop and axial directions. It is also found that the lamina sequence is very critical for the stress analysis and the optimization of, in particular, thick cylinders. After identification of the most important parameters for stress analysis with respect to thick-walled composite cylinders, it may be concluded that the stress and strain distributions are most dependent on the lamina sequence, and, in the second place, on different loading conditions such as thermal loading and twisting moment.

The assumption of generalized plane strain, in which the axial strain of the cylinder is a constant rather than zero, has been widely applied in stress analysis of thick-walled filament-wound cylinders. Twisting, due to lack of exact symmetry in ply stacking, can be calculated on an individual layer basis. The absence of this twisting may create erroneous results in calculations that assume axisymmetry of the system. This effect can be considered negligible for low pressure but becomes significant for cylinders at relatively high internal pressure.

Thermal stresses are associated with thermal strain incompatibility. These stresses can exist without the action of external forces. In anisotropic solids, the stresses can occur even under a uniform temperature change due to thermal anisotropy. Some studies investigated the "hygrothermal problem" due to elevated temperature and moisture absorption. It can be solved mainly in three steps: First, the temperature distribution and the moisture content inside the material are calculated. Then from known temperature and moisture distribution, the hygrothermal deformations and stresses are calculated. Finally, the changes in performance due to both effects are superposed.

Several studies have been published regarding the 3D effective elastic constants for filament-wound cylindrical pressure vessels and pipes, including the effective elastic

Three-dimensional Stress, Strain & Displacement Analysis

constants in the through-thickness direction. Results have been presented to show how all the elastic constants for filament-wound cylinders vary with winding angle and the effective through-thickness Young's modulus was found to be only slightly bigger than the transverse modulus of the unidirectional fiber-reinforced material for all winding angles. The through-thickness shear modulus decreased approximately linearly with winding angle and the through-thickness Poisson's ratios varied greatly with the winding angle and even decreased to negative values in some cases.

The stress analysis based on three-dimensional elasticity solution allows the burst pressure for both open-ended (pipes) and closed-ended (pressure vessels) cylinders to be predicted accurately, and allows us to evaluate a multilayered pressure vessel with an arbitrary number of layers of any thickness. The previous studies also showed that the stacking sequence can be employed effectively for maximizing burst pressure of thick-walled multilayered pressure vessels. A reliable design method for thick cylinders is formulated with the use of an appropriate 3D failure criterion which includes the contribution of all stress components to the failure.

Failure of composites has been investigated extensively from micromechanical and macromechanical points of view. The accuracy of the prediction strongly depends on the selected criteria. The most widely used failure theories have been categorized in terms of two main groups: tensor polynomial criteria and failure modes based criteria. The first category consists of failure criteria that do not integrate any physical consideration or failure modes. Failure theories of the second group incorporate the effect of failure modes in their formulation. Failure-modes based criteria consider that the non-homogeneous character of composites causes different failure modes for the constituents. These failure theories are formulated in terms of several sub-criteria corresponding to various failure modes and related conditions for validity. The criteria, which are represented by mathematical expressions that incorporate material strength values, are able to predict failure modes and become thus adequate to deal with progressive damage analysis. The validity and applicability of a failure theory depend on the convenience of applying it, and the agreement with experimental results. In general, a large divergence has been observed in the failure prediction by the different theories. The modeling and solutions for laminate failure analysis should be deliberately applied and the adapted failure theories need to be selected in view of the expected failure modes and locations.

For a multi-layered thick-walled cylindrical pressure vessel consisting of an angle-ply laminate and an isotropic liner, the magnitude of all stress components in the cylindrical

Chapter 12

coordinates decreases from the inside out. The hoop-to-axial stress ratio varies along the wall thickness and is no longer a constant; this is mainly triggered by a faster decline of the hoop stress than the axial stress through the wall of the vessel. The through-thickness normal stress distributions show nearly linear variations that are relatively smaller compared to those in hoop and axial directions. To evaluate the effect of the liner's thickness on the stress distributions of the composite overwrap, the stress components in the cylindrical coordinates are evaluated with various thicknesses of the aluminum liner. It is found that the addition of the liner and the increase of the liner thickness results in smoother stress gradients and more homogenous stress distributions through the wall of the shell and can thus improve the structural performance of pressure vessels. It is also shown that the addition of the liner considerably reduces the in-plane twisting of the vessel and, meanwhile, increases the strength reserve of the composite reinforcement.

The stress distributions through the wall thickness of the pressure vessel are outlined for various anisotropic composite and isotropic liner combinations, in order to locate the best combination of fiber/matrix/liner materials for internally pressurized multilayered anisotropic vessels. It is concluded that the use of a high-anisotropy composite material or a low-modulus metal liner can lead to lower equivalent stress of the liner and should be chosen when the yield of metal inner liner becomes a critical issue for the failure of a pressure vessel; in addition, under a given internal pressure, a high-anisotropy composite material combined with a high-modulus metal liner reserves more additional strength to which the composite overwrap may be subjected prior to failure.

References

1. Lekhnitskii SG. Anisotropic plates. New York: Gordon and Breach, 1968. Translated by S.W. Tsai and T. Cheron.
2. Lekhnitskii SG. Theory of elasticity of an anisotropic elastic body. San Francisco: Holden-Day, Inc.; 1963. Translated by P. Fern.
3. Tsai, S.W. Composites Design, 4th Ed., Think Composites, Dayton, OH, 1988.
4. Rohrauer G. Ultra-high pressure composite vessels with efficient stress distributions. PhD thesis, Concordia University, 1999.
5. Witherell, M.D. A Generalized Plane-Strain Elastic Stress Solution for a Multiorthotropic- Layered Cylinder". US Army Armament Research, Development and Engineering Center. Benet Laboratories, Technical Report ARCCB-TR-92013, March.

Three-dimensional Stress, Strain & Displacement Analysis

- 1992: 1-19.
6. Roy AK, Tsai SW. Design of thick composite cylinders. *J Press Vessel Technol* 1988; 110: 255–62.
 7. Xia M, Takayanagi H, Kemmochi K. Analysis of multi-layered filament wound composite pipes under internal pressure. *Compos Struct* 2001; 53: 483–91.
 8. Xia M, Kemmochi K, Takayanagi H. Analysis of filament-wound fiber-reinforced sandwich pipe under combined internal pressure and thermomechanical loading. *Compos Struct* 2001; 51: 273–83.
 9. Noor AK, Burton WS and Peters JM. Assessment of computational models for multilayered composite cylinders, *Int J Solids Struct* 1991; 27(10): 1269–86.
 10. Mackerle J. FEM and BEM analysis and modelling of residual stresses – a bibliography (1998-1999). *Finite Elem Anal Des* 2001; 37: 253-62.
 11. Tabakov PY. Design of laminated cylinders using genetic algorithm. *J Appl Comput Sci* 2000; 8(2):7–29.
 12. Wild PM, Vickers GW. Analysis of filament-wound cylindrical shells under combined centrifugal pressure and axial loading. *Compos Part A: Appl Sci Manuf* 1997; 28:47-55.
 13. Hyer MW. Hydrostatic response of thick laminated composite cylinders. *J Reinf Plastic Compos* 1988; 7: 321–40.
 14. Mirza S, Bryan A, Noori M. Fiber-reinforced composite cylindrical vessel with lugs. *Compos Struct* 2001; 53:143–51.
 15. Kam TY, Liu YW, Lee FT. First-ply failure strength of laminated composite pressure vessels. *Compos Struct* 1997;38:65–70.
 16. Chang RR. Experimental and theoretical analyses of first-ply failure of laminated composite pressure vessels. *Compos Struct* 2000;49: 237–43.
 17. Ruddock, G.J. and Spencer, A.J.M., A new approach to stress analysis of anisotropic laminated elastic cylinders. *Proc R Soc, Lond, A.* v453. 1067-1082
 18. D. Kokan and K. Gramoll. Analysis of Orthotropic Composite Cylinders. *Composite Engineering* 1994; 4(10): 979–93.
 19. Kalinnikov AE, Korlyakov SV. Optimization of the stress–strain state of a thick-walled pipe on the basis of Young's modulus of the material. *Problemy Prochnosti* 1988; 2: 88–91 (English translation of Plenum Publishing Corporation, 1988).
 20. Ren, J.G. Analysis of laminated circular cylindrical shells under axisymmetric loading. *Composite structures*, 1995, 30: 271-80.
 21. Ren JG. Analysis of simply supported laminated circular cylindrical shell roofs. *Compos*

Chapter 12

- Struct 1989;11(4):277–92.
22. Chandrashekhara K, Gopalakrishnan P. Elasticity solution for multilayered transversely isotropic circular cylindrical shells. *J Appl Mech* 1982; 49:108–14.
 23. Chandrashekhara K, Nanjunda Rao KS. Approximate elasticity solution for a long and thick laminated circular cylindrical shell of revolution. *Int. J. Solids Structures* 1997; 34(1): 1327-1341.
 24. Noor AK, Rarig PL. Three-dimensional solutions of laminated cylinders. *Comput Methods Appl Mech Eng* 1974; 3:319–34.
 25. Grigorenko YM, Vasilenko AT, Pankratova ND. Computation of the stressed state of thick-walled inhomogeneous anisotropic shells. *Sov Appl Mech* 1974; 10: 523–8.
 26. Noor AK, Peters JM. Stress, vibrations and buckling of multilayered cylinders. *J Struct Eng* 1989; 115: 69–88.
 27. Noor, A. K., Burton, W. S. Assessment of computational models for multilayered composite shells. *Appl. Mech. Rev.*, 43 (1990) 67-96.
 28. S. B. Dotvc and F. K. W. Tso. On a laminated orthotropic shell theory including shear deformation. *J. Appl. Mech. Trans. ASME Series E* 1972; 39:1091-7
 29. J. M. Whitney, C. T. Sun, A refined theory for laminated anisotropic cylindrical shells. *J. Appl. Mech Trans. ASME Series E* 1974; 41: 471-6.
 30. Lee SY, Springer GS. Filament winding cylinders: I. Process model. *J Comp Mater* 1990; 24: 1270–98.
 31. Ding K, Tang L. Exact solution for axisymmetric thick laminated shells. *Compos Struct* 1999; 46(2): 125-9.
 32. Spencer AJM, Watson P, Rogers TG. Mathematical analysis of the springback effect in laminated thermoplastic channel sections. *Comp Manuf* 1991; 2: 253–8.
 33. Chandrashekhara K, Kumar BS. Static analysis of a thick laminated circular cylindrical shell subjected to axisymmetric load. *Compos Struct* 1993; 23: 1-9.
 34. Chandrashekhara K, Nanjunda Rao KS. Static analysis of along and thick orthotropic circular cylindrical shell of revolution. *Archive of Applied Mechanics* 1995; 65: 425-36.
 35. Kollar LP, Springer GS. Stress analysis of anisotropic laminated cylinders and cylindrical segments. *Int J Solid Struct* 1992; 29: 1499–1517.
 36. Flügge W. *Stresses in Shells*. 2nd ed. New York: Springer, 1973.
 37. Roy A K. Response of thick laminated composite rings to thermal stress. *Compos Struct* 1991; 18: 125-39.
 38. Ben G. Structural analyses of thick-walled cross-ply laminated FRP cylindrical shells.

Three-dimensional Stress, Strain & Displacement Analysis

- Trans Jpn Soc Mech Eng Part A (in Japanese) 1991; 57:1412-7.
39. Parnas L, Katirci N. Design of fiber-reinforced composite pressure vessels under various loading conditions. *Compos Struct* 2002; 58: 83-95.
 40. Jacquemin F, Vautrin A. The effect of cyclic hygrothermal conditions on the stresses near the surface of a thick composite pipe. *Compos Sci Technol* 2002; 62: 567-70.
 41. Hyer MW, Cooper DE, Cohen D. Stress and deformations in cross-ply composite tubes subjected to uniform temperature change. *J Therm Stress* 1986; 9: 97-117.
 42. Hyer MW, Rosseau CQ. Thermally induced stresses and deformations in angle-ply composite tubes. *J Comp Mater* 1987; 21: 454-80.
 43. Xia M, Kemmochi K, Takayanagi H. Analysis of filament-wound fiber-reinforced sandwich pipe under combined internal pressure and thermomechanical loading. *Compos Struct* 2001; 51: 273-83.
 44. Khdeir AA, Aldraihem OJ. Analytical models and solutions of laminated composite piezoelectric plates, *Mech Adv Mater Struct* 2007; 14: 67-80
 45. Sayman O. Analysis of multi-layered composite cylinders under hygrothermal loading. *Compos Part A: Appl Sci Manuf* 2005; 36: 923-33.
 46. Akcay I, Hakki, Kaynak Idriis Analysis of multilayered composite cylinders under thermal loading. *J Reinforc Plast Compos* 2005; 24(11): 1169-79.
 47. Sherrer RE. Filament wound cylinders with axial symmetric loads. *J Compos Mater* 1967; 1: 344-55
 48. Amiouny SV, Hoa SV. Heuristics for the design of thick composite cylinders. *Computer methods in composite materials VI*, Editors: C. A. BREBBIA, W.R. BLAIN & W.P. DE WILDE, Transaction of Wessex Institute of Technology, United Kingdom.1998
 49. Hoa SV, Mannarino G. Twisting of filament wound cylinders under internal pressure, *Journal of Reinforced Plastics and Composites* 1989; 8: 212-231.
 50. Eme EB, Rizzo RR. Three-dimensional laminate theory. *J Compos Mater* 1970; 4: 150-4.
 51. Chou PC, Carleone J, Hsu CM. Elastic constants of layered media. *J Compos Mater* 1972; 6: 80-93.
 52. Sun CT, Li S. Three-dimensional effective elastic constants for thick laminates. *J Compos Mater* 1988; 22: 629-39.
 53. Pagano NJ. Exact moduli of anisotropic laminates, in *Mechanics of Composite Materials* (edited by G. P. Sendeckyi), Chap. 2, pp. 23-44. Academic Press, 1974, New York.
 54. Roy AK, Tsai SW. Three-dimensional effective moduli of orthotropic and symmetric laminates. *ASME J Appl Mech* 1992; 59: 39-47.

Chapter 12

55. Herakovich CT. Composite laminates with negative through-thickness Poisson's ratios. *J Compos Mater* 1984; 18: 447-55.
56. Vasiliev VV. *Composite Pressure Vessels - Analysis, Design, and Manufacturing*. Bull Ridge Publishing, Blacksburg, Virginia, USA, 2009.
57. Kitao K, Akiyama H. Failure of thick-wall filament wound plastic pipes under internal pressure. *J Soc Mater Sci Japan* 1994; 43:1134-40.
58. Roy AK, Mansard TN. A design study of thick multilayered composite spherical pressure vessels, *J Reinf Plast Comp* 1992; 2: 479-93.
59. Tsai SW, Wu EM. A general theory of strength for anisotropic materials. *J Compos Mater* 1971; 5(1): 58-80.
60. Adali S, Summers EB, Verijenko VE. Optimization of laminated cylindrical pressure vessels under strength criterion. *Compos Struct* 1993;25:305–12
61. Sun XK, Du SY, Wang GD. Bursting problem of filament wound composite pressure vessels. *Int J Press Vessels Piping* 1999; 76:55–9.
62. Onder A, Sayman O, Dogan T, Tarakcioglu N. Burst failure load of composite pressure vessels. *Compos Struct* 2009; 89: 159-66.
63. Hinton MJ, Soden PD, Kaddour AS. *Failure criteria in fiber-reinforced-polymer composites*. Oxford: Elsevier; 2004.
64. Gol'denblat II and Kopnov VA. Strength of glass-reinforced plastics in the complex stress stat. *Mekhanika Polimerov* 1965; 1(2): 70-78.
65. Hart-Smith LJ. Predictions of the original and truncated maximum-strain failure models for certain fibrous composite laminates. *Compos Sci Technol* 1998; 58: 1151-79.
66. Tsai SW. *Strength characteristics of composite materials*. NASA CR-224, 1965.
67. Hoffman O. The brittle strength of orthotropic materials. *J Compos Mater* 1967; 1: 200-6.
68. Chamis CC. Failure criteria for filamentary composites. *Composite Materials: Testing and Design*, STP 460, ASTM, Philadelphia, 1969: 336-51.
69. Jones RM. *Mechanics of composite materials*. McGraw-Hill Book Co., New York, 1975.
70. Hashin Z, Rotem A. A fatigue failure criterion for fiber reinforced materials. *J Compos Mater* 1973; 7(4): 448-64.
71. Hashin Z. Failure criteria for unidirectional fiber composites. *J Appl Mech-T ASME* 1980; 47: 329-34.
72. Puck A, Schürmann H. Failure analysis of FRP laminates by means of physically based phenomenological models. *Compos Sci Technol* 2002; 62(12-13): 1633-62.
73. Puck A, Schürmann H. Failure analysis of FRP laminates by means of physically based

Three-dimensional Stress, Strain & Displacement Analysis

- phenomenological models. *Compos Sci Technol* 1998; 58(7): 1045-67.
74. Dávila C, Camanho PP, Rose CA. Failure criteria for FRP laminates. *J Compos Mater* 2005; 39: 323-45.
 75. Pinho ST, Dávila CG, Camanho PP, Iannucci L, Robinson P. Failure models and criteria for FRP under in-plane or three-dimensional stress states including shear non-linearity. Research report, NASA/TM-2005-213530, NASA Langley Research Center, Feb. 2005.
 76. Christensen RM. Stress based yield/failure criteria for fiber composites. *Int J Solids Struct* 1997; 34(5): 529-43.
 77. Christensen RM. The numbers of elastic properties and failure parameters for fiber composites. *J Eng Mater-T ASME* 1998; 120(2): 110-3.
 78. Hinton MJ, Kaddour AS, Soden PD. A comparison of the predictive capabilities of current failure theories for composite laminates, judged against experimental evidence. *Compos Sci Technol* 2002; 62(12-13): 1725-97.
 79. Daniel IM, Luo JJ, Schubel PM. Three-dimensional characterization of textile composites. *Compos Part B*, 2008; 39: 13-9.
 80. Daniel IM, Luo JJ, Schubel PM, Werner BT. Interfiber/interlaminar failure of composites under multi-axial states of stress. *Compos Sci Technol* 2009; 69: 764-71.
 81. Daniel IM, Cho JM, Werner BT, Fenner JS. Interfiber Failure Criteria of Composites under Static and Dynamic Loading. in *Proceedings of Annual Conference of the American Society for Composites*, University of Delaware, Delaware, USA, Sept. 2009.
 82. Daniel IM, Werner BT, Fenner JS. Strain-rate-dependent failure criteria for composites. *Compos Sci Technol* 2011; 71(3): 357-64.
 83. Daniel IM. Failure of Composite Materials. *Strain*, 2007; 43: 4-12.
 84. Sun CT, Quinn BJ, Tao, J, Oplinger DW. Comparative evaluation of failure analysis methods for composite laminates. NASA, DOT/FAA/AR-95/109, May 1996.
 85. Cuntze RG. Efficient 3D and 2D failure conditions for UD laminae and their application within the verification of the laminate design. *Compos Sci Technol* 2006; 66:1081-96.
 86. Yamada SE, Sun CT. Analysis of laminate strength and its distribution. *J Compos Mater* 1978; 12: 275-84.
 87. Kopp J, Michaeli W. Dimensioning of thick laminates using new IFF strength criteria and some experiments for their verification. in *Proceedings of the ESA-ESTEC Conference*, Noordwijk, Netherlands, March 1996: 305-312.
 88. Kroll L, Hufenbach, W. Physically based failure criteria for dimensioning of thick-walled laminates. *Appl Compos Mater* 1997; 4: 321-32.

Chapter 12

89. Zinoviev PA, Griogoriev SV, Lrbedeva OV, Tairova LP. The strength of multilayered composites under a plane-stress state. *Compos Sci Technol* 1998; 58: 1209-14.
90. Gosse JH. Strain invariant failure criteria for polymers in composite materials. in *Proceedings of the 42nd AIAA/ASME/ASCE/AHS/ASC Structures, Structural Dynamics and Materials Conference*. Seattle, WA, USA, Apr. 2001, pp. 45-55.
91. Hart-Smith LJ. Predictions of a generalized maximum-shear-stress failure criterion for certain fibrous composite laminates. *Compos Sci Technol* 1998, 58: 1179–208.
92. Echaabi J, Trochu F, Gauvin R. Review of failure criteria of fibrous composite materials. *Polym. Compos* 1996; 17(6): 786-98.
93. Gere JM, Timoshenko SP. *Mechanics of materials*. 4th Edition, Boston: PWS Publishing Company, 1997.
94. Goetschel DB, Radford DW. Analytical development of through-thickness properties of composite laminates. *J Adv Mater* 1997; 29(7):37-46.
95. Liu KS, Tsai SW. A progressive quadratic failure criterion for a laminate. *Compos Sci Technol* 1998; 58(7): 1023-32.
96. Tsai SW, Hahn HT. *Introduction to composite materials*. Westport, Conn.: Technomic Publishing Company, Inc., 1980.
97. Vasiliev VV, Krikanov AA. New generation of filament-wound composite pressure vessels for commercial applications. *Compos Struct* 2003; 62(3): 449-59.
98. Vasiliev VV, Morozov EV. *Advanced mechanics of composite materials*. UK: Elsevier Ltd, 2007.
99. Zu L, Koussios S, Beukers A. Integral design for filament-wound composite pressure vessels. *Polym Polym Compos* 2011; 19: 413-20.
100. Zu L, Koussios S, Beukers A. Optimal cross sections of filament-wound toroidal hydrogen storage vessels based on continuum lamination theory. *Int J Hydrogen Energy* 2010; 35: 10419-29.
101. Zu L, Koussios S, Beukers A. Design of filament-wound domes based on continuum theory and non-geodesic roving trajectories. *Comp Part A: Appl Sci Manuf* 2010; 41: 1312-20.

Chapter 13

Conclusions and Recommendations

13.1 Introduction

In this dissertation we have presented an overview and performed an elaboration of the design and optimization procedure associated with filament wound toroidal pressure vessels and domed pressure vessels. Among possible shapes of pressure vessels, toroids have been recently gaining wide attention for the storage of pressurized liquids and gases, due to their high structural efficiency and novel configuration. Since the dome regions are the most critical locations with regard to structure failure, the optimal design of the domes became also one of the most imperative issues in pressure vessel design. Beginning with the outline of several fundamental issues related to the stability analysis of fiber trajectories and the generalized optimality condition for coupling the vessel geometry and the laminate layup, we have proceeded to the presentation of several types of pressure vessel designs for geodesic-isotensoids, non-geodesic-isotensoids, non-geodesic bellow-shape vessels, continuum-based optimal domes, continuum-based optimal toroids, isotensoids with unequal polar openings, and thick-walled cylinders. The netting theory and the orthotropic plate theory were employed to predict the mechanical behavior of pressure vessels, corresponding to various design scenarios. Non-geodesic trajectories were extensively applied to replace the conventionally used geodesics, in order to improve the structural performance, and to produce unique vessel shapes, e.g. domes with unequal polar openings. The optimal cross sectional shapes (quasi-ellipses) of the toroids were determined and compared to circular toroids. The non-geodesics-based dome profiles were also derived and proved to show better performance as compared to the geodesics-based ones. In addition, an overview was conducted on 3D elasticity solutions and failure theories of multi-layered thick-walled pressure vessels, taking

Chapter 13

into account the several effects like hygrothermal loading and twisting. The effects of the inner liner and its thickness on the stress distribution of the composite overwrap are evaluated using various liner thicknesses. The equivalent stress of the liner and the Tsai-Wu strength ratio of the composite overwrap were also calculated for various liner/fiber/resin material combinations to find the best material combination. The conclusions and recommendations are summarized as follows.

13.2 Conclusions

13.2.1 Fiber stability analysis for winding toroidal pressure vessels

An analysis for fiber trajectory stability was elaborated for providing a design reference of filament-wound toroidal pressure vessels. It was revealed that toroidal pressure vessels with larger relative bend radius and lower hoop-to-helical thickness ratio lead to better fiber stability in terms of either slippage or bridging tendency. The results also imply that for the most commonly used toroids, the winding trajectories designed by the netting theory satisfy both the non-slippage and non-bridging criteria, and show good fiber stability for the winding process.

13.2.2 Netting-based design of toroidal pressure vessels

- **Circular toroids:** A netting-based approach is outlined for the optimal design of helically and hoop wound toroidal pressure vessels. The optimal fiber trajectories with non-constant slippage coefficients are aligned in the principal stress direction throughout the whole structure. Compared to the geodesic winding, the results demonstrated that the optimal fiber trajectories lead to a better stress distribution and hence maximize the use of the fiber strength under internal pressure.
- **Isotenoid toroids:** Design approaches for determining the geodesic and non-geodesic isotenoid toroids were presented. The results indicated that the meridian curve of the classical isotenoid dome can become closed if the axial load reaches a sufficient value. The results showed that the isotenoid toroid has a significantly lower weight than the circular toroid at any equal volume and internal pressure. In addition, the combination of isotenoids with non-geodesics provides a novel and effective solution to improve the weight efficiency of toroidal vessels as well as to increase the gravimetric and volumetric

densities of compressed gaseous storage. The ability for improving the structural performance and satisfying the manufacturing requirements becomes here a fact.

13.2.3 Isotensoid pressure vessels with unequal polar openings

A design method for determining isotensoid domed pressure vessels with unequal polar openings was elaborated. With the root searching algorithm for determining two slippage coefficients that fulfilled the winding conditions, the isotensoid domed pressure vessels with unequal polar openings were created. The present method provided a straightforward tool for immediate creation of domed pressure vessels with unequal polar openings. While providing sufficient flexibility for dimensioning winding trajectories, the fibers placed according to the non-geodesic trajectories are still equally tensioned throughout the whole structure.

13.2.4 Continuum-based design of pressure vessels

- **Domed pressure vessels:** A design method for determining the optimal meridian shape and related structural efficiency for continuum-based domes was outlined, and the effect the employment of non-geodesic trajectories can have on the dome geometry and performance was evaluated. It is concluded that the structural efficiency of filament-wound domes can be improved by using non-geodesic trajectories, and that the vessel performance increases with the increase of the slippage coefficient. The results also revealed that the non-geodesic domes form a preferable alternative for storage spaces having limited height. The available design space is sufficiently enlarged by the use of non-geodesics; this particularly reflects on improved structural performance, while still being able to satisfy the conditions of the winding process.
- **Toroidal pressure vessels:** A design method for determining the optimal meridian profiles of continuum-based toroids was presented, and the effect of the cross-sectional shapes on the geometry and the weight of the continuum-based toroids was also evaluated. The cross-sectional shapes and the vessel weight of the circular and the continuum-based optimal toroids were respectively determined at equal volumes and internal pressures; the results demonstrated that the optimal toroidal pressure vessel provides a significantly lower weight and lower aspect ratio than the circular one, and thus leads to better performance and an interesting alternative to spaces having limited height and volume. In addition, the optimal toroids has better structural performance as compared to the optimal

Chapter 13

classical vessel (quasi-ellipsoidal); this is mainly triggered by the relatively homogeneous thickness distribution over the vessel surface as a result of the absence of end enclosures.

13.2.5 Integral design and manufacturing of toroidal pressure vessels

An integral design and production method for filament-wound toroidal pressure vessels was systematically developed. The number of required fiber bands (dictated by structural optimization) corresponded exactly to the necessary number of wound circuits in order to create a uniform and full coverage patterns. The optimal fiber trajectories suited various possible winding patterns due to their geometric flexibility and did satisfy the uniform and full coverage conditions well. The solution eliminates excess windings and guarantees minimum number of wound circuits and maximum utilization of the fiber strength. Compared to optimal geodesics, the results also showed that optimal non-geodesic patterns lead to better distribution of the fiber strength in meridional and parallel directions and consequently improve the structural efficiency of toroidal pressure vessels.

13.2.6 Elasticity solution of thick-walled filament wound pressure vessels

An overview of 3D elasticity solutions of the stresses and strains induced by the internal pressure loading, the hygrothermal effects and the twisting moment was presented. The 3D effective elastic constants and the most commonly used 3D failure criteria for cylindrically anisotropic materials were also presented. A simple and efficient elasticity solution for thick-walled filament-wound pressure vessels was given, taking the through-thickness stress gradients and the in-plane twisting into account. It was found that the addition of the liner and the increase of its thickness result in smoother stress gradients and more homogenous stress distributions through the vessel wall and can thus improve the vessel performance. In addition, it is concluded that the use of a high-anisotropy composite material or a low-modulus metal liner can lead to a lower equivalent stress of the liner and should be chosen when the yield of metal inner liner becomes a critical issue for the failure of a pressure vessel; a high-anisotropy composite material combined with a high-modulus metal liner reserves more additional strength to which the composite overwrap may be subjected prior to failure.

13.3 Achievements

- Derivation of generalized optimality conditions from the minimum strain energy criterion, which relates the vessel geometry, material anisotropy parameter and the winding angle.
- The specific applications and feasible intervals of the optimality condition for various types of lamination.
- Determination of netting-based optimal fiber trajectories for winding circular toroidal pressure vessels, instead of using geodesics and semi-geodesics.
- Investigation of fiber trajectory stabilities on the torus in terms of the slippage and bridging tendencies.
- Determination of the cross-sectional shapes of geodesic-isotensoid toroidal pressure vessels, by forcing the geodesic-isotensoid dome profiles to be closed.
- A novel design combining isotensoid conditions with non-geodesic trajectories, which is able to improve the geometric flexibility and structural performance of pressure vessels.
- Determination of the isotensoid pressure vessels with unequal polar openings.
- Determination of the non-geodesic-isotensoid toroidal pressure vessels.
- Determination of the bellow-shaped pressure vessels based on non-geodesic trajectories and continuum lamination theory.
- Determination of the optimal dome shapes through the combination of the non-geodesic equations and the optimality conditions, where a specific function was chosen to describe the distribution of the slippage coefficients.
- The feasible intervals of the governing equations for netting- and continuum-based dome profiles.
- Determination of the optimal non-geodesic trajectories for winding circular toroidal pressure vessels based on the continuum lamination theory, which showed the use of the non-geodesics can achieve better vessel performance.
- Determination of the optimal cross-sectional shapes for toroidal pressure vessels based on the optimality condition and continuum lamination theory.
- Derivation of the kinematic model and machine movement of the toroidal winder.
- Derivation of the "Diophantine" equations that enable the fibers to fully cover the mandrel surface.
- 3D elasticity solution for thick-walled filament-wound pressure vessels taking the through-thickness stress gradients and in-plane twisting into account, where the best combinations of fiber/matrix/liner materials were demonstrated.

13.4 Recommendations and Future Directions

13.4.1 Strength prediction based on progressive failure analysis

In this dissertation the failure of composite pressure vessels was predicted using first ply failure (FPF); however, filament wound structures can retain significant internal pressure after failure of the first ply. Thus, a progressive failure analysis, which takes into account the material properties degradation, should be considered to provide a more accurate prediction for the ultimate strength and burst pressure of filament wound pressure vessels.

13.4.2 Closed-form solution of composite toroidal shells

The linear membrane theory presented here for obtaining the stress and deformation of a toroidal shell does yield a singularity at the crest (a transition from positive to negative curvature of the torus). It is thus difficult to find an exact solution valid for a complete meridian ($0 \leq \varphi \leq 2\pi$); in addition, the displacement form governing equation is very complicated and hard to be resolved. In the future some simplified or reduced forms of the general toroidal equation would be considered to give more reasonable and effective solutions around the crests.

13.4.3 Finite element analyses

The basic equations were here presented using anisotropic elasticity theory; however, in the case of some complex design scenarios, e.g. stress concentration around the pole or the cut-outs, thick-walled designs considering transverse shear effects and progressive damage prediction, the analytical solutions are rather complicated and difficult. It is therefore necessary to use finite element method (FEM) to analyze the behavior of filament wound pressure vessels having a complex geometry and loading distribution, taking into account not only the modeling of (non-) geodesic trajectories, but also the complex failure mechanism.

13.4.4 Accurate estimation for laminate thickness distribution

The present prediction for the laminate thickness over the vessel surface can only be considered as a simple and rough approximation at the polar area. When the winding angle approaches 90° the laminate thickness becomes infinitely high. This singularity appears because in deriving the thickness distribution we actually assume that the fiber band width is considered negligible and all the fiber bands have the same winding angle and are tangent to same parallel circle. Therefore, a more reliable and accurate thickness schematization would be created by considering the applied fiber band dimensions. Although this subject is sufficiently covered in the literature, the assessment and refinement of the available thickness approximations would be needed.

13.4.5 Shape optimization for thick-walled filament wound domes

To the best of the author's knowledge, no extensive study has yet been conducted on the inverse optimization problem for determining the optimal meridian shapes of 3D thick-walled domes with arbitrary curvature and variable thickness along the meridian direction. Due to the increased laminate thickness, the dome shape will significantly deviate from the 2D-based optimal one, particular at the regions near the poles where the thin-walled analysis is no longer applicable. When the optimal design is based on 2D thin-walled theory, the obtained ultimate strength and vessel performance are usually overestimated as compared to the actual values. Therefore, a novel approach based on 3D thick-shell theory would be proposed for calculating the optimal dome shapes including the effects of thickness accumulation.

13.4.6 Transverse shearing, liner elastoplasticity and stacking sequence

Since the present analysis for thick-walled pressure vessels can only be considered as a simple solution for which the transverse shear effects are considered negligible, a more complete and reliable solution should be created by considering through-thickness shear stresses and deformations. Future study should also focus on the non-linear elastic solution which incorporates the full transverse shear effects; in addition, the metal liner would be also considered as an elasto-plastic material, able to yield prior to the failure of the composite overwrap. The influence of the stacking sequence on the stress and displacement distributions would also be investigated to find the optimal laminate lay-up.

13.4.7 Advanced toroidal winders

Since a winding machine can have up to 6 individual axes, multi-axis (3~6 axes) toroidal winder configurations would be developed to produce toroidal vessels with higher placement accuracy and performance. A dedicated CAD system with a more reliable collision avoidance procedure would also be developed to automatically calculate the optimal fiber patterns and offer kinematic simulations of the toroidal winder.

13.4.8 Other vessel shapes, computer software and experiment

In addition to cylinders, domes and toroids, several other pressure vessels like spheres, ellipsoids, paraboloids, and hyperboloids are also frequently used in various industries; these shapes of pressure vessels would also be considered as design objectives in the future study. Moreover, a dedicated and all-embracing software and database for design, optimization and production of filament-wound pressure vessels should be created. Further elaboration and experimental verification of the proposed designs for pressure vessels is also here recommended.

Acknowledgements

First and foremost, I would like to express my deepest and sincerest gratitude to my supervisor, Dr. Sotiris Koussios, for his remarkable patience and continuous support throughout this study. His support to my research, particularly his brilliant idea of the isotenoid-based cross sections for toroids, and his insight into the importance of thick-walled designs in successfully commercializing hydrogen storage vessels, are essential and proved extremely significant. His solid theoretical background and rigorous professional attitude are good examples of mine. His critical comments at the periodical assessments always guide the research to a right direction.

I also wish to extend my deepest gratitude to my promotor, Prof. Adriaan Beukers, for providing me with his continued guidance, advice, encouragement and financial support throughout the course of the investigation and successful completion of this dissertation. Adriaan acts like my academic father, who accepted me in Kyoto, Japan and then helped me realize my desire for research in filament wound structures.

Special thanks to Lisette Vollmer for her encourage and workload relief. I appreciate her helping me adapt to the Dutch way of life, especially at the beginning of my arrival.

I would like to take this opportunity to thank Lucas Van Den Akker and Jack Wetzels from Protension Composites B.V for sharing their insights and considerable knowledge and experience in filament winding with me.

I highly appreciate all members of my doctoral examination committee for taking the time to review and comment on my thesis, and for taking the long journey to attend my defence.

Acknowledgements

Special thanks are here given to Chongxin Yuan, Lucas Van Den Akker and Bradley Regina for being excellent office mates, for having many interesting and helpful discussions, for listening to my complaints and for supporting me in the difficult times that inevitably occur when doing a Ph.D. I would like to extensively thank other colleagues who also contributed to this dissertation with their ideas, expertise and critical remarks: Hao Cui, François Geuskens, Otto Bergsma and Kurian Joseph. In addition, Huajie Shi, Lei Shi, Duanke Zhang, Peng Zhuo, Xiaofeng Ma, Shafqat Rasool, Jordy Balvers, Natcha Chamnandechakun, Peerawan Wiwattananon, Paola Carnevale, Adrian Fernandez Vigo, Ab van Geenen belong also to the group of fun-increasing parameters.

In regard to my living environment, special thanks to Hui Yu, Qingshi Song, Yingxia Qu, Hong Liu, Ning Kang, Jianing Wang, Hao Chen, Jie Yang, Jia Wan, Junchao Shi, Ping Liu, Wei Liu for being the best friends one can have.

I wish to express my greatest appreciation to my parents, for their understanding, patience, encouragement, support, and for helping realize and accomplish my childhood dreams.

Finally I come to the very dedicated last paragraph, where the meaning of words is not sufficient enough to deliver my appreciation. I would like to thank my wife Dongjuan Xiao, for her love, understanding, encouragement and emotional sustenance during these difficult, but unforgettable times. Thanks a million for doing most of the housework and for putting a smile on my face everyday. Without her, this work would not have been possible at all.

Curriculum Vitae

Lei Zu was born on the 9th December, 1983 in Anqing, China. After finishing his secondary education at Anqing No.1 middle school, China, he majored in Mechanical Engineering at Hefei University of Technology, Hefei, China. He graduated in July 2004, with “cum laude” for his B.Sc. in Mechanical Engineering. In the same year, he attended the Department of Engineering Mechanics, Xi’an University of Technology, where he obtained his M.Sc. with “cum laude” in April 2007, on the development of filament wound toroidal pressure vessels. During February 2007 to November 2007, he was employed as a technical staff at the Research Institute for Applied Mechanics at Kyushu University, Japan. In December 2007 he moved to Delft University of Technology and started his Ph.D. research at the group for Design & Production of Composite Structures, headed by Prof. A. Beukers. The research he conducted in this group has resulted in more than 20 international publications. His interests are composite pressure vessels, filament winding process, composites design & optimization, football, pingpong and karaoke.

List of Publications

Journal Papers

1. Zu L, Koussios S, Beukers A. Design of filament-wound circular toroidal hydrogen storage vessels based on non-geodesic fiber trajectories. *International Journal of Hydrogen Energy* 2010; 35: 660-70. (IF: 4.053)
2. Zu L, Koussios S, Beukers A. Optimal cross sections of filament-wound toroidal hydrogen storage vessels based on continuum lamination theory. *International Journal of Hydrogen Energy* 2010; 35: 10419-29. (IF: 4.053)
3. Zu L, Koussios S, Beukers A. Design of filament-wound domes based on continuum theory and non-geodesic roving trajectories. *Composites Part A: Applied Science and Manufacturing* 2010; 41: 1312-20. (IF: 2.338)
4. Zu L, Koussios S, Beukers A. Design of filament-wound isotensoid pressure vessels with unequal polar openings. *Composite Structures* 2010; 92: 2307-13. (IF: 2.028)
5. Zu L, Koussios S, Beukers A. Shape optimization of filament wound articulated pressure vessels based on non-geodesic trajectories. *Composite Structures* 2010; 92: 339-46. (IF: 2.028)
6. Zu L, Koussios S, Beukers A. Integral design for filament-wound composite pressure vessels. *Polymers & Polymer Composites* 2011; 19: 413-20. (IF: 0.058)
7. Cui H, Li Y, Koussios S, Zu L, Beukers A. Bridging micromechanisms of Z-pin in mixed mode delamination. *Composite Structures* 2011; 93: 2685-95. (IF: 2.028)
8. Yuan C, Bergsma OK, Koussios S, Zu L, Beukers A. Optimization of sandwich composites fuselages under flight loads. *Applied Composite Materials* 2011, Article in Press. (IF: 0.723)
9. Zu L, Koussios S, Beukers A. Design of filament wound toroidal pressure vessels with circular and isotensoid-based cross sections. *Journal of Materials Engineering*, 2008, S1: 78-86.

List of Publications

10. Zu L, Koussios S, Beukers A. Optimal design of filament-wound composite toroids. *Journal of Materials Engineering*, 2009, S2: 413-19.
11. Zu L, Koussios S, Beukers A. Design and production of toroidal pressure vessels based on non-geodesic roving trajectories. *World Journal of Engineering* 2008; 5: 230-1.
12. Zu L, Koussios S, Beukers A. Analysis of multi-layered thick-walled filament-wound pressure vessels. *Composite Structures*, Submitted.
13. Zu L, Koussios S, Beukers A. Three-dimensional stress analysis of thick-walled filament-wound cylinders under internal pressure – A review of the literature – Part I: Linear elastic solutions. *Composites Part A: Applied Science and Manufacturing*, Submitted.

Conference Proceedings

1. Zu L, Koussios S, Beukers A. Design and production of toroidal pressure vessels based on non-Geodesic roving trajectories. 16th Annual International Conference on Composites / Nano Engineering. Kunming, China, July 10-16, 2008.
2. Zu L, Koussios S, Beukers A. Design of filament wound toroidal pressure vessels. 23rd Annual Conference of the American Society for Composites. Memphis, TN, September 9-11, 2008.
3. Zu L, Koussios S, Beukers A. Pattern design and optimization of filament wound articulated pressure vessels. 23rd Annual Conference of the American Society for Composites. Memphis, TN, September 9-11, 2008.
4. Zu L, Koussios S, Beukers A. Design of filament-wound toroidal pressure vessels with circular and isotenoid-based cross sections. In: Cui J Ed: SAMPE China Conference & Exhibition. Beijing, 2008.
5. Zu L, Koussios S, Beukers A. Design and production of toroidal pressure vessels based on non-geodesic roving trajectories. In: Hui D, Ed: 16th Annual International Conference on Composites Engineering. Kunming, China, 2008.
6. Zu L, Koussios S, Beukers A. Design of filament-wound isotenoid toroids based on non-geodesic roving trajectories. In: Gillespie JW & Hoa SV, Eds: Proceedings of the 24th Annual American Society for Composites Technical Conference, Newark DE. DEStech Publications, Lancaster PA, USA.
7. Zu L, Koussios S, Beukers A. Design of filament-wound isotenoid pressure vessels with

- unequal polar openings. In: Ferreira AJM, Ed.: Proceedings of the 15th International Conference on Composite Structures. Porto FEUP.
8. Zu L, Koussios S, Beukers A. Design of filament wound toroidal pressure vessels with circular and isotensoid-based cross sections. In: Cui J, Ed: Proceedings of the 2008 SAMPE Conference, Beijing, China.
 9. Zu L, Koussios S, Beukers A. Optimal design of filament-wound composite toroids. In: Cui J, Ed: Proceedings of the 2009 SAMPE Conference, Beijing, China.
 10. Zu L, Koussios S, Beukers A. Integral design for filament-wound composite pressure vessels. In: Proceedings of 1st International Conference on Advanced Polymer Matrix Composites. Thin Films Society & Harbin University of Technology. Harbin, China, 2010.
 11. Zu L, Koussios S, Beukers A. Optimal cross-sectional shapes of filament-wound toroids based on the continuum lamination theory. In: Kollar L, Ed: 14th European Conference on Composite Materials, ECCM 14. Budapest University of Technology & Economics, Budapest, Hungary.
 12. Zu L, Koussios S, Beukers A. Three-dimensional elasticity solution of thick-walled filament-wound hydrogen storage vessels. In: Ferreira AJM, Ed.: Proceedings of the 15th International Conference on Composite Structures. Porto FEUP.

Nomenclature

Abbreviations

2D/3D	Two / Three-dimensional
LaRC	NASA Langley Research Center
Aspect ratio	Height-to-width ratio of a cross section
CAD	Computer aided design
CFRP	Carbon fiber reinforced polymer/plastic
CNC	Computerized Numerical Control
CNG	Compressed natural gas
DOE	U.S. Department of Energy
FEA/FEM	Finite element analysis / method
FW	Filament winding
PF	Performance factor
PVC	Polyvinyl chloride
SQP	Sequential quadratic programming
UD	Unidirectional

Matrices & Vectors

A	Extensional stiffness matrix
a	Extensional compliance matrix
B	Coupling stiffness matrix
D	Bending stiffness matrix
C	Arclength vector describing a curve
F	Force vector, general

Nomenclature

N	Principal normal vector to a curve
n	Unit vector normal to a surface
P	Position vector of a doffing point
Q	Reduced stiffness matrix
\bar{Q}	Transformed reduced stiffness matrix
R	<i>Reuter</i> matrix
S	Vector function describing a surface Reduced compliance matrix
\bar{S}	Transformed reduced compliance matrix
T	Unit vector tangent to a curve Transformation matrix
X	Vector of design variables
κ	Principal normal curvature vector

Scalars (Latin)

<i>A</i>	External axial force
<i>a</i>	Dimensionless axial force
<i>B</i>	Fiber band width
<i>C</i>	Constant, general
<i>c</i>	Polar opening radius Maximum value of slippage coefficients Constant of integration Moisture concentration
<i>D</i>	Constant of integration
<i>E</i>	Coefficient of the first fundamental form Modulus of elasticity
<i>F</i>	Coefficient of the first fundamental form Force magnitude, general Strength parameters Failure index of Tsai-Wu criterion Stress function

f	Coefficient of the second fundamental form Fiber force per unit length Function, general
G	Coefficient of the first fundamental form Shear modulus
g	Function, general
H	Mean curvature
h	Height, general 90° layer
I	Performance factor
i	Counter
j	Counter
K	Gaussian curvature Ratio of fiber stress at an arbitrary parallel to stress at the equator Relative bending radius Rotation number of the feed eye
k	Material anisotropy parameter Counter
L	Coefficient of the second fundamental form Curve length
M	Coefficient of the second fundamental form Mass, general
m	Functions of the fiber angle and material properties
N	Coefficient of the second fundamental form Membrane force in a shell Rotation number of the mandrel Number of fiber bundles
n	Counter Number of laminae Number of interpolation knots
O	Origin of coordinates
P	Points or knots
p	Internal pressure Burst pressure

Nomenclature

R	Radius of curvature Equatorial radius
r	Radial coordinate Radius of the tube of a torus
S	In-plane shear strength
s	Arc length
t	Thickness, general Time, general
U	Elastic strain energy density
u	Curvilinear coordinate in the parametric surface (u -curve) Displacement, general
V	Internal volume of a pressure vessel
v	Curvilinear coordinate in the parametric surface (v -curve)
W	Weight of a pressure vessel
X	Strength in the fiber direction (tensile or compressive) X -coordinate
Y	Strength in the transverse direction (tensile or compressive) Y -coordinate
Z	Strength in the through-thickness direction (tensile or compressive) Z -coordinate
z	Axial coordinate

Scalars (Greek)

α	Winding angle Thermal expansion coefficient
β	Lagrange multiplier Hygroscopic expansion coefficient
Γ	Christoffel symbol of the second kind
γ	Specific weight Shear strain
ε	Strain, general Level of accuracy necessary to ensure iterative convergence
ζ	Dimensionless axial coordinate

η	Hoop-to-helical thickness ratio
θ	Angular coordinate in the parallel direction
κ	Curvature
λ	Slippage coefficient
μ	Coefficient of friction
ν	Poisson's ratio
ρ	Dimensionless radial coordinate
σ	Stress, general
	Ultimate fiber stress in tension
τ	Shear stress, general
Φ	Rotation angle of the mandrel
φ	Angular coordinate in the meridional direction
χ	Parallel-to-meridional force ratio (biaxial ratio)
ω	Angular velocity

Indices

0	Polar opening related
	Initial position related
1	First principal material direction (Longitudinal direction)
2	Second principal material direction (Transverse direction)
3	Third principal material direction (Through-thickness direction)
C	Compressive
c	Circular toroids
eq	Equator
f	Fiber related
	Friction
g	Geodesic
iso	Isotenoid
m	Mandrel
max	Maximum value
min	Minimum value
n	Normal direction
net	Netting-based

Nomenclature

opt	Optimal
S	Shear stress/strength
T	Tensile stress/strength
α	$\pm\alpha$ layers

Special Functions & Operations

∞	Infinity
C	Shortcut for “continuity”
c	Shortcut for “cosine”
	Shortcut for “constant value”
d	Differential
f	Functional operation
s	Shortcut for “sine”
\times	Vector outer product (cross product)
\cdot	Vector inner product (dot product)
	Scalar multiplication
'	First derivative
"	Second derivative
&	And